Misfit-layered cobalt oxides for thermoelectric energy conversion

Von der Fakultät Chemie der Universität Stuttgart
zur Erlangung der Würde eines Doktors der
Naturwissenschaften (Dr. rer. nat.) genehmigte Abhandlung

Vorgelegt von
Gesine Büttner
aus Uelzen

Hauptberichter:	**Prof. Dr. Anke Weidenkaff**
Mitberichter:	**Prof. Dr. Jochen Mannhart**
Prüfungsausschussvorsitzender:	**Prof. Dr. Thomas Schleid**

Tag der mündlichen Prüfung: 02.06.2017

Institut für Materialwissenschaft der Universität Stuttgart
2017

Dedicated to my parents Gernot and Irmtraut Saucke

Table of Contents

Symbols and Abbreviations

α	Seebeck coefficient
δ	Oxygen content in $[Ca_2CoO_{3-\delta}][CoO_2]_{1.62}$
Δ_{cf}, Δ_D	Energy splitting of the 3d t_{2g} und e_g states through crystal field splitting and distortion
ϵ	Emissivity of light
η	Conversion efficiency
η_C	Carnot efficiency
η_r	Reduced efficiency
θ	Incident angle in (XRD)
θ_D	Debye temperature
$\kappa, \kappa_l, \kappa_e$	Thermal conductivity, lattice and electronic thermal conductivity
λ	Thermal diffusivity
Λ	Mean free path of phonons
μ	Mobility of charge carriers
ν	Phonon speed of sound
ρ	Electrical resistivity
ρ_H	Hall resistivity
$\varrho, \varrho_{th}, \varrho_{rel}$	Measured density, theoretical density, and relative density $\varrho_{rel} = \varrho/\varrho_{th}$
σ	Electrical conductivity
τ	Relaxation time
A_p, A_n	Cross-sectional area of a leg in a converter
a, b_1, b_2, c	Lattice parameter of $[Ca_2CoO_{3-\delta}][CoO_2]_{1.62}$
e	Elementary charge
c_p, C_p	Specific heat at constant pressure, $C_p = c_p/\bar{M}$
c_V	Specific heat at constant volume
E	Energy

E_F	Fermi level
k	Wave number
k_B	Boltzmann constant
I	Electrical current
J	Electrical current density
L	Lorenz number
l	Length of a thermoelectric leg
$m, \bar{M}$	Mass, and average atomic mass of a compound material
n, p	Hall carrier concentration
q	Heat flux
Q	Heat flow
P	Power output
R	Electrical resistance
t	Time
T, ΔT	Temperature, temperature difference
V	Volume
V, V_{OC}, V_H	Voltage, Open circuit voltage, Hall voltage
y^{nom}	Nominal Co content in $Ca_3Co_{ynom}O_{9+\delta}$
ZT	Figure of merit
DOS	Density of states
DSC	Differential scanning calorimetry
LFA	Laser flash apparatus
RBS	Rutherford backscattering spectrometry
SC	Soft chemistry
SEM	Scanning electron microscopy
SPS	Spark plasma sintering
SSR	Solid state reaction

TGA	Thermal gravimetric analysis
PPMS	Physical property measurement system
XRD	X-ray diffractometer

Abstract

The conversion of waste heat into electrical current by a thermoelectric converter can significantly contribute to a more sustainable usage of our resources. The p-type misfit-layered $[Ca_2CoO_{3-\delta}][CoO_2]_{1.62}$ *is known for its promising conversion efficiency, which yet needs to be improved significantly for commercial applications. The efficiency of a material increases with the Figure of Merit* $ZT = \sigma\alpha^2/\kappa$*, with Seebeck coefficient* α*, electrical conductivity* σ*, and thermal conductivity* κ*. The aim of this thesis is to provide a better understanding of the electrical and the thermal properties of the complex* $[Ca_2CoO_{3-\delta}][CoO_2]_{1.62}$ *and to use this understanding to improve the efficiency of converters. Accordingly, (i) the increase of ZT via cation substitution is shown; (ii) a better understanding of the electrical transport above room temperature is developed; (iii) the effect of stoichiometric defects and secondary phases on the thermoelectric properties is investigated. Finally, (iv)* $[Ca_2CoO_{3-\delta}][CoO_2]_{1.62}$ *-* $CaMn_{0.97}W_{0.03}O_{3-\delta}$ *– converters are fabricated and the efficiency is increased by a suitable converter design.*

More specifically, the unexplored influence of Ru and In substitution on the thermoelectric properties of the polycrystalline $[Ca_2CoO_{3-\delta}][CoO_2]_{1.62}$ *is investigated. While In does not have a positive effect, Ru for Co substitution increases ZT up to 20 %. This increase stems from a strong reduction of the thermal conductivity - which is probably induced by resonance scattering - while the decrease of the power factor* $\alpha^2\sigma$ *is minor.*

The electrical transport mechanism of pure and Ru-substituted $[Ca_2CoO_{3-\delta}][CoO_2]_{1.62}$ *between room temperature and 800 K so far lacks a coherent theoretical model. Surprisingly, the framework of Anderson localization, which was developed to describe conduction in an impurity band of semiconductors, can be applied to the oxide. The Anderson model assumes that transport happens via charge-carrier hopping in a random Coulomb potential. For* $[Ca_2CoO_{3-\delta}][CoO_2]_{1.62}$*, charges are considered to hop between Co sites in the* CoO_2 *layer, while the random potential originates from interactions with the mismatched* $Ca_2CoO_{3-\delta}$ *layer. The presence of the ionized Ru atoms further alters the Coulomb potential, which increases the activation energy of the transport behavior. This understanding might contribute to the development of better theoretical models for the prediction of the thermoelectric properties of substituted* $[Ca_2CoO_{3-\delta}][CoO_2]_{1.62}$ *compounds.*

A further improvement of the materials efficiency can be achieved by systematic introduction of stoichiometric defects and impurity phases. Here, the unexplored influence of the Co/Ca ratio on the thermoelectric properties of $[Ca_{2-w}CoO_{3-\delta}][CoO_2]_{1.62}$*, and the effect of* Co_3O_4 *impurity phase are investigated. It is shown that an increasing Co/Ca ratio in the* $[Ca_{2-w}CoO_{3-\delta}][CoO_2]_{1.62}$ *phase leads to a larger figure of merit ZT induced by a strong resistivity drop. The decrease of resistivity stems from additional p-type charge carriers created by the formation of Ca vacancies. The* Co_3O_4 *impurity phase increases the thermal conductivity of the composite samples and leads to a reduction of ZT when the volume fraction of the* Co_3O_4 *phase is increased from 1% to 3%. Hence, the best figure of merit is expected close to the upper phase boundary of the* $[Ca_{2-w}CoO_{3-\delta}][CoO_2]_{1.62}$ *phase.*

Not only the figures of merit of the materials, but also the design of a thermoelectric converter determines the device efficiency. In a converter, a p-type and a suitable n-type thermoelectric material are connected electrically in series and thermally in parallel. Here, $[Ca_{2-w}CoO_{3-\delta}][CoO_2]_{1.62}$ *is combined with the n-type* $CaMn_{0.97}W_{0.03}O_{3-\delta}$ *and the device efficiency is improved by a variation of the ratio* A_p/A_n *of the cross section areas of the legs. The good agreement between the experimental values and the predictions of the compatibility model show the high quality of the fabricated devices and the value of the model for the optimization of the converter design. The adjustment of* A_p/A_n *improves the power output and the efficiency of the converters, where the best volume and area power densities exceed published high temperature values. The achieved efficiency of 1.08 % at a temperature of 1085 K at the hot side is close to the theoretical expected efficiency and can be further improved via ZT.*

Zusammenfassung

Die Wandlung von Abwärme in elektrischen Strom mittels thermoelektrischer Konverter kann beträchtlich zur nachhaltigeren Nutzung unserer Ressourcen beitragen. Das p-leitende geschichtete Misfit-Kobaltoxid $[Ca_2CoO_{3-\delta}][CoO_2]_{1.62}$ zeichnet sich durch eine vielversprechende Konversionseffizienz aus, die für eine kommerzielle Anwendungen jedoch noch deutlich verbessert werden muss. Die Effizienz eines Materials steigt mit der thermoelektrischen Gütezahl $ZT = \sigma\alpha^2/\kappa$, wobei α den Seebeck Koeffizient, σ die elektrische und κ die thermische Leitfähigkeit bezeichnet. Ziel dieser Arbeit ist es, die thermischen und elektrischen Eigenschaften des komplexen $[Ca_2CoO_{3-\delta}][CoO_2]_{1.62}$ besser zu verstehen und somit die Effizienz von Konvertern gezielt zu steigern. Hierzu wird (i) die Erhöhung von ZT mittels Kation-Substitution gezeigt, (ii) ein besseres Verständnis des elektrischen Transportes oberhalb von Raumtemperatur entwickelt, (iii) der Effekt stöchiometrischer Defekte und Fremdphasen auf die thermoelektrischen Eigenschaften untersucht und (iv) schließlich die Effizienz von $[Ca_2CoO_{3-\delta}][CoO_2]_{1.62}$ - $CaMn_{0.97}W_{0.03}O_{3-\delta}$ - Konvertern durch ein geeignetes Design gesteigert.

Im Detail wird der Effekt von Ru- und In-Substitution auf die thermoelektrischen Eigenschaften von polykristallinen $[Ca_2CoO_{3-\delta}][CoO_2]_{1.62}$ untersucht. Während In keinen positiven Einfluss hat, steigert die Substitution von Co mit Ru die Gütezahl ZT um bis zu 20%. Diese Verbesserung resultiert aus der starken - wahrscheinlich durch Resonanzstreuung induzierten - Verringerung der thermischen Leitfähigkeit bei nur geringer Verringerung des Leistungsfaktors $\alpha^2\sigma$.

Zwischen Raumtemperatur und 800 K konnte bisher kein passendes Model identifiziert werden, das den elektrischen Transport in $[Ca_2CoO_{3-\delta}][CoO_2]_{1.62}$ und den Effekt von Substitutionen zufriedenstellend beschreibt. Überraschenderweise kann das Anderson-Lokalisierung-Models, das eigentlich für Störstellenleitung in Halbleitern entwickelt wurde, die Transportdaten von reinem und Ru-substituierten Kobaltoxid gut erklären. In diesem Model hüpfen die Ladungsträger in einem zufälligen Coulomb-Potential. Im $[Ca_2CoO_{3-\delta}][CoO_2]_{1.62}$ wird von einem Hüpfen zwischen den Co-Plätzen in der CoO_2 Schicht ausgegangen, wobei das zufällige Potenzial durch die Wechselwirkung mit der fehlangepassten $Ca_2CoO_{3-\delta}$ - Schicht erzeugt wird. Die Präsenz von ionisierten Ru-Atomen

verändert das Coulomb-Potentials zusätzlich, was zu einer Erhöhung der Aktivierungsenergie führt. Diese Erkenntnis könnte zur Entwicklung bessere Modelle für die Vorhersage der thermoelektrischen Eigenschaften von substituiertem $[Ca_2CoO_{3-\delta}][CoO_2]_{1.62}$ beitragen.

Eine weitere Verbesserung der Materialeffizienz kann durch die systematische Einführung von stöchiometrischen Defekte und Fremdphasen erreicht werden. Konkret wird hier der noch unbekannte Einfluss des Co/Ca-Verhältnisses auf die thermoelektrischen Eigenschafen von $[Ca_{2-w}CoO_{3-\delta}][CoO_2]_{1.62}$, sowie der Einfluss der Co_3O_4 Fremdphase untersucht. Es wird gezeigt, dass ZT mit zunehmendem Co/Ca-Verhältnis in der $[Ca_{2-w}CoO_{3-\delta}][CoO_2]_{1.62}$-Phase durch eine starke Abnahme des Wiederstandes ansteigt. Die Abnahme des Widerstandes resultiert aus der Erhöhung der p-Typ Ladungsträgerdichte durch die Erzeugung von Ca-Leerstellen. Die Fremdphase Co_3O_4 steigert die thermische Leitfähigkeit des Stoffgemisches und verringert ZT bei Erhöhung des Volumenanteils von 1% auf 3%. Das beste ZT wird demnach an der oberen Phasengrenze der $[Ca_{2-w}CoO_{3-\delta}][CoO_2]_{1.62}$-Phase erwartet.

Nicht nur die Gütezahl der Materialien, sondern auch das Design eines thermoelektrischen Konverters beeinflusst dessen Effizienz. In einem Konverter wird ein p- mit einem passenden n-leitenden Material thermisch parallel und elektrisch in Reihe geschaltet. Hier wird $[Ca_{2-w}CoO_{3-\delta}][CoO_2]_{1.62}$ mit dem n-leitende $CaMn_{0.97}W_{0.03}O_{3-\delta}$ kombiniert und die Effizienz durch Variation des Verhältnisses der Querschnittsflächen der Schenkel A_p/A_n verbessert. Die gute Übereinstimmung der experimentellen Werte und mit den Vorhersagen des Kompatibilitäts-Models zeigt die hohe Qualität der fabrizierten Module und den Nutzen des Models bei der Optimierung des Konverter-Designs. Durch die A_p/A_n- Anpassung wird eine Erhöhung der Konverter-Leistung und der Effizienz erziel, wobei die besten Volumen- und Flächenleistungsdichten publizierte Hochtemperaturwerte übertreffen. Die erreichte Effizienz von 1.08 % bei einer Temperatur von 1085 K auf der heißen Seite liegt nahe an der theoretisch erwarteten Effizienz und kann über ZT weiter verbessert werden.

1 General Introduction

Global warming is one of the main challenges humanity is facing and improving the energy efficiency of industrial production processes and vehicle engines is key to a solution. The development of cost-efficient and reliable high temperature thermoelectric converters with high conversion efficiencies can significantly contribute toward this end. Thermoelectric heat recovery can help to limit global warming by reducing greenhouse-gas emissions, decrease the dependence of the society on fossil fuels, and secure the coverage of the rising energy demands [1]. In contrast to other heat conversion techniques, thermoelectric modules are characterized by high reliability and low maintenance costs since no moving parts are involved [2]. Due to these advantages, thermoelectric generators have been used successfully in niche applications where costs are of minor importance, such as nuclear batteries in deep space missions [3] or self-powered remote data communication systems for, e.g., oil and gas pipelines or polar weather stations [2]. In contrast, for consumer market applications, such as solar power conversion [4–7] or heat recovery in automotive applications [3, 8], efficient thermoelectric converters need to be available at low costs. Accordingly, this work focuses on the development of cheap oxide thermoelectric converters.

Fundamentally, a thermoelectric material is a material that generates a significant electrical power output if a temperature difference ΔT is applied. The conversion efficiency η increases with the figure of merit $ZT = \frac{\sigma \alpha^2}{\kappa} T$, where $T = \frac{T_h + T_c}{2}$ is the average of the hot and the cold side temperatures T_h and T_c. The quality of a thermoelectric material is commonly described by ZT, which can be improved by increasing the electrical conductivity σ and the Seebeck coefficient α, or by decreasing the thermal conductivity κ. In the 1960s, ZT was believed to be limited to values smaller than one, but this barrier was surpassed in the last decades. Ideas like the Phonon Glass Electron Crystal (PGEC) concept and nanostructuring approaches [9, 10] led to significant improvements and the discovery of new material classes. In Figure 1.1 the temperature dependence of ZT values of state-of-the-art materials is summarized: Around room temperature, bulk bismuth telluride based materials reach outstanding ZT values of about 1.86 [11], which can be further improved up to 2.4 by using superlattices [12]. However, these materials degrade at temperatures $T \geq 550$ K [13], which renders them unsuitable for many applications. A limited number of materials with promising ZT values, such as half-Heusler alloys [14–17], PbTe [18], Zn_4Sb_3, [19], skutterudites [20, 21] and MnSi

[22] exists for conversion between 400 K-800 K, while Zintl compounds [23], SiGe [24] and oxide materials [25] show promising values between 800 K and 1200 K. The conventional high temperature materials often contain rare or toxic elements like Te, Se, Sb and Pb [26], while other materials like SiGe are expensive and deteriorate in oxidizing atmosphere. In contrast, many oxides show a high chemical stability at elevated temperatures in oxidizing atmospheres and are often composed of abundant elements, which are non-toxic in their oxidized form. Oxides combine promising ZT values with low material cost and allow an environmentally friendly and safe application in air. Due to this high potential for the fabrication of economical converters, the present study concentrates on the investigation of promising cost-efficient high temperature oxides.

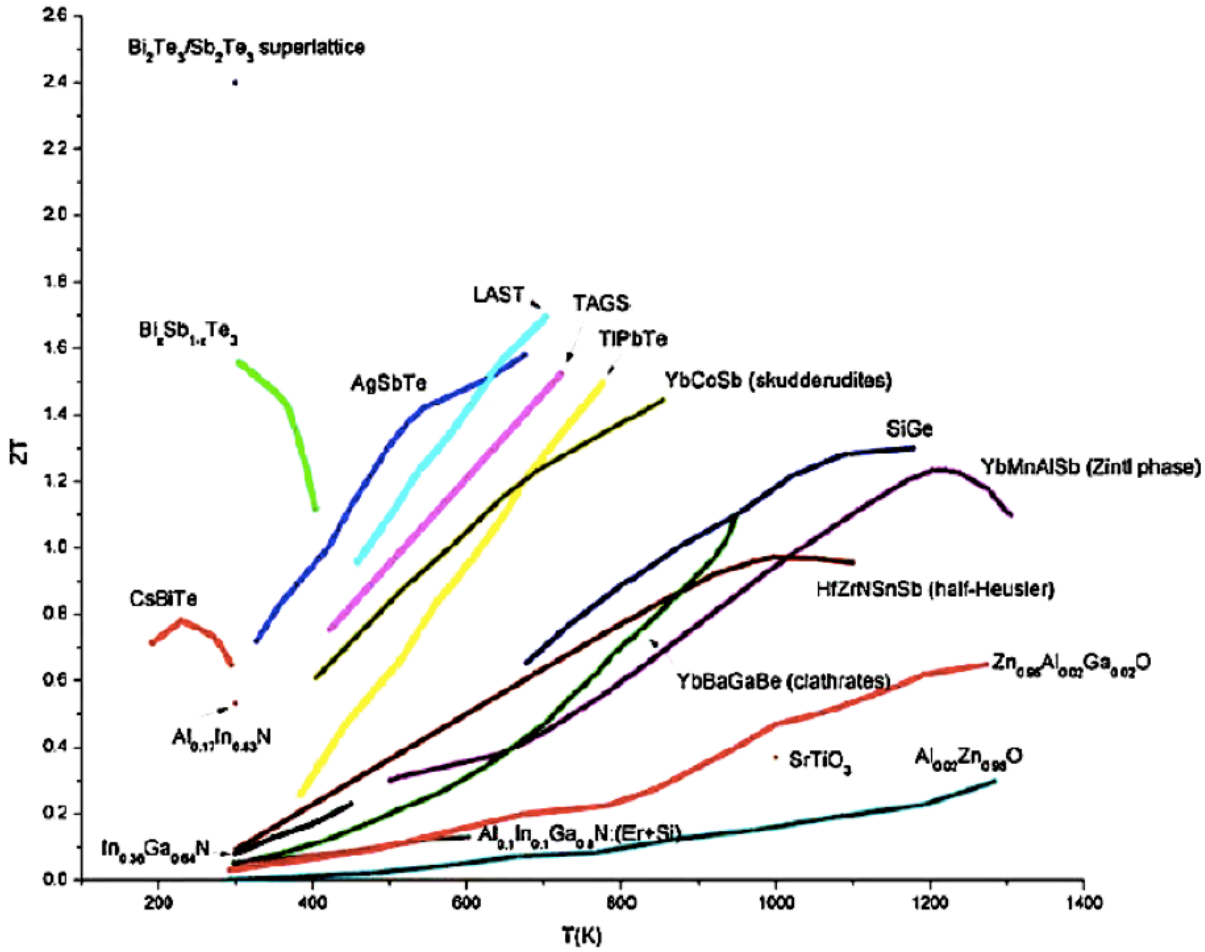

Figure 1.1: Temperature dependent *ZT* values for various state-of-the-art materials, taken from [27].

One of the most promising p-type oxides is the misfit-layered cobalt oxide $[Ca_2CoO_{3-\delta}][CoO_2]_{1.62}$. In the present study it is conveniently abbreviated as "$Ca_3Co_4O_9$" or by its elemental formula (e.g. $Ca_3Co_{3.92}O_{9+\delta}$) in case the exact stoichiometry is relevant and the layer of Co substitution is not clear. This oxide has a good maximum figure of merit of $ZT = 0.87$ at 973 K in single crystals [28], while a maximum of $ZT = 0.61$ at 1118 K was

reached for substituted $Ca_{2.87}Ag_{0.05}Lu_{0.15}Co_4O_9$ bulk material with a complex multi-scale microstructure [29]. The misfit-layered cobalt oxide is characterized by a natural nanoscale superlattice consisting of incommensurate CoO_2 and rock salt-type Ca_2CoO_3 layers. The unusually large Seebeck effect and the good electrical conductivity of the half-metal result from the band structure around the Fermi level E_F, which is mainly determined by the CoO_2 layers. The low thermal conductivity stems from the unique misfit-layered crystal structure. A substitution in the rock salt-type layer allows to further decrease the thermal conductivity and to adjust the carrier concentration without enhancing the electrical charge carrier scattering in the conductive CoO_2 layers.

For large scale industrial applications of $[Ca_2CoO_{3-\delta}][CoO_2]_{1.62}$, several key factors require a deeper understanding and significant improvement. In particular, those are: (i) the figure of merit, which is too low; (ii) the poorly predictable transport behavior at high temperatures; (iii) the effect that impurities and stoichiometric defects have on the thermoelectric properties, since low cost commercial quality devices will inevitably come with such defects; and (iv) the development of stable converters with a suitable n-type material and a proper design to extract the charge current from $[Ca_2CoO_{3-\delta}][CoO_2]_{1.62}$, which is often neglected in the discussion. All of these questions are addressed in this thesis, as described in more detail in the following.

Thus far, ideas for improvement of the figure of merit have largely been obtained from intuition. A coherent theory that predicts the effect of a dopant on the thermoelectric properties of oxides, in particular $[Ca_2CoO_{3-\delta}][CoO_2]_{1.62}$, is still elusive. In this context, the present dissertation systematically investigates the thermoelectric properties of polycrystalline $[Ca_2CoO_{3-\delta}][CoO_2]_{1.62}$ as a function of doping with ruthenium and indium and provides a better understanding of the material properties and the adjustability by systematic cationic substitution. Ruthenium and indium atoms were chosen as substituent because a decrease of the thermal conductivity is expected due to point defect scattering on the heavier atoms.

The transport properties of $[Ca_2CoO_{3-\delta}][CoO_2]_{1.62}$ in the intermediate temperature range between room temperature and 800 K are not well understood yet. At elevated temperatures, the transport can be described by small-polaron hopping. But in the intermediate temperature range, a consistent model that can explain the temperature dependence of the electrical conductivity and the linear increase of the Seebeck coefficient was not presented yet. In the present work, the transport behavior of the non-substituted and the Ru substituted compounds is analyzed in the framework of Anderson localization, which is normally used to describe

impurity band conduction in semiconductors. Based on this model a comprehensive picture of the intermediate temperature transport is developed. This understanding might lead to better theoretical models for the prediction of the thermoelectric properties of substituted $[Ca_2CoO_{3-\delta}][CoO_2]_{1.62}$ compounds.

The *ZT* values reported for misfit-layered cobalt oxide vary strongly [25]. These variations are suspected to partly result from the variable Co/Ca stoichiometry within the stability range of the $[Ca_2CoO_{3-\delta}][CoO_2]_{1.62}$ phase or the formation of tiny amounts of Co_3O_4 or $Ca_3Co_2O_6$ secondary phases. To test this hypothesis, the mechanism responsible for the Co/Ca flexibility within the stability range of $[Ca_2CoO_{3-\delta}][CoO_2]_{1.62}$ and the effect of the flexible Co/Ca ratio on the thermoelectric properties are studied in the present work for the first time. Misfit-layered cobalt oxides with different Co/Ca ratios were fabricated and the differences in the thermoelectric properties are correlated with the appearance of different amounts of Co_3O_4 impurity phase and the changes of the Co/Ca stoichiometry in the $[Ca_2CoO_{3-\delta}][CoO_2]_{1.62}$ phase.

The good thermoelectric properties and the potentially low costs make $[Ca_2CoO_{3-\delta}][CoO_2]_{1.62}$ a good starting material for the fabrication of thermoelectric generators for the demonstration of energy conversion. In a converter, a suitable n-type material has to be combined with the p-type $[Ca_2CoO_{3-\delta}][CoO_2]_{1.62}$. In the present work, $CaMn_{0.97}W_{0.03}O_3$ is chosen as n-type material because it is one of the best high temperature n-type oxides which shows a good *ZT* over a wide temperature range [30]. In addition, the thermal expansion coefficients of the two oxides are very similar [31], which is beneficial for the stability and the reliability of the entire converter. For the fabrication of efficient devices, improvements on various levels are necessary: In addition to the improvement of the material properties, the entire converter has to be designed and tailored with the total conversion efficiency in mind to make best use of the developed materials. In the present work, converter designs with various ratios of the cross-sectional areas for the p- and the n-type leg are investigated experimentally and theoretically in the framework of the compatibility approach. The efficiencies are measured as a function of temperature and show good agreement with the theoretical predictions. Finally, reliable thermoelectric energy conversion is demonstrated in the lab and under rough industrial production conditions including mechanical vibrations and strong temperature variations in the foundry vonRoll casting.

The thesis is structured in 9 chapters. After this general introduction, an overview about thermoelectricity including strategies for the improvement of ZT is given in Chapter 2. Chapter 3 is a comprehensive review about the crystal structure, electronic and thermoelectric properties of $[Ca_2CoO_{3-\delta}][CoO_2]_{1.62}$, which is followed by a brief description of the synthesis and the experimental methods in Chapter 4. The main results of this work are presented and discussed in the Chapters 5-8. The Chapters 5 and 6 cover the effect of Ru and In substitution and analyze the electrical transport mechanism above room temperature. Afterward, the effect of the Co/Ca non-stoichiometry and impurity phases on the thermoelectric properties is discussed, while the improvement of the converters is presented in Chapters 8. Finally, a summary of the results and an outlook are given in Chapter 9.

2 Theoretical background

The quality of a thermoelectric material is usually described by its thermoelectric figure of merit ZT. The first part of this chapter introduces ZT and explains its connection to the thermoelectric conversion efficiency. A good figure of merit can be reached by a large Seebeck coefficient, a large electrical and a small thermal conductivity. For the improvement of ZT a basic understanding of these properties is necessary because their intercorrelation makes enhancement tricky. Accordingly, the aim of this chapter is to impart basic knowledge about the Seebeck effect, the thermal conductivity and their correlation with the electrical conductivity due to electrical charge carriers. The second part of this chapter focuses on thermoelectric converters consisting of p-and n-type materials. After a short description of the structure of a thermoelectric converter, the compatibility approach is introduced. This theoretical model is applied in Chapter 8 for the improvement of the converter efficiency by adjusting the converter geometry. Finally, an overview of state of the art oxide converters and their reported performances is given.

2.1 Thermoelectricity

The following section provides the definition of the relevant quantities of thermoelectricity, namely the figure of merit, the Seebeck coefficient, and the electrical and thermal conductivity. These parameters are interdependent which is shown to arise from a common fundamental origin. Finally, the temperature dependence of these parameters is discussed.

2.1.1 Thermoelectric efficiency and the figure of merit

If a temperature difference ΔT is applied across a thermoelectric material, the Seebeck effect generates an electrical voltage $V = \alpha\Delta T$. This voltage drives an electrical current I through the thermoelectric material with resistance R and a connected load, whose resistance R_l determines the produced power output:

$$P = I^2 R_l = \left(\frac{V}{R_l+R}\right)^2 R_l = \left(\frac{\alpha\Delta T}{R_l+R}\right)^2 R_l. \quad (1)$$

The conversion efficiency

$$\eta = \frac{P}{Q_h}. \tag{2}$$

of a thermoelectric material is generally defined by the ratio of produced power P and the power entering the material in the form of a heat flow from the hot side

$$Q_h = \kappa\Delta T + \alpha T_h I - \frac{I^2 R}{2}. \tag{3}$$

Three effects contribute to the total heat flow Q_h: (i) the conductive heat flow $\kappa\Delta T$, (ii) heating induced by the Peltier effect $\alpha T_h I$, and (iii) and resistive losses due to Joule heating $I^2\,R/2$. With given material properties and a temperature difference ΔT, the efficiency η can be maximized experimentally via an adjustment of the external load resistance R_l. The maximum efficiency

$$\max(\eta) = \frac{\Delta T}{T_h}\,\frac{\sqrt{1+ZT}-1}{\sqrt{1+ZT}+\frac{T_c}{T_h}} \coloneqq \eta_C \eta_r \tag{4}$$

is reached for a load resistance of $R_l = R\sqrt{1+ZT}$ [32]. This equation defines the figure of merit

$$ZT = \frac{\sigma\alpha^2}{\kappa}T, \tag{5}$$

and $\eta_C = \Delta T/T_h$ and η_r are the Carnot efficiency and the reduced efficiency, respectively. The parameters σ, α, κ, ZT and $T = (T_h + T_c)/2$ are average values across the sample. The dependence of the maximum efficiency on ZT is illustrated as a function of the hot side temperature T_h for a fixed cold side temperature T_c =300 K in Figure 2.1. The total efficiency increases with increasing ZT and converges against the Carnot efficiency $\eta_C = \Delta T/T_h$ (η_r converges against unity) as ZT goes to infinity.

Because the efficiency depends on ZT, thermoelectric research focuses on the enhancement of the figure of merit by tailoring of the material properties. In general, the figure of merit can be improved by (i) reduction of the thermal conductivity κ, and (ii) the increase of the power factor $\sigma\alpha^2$ (enumerator of ZT in Equation (5)). However, these material parameters are not independent from each other. Given this complication, tailoring of ZT requires a deep

understanding of the origin the Seebeck effect, the electrical, and the thermal conductivity. The following sections summarize basic knowledge for each of these parameters.

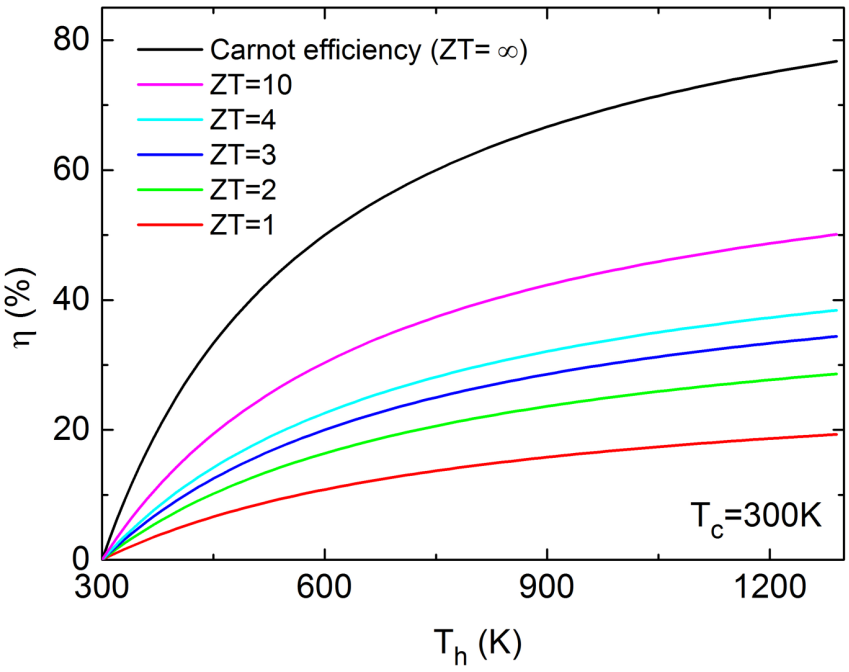

Figure 2.1: Maximum conversion efficiency η as a function of the hot side temperature T_h for a fixed cold side temperature T_c = 300 K for several ZT (cf. Equation (4)). For increasing ZT, the efficiency converges against the Carnot efficiency.

2.1.2 Thermal conductivity

In a solid material, heat can be transported through lattice vibrations (phonons) or by electric charge carriers. The total thermal conductivity of a material is given by the sum of the individual contributions,

$$\kappa = \kappa_l + \kappa_e, \tag{6}$$

where κ_l and κ_e are the lattice and the electronic conductivity, respectively.

For cobalt oxides, the thermal conductivity is typically dominated by the lattice contribution (cf. Section 3.1.5.3). In line with the kinetic theory of gases, the lattice thermal conductivity can be described by

$$\kappa_l = \frac{1}{3} c_V v^2 \tau, \tag{7}$$

with the phonon speed of sound v, the volumetric specific heat capacity c_V, and the phonon relaxation time $\tau = \Lambda/v$ that is determined by the mean free path Λ of the phonons [33]. Phonons can be scattered by other phonons or by all kind of lattice defects, such as boundaries or point-defects. Assuming the fundamental scattering processes with relaxation time τ_i to be independent from each other, Matthiessen's rule can be used to calculate the total effective relaxation time τ by applying the formula $\tau^{-1} = \sum_i \tau_i^{-1}$. Therefore, the total relaxation time τ, and therefore κ_l, are mainly determined by the scattering mechanism with the smallest relaxation time.

In order to understand the temperature dependence of the lattice thermal conductivity, the temperature dependence of τ and c_V have to be considered: The temperature dependence of τ is determined by different scattering mechanisms, where three of them are present in all polycrystalline samples: (i) phonon scattering on point defects, (ii) on boundaries, and (iii) on other phonons. The relaxation times of the first two scattering mechanisms do not depend on temperature because the density of the point defects and grain boundaries and hence the mean free path is independent of the temperature. The temperature dependence of the relaxation time of phonon-phonon scattering is more complicated. In general, there exist two different kinds of phonon scattering processes: (a) elastic normal or N-scattering processes, for which the wave vector of the scattered phonon lies within the Brillouin zone and (b) inelastic Umklapp or U-processes, where the wave vector of the scattered phonon is so large that it points outside of the first Brillouin zone. Physically, this wave vector is equivalent to a vector within the first Brillouin zone, which results in a change of momentum. N-processes do not influence κ_l because the momentum of the phonons is conserved and energy is just transfers between the phonon modes. Therefore, only U-scattering decreases the thermal conductivity κ_l by changing the momentum.

The relaxation time of Umklapp phonon-scattering τ_U and its temperature dependence is determined by the number of scattering events with large enough wave vectors. The number of scattering events depends on the number of phonons, which is described by the Bose-Einstein statistics. It states that the average occupation number of phonons n in the energy state $E = \hbar\omega(k)$ is given by $n(E) = \left(\exp\frac{E}{k_B T} - 1\right)^{-1}$. The total number of phonons n increases with temperature, and thus the relaxation time $\tau_\mathrm{U} \propto \Lambda_\mathrm{U} \propto n^{-1}$ decreases with mean free path Λ_U. For large temperatures, when $k_B T \gg \hbar\omega$, the increase shows a linear temperature dependency and $\tau_\mathrm{U} \propto T^{-1}$ [34]. At low temperatures, the low thermal energy and

the connected small phonon wave vectors do not allow for U-scattering, but with rising temperature first phonons with large enough wave vectors are excited and their number increases exponentially with T ($\tau_U \propto \exp\left(\frac{\theta_D}{T}\right)$, where θ_D is the Debye temperature). Considering the different mechanisms, the total relaxation time τ is constant at low and intermediate temperatures, where it is dominated by scattering on boundaries and point-defects. At higher temperatures U-processes become dominant and τ decreases first exponentially and then linearly with T.

Additionally, the specific heat capacity c_V has to be kept in mind when discussing the temperature dependence of the total lattice thermal conductivity κ_l. According to the Debye-model, the specific heat capacity is determined by a cubic temperature dependence $c_V \propto T^3$ at low temperatures, while it converges to the constant Dulong-Petit limit at high temperatures. The resulting typical dependence of the lattice thermal conductivity κ_l on temperature is illustrated in Figure 2.2. The curve shows a clear maximum because the low temperature behavior is decreased by the small specific heat, while Umklapp scattering dominates and limits κ_l in the high temperature range. In addition to the basic scattering mechanism discussed in this section, the unique misfit-layered structure of $[Ca_2CoO_{3-\delta}][CoO_2]_{1.62}$ gives rise to additional scattering processes, which will be discussed in Chapter 3.

In addition to the lattice vibrations, charge carriers contribute to the heat transport. For metallic or degenerate systems, the electronic contribution to the thermal conductivity

$$\kappa_e = (L_0 - \alpha^2)\sigma T \tag{8}$$

is proportional to the electrical conductivity and can be estimated from the Lorenz number $L_0 = 2.4453 \cdot 10^{-8}$ WΩ/K^2 ([34], Chapter: 1.2, Section 3.3). For a metallic system, the Seebeck coefficient is usually negligible and the equation is equal to the Wiedemann-Franz-law. Even though the law is a good approximation at high T, it is fails due to inelastic scattering of charge carriers at lower T. Additionally, a reduction of the Lorenz number up to 20% is possible for low carrier concentrations [35]. In semiconductors also bipolar diffusion can contribute to the electronic thermal conductivity: while the electrical electron and hole currents cancel each other, heat is transported by the movement of both carrier types because electron-hole pairs are thermally excited at the hot side and recombine at the cold side ([34], Chapter: 1.1, Section 3).

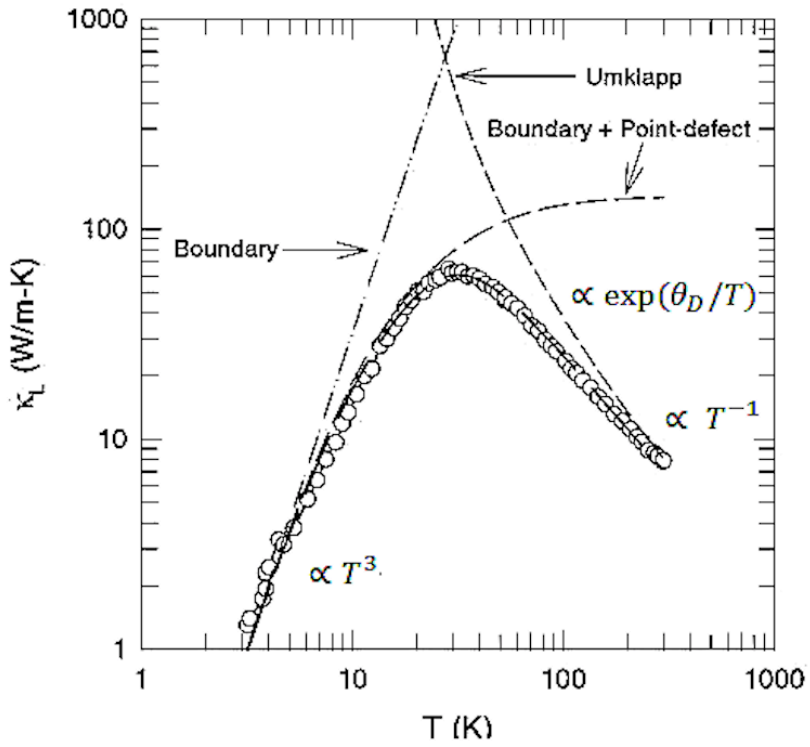

Figure 2.2: Lattice thermal conductivity κ_l as a function of temperature depicted for a $CoSb_3$ sample. In addition to the experimental values (circles) and the theoretical fit (solid line), the theoretical limits of κ_l induced by boundary, boundary + point-defect and Umklapp scattering are illustrated. Modified from Ref. [34], Chapter 1.1.

The electronic part of the thermal conductivity $\kappa_e \propto \sigma \propto n$ could be reduced by decreasing the carrier concentration n, but a reduction would also have a negative effect on the power factor. The lattice thermal conductivity $\kappa_l \propto \tau$ can be decreased by all kind of scattering processes that disturb the periodicity of the lattice. The various attempts can be categorized in two main strategies: The first strategy (i) is the introduction of point-defects, like substitution atoms with large mass contrast [36], interstitials or vacancies. Here, softly bound atoms can give rise to resonance scattering [37], and for structures with spacious void such as clathrates [38] or skutterudites, loosely bound atoms can produce localized rattling phonon modes [35, 36]. The second strategy (ii) is based on the introduction or enhancement of two-dimensional crystallographic defects: the enlargement of surfaces, interfaces and grain boundaries, e.g., via nanostructuring, reduction of the grain size [39], or the introduction of additional interfaces via the inclusion of a second material or the fabrication of thin-film 2D superlattices [9].

The discussed scattering mechanisms show, that the lattice thermal conductivity can be tailored by controlling the microstructure of a material. In the present work, soft chemistry synthesis and quick sintering methods are used to produce polycrystalline $[Ca_2CoO_{3-\delta}][CoO_2]_{1.62}$ with small particle sizes. In addition, the two main strategies are

followed to further decrease the thermal conductivity: (i) heavier ruthenium and indium atoms are substituted on the Co site in Chapter 5 and (ii) boundary scattering is increased by the introduction of Co_3O_4 impurity phases in Chapter 7.

A variety of further scattering mechanisms and their relaxation times are summarized in [34] and [36]. In general, the simultaneous application of different strategies on different length scales is most promising to reduce κ_l because the efficiency of the scattering mechanisms changes with the frequency of a phonon [36]. For instance for PbTe, the introduction of atomic-scale lattice disorder, nanoscale precipitates and mesoscale grain-boundaries resulted in a significant reduction of κ due to phonon scattering on a broad range of length scales [40].

2.1.3 Seebeck effect

If a temperature gradient ∇T is applied on a thermoelectric material, e.g. a semiconductor, the majority charge carriers (electrons or holes) on the hot side possess a larger kinetic energy than on the cold side. This induces a net diffusion of charge carriers to the cold side, where they accumulate. Due to the accumulation, a repulsive electric field builds up, which prevents further diffusion. The generation of this temperature induced electrical field is known as the Seebeck effect and results in a voltage

$$V = \alpha \nabla T, \tag{9}$$

which proportional to the Seebeck coefficient α.

The high temperature transport behavior of $[Ca_2CoO_{3-\delta}][CoO_2]_{1.62}$ is still under debate and a theory that consistently explains the temperature dependence of the electrical conductivity and the Seebeck coefficient has not been presented. While the Seebeck coefficient is often interpreted as that of a degenerate system, many authors claimed small-polaron transport via localized states to be the dominant transport mechanism. As a basis for latter discussion (cf. Chapter. 6), this chapter briefly presents the known temperature dependence of the Seebeck coefficient for itinerant and localized carriers.

The Seebeck coefficient

$$\alpha = \mp \frac{1}{eT} \frac{\int_{E_0}^{\infty} (E - E_F) \frac{\partial f(E)}{\partial E} \sigma(E) \mathrm{d}E}{\sigma} \tag{10}$$

can be derived from the linearized Botlzmann transport equations [33, 41], where e is the elementary positive charge, $\sigma = -\int_{E_0}^{\infty} \frac{\partial f(E)}{\partial E}\, \sigma(E) \mathrm{d}E$ the total electrical conductivity, $\sigma(E)$ the energy dependent electrical conductivity and $f(E)$ the Fermi function. The maximum of the derivative $\frac{\partial f(E)}{\partial E}$ is located at the Fermi level, and thus the electrical conductivity is dominated by the states around E_F.

For a metallic or degenerate systems, the widely-used Mott formula of the Seebeck coefficient

$$\alpha_{\mathrm{deg}} = -\frac{\pi^2 k_B^2 T}{3e}\left(\frac{1}{\sigma}\frac{\partial \sigma}{\partial E}\right)_{E=E_F} = -\frac{\pi^2 k_B^2 T}{3e}\left(\frac{\partial \ln(\sigma)}{\partial E}\right)_{E=E_F} \tag{11}$$

can be derived from Equation (10) using a Sommerfeld expansion [42]. In the degenerate system, the magnitude of the Seebeck coefficient is determined by $\sigma(E)$ and the slope $\partial\sigma/\partial E$, which are determined by the density of states (DOS) and the energy dependent scattering rates and carrier velocities. The slope $\partial\sigma/\partial E$ defines the sign of the Seebeck coefficient[a], which is negative when electrons determine the transport ($\partial\sigma/\partial E > 0$) and positive when conduction below the Fermi level dominates (p-type conduction, $\partial\sigma/\partial E < 0$). Equation (11) shows, that a large Seebeck coefficient can be reached, if $\partial\sigma/\partial E$ is large and σ rather small, which is the case if E_F is located in the vicinity of a peak in the DOS. For the half-metal $[Ca_2CoO_{3-\delta}][CoO_2]_{1.62}$, the origin of the large Seebeck coefficient can, e.g. be explained by a peak in the DOS which results from the overlapping of two bands (cf. Sections 3.1.3 and 3.1.5.2).

For $[Ca_2CoO_{3-\delta}][CoO_2]_{1.62}$, different authors assume hopping transport above room temperature. The high temperature thermopower in the correlated hopping regime can be described by the Heikes formula [43, 44]

[a] The magnitude and sign of the Seebeck coefficient (Equation (11)) can be understood in a visual way: At higher temperatures, the broadening of the Fermi Dirac function leads to an excess of high energy electrons with $E > E_F$ at the hot side and an excess of low energy electrons with $E < E_F$ at the cold side. Therefore, high energy electrons diffuse toward the empty high energy states at the cold side (above E_F), while excess low energy electrons diffuse in the opposite direction below E_F (equivalent to holes moving from the hot to the cold side). Thus, electrons and holes both drift in the direction of the heat flow and their currents cancel each other. Therefore, the thermoelectric voltage and the Seebeck coefficient increase with the asymmetry of σ around the Fermi level, which increases with the slope $\partial\sigma/\partial E$.

$$\alpha = -\frac{k_B}{e}\ln\left((1-x)/x\right) \tag{12}$$

which can be derived from the Hubbard model in the high temperature limit. Here, e is the positive electron charge and the sign is determined by the charge carrier concentration x on the available hopping sites. This formula is valid for small-polaron conduction via localized states in the high temperature limit, and was generalized for the $[Ca_2CoO_{3-\delta}][CoO_2]_{1.62}$ system

$$\alpha = -\frac{k_B}{e}\ln\left(\frac{g_3}{g_4}\frac{x}{(1-x)}\right), \tag{13}$$

where g_3 and g_4 describe the degeneracy of the Co^{3+} and the Co^{4+} atoms [45]. In a non-degenerate semiconductor, the temperature dependence of the Seebeck coefficient is dominated by the term $E/2k_BT$, where the majority carriers are excited from an energy level with energy E below the band edge. According to Mott, the same temperature dependence $\alpha \propto T^{-1}$ is expected, when electrons are excited into a narrow band, where small-polarons are formed [46]. For small-polaron hopping the Seebeck coefficient can be described in the narrow band limit of a p-type semiconductor

$$\alpha = \frac{k_B}{e}\left(\frac{E_A^{\alpha}}{k_BT} + A'\right). \tag{14}$$

The activation energy $E_A^{\alpha} = E_F - E_B$ is determined by the distance between the p-type polaron band energy E_B and the Fermi level E_F; and A' is a constant [47, 48].

In Chapter 6 it will be shown, that the high temperature electrical conductivity and the increase of the Seebeck coefficient $\alpha \propto T$ can be understood within the framework of Anderson localization usually described to describe impurity conduction in semiconductors. According to Anderson, a lattice with random potential (cf. Figure 2.3) can induce a localization of charge carriers within an electronic band or at the band edges [49]. Within such a potential, charge carriers hop between adjoining localized energy states with different energy. In this case, the electrical conductivity is given by

$$\sigma = \frac{e^2L^2}{\tau_0}N(E_F)\exp(-W(E_F)/k_BT), \tag{15}$$

where $N(E_F)$ is the DOS at the Fermi level, L^2 is the mean-squared distance between states with the same energy, and $\frac{1}{\tau} = \frac{1}{\tau_0}\exp(-W(E_F)/k_BT)$ the mean frequency of hopping with phonon frequency τ_0 [50]. The hopping frequency is determined by the overlap integral and the energies of the spatially intermittent states, where the activation energy $W(E)$ is determined by the highest intermittent energy level between two states with the same energy E. Introducing Cutler's conductivity (Equation (15)) into the Mott formula (Equation (11)) for states distributed over an energy range leads to

$$\alpha = -\frac{\pi^2 k_B^2 T}{3e}\left(\frac{\partial \ln(\sigma)}{\partial E}\right)_{E=E_F} = -\frac{\pi^2 k_B}{3e}\left(k_B T \frac{\partial \ln(\mu_0 N)}{\partial E} + \frac{\partial \mathrm{W}}{\partial E}\right)_{E=E_F}, \quad (16)$$

where $\mu_0 = \frac{eL^2}{\tau_0 k_B T}$ [50]. Accordingly, the Seebeck coefficient is dominated by a linear temperature dependence and the values $\frac{\partial \ln(\mu_0 N)}{\partial E}$ and $\frac{\partial \mathrm{W}}{\partial E}$ can be extracted from the slope and the y-intercept.

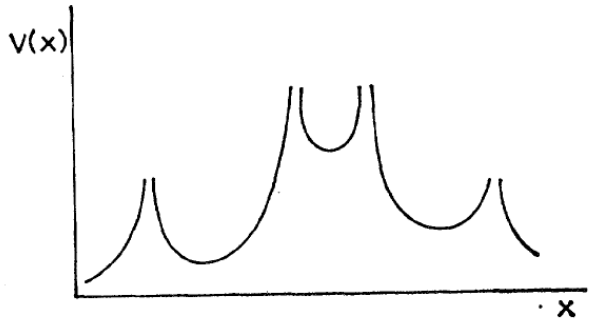

Figure 2.3: Schematic random potential energy $V(x)$ as a function of the location x. The variation of the potential energy in the CoO_2 layer of $[Ca_2CoO_{3-\delta}][CoO_2]_{1.62}$ is assumed to result from Coulomb interactions with the incommensurate rock salt layer and its randomly distributed oxygen vacancies, reproduced from [50].

2.1.4 Charge carrier concentration and the electronic density of states

An improvement of ZT is possible by tailoring of the electronic density of states, which influences σ and α. Theoretical studies predict that for a given charge carrier concentration n the maximum figure of merit can be reached if E_F is about $2.4k_BT$ above or below a peak in the density of states-versus-energy function, which should be as high (compared to the background DOS) and as narrow as possible [51]. The resulting steep slope and the low value of the DOS at E_F are favorable for a large Seebeck coefficient (cf. Equation (11)).

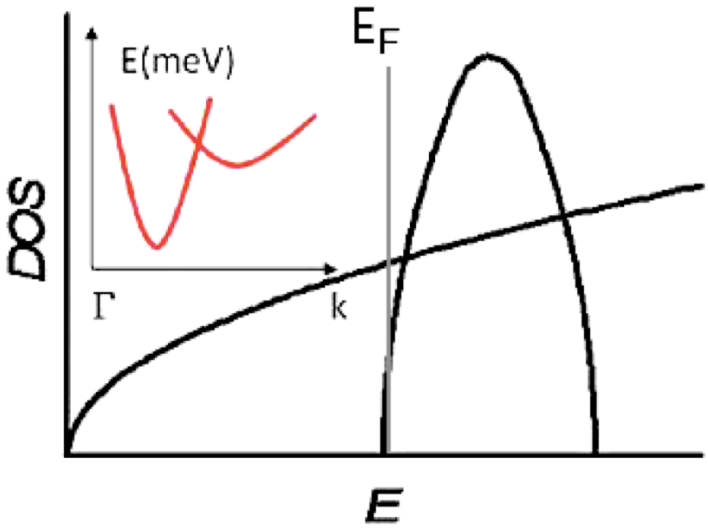

Figure 2.4: Density of states (DOS) of two overlapping bands as a function of energy *E*. The DOS originates from a heavy (peak shaped curve) and a light band (root shaped curve). The Fermi energy E_F is located at the onset of the peak. Inset: Schematic band structure showing the energy bands as a function of wave number *k*, where the light band is characterized by a stronger curvature compared to the heavy one. Modified from Ref. [52].

Various experimental scenarios can reach these theoretical demands approximately. One possibility is the presence of two bands in the vicinity of E_F (Figure 2.4). Here E_F is located within a light band with relatively small density of states and high carrier mobility which is responsible for good electrical conductivity. In contrast, the second band is flatter and the band edge is shifted in energy, resulting in a large DOS with a steep rise in the vicinity of E_F ensuring a large α. This two-band-scenario also seems to be important for the good performance of the layered cobalt oxides. Additional phenomena that can create a peak in the density of states are reviewed in Ref. [52].

In addition to the density of states, the charge carrier density has a significant influence on the power factor and the ZT. For degenerate system, the interrelation between Seebeck coefficient

$$\alpha_{\mathrm{deg}} = \frac{8\pi^2 k_B^2 T}{3eh^2} m^* \left(\frac{\pi}{3n}\right)^{2/3}, \tag{17}$$

and charge carrier density n can be derived from the Mott formula (Equation (11)), using the parabolic bands approximation and energy-independent scattering [35, 53]. Here, m^* is the effective mass and h is the Planck constant. For lower n in the non-degenerate regime, the dependence of the Seebeck coefficient on n is given by $\alpha_{\mathrm{non-deg}} \propto -\ln\left(T^{2/3} n^{-1}\right)$ [54, 55]. The Seebeck coefficient α_{deg} increases with rising n, while the electrical conductivity $\sigma = en\mu$ increases, where μ is the mobility of the charge carriers. The low electrical conductivity

suppresses the power factor $\alpha^2\sigma$ for low n, while the decreasing Seebeck dominates at high T. In total, the opposing dependency of α and σ on n leads to a maximum of the power factor (Figure 2.5). Considering the linear dependence of κ or more precise its electronic part on σ or n (cf. Section 2.1.2), the maximum ZT is usually located in the region of heavily doped or degenerate semiconductors. The carrier concentration of $[Ca_2CoO_{3-\delta}][CoO_2]_{1.62}$ is in this range [56] and a fine adjustment of n can be done by substitutional doping. Hence, this interdependence is relevant for the doping effects induced by Ru and In substitution discussed in Chapter 5.

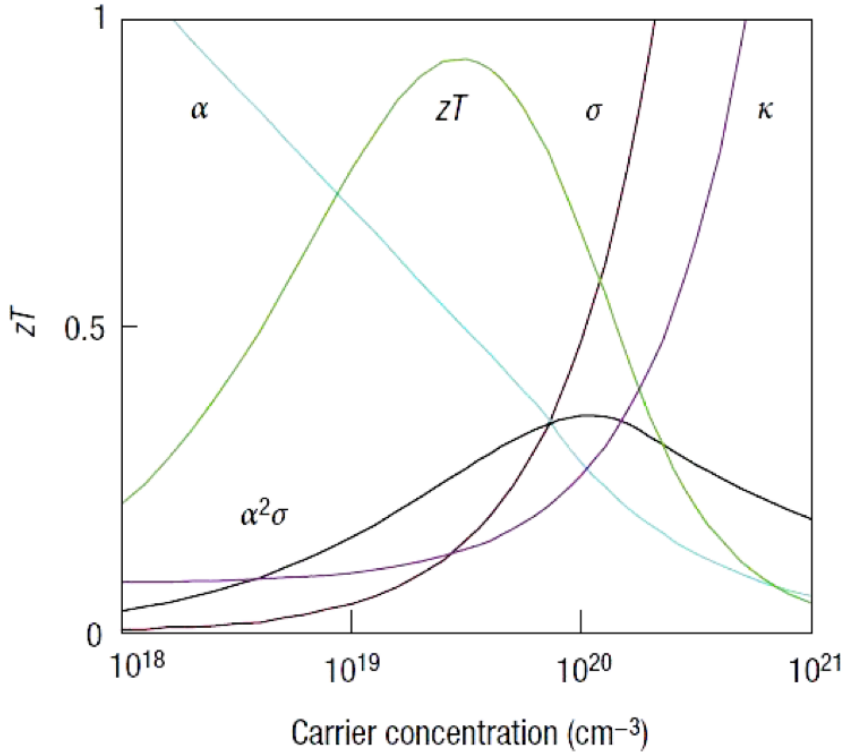

Figure 2.5: Dependence of the figure of merit *ZT*, the power factor $\sigma\alpha^2$, the electrical conductivity σ, the Seebeck coefficient α, and the total thermal conductivity κ on the charge carrier concentration. Reproduced from Ref. [35].

2.2 Thermoelectric converters

The following section describes the typical structure of a thermoelectric converter and introduces the idea of compatibility between thermoelectric materials. A good compatibility is crucial to allow different materials, which are combined in a converter, to work with high efficiency. Finally, the performances of state-of-the-art oxide converters are reviewed.

2.2.1 Structure of thermoelectric converters

A thermoelectric converter typically consists of two insulating AlO_2 plates, a variable number of thermoelectric p- and n-type legs, metallic electrodes that inter-connect the legs, and two lead wires to extract the electrical current (Figure 2.6(a)).

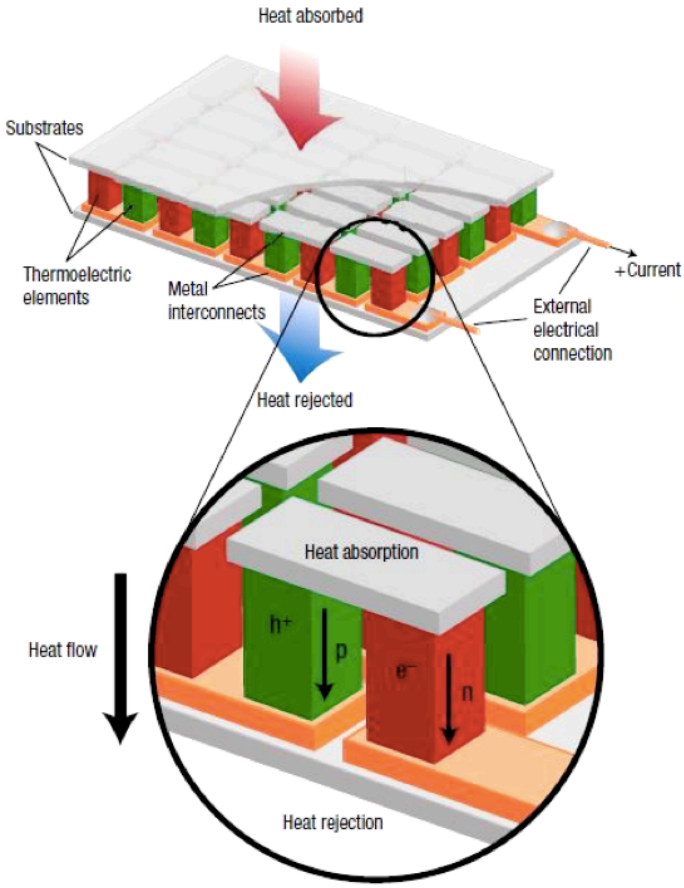

Figure 2.6: Schematic picture of a thermoelectric converter consisting of insulating substrates and the p- and n-type legs connected in series by metallic interconnects. Reproduced from Ref. [35].

An applied heat current flows from the hot side with temperature T_h through the parallel-aligned p- and n-type legs to the cold side. The electrons in the n-type and the holes in the p-type leg diffuse from the hot to the cold side and therefore the legs are connected antiparallel in series to positively add the thermoelectric voltages. To achieve high power output, a large number of legs is connected in series such that the output voltage of the individual legs adds up. The output current can be increased by enlarging the cross-section area of the legs, but enlargement makes the individual legs more prone for friction cracks due to different thermal expansion coefficients of the insulating Al_2O_3 plates, the electrode, and the thermoelectric material. To deliver maximum power output or maximum efficiency, the p- and the n-type leg should be compatible with each other. This concept of the compatibility is explained in the following section.

2.2.2 Compatibility approach for the enhancement of thermoelectric converters[b]

As presented in the introduction, each thermoelectric material has a characteristic temperature range where it shows its best performance (cf. Figure 1.1). For a beneficial combination of different materials in one segmented leg, or for combining p- and the n-type legs in one converter unit, requirements on the electrical current relative to the heat flow have to be considered. This question of compatibility was discussed by Snyder and Ursell [57].

The efficiency $\eta = \eta_r \eta_C$ of a thermoelectric material operating at a small ΔT can be calculated from the Carnot efficiency $\eta_C = \Delta T / T_h$ and the reduced efficiency η_r. According to Snyder and Ursell [57], the reduced efficiency

$$\eta_r = \frac{u(\alpha - u\kappa/\sigma)}{u\alpha + 1/T} \tag{18}$$

can be expressed in terms of the reduced current density

$$u = \frac{J}{\kappa \nabla T}, \tag{19}$$

which is defined as the ratio of the electrical current density J and the conductive heat flux $\kappa \nabla T$, wher ∇T is the temperature gradient. Because the electrical conductivity σ, u, α and κ depend on temperature, $\eta_r(T)$ is calculated by using their average values within a small temperature interval.

The efficiency reaches a maximum at $\eta_r = \eta_r^{max}$ and the corresponding reduced current density is called the compatibility factor

$$s = u(\eta_r^{max}) = \frac{\sqrt{1 + ZT} - 1}{\alpha T}, \tag{20}$$

which is fixed by the material properties at a given temperature $T = (T_h + T_c)/2$. To reach a high leg efficiency, u should be close to s in the whole leg. The behavior of u within the leg is determined by the steady-state heat equation. For a one-dimensional problem with constant

[b] Partly adapted from: Saucke, G., Populoh, S., Thiel, P., Xie, W., Funahashi, R., Weidenkaff, A.: Compatibility approach for the improvement of oxide thermoelectric converters for industrial heat recovery applications. Journal of Applied Physics. 118, 035106 (2015).

cross section area it can be written as $du/dT = u^2\ T\ d\alpha/dT + u^3\ \kappa/\sigma$. The solution of the equation can be approximated [58] by a combination of the zero Thomson effect solution and the zero resistance solution

$$\frac{1}{u_\mathrm{i}} = \frac{1}{u_{\mathrm{i}-1}}\sqrt{1 - 2(T_\mathrm{i} - T_{\mathrm{i}-1})u_{\mathrm{i}-1}^2\overline{\rho\kappa}} - \frac{(T_\mathrm{i} + T_{\mathrm{i}-1})}{2}(\alpha_\mathrm{i} - \alpha_{\mathrm{i}-1}). \tag{21}$$

Here, $\overline{\rho\kappa}$ is the average value between T_i and T_{i-1} and u_i and α_i denote the relative current and the Seebeck coefficient at the temperatures T_i, that subdivides $[T_c, T_h]$ into small intervals (with a width of 10 K for the calculations in Chapter 8). From the material properties measured at different T, the parametric function $u(T)$ can be calculated along the leg for a chosen hot side starting value $u_0 = u_{0,h}$.

Based on $u(T)$, the reduced efficiency $\eta_r(T)$ can be calculated using Equation (18) and for the calculation of the leg efficiency $\eta_{leg} = \int_{T_c}^{T_h} \eta_r(T)dT$ it is integrated over the whole temperature range. Finally, the relative current $u^{opt}(T)$, which maximizes the efficiency η_{leg} of the whole leg can be found via a variation of $u_{0,h}$.

Furthermore, for a given leg length l_{tot} the electrical current density

$$J = \frac{1}{l_{tot}}\int_{T_c}^{T_h} u\kappa\ \mathrm{d}T \tag{22}$$

can be calculated for the chosen $u(T)$, and for the fixed electrical current density the temperature-length profile $l(T_i) = \frac{1}{J}\int_{T_i}^{T_h} u\kappa\ \mathrm{d}T$ across the leg can be calculated, whereas the length l is measured from the hot side of the leg.

In a thermoelectric converter, the thermoelectric legs are connected in series and thus the electrical current $I = J_pA_p = -J_nA_n$ in both legs is the same, where A_p, A_n, J_p and J_n are the cross-sectional areas and the electrical current densities in p- and the n-type leg, respectively. To ensure that both legs work with maximum efficiency, the cross-section area ratio

$$\frac{\mathrm{A_p}}{\mathrm{A_n}} = \frac{-\mathrm{J_n}}{\mathrm{J_p}} = \frac{-\int_{\mathrm{T_c}}^{\mathrm{T_h}} \mathrm{u_n}\kappa_\mathrm{n}\ \mathrm{dT}}{\int_{\mathrm{T_c}}^{\mathrm{T_h}} \mathrm{u_p}\kappa_\mathrm{p}\ \mathrm{dT}}. \tag{23}$$

has to be adjusted accordingly (using $u_p = u_p^{opt}$ and $u_n = u_n^{opt}$). However, this optimal ratio depends on temperature and for varying boundary conditions the ratio is not optimal anymore and the efficiency decreases. For an arbitrary A_p/A_n Equation (23) still remains valid. Therefore the choice of $u_{0,h,p}$ of the p-type leg fixes the relative current and thus the starting value $u_{0,h,n}$ in the n-leg. Via a calculation of the n-type integrals for different starting values, for each $u_{0,h,p}$ an appropriate $u_{0,h,n}$ can be found.

Finally, the efficiency of the couple consisting of n-type and p-type leg

$$\eta_{\mathrm{n+p}} = \frac{\eta_{\mathrm{p}} \mathrm{Q}_{\mathrm{p}}^{\mathrm{h}} + \eta_{\mathrm{n}} \mathrm{Q}_{\mathrm{n}}^{\mathrm{h}}}{\mathrm{Q}_{\mathrm{p}}^{\mathrm{h}} + \mathrm{Q}_{\mathrm{n}}^{\mathrm{h}}} = \frac{\Delta\Phi_{\mathrm{p}} - \Delta\Phi_{\mathrm{n}}}{\Phi_{\mathrm{p}}^{\mathrm{h}} - \Phi_{\mathrm{n}}^{\mathrm{h}}} \tag{24}$$

can be calculated from the efficiencies of the single legs weighted by the heat flows Q_p^h and Q_n^h entering the hot side of the legs. Here the heat flow

$$\mathrm{Q} = \mathrm{J}\Phi\mathrm{A} \tag{25}$$

is determined by the thermoelectric potential $\Phi = \alpha T + \frac{1}{\mathrm{u}} = \alpha T + \frac{\kappa \nabla T}{J}$ and $\Delta\Phi = \Phi^h - \Phi^c$ is the difference between the hot side value Φ^h and the cold side value Φ^c. The open circuit voltage of a single leg can be calculated via

$$\mathrm{V}_{\mathrm{OC}}^{\mathrm{T_h - T_c}} = \sum_{\mathrm{i}} \frac{\alpha_{\mathrm{i}} + \alpha_{\mathrm{i-1}}}{2} (\mathrm{T_i} - \mathrm{T_{i-1}}) \,. \tag{26}$$

The open circuit voltage of the entire module is determined by the sum of the open circuit voltages V_{OC} of all legs. The current-voltage characteristic of the converter and the power output $P = UI$ can be calculated by an evaluation of the output voltage $V = N(\Delta\Phi_{\mathrm{p}} - \Delta\Phi_n)$ and the electrical current $I = J_p A_p$ (Equation (22)), whereas N is the number of pn-couples. The derivation of the formulas and a detailed example calculation can be found elsewhere [59–61]. While for the compatibility approach $u(T)$ is considered to depend only on T, a related concept developed in the 1960s [62] shows that u is also a function of the local electrochemical potential. Thus, the latter approach is more accurate, but our results show that Snyder's approximation of $u(T)$ forms a good basis for the A_p/A_n optimization.

2.2.3 State-of-the-art oxide thermoelectric converters[c]

In literature, the manufacturing and characterization of various high temperature oxide converters is discussed [7, 63–68], with many of them based on the promising p-type misfit-layered $[Ca_2CoO_{3-\delta}][CoO_2]_{1.62}$ and its Gd or Bi substituted compounds. The cobalt oxide was combined with n-type materials like $La_{0.9}Bi_{0.1}NiO_3$ [64, 69, 70], $(ZnO)_7In_2O_3$ [63], $Zn_{0.98}Al_{0.02}O$ [67, 71] and $CaMnO_3$ based materials with La, Nd, Mo, Sm or Nb substitution [31, 66, 72, 73]. The highest measured output power densities so far are 0.45 W/cm^2 or 0.96 W/cm^3 for a $Ca_{2.7}Bi_{0.3}Co_4O_9$ /$LaNiO_3$ generator for a hot side temperature of 1073 K [70]. Besides, for a $Ca_{2.7}Bi_{0.3}Co_4O_9$/$La_{0.9}Bi_{0.1}NiO_3$ module a volume and a mass power density of 0.66 W/cm^3 and 0.14 W/g were measured [64].

Although methods like the Harman method and heat flow methods are available for the determination of module efficiencies [74], the converter efficiencies for high temperature oxide modules are rarely reported. While for a $Ca_{2.7}Bi_{0.3}Co_4O_9$/$Ca_{0.9}Yb_{0.1}MnO_3$ module a theoretical conversion efficiency of about 3% was predicted from the material properties [75], much lower measured efficiencies of 0.15 %-0.082 % and 0.37 % were stated for $La_{1.98}Sr_{0.02}CuO_4$/$CaMn_{0.98}Nb_{0.02}O_3$ [6, 76] and $Ca_3Co_4O_9$/2%Al-doped ZnO converters [77], respectively. For the latter converter, a much better efficiency of 1.16% could be achieved for additional segmentation of the p-type leg with $Ti_{0.3}Zr_{0.35}Hf_{0.35}CoSb_{0.8}Sn_{0.2}$ [77]. For the oxide modules, the efficiency is strongly limited by the n-type material with inferior ZT and additional parasitic resistances. For a single p-type segmented leg constructed from $Ca_{2.8}Lu_{0.15}Ag_{0.05}Co_4O_9$ and the half-Heusler alloy $Ti_{0.3}Zr_{0.35}Hf_{0.35}CoSb_{0.8}Sn_{0.2}$ a maximum efficiency of about 5% was measured at $T_h = 1153$ K, which corresponds to 65 % of the theoretical efficiency [78]. Although 5% sounds promising, this value cannot be compared with a module efficiencies because the ZT of available n-type materials are much smaller and simple metal interconnects would reduce the total efficiency of a module even more.

As stated above, various high T oxide converters were manufactured and characterized, but usually no attention is put on adjusting the A_p/A_n ratio or determining the efficiency [7, 63–66, 68]. Thus, in Chapter 8 we optimize the A_p/A_n ratio of our oxide converters according to the compatibility approach and address the determination of the efficiency.

[c] Adapted and partly verbatim from: Saucke, G., Populoh, S., Thiel, P., Xie, W., Funahashi, R., Weidenkaff, A.: Compatibility approach for the improvement of oxide thermoelectric converters for industrial heat recovery applications. Journal of Applied Physics. 118, 035106 (2015).

3 Thermoelectric materials

$[Ca_2CoO_{3-\delta}][CoO_2]_{1.62}$ has exceptionally good thermoelectric properties that result from the complex misfit-layered crystal structure. This anisotropic layered structure is the reason why $[Ca_2CoO_{3-\delta}][CoO_2]_{1.62}$ has simultaneously a low thermal conductivity and a high electrical conductivity, where these parameters are usually positively correlated. In this chapter, the physics behind this effect is discussed on an electronic and chemical level. Additionally, the phase diagram of the Co-Ca-O system is introduced as a basis for the later discussion of the influence of the compositional stability range of $[Ca_2CoO_{3-\delta}][CoO_2]_{1.62}$ and the formed secondary phases on the thermoelectric properties. Finally, the properties of the n-type material $CaMnO_3$ used for the fabrication of thermoelectric generators are briefly summarized.

3.1 Misfit-layered cobalt oxide (p-type)

3.1.1 Crystal structure

Misfit-layered cobalt oxide $[Ca_2CoO_{3-\delta}][CoO_2]_{1.62}$, also abbreviated as $Ca_3Co_4O_9$ in the following, is composed of alternating CoO_2 and a triple rock salt-type Ca_2CoO_3 layers stacked along the c-axis [79]. Its crystal structure is illustrated in Figure 3.1. The hexagonal CdI_2-type CoO_2 layer is built up of CoO_6 octahedrons that share half of the edges with the neighboring octahedrons (Figure 3.1 (a)-(b)). This leads to a distortion of the octahedrons and a compression of the layer along the c-axis direction [80]. The rock salt-type Ca_2CoO_3 layer consists of three rock salt type sub layers (CaO-CoO-CaO) that result in an octahedral oxygen coordination of the Co cations. In contrast to the high ordering of the oxygen atoms in the CoO_2 layers, displacements of the oxygen atoms were observed in the Ca_2CoO_3 layers via annular bright-field imaging [81].

The structure of the two cobalt oxide sub lattices can be described by the space group C2/m using different parameter b_1 and b_2 for the CoO_2 and the Ca_2CoO_3 subsystems with common lattice parameters a, c and β [80]. As illustrated in Figure 3.1 (b), the two layers have an incommensurate structure with a lattice misfit in the b-direction ($b_2/b_1 \approx 1.62$). Typical values of the lattice parameters are $a = 54.8376(7)$ Å, $c = 510.833(1)$ Å, $\beta = 98.06(1)°$, $b_2 = 4.5565(6)$ Å, and $b_1 = 2.8189(4)$ Å [79]. In addition to this structure, for single crystals

two polymorphs were found that differ due to a variable orientation of the octahedrons in subsequent CoO_2 layers [80].

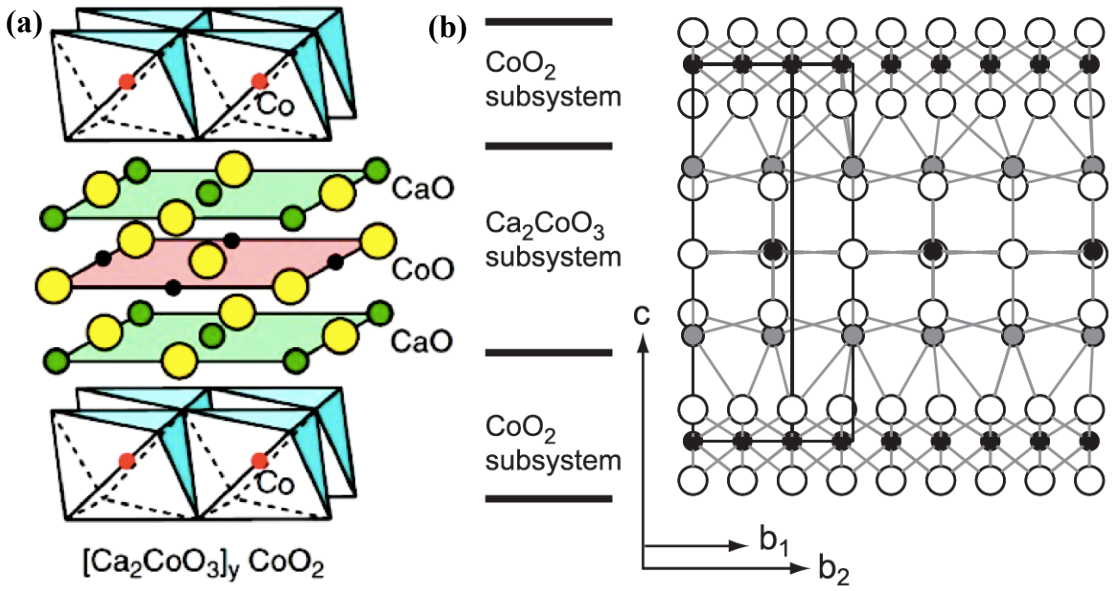

Figure 3.1: Structure of the misfit-layered $[Ca_2CoO_{3-\delta}][CoO_2]_{1.62}$ projected along the b-axis (a) and the c-axis (b). Black and red circles represent Co atoms, while green or grey mark the Ca atoms. Oxygen is drawn in yellow or open circles and omitted in (a) at the corners of the CoO_6 octahedrons in the CoO_2 layers. The misfit between the lattice parameter b_2 of the rock salt-type Ca_2CoO_3 layer and the b_1 parameter of the CoO_2 layer is illustrated in (b). Illustrations are reproduced from [82] and [83].

3.1.2 Phase equilibria in the Ca-Co-O system

The phase diagram of the Ca-Co-O system was investigated and calculated based on the phase transition temperatures measured by DSC and TGA, XRD measurements and microscopic and SEM studies on quenched samples [84–86]. The studies derive similar diagrams, but they disagree about the decomposition of the $Ca_3Co_2O_6$ phase below about 1064 K (791°C). Figure 3.2 presents the phase diagram, including the phase transition temperatures determined via DSC [85]. On the abscissa, the atomic percentage $x_{Co} = \frac{Co}{Ca+Co}$ is given, but it is not a binary phase diagram as the oxygen content varies for the different phases.

The $[Ca_2CoO_{3-\delta}][CoO_2]_{1.62}$ phase is considered to be stable for a compositions $0.559 < x_{Co} < 0.571$ up to a temperature of 1222 K [85, 86]. Above this temperature, it decomposes into a mixture of $Ca_3Co_2O_6$ and $Co_{1-x}Ca_xO$, where the variable x ($\neq x_{Co}$) denotes the stoichiometric flexibility of the different phases in the phase diagram. Upon further heating, $Ca_3Co_2O_6$ becomes instable and a mixture of $Co_{1-x}Ca_xO$ and $Ca_{1-x}Co_xO$ is obtained around 1313 K.

Above the eutectic temperature of about 1623 K, a mixture of $Ca_{1-x}Co_xO$ with a liquid phase is formed in equilibrium [86].

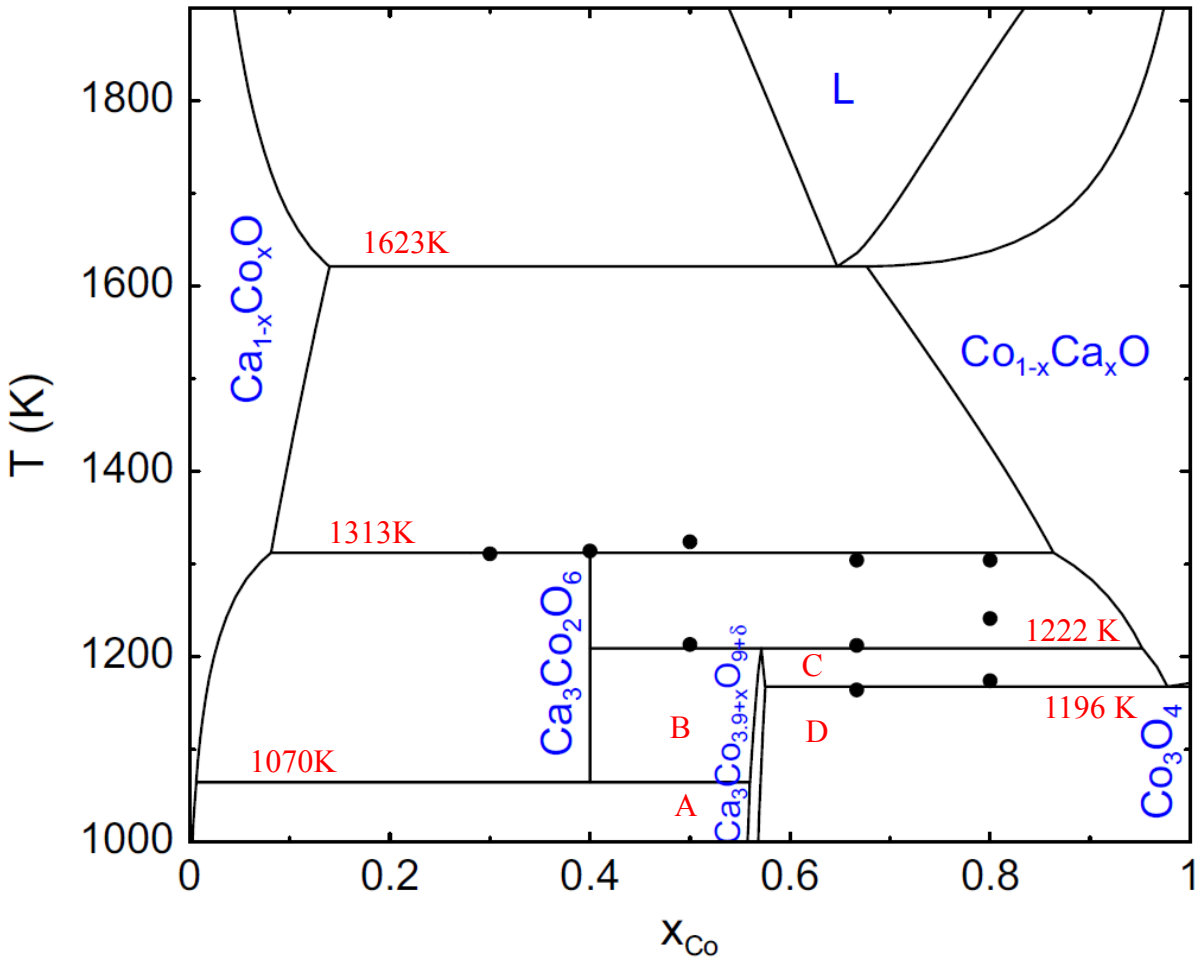

Figure 3.2: Phase diagram with transition temperatures in air, modified from Ref. [85]. Additional temperatures were added [84, 86]. Depending on the non-stoichiometry in x_{Co} and the temperature, four different secondary phases can form a mixture with the $[Ca_2CoO_{3-\delta}][CoO_2]_{1.62}$ phase abbreviated as $Ca_3Co_{3.9+x}O_{9+\delta}$ in the diagram (cf. A-D).

The stability range of the $[Ca_2CoO_{3-\delta}][CoO_2]_{1.62}$ phase ($0.559 < x_{Co} < 0.571$) corresponds to elemental formulas between $Ca_3Co_{3.8}O_{9+\delta}$ and $Ca_3Co_{4.0}O_{9+\delta}$, where the oxygen content δ is variable. For a higher or lower Co concentration, a second phase additionally to the $[Ca_2CoO_{3-\delta}][CoO_2]_{1.62}$ phase is formed due to miscibility gaps. Therefore, at low temperatures, a Co deficient sample forms $Ca_{1-x}Co_xO$ impurities (Figure 3.2 condition A), while at higher temperatures $Ca_3Co_2O_6$ is the stable secondary phase (B). Co excess leads to a mixture with $Co_{1-x}Ca_xO$ or Co_3O_4 (C,D).

It has to be noted that phase diagrams describe the equilibrium state, which will be reached after the system has been kept at a certain temperature for a long time. This time depends on the temperature because the phase formation is a kinetic process. At low temperatures, the

mobility of the atoms is limited, thus the time to reach equilibrium can be very long. Therefore, high temperature states can be preserved by quick cooling.

In Chapter 6 the effect of Co_3O_4 inclusions on the thermoelectric effects of $[Ca_2CoO_{3-\delta}][CoO_2]_{1.62}$ will be discussed. Experimentally, the secondary phase is introduced by synthesizing of non-stoichiometric powder samples (miscibility gap D in Figure 3.2), SPS sintering and post-annealing in air at 1132 K, followed by free cooling in the furnace.

3.1.3 Electronic structure and magnetic properties

Photoemission spectroscopy (PES) showed that the bands close to the Fermi energy E_F have mainly O 2p character with small contributions from the Co 3d states [87]. More precise, the density of states (DOS) at the upper part of the valence band (about 1eV below the upper edge) was found to be dominated by states from the CoO_2 layer [88, 89]. This assignment is supported by the observation of delocalized holes in the CoO_2 layer [81]. Photoemission measurements also revealed that the energy dependent DOS decreases with increasing energy, which is in line with the positive Seebeck coefficient [87, 89]. This energy dependence of the DOS is confirmed by the fact that a larger DOS is observed for the smaller E_F, when E_F is shifted to lower energies by an increase of the oxygen content [90].

A general understanding of the band structure of the CoO_2 layer can be developed from the hybridization of the atomic levels: The cluster diagram (Figure 3.3 (a)) shows the hybridization of the Co 3d states with the O 2p orbitals. Due to the crystal field that originates from the octahedral oxygen coordination, the Co 3d orbitals are not degenerate anymore. The energy of the two e_g d-Orbitals that point in the direction of the O 2p orbitals increases due to the coulomb repulsion from the O 2p electrons, while the energy of the three t_{2g} orbitals between the p orbitals is decreased. This crystal field splitting was calculated to be on the order of $\Delta_{CF} \approx 3.6$ eV [91]. Furthermore, the hybridization of these Co t_{2g} and e_g orbitals with the overlapping O 2p orbitals results in bonding (B) and antibonding (AB) orbitals additionally to the non-bonding (NB) O orbitals. A schematic picture of the DOS is shown in Figure 3.3 (b).

The degeneracy of the bonding orbitals of CoO_2 is further lifted by the compression of the CoO_6 octahedrons along the c-axis [80]. This distortion results in a splitting of the t_{2g} orbitales into a doublet (e_g') and a singlet (a_{1g}) with an energy gap of Δ_D (cf. Figure 3.3 (c)). Quantum chemical fully correlated ab initio calculations revealed that the a_{1g} orbital is located about $\Delta_D = 240$ meV above the e_g' orbitals due to hybridization of e_g and t_{2g} [92, 93]. While for Co^{4+} the a_{1g} orbital is filled with one electron, it is filled with two electrons for Co^{3+}. Hence, the electrical transport is determined by mobile holes in the a_{1g} orbital.

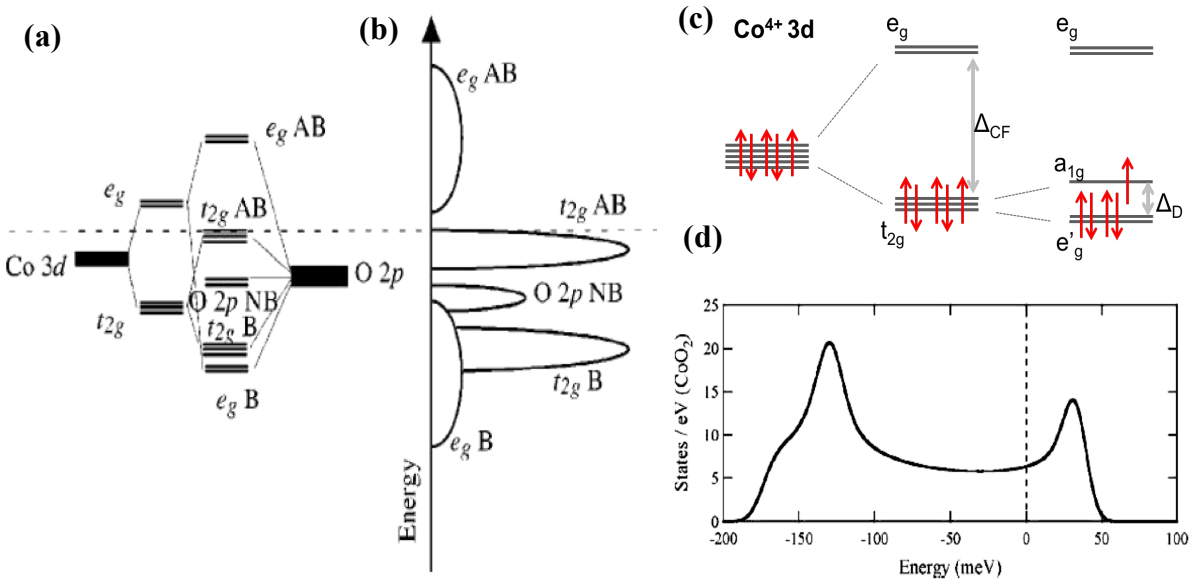

Figure 3.3: Band structure of $[Ca_2CoO_{3-\delta}][CoO_2]_{1.62}$ close to E_F. (a) Schematic illustration of cluster levels in the CoO_6 octahedron and (b) energy diagram with the corresponding density of states, both reproduced from [89]. B, NB and AB denote bonding, non-, and anti-bonding states. (c) Splitting of Co 3d orbitals in the CoO_2 layer due to crystal field splitting $\Delta_{CF} \approx 3.6$ eV and splitting $\Delta_D \approx 240$ meV of the t_{2g} orbitales due to the distortion of the octahedrons along the c-axis. (d) Experimental density of states, which results from the Co t_{2g} states in the CoO_2 layer, reproduced from [88]. The Fermi energy $E_F = 0$ is located about 50 meV below the valence band edge.

Close to E_F, the DOS of the CoO_2 layer was estimated from a tight binding fit of ARPES (Angle Resolved PES) data (Figure 3.3 (d)). The Co t_{2g} band that crosses E_F was found to have a small width of about 250 meV. E_F is located about 50 meV below the upper edge of the valence band [88]. The position of E_F close to the band edge agrees with the p-type conductivity but the single band cannot explain the large positive Seebeck coefficient, which means that the other t_{2g} bands might contribute additionally.

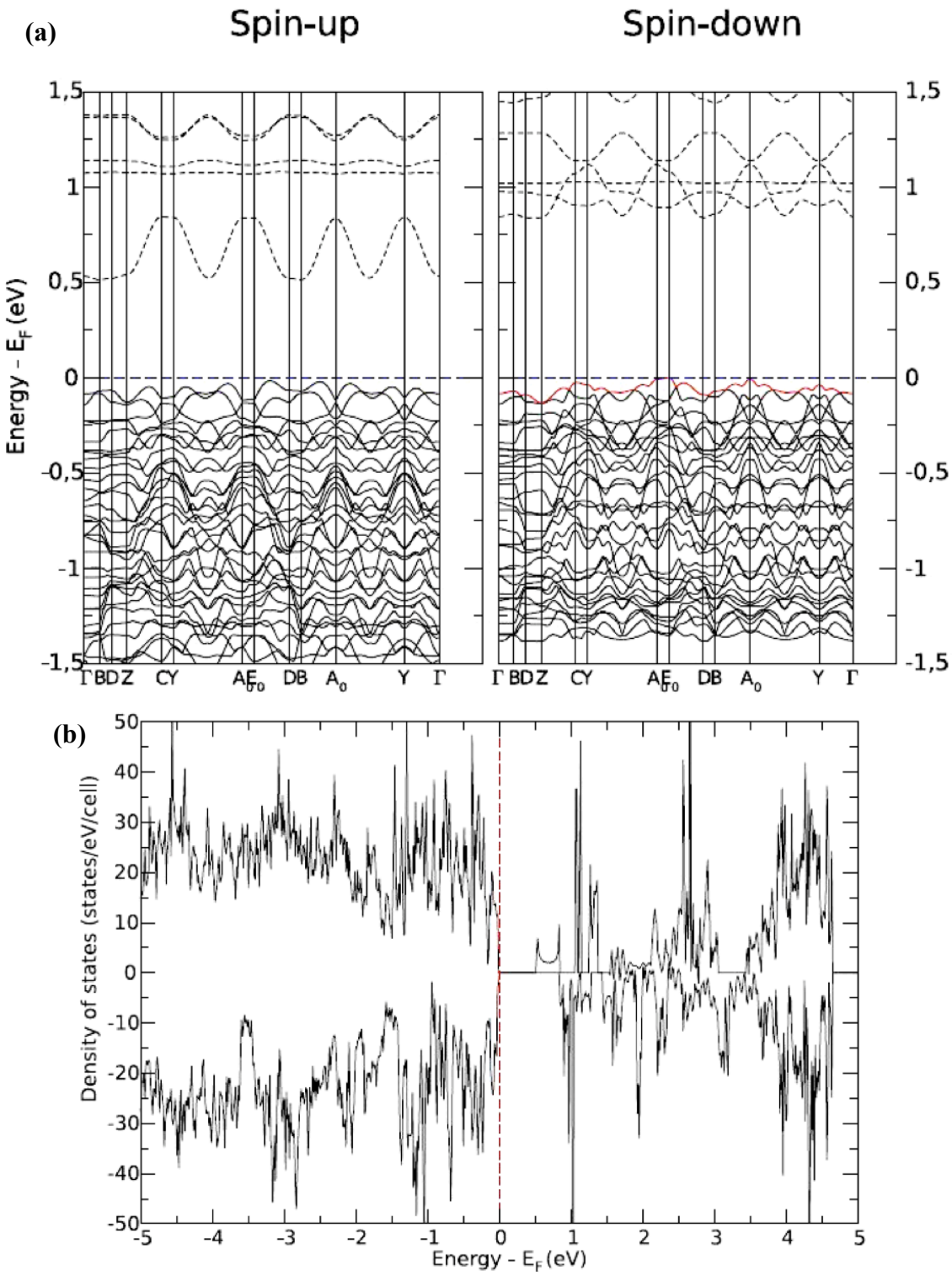

Figure 3.4: Band structure (a) and total density of states (b) of $[Ca_2CoO_{3-\delta}][CoO_2]_{1.62}$. The band structure is depicted for spin up and spin down states separately. The band with a_{1g} character that cuts E_F is marked in red. In the DOS, spin-down is plotted in the negative direction. Reproduced from Ref. [91].

First principle local density approximation (LDA) calculations for Na_xCoO_2 were performed by Singh and Kasinathan [94]. They indicate that the large Seebeck effect and the good electrical transport properties of the misfit-layered cobalt oxides are determined by the Co t_{2g} states of the CoO_2 layer, which form a narrow band in the vicinity of E_F. However, for

$[Ca_2CoO_{3-\delta}][CoO_2]_{1.62}$, LDA [95] and DFT calculations [96] failed to reproduce that the density of states at E_F results mainly from the CoO_2 layer. Better agreement with the experimental results was achieved with DFT+U calculations with Hubbard correction [96] and the exchange-correlation hybrid functional B1WC, which treats exchange effects better than the LDA functional [91]. Here, we will briefly present the findings of the B1WC based calculations, as they reproduce the thermoelectric properties better.

The calculated band structure for the approximated commensurate structure with $b_1/b_2 = 5/3$ and the density of states are presented in Figure 3.4. Both are presented for spin-up and spin-down separately, revealing the half-metallic character of $[Ca_2CoO_{3-\delta}][CoO_2]_{1.62}$: For spin-up, E_F is located within a band gap of about 0.5 eV and the valence states are completely occupied. In contrast for spin-down, E_F cuts the edge of the valence band (red band in Figure 3.4 (a)), which stems from the Co t_{2g} states of the CoO_2 layer and is thus responsible for its good electrical conductivity.

In summary, around room temperature $[Ca_2CoO_{3-\delta}][CoO_2]_{1.62}$ is a half-metal, with E_F located in the narrow Co t_{2g} bands of the CoO_2 layer. Thus, the electrical conduction and thermoelectric behavior are determined by these bands with a_{1g} character at the upper edge. For decreasing temperature below 50 K, the opening of a band gap $E_g \approx 15$ meV with E_F positioned in the gap was observed [87]. The gap opening might originate from a spin density wave (SDW) [97] or electron-electron correlation [98]. Also transport data suggest the opening of a pseudo-gap due to an anomalous suppression of the DOS [99]. Above room temperature, a metal-semiconductor transition occurs and activated behavior is observed above about 510 K [100]. A more detailed discussion will follow in the context of the electrical conductivity in Section 3.1.5.1.

The magnetic properties and transitions are illustrated in Figure 3.5. At low temperatures $[Ca_2CoO_{3-\delta}][CoO_2]_{1.62}$ is ferrimagnetic and an incommensurate spin density wave state (IC-SDW) was found in the CoO_2 layer [101]. With increasing temperature, the range of the magnetic ordering decreases and above about 100 K the cobalt oxide becomes paramagnetic. Ab initio calculations indicate that the energetically most favorable occupation of the orbitals is a low spin state [92, 93], which is illustrated for Co^{4+} in Figure 3.3. At higher temperatures, the spin state is still under discussion [102, 103]. A detailed discussion of the magnetic states is beyond the scope of this work.

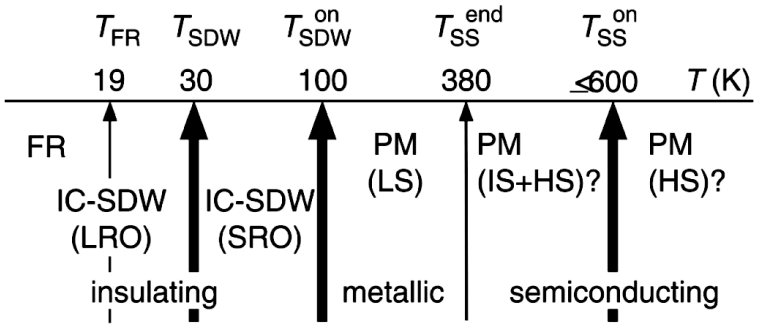

Figure 3.5: Summary of the magnetic states of $[Ca_2CoO_{3-\delta}][CoO_2]_{1.62}$ as a function of temperature. The abbreviations denote ferrimagnetism (FR), paramagnetism (PM), low (LS), intermediate (IS) and high spin state (HS), incommensurate spin-density wave state (IC-SDW), long-range (LRO) and short-range orders (SRO). Reproduced from [103].

3.1.4 Valence states and oxygen content

For Ca^{2+} and O^{2-} only one possible valence state exists, while the Co valence is different in the two sublayers and under heavy debate. If both sub layers are assumed to be neutral, cobalt valences of 2+ and 4+ are expected ($[Ca_2^{2+}Co^{2+}\ O_3^{2-}]_{0.62}[Co^{4+}\ O_2^{2-}]$). Hints for the existence of Co^{2+} in the rock salt layer were given by X-ray appearance near-edge structure (XANES) measurements [79], but later it could be excluded by further X-ray absorption studies [104]. Given the findings of the present study, this inconsistence might result from a small amount of Co_3O_4 secondary phase (contains Co^{2+}), which is barely visible via X-ray diffraction (cf. Chapter 6). According to valence bond analysis [80], the Co atom in the CoO_2 layer has a mixed valence state of 3.5+, while the Co valence state in the rock salt layer fluctuates with disorder around an average value of 2.8+ in agreement with charge neutrality. Similar valences were found via electron energy loss spectroscopy (EELS), which revealed a nominal Co valence of 3.5+ in the CoO_2 layer and a value 3.0+ in the rock salt layers. These values suggest that, compared to the neutral formula, the CoO_2 layer is negatively charged $(CoO_2)^{0.5-}$, while the CoO layer in the rock salt layer is positively charged $(CoO)^{1+}$. This charge difference initiates a transfer of holes to the CoO_2 layer, which leads to the high electrical conductivity [105]. Due to the adjustable charge transfer, the rock salt layers are often considered as a charge reservoir.

Via titration [106] and thermo-gravimetric measurements [107, 108], the variable oxygen content and the existence of a significant amount of oxygen vacancies in air-annealed $[Ca_2CoO_{3-\delta}][CoO_2]_{1.62}$ samples was proven. According to Ling *et al.* the formation of oxygen vacancies is limited to the central CoO layer in the rock salt block and the formation mainly

cause a decrease of the lattice parameter b_{RS} of this layer. For air annealed $[Ca_2CoO_{3-\delta}][CoO_2]_{1.62}$, about 14(2) % of the oxygen sites in the CoO layer are vacant, while a total amount of 27 % vacancies was found after argon annealing [109]. Electronically, the creation of vacancies introduces electrons into the system, which tend to recombine and thus reduce the mobile holes in the CoO_2 layer instead of decreasing the average Co-valence in the rock salt layer. Thus, oxygen vacancies were found to reduce the electrical conductivity and to increase the Seebeck coefficient [107].

The rock salt subsystem is assumed to be responsible for the entire flexibility of the compound: Oxygen vacancies are known to form in the $Ca_2CoO_{3-\delta}$ layer [109], while the present work (cf. Chapter 7) suggests that a non-stoichiometric Co/Ca ratio results in the formation of Ca vacancies above the ideal composition. The formation of Ca vacancies and the substitution of Ca are naturally restricted to the $Ca_2CoO_{3-\delta}$ layer. In contrast, Co is present in both layers and cationic substitution was observed in the rock salt [109] and the CoO_2 layer [110, 111]. According to Ling *et al.,* the cationic substitution influences the oxygen content after a defined annealing process: The increase of the cationic charge in the rock salt layer e.g. by Ti^{4+} for $Co^{3+\ldots4+}$ or Nd^{3+} for Ca^{2+} substitution reduces the number of oxygen vacancies because the two extra electrons per occupied vacancy can counter balance the substituted holes. Additionally, the substituted atom determines the flexibility of the material concerning oxygen vacancies: after argon annealing the Nd substituted sample shows only 4% of vacancies in the CoO layer, while 14% and 27% were found in Ti^{4+} for $Co^{3+\ldots4+}$ substituted compounds and unsubstituted $[Ca_2CoO_{3-\delta}][CoO_2]_{1.62}$ [109].

3.1.5 Thermoelectric properties

Among the oxides, the misfit-layered $[Ca_2CoO_{3-\delta}][CoO_2]_{1.62}$ stands out because of its relatively large ZT that results from a combination of large Seebeck coefficient, large electrical and small thermal conductivity. This combination results from its unique layered structure that limits the thermal conductivity but allows for good electrical conductivity within the CoO_2 layers (phonon glass-electron crystal). In the following the properties will be discussed in detail.

3.1.5.1 Electrical conductivity

As described in Section 3.1.3, the layered cobalt oxide has a half-metallic character and the electrical conductivity results from the Co t_{2g} orbitals of the CoO_2 layers, while the Ca_2CoO_3 layers are insulating because they do not contribute to the density of states near E_F. The layered structure leads to an anisotropic resistivity [79], with the out-of-plane resistivity ρ_c of the single crystals exceeding the in-plane resistivity ρ_{ab} (Figure 3.6 (a)). In the out-of-plane direction the insulating rock salt layers are in series with the CoO_2 layers, therefore the former dominate the transport in this direction and in total insulating temperature dependence ($d\rho/dT < 0$) is observed. The in-plane resistivity is dominated by the more conductive CoO_2 layers, which show complex behavior due to correlation effects.

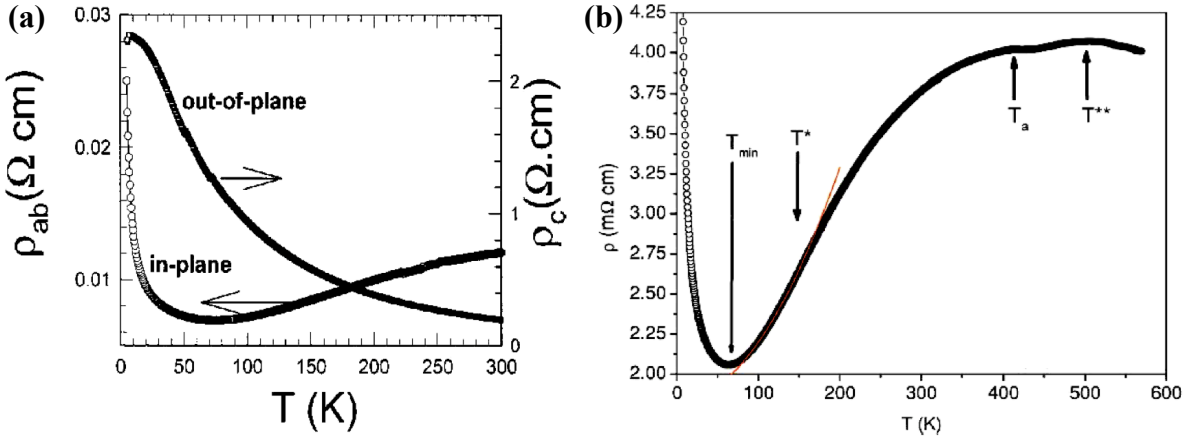

Figure 3.6: Resistivity of $[Ca_2CoO_{3-\delta}][CoO_2]_{1.62}$ single crystals as a function of temperature. (a) Anisotropy of the resistivity ρ_{ab} parallel and ρ_c perpendicular to the CoO_2 layers; and (b) temperature dependence of ρ_{ab} in in-plane direction (b). The temperatures $T_{min} \approx 63$ K, $T^* \approx 142$ K, and $T^{**} \approx 510$ K mark the transitions between the four different transport regimes, while T_a marks to an anomaly associated with a spin-state transition. Reproduced from Refs. [79, 100].

The in-plane resistivity shows four distinct transport regimes (Figure 3.6 (b)) [100]: insulating behavior is observed up to $T_{min} \approx 63$ K, with is conform with the low temperature band gap (cf. Section 3.1.3). Between T_{min} and $T^{**} \approx 510$ K, the half-metallic band structure results in a metallic temperature dependence ($d\rho/dT < 0$). In this regime, a Fermi liquid behavior was observed below $T^* \approx 142$ K (cf. inset in Figure 3.6 (b)) and a bad metal behavior for higher temperatures. Finally, $[Ca_2CoO_{3-\delta}][CoO_2]_{1.62}$ shows activated behavior above T^{**}.

The low temperature transport data show linear temperature dependence, differing from variable range hopping. Thus, carrier localization is excluded in favor of an anomalous suppression of the DOS [99]. For higher T, the non-monotonic temperature dependence and the metal-semiconductor transition (MST) at T^{**} can be explained by strong correlation

effects that appear in the vicinity of a Mott metal insulator transition [100, 112]: Between T_{min} and T^* the resistivity is proportional to T^2, suggesting a strongly correlated Fermi liquid, where the electron-electron-interaction is the dominant scattering mechanism (cf. fit in Figure 3.6 (b)). At T^* the resistivity deviates from the T^2 behavior and shows a crossover to an incoherent metal (or bad metal), which means that the quasi-particle description valid in the Fermi-liquid regime breaks down. A bad metal shows an exceptional high resistivity in comparison to a conventional metal: for a conventional metal the mean free path of the charge carriers is much larger than the wavelength ($\sim 1/k_F$) of the charge carriers and the transport can be described by the Boltzmann equation. In contrast, for bad metals strong scattering effects occur and the mean free path decreases below the lattice parameter. In this case, the quasiparticle description breaks down (Mott-Ioffe-Regel limit) and the transport cannot be described by the Boltzmann equations anymore. The resistivity increase to values that correspond to mean free paths much smaller than the lattice parameter [112].

At high temperatures, the electrical conductivity and the Seebeck coefficient increase with temperature. Different models were suggested to explain the metal-semiconductor transition (MST) at T^{**} and the high T behavior of σ and α. Historically, the MST was first associated to a Co spin-state transition [79]. However, this seems unlikely because according to Figure 3.6 (b) the anomaly associated with a spin-state transition at temperature T_a differs by about 100 K from the MST temperature T^{**} [100]. Additionally, it was calculated that the energy needed for the excitation of the spin transition is much higher than the available thermal energy [93]. According to Cheng *et al.* the first order transition can be understood in terms of a Mott-Hubbard transition, which results in a localization of the itinerant electrons in the narrow e_g' band due to thermal expansion [113]. Because the pure layered CoO_2 compound is a Mott insulator [114], the strong electronic interaction between the CoO_2 and the Ca_2CoO_3 layers are responsible for the MST [37]. More precisely, a rearrangement of the CoO layer in the rock salt subsystem was observed [115] and the interaction of these modulations with the CoO_2 layers are believed to induce a partial localization of the carriers at the Fermi energy and hence influence the high T properties [93]. The high temperature transport is usually discussed as small-polaron hopping [116–120], while other authors excluded small-polaron transport at high temperatures in favor of an itinerant transport model above 400 K [107].

The localization of the charge carriers and the resulting temperature dependence of the electrical conductivity will be discussed in more detail in Chapter 6. The transport will be

interpreted within the framework of Anderson localization in the intermediate temperature regime and by small-polaron hopping at high temperatures.

3.1.5.2 Seebeck coefficient

Despite its good electrical conductivity, $[Ca_2CoO_{3-\delta}][CoO_2]_{1.62}$ has a surprisingly large Seebeck coefficient reaching values between $120\,\mu V/K$ and $150\,\mu V/K$ around room temperature [25]. Two different models were proposed to explain the coexistence of the large σ and α in the layered cobalt oxides.

The first model suggests that the large α result from the degeneracy associated with the different cobalt valence and spin states [45]. In the high T limit the Seebeck coefficient can be calculated by the generalized Heikes formula in the Hubbard model $\alpha = -\frac{k_B}{e}\ln\left(\frac{g_3}{g_4}\frac{x}{1-x}\right)$, which considers transport via localized states and strong Coulomb repulsion. The Seebeck coefficient depends on the concentration $x = \mathrm{Co^{4+}}/(\mathrm{Co^{3+}} + \mathrm{Co^{4+}})$ of the Co^{4+} ions in the CoO_2 layer (concentration of charge carriers) and the number of possible configurations g_3 and g_4 of the trivalent and the tetravalent Co ions, respectively. Due to the competition of the crystal field and the Hund's rule coupling, high, low and intermediate spin states are considered to be close in energy, producing high degeneracy levels g_3 and g_4. Not only the large degeneracies in the Co^{3+} and Co^{4+} sites, but also the ratio g_3/g_4 between them is important. According to this model, large Seebeck coefficients $\alpha \approx 154 - 214\,\mu\mathrm{V/K}$ can be reached, which result from the degeneracy together with the strong correlation of the $3d$ electrons.

Alternatively, the high Seebeck can be explained based on the band structure (cf. Section 3.1.3). It was found that the Co t_{2g} states in the CoO_2 layer determine the band structure close to E_F. More precisely, a single band of a_{1g} character crosses E_F and forms the upper edge of the valence band. The band dispersion of this narrow band leads to singularities in the DOS (cf. Figure 3.4 in Section 3.1.3), where the one at about 120 meV below E_F should be responsible for the large positive α. However, it is argued that the single-band picture cannot fully explain the large α because the group velocity of the conduction electrons in the vicinity of the singularity is too small [88]. Thus, the more dispersive e_g' bands, are assumed to contribute additionally to achieve a considerable $\sigma(E)$ around the singularity. As described in Section 2.1.3, a large Seebeck coefficient is reached because a narrow band of heavy carriers

creates a peak in the density of states close to E_F, which leads to a high $\sigma'(E)$. Additionally, dispersive bands with light carriers lead to a considerable $\sigma(E)$ around the singularity.

Indeed, it was shown that the large α and a good σ can be derived from the Boltzmann transport equations based on the full band structure [91]. Additionally, Schrade *et al.* concluded from the variable oxygen deficiency that the modified Heikes formula (first model) can only roughly describe the change of α with the charge carrier concentration, whereas a better description is given by the modified Mott formula derived from the Boltzmann transport equations for itinerant charge carriers without electronic correlations [107]. Accordingly, the second model seems to be more realistic.

3.1.5.3 Thermal conductivity

The thermal conductivity κ of polycrystalline samples is typically on the order of 2 W/Km between 300 K and 1100 K [25] and decreases with increasing temperature due to enhanced Umklapp phonon scattering. The main contribution to κ results from the lattice contribution κ_l, while the electronic part κ_e estimated from the Wiedemann-Franz law is rather small [28, 121].

A comparison between single crystalline layered cobalt oxides with different charge reservoir blocks between the CoO_2 layers (Ca_2CoO_3, Na or $Bi_{2-x}Pb_xSr_2$) revealed that the main contribution to the in-plane thermal conductivity results from the phonon contribution in the charge reservoir block [121]. For the layered cobalt oxides, the thermal conductivity decreases with increasing atom mass in the charge reservoir layers. However, κ seems to be particularly reduced for $[Ca_2CoO_{3-\delta}][CoO_2]_{1.62}$, which was interpreted to result from the high distortion of the Co-O layer in the rock salt blocks connected with the misfit structure [121]. The misfit structure also results in a slight anisotropy of the thermal conductivity in the a- and the b-direction.

A better understanding about the thermal conductivity can be achieved by theoretical calculations. First principal phonon dispersions for a rational 5/3 unit cell approximation were calculated via DFT+U using the PBE functional [122]. The resulting phonon dispersion curves and the phonon DOS are presented in Figure 3.7 (a) and (b). Due to the large number of atoms in the unit cell, the phonon DOS is determined by diverse optical branches in addition to the acoustic branches. In total, the braches lead to a phonon DOS with two bell-

shaped peaks centered around 6 and 14 THz. The lower frequencies result from vibrations of the heavy Ca and Co atoms, while the higher frequency modes are mostly associated with vibrations of the lighter oxygen atoms.

The lattice thermal conductivity can be calculated via the Boltzmann transport equations, using the phonon velocities derived from the phonon DOS and a constant phonon lifetime of $\tau = 2$ ps [122]. While the in-plane conductivities κ_a and κ_b are of comparable magnitude, the out-of-plane conductivity κ_c is 6-8 times smaller (Figure 3.7 (c)). In agreement with the experimental findings, the calculated partial contributions resulting from the rock salt and the CoO_2 layers reveal that the main contribution to the lattice thermal conductivity κ_l results from the insulating rock salt subsystem (Figure 3.7 (d)). The magnitude of the experimental lattice contribution κ_l was reproduced by the calculations, with deviations to the exact T dependence probably resulting from the assumed constant τ.

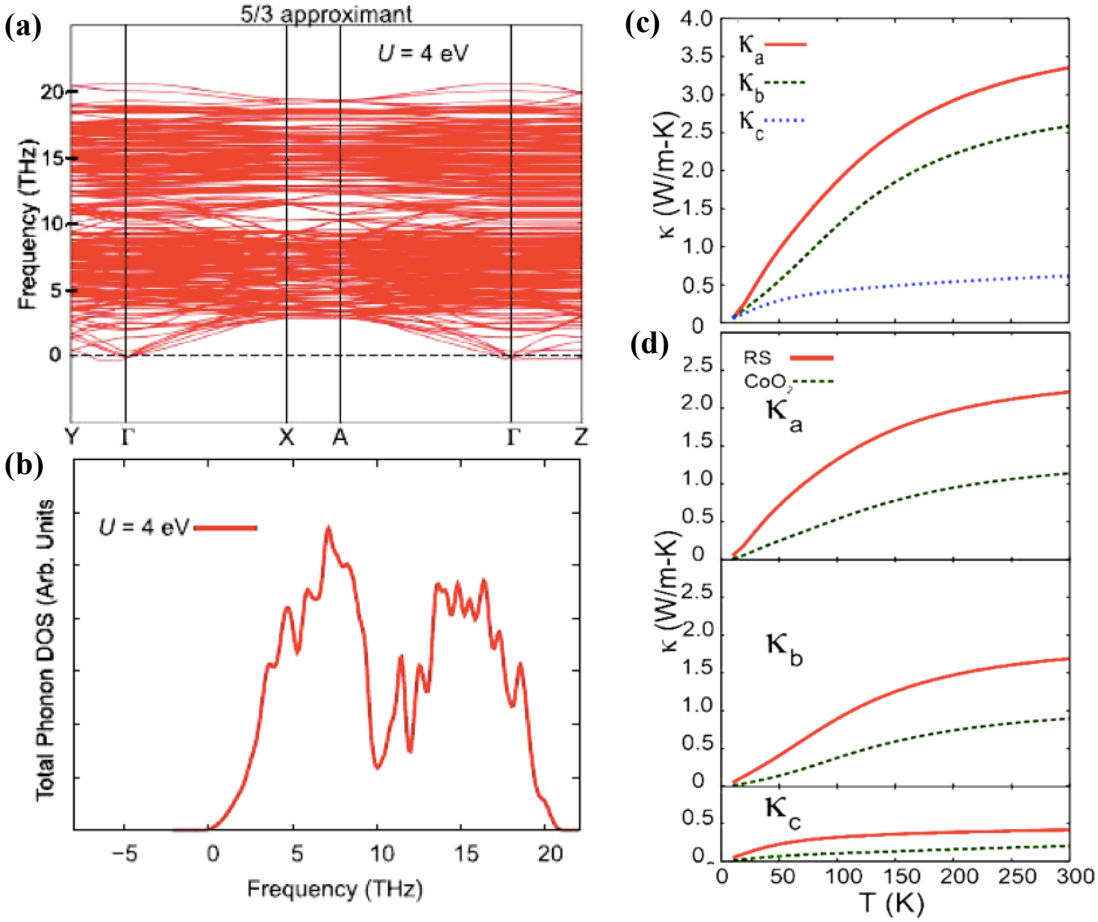

Figure 3.7: Phonon dispersion curves (a) and total phonon DOS (b) of $[Ca_2CoO_{3-\delta}][CoO_2]_{1.62}$. The theoretical total thermal conductivities κ_a, κ_b, and κ_c in the lattice directions a, b, and c are presented in (c), while the contributions of the rock salt and the CoO_2 system are illustrated in for each direction separately in (d). Figures modified from [122].

The origin of the small thermal conductivity was further analyzed by interpreting the static and the thermal atomic displacements recorded by annular-dark-field scanning transmission electron microscopy in combination with phonon scattering and DFT calculations. It was found that the interaction between the two incommensurate crystalline layers leads to anisotropic static and dynamic displacements, which are almost entirely localized in the Ca_2CoO_3 sub layer. The resulting contributions to the total thermal conductivity $\kappa(T)$ are summarized in Figure 3.8 (a). At low temperatures, κ is limited by resonance scattering of low-frequency acoustic phonons due to large in-plane vibrations of the soft Ca_2CoO_3 layer with respect to the rigid CoO_2 layer. In this case, traversing phonons with frequency ω_1 can be absorbed if they are in resonance with the localized vibrations in the soft layer (Figure 3.8 (c)). In contrast, between 80 K and 300 K higher frequency phonons are scattered by modulated in-plane atomic displacement in the Ca_2CoO_3 sub layer (Figure 3.8 (b)), and at high temperatures Umklapp scattering dominates [37].

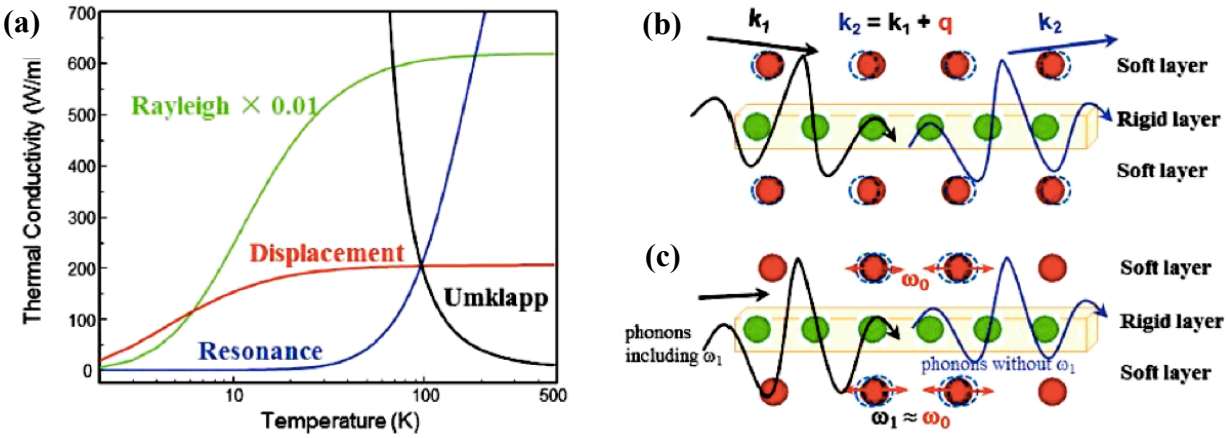

Figure 3.8: Temperature dependent contributions to the thermal conductivity (a) and schematic picture of displacement (b) and resonance scattering (c). Reproduced from Ref. [37].

The above summary of the thermoelectric properties reveals that the main contributions to the electrical and the thermal conductivity result from different subsystems. This makes heavy cation substitution in the rock salt layer a very promising strategy for the ZT improvement: Via the substitution κ can be decreased in the rock salt layer by increased Rayleigh scattering due to point defects without decreasing the charge carrier mobility in the CoO_2 layer. Additionally, at the same time the charge carrier concentration can be adjusted.

For the $[Ca_2CoO_{3-\delta}][CoO_2]_{1.62}$ system the thermal conductivity was successfully decreased via substitution of Ca with cations like Na [110], Bi [90] , Ag [123, 124], Eu [125], Ho [126], Dy [126], Lu [126], Y [127], Gd [117], Sr [128], Cr [129], B [130]. But also Co substitutions with Cu [131], Fe [131], Mn [131], Ti [132], Rh [111] and Ga [112] lead to lower thermal

conductivities. An interesting route is also the misplaced substitution of Na (which prefers the larger Ca site) on the Co site, which reduces κ and increases ZT [110]. Most of these elements have a larger mass than the substituted atom, but even for lighter atoms like Na and B the mass difference results in an increased point defect scattering.

3.1.5.4 Figure of merit *ZT* and its enhancement

A summary of ZT literature values shows a huge variation between the figures of merit of unsubstituted $[Ca_2CoO_{3-\delta}][CoO_2]_{1.62}$ (Figure 3.9 (a)). The deviations can result from variations in the oxygen content [107], the exact material synthesis or sintering procedure, which influence the microstructure of the polycrystalline samples, or the change of the Co/Ca ratio which is addressed in Chapter 7. The power factor, for example, can be considerably improved by using hot pressing and spark plasma sintering rather than conventional pressing. The improvement can be attributed to an increased density of the sample and texturing effects [134], which both have a positive effect on the electrical conductivity. Furthermore, the sintering parameters like the pressure level and the dwell temperature during SPS were found to strongly influence the microstructure in terms of density and hence the thermoelectric properties [135].

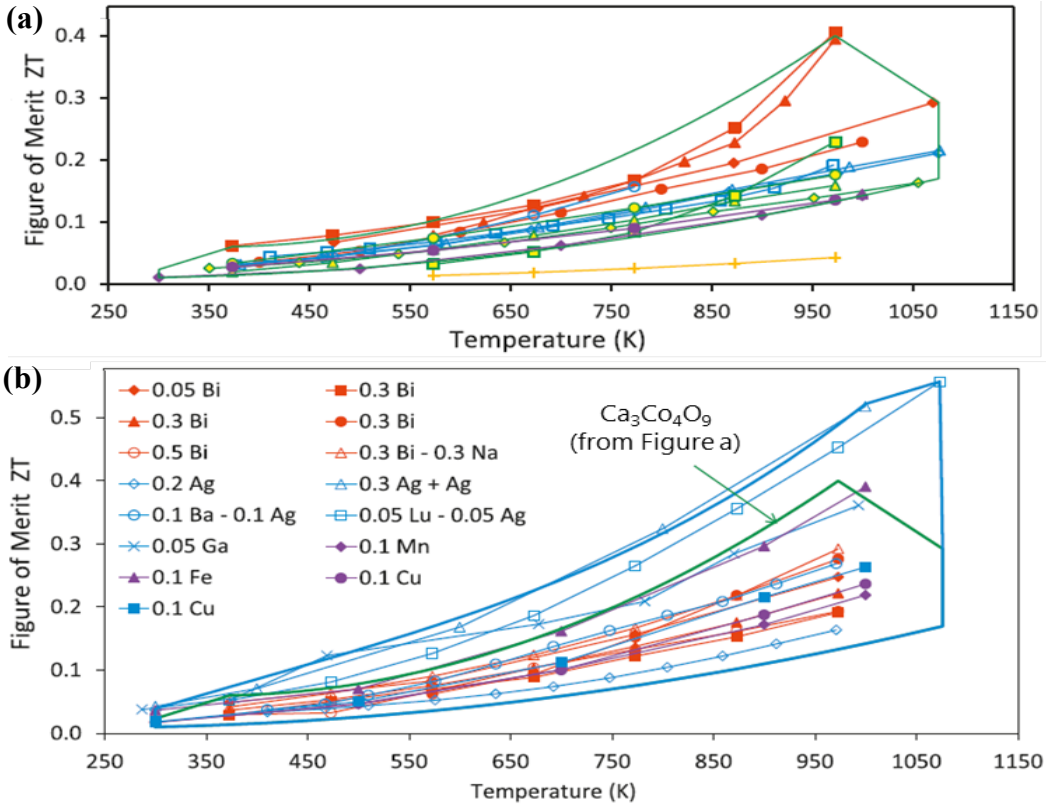

Figure 3.9: Comparison of the *ZT* of non-substituted (a) and substituted $[Ca_2CoO_{3-\delta}][CoO_2]_{1.62}$ (b), modified from [25].

Cationic substitution trend to increase the *ZT* compared to non-substituted compounds (Figure 3.9 (a)), although only few substituted samples outperform the best $[Ca_2CoO_{3-\delta}][CoO_2]_{1.62}$ values. Previous research on different substitutions is summarized using a periodic table (Figure 3.10): The site of the substitution is identified with a blue frame for Co substitution and a red frame for Ca substitution. An observed increase of *ZT* is highlighted in yellow. A large variety of atoms was substituted on the Ca and the Co site:

- ➔ **Ca site:** Na [110, 136], Bi [90] , Ag [123, 124, 136, 137], Eu [125], Ho [126], Dy [126], Lu [126], Y [127], Gd [117], Sr [128], Cr [129], B [130], La [136, 138], Nd [139], Er [126], Yb [140, 141], K [142, 143], Ba [144], Pr [145], Sm [145], Tb [145].
- ➔ **Co-site:** Cu [131, 146], Fe [131], Mn [131], Ti [132], Rh [111] and Ga [133], Ni [120] Ta [147], Pb [147], W [148], Ir [149], Zn [150], Ru [151], In [151, 152]

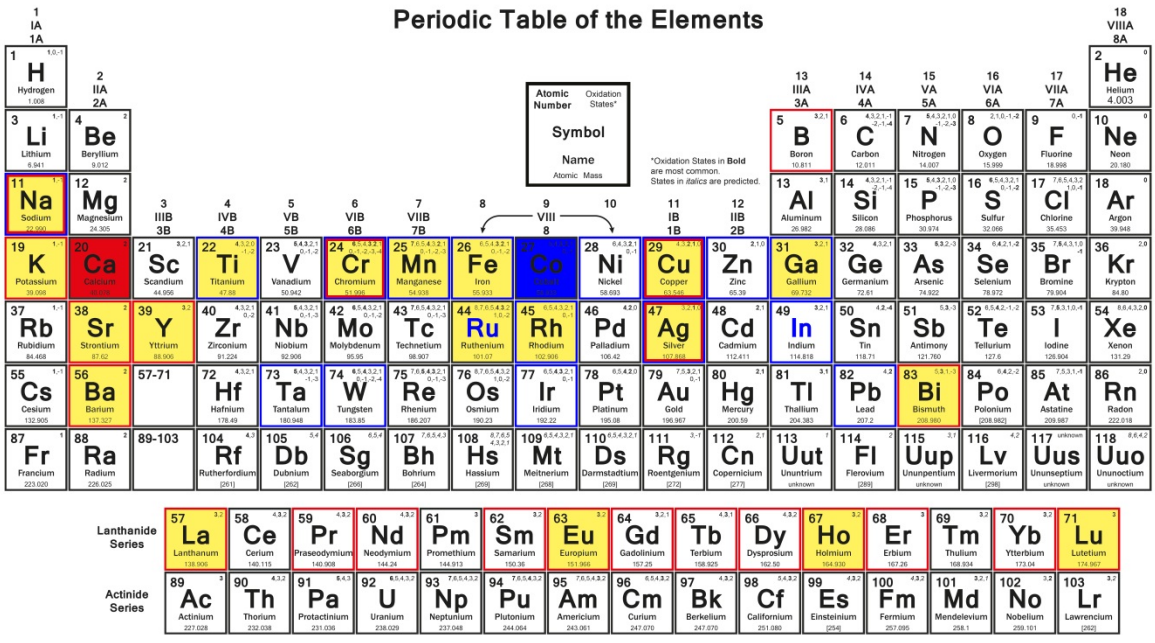

Figure 3.10: Periodic table summarizing the studied $[Ca_2CoO_{3-\delta}][CoO_2]_{1.62}$ substitutions. An observed increase in *ZT* is highlighted in yellow and the substitution on the Ca- and the Co-site are marked in red and blue respectively. References are given in the text. Color code added to plane periodic table taken from [153].

The best figure of merit for $[Ca_2CoO_{3-\delta}][CoO_2]_{1.62}$ was reported for single crystals with $ZT = 0.87$ at 973 K, with κ extrapolated from low T measurements [28]. However, for the fabrication of cost-effective thermoelectric converters, cheap polycrystalline materials are more relevant. The most promising *ZT* values for polycrystalline materials were reached for Lu and Ag substituted samples. While $Ca_{2.8}Lu_{0.2}Co_4O_{9+\delta}$ exhibited *ZT* values up to 0.36 at

1073 K [126], a very high figure of merit $ZT = 0.5$ is reached at 1000 K for Ag-doped polycrystalline cobalt oxide $Ca_{2.7}Ag_{0.3}Co_4O_9$/Ag-10% with additional Ag added as a second phase [154]. The figure of merit can be further improved by Ag^{1+}/Lu^{3+} co-substitution for Ca^{2+} atoms with nominal composition $Ca_{2.87}Ag_{0.05}Lu_{0.15}Co_4O_9$, which forms a complex multi-scale microstructure [29]. In contrast to the Ag substituted/added samples, the Lu co-substituted samples did not show any degradation effects. In detail the very high figure of merit of $ZT = 0.61$ at 1118 K is discussed to result from:

- Lamella nanostructure of $[Ca_2CoO_{3-\delta}][CoO_2]_{1.62}$,
- alignment of lamella nanostructures along favorable transport directions,
- increase of α, due to a decrease of carrier concentration by Lu^{3+} for Ca^{2+} substitution,
- reduction of κ due to heavy cationic substitution of Ca with Lu,
- reduction of κ due to phonon scattering by Ag-rich grains and their interfaces,
- enhanced grain boundary scattering, due to a variety of grain sizes ranging from several hundred nanometers to micrometers,
- high population of high angle grain boundaries
- decrease of ρ due to better conductivity in Ag grains or a better connection between the grain.

However, a large amount of Ag can have a negative effect on ZT because the percolation or agglomeration of Ag particles increases the thermal conductivity and can lead to shortcutting of the Seebeck voltage of the $[Ca_2CoO_{3-\delta}][CoO_2]_{1.62}$ grains [29]. In total, this section shows that ZT can be increased by various strategies and the given example proves that the combination of different strategies is most efficient to reach a large figure of merit.

The unique structure and the complexity of $[Ca_2CoO_{3-\delta}][CoO_2]_{1.62}$ presented in this chapter make the misfit-layered cobalt oxide an interesting thermoelectric material for further investigations. To better understand the material, the present study focuses on two separate strategies aiming to increase the figure of merit: (i) systematic cationic substitution with Ru and In and (ii) a variation of the Co/Ca ratio leading to the formation of nanoinclusions.

3.2 Calcium manganese(IV) (n-type)

Doped n-type calcium manganese(IV) $CaMnO_{3-\delta}$ is the material of choice for the fabrication of thermoelectric converters in this thesis because (i) it is a promising high temperature n-type oxides which shows a good *ZT* over a wide temperature range [30]; (ii) the thermal expansion coefficients of the two oxides are very similar [31], which is beneficial for the stability and the reliability of the entire converter; and (iii) good contacting methods were developed already, necessary for low parasitic resistances [31].

The n-type material reaches good *ZT* values for different substitutions. Here, tungsten substitution was chosen. $CaMn_{1-x}W_xO_{3-\delta}$ with $x \leq 0.05$ has a perovskite structure with the orthorhombic space group *Pnma* below 1200 K and a cubic structure at higher temperatures [30] (Figure 3.11 (a) and (b)). The transition metal occupies the corners (B-site) and the alkaline earth metal atom the central site (A-site) of a body-centered structure, with oxygen atoms located in the middle of the edges. A detailed analysis about the influence of tungsten substitution on the thermoelectric properties of $CaMn_{1-x}W_xO_{3-\delta}$ is given in Ref. [30] and the achieved *ZT* values are presented in Figure 3.11 (c). The best thermoelectric figures of merit are reached for x between 0.03 and 0.05. As Mn is more abundant than W [26], $CaMn_{0.97}W_{0.03}O_3$ with the smallest substitution level $x = 0.03$ is chosen for the fabrication of cost efficient generators.

$CaMn_{0.97}W_{0.03}O_3$ and $[Ca_2CoO_{3-\delta}][CoO_2]_{1.62}$ are a promising material combination for the fabrication of efficient and reliable converters. Due to the mentioned advantage, they form a good basis for testing of the compatibility approach in Chapter 8.

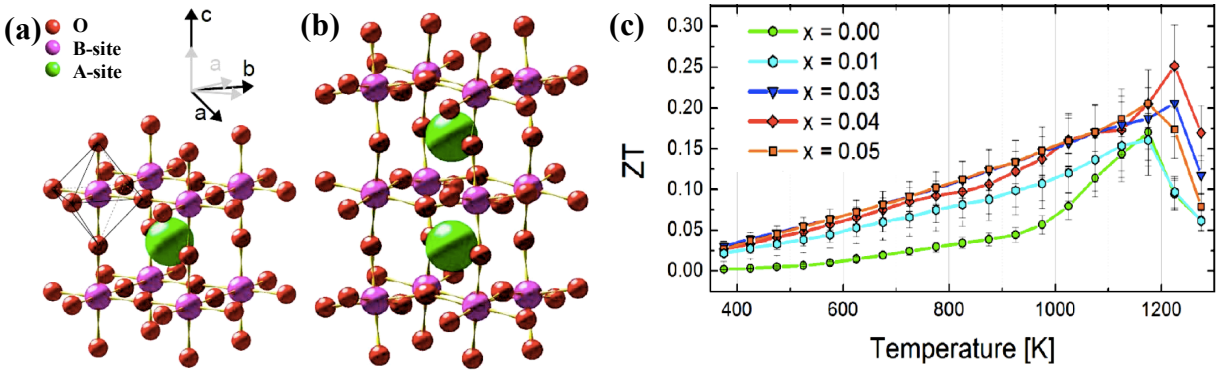

Figure 3.11: Schematic picture of (a) the high temperature cubic (*Pm$\bar{3}$m*) and (b) the orthorhombic (*Pnma*) perovskite structure. (c) Figure of merit of $CaMn_{1-x}W_xO_3$ as a function of temperature for different substitution levels. The best values are reached for a substitution level between x = 0.003 and 0.005, modified from [30].

4 Experimental methods

In this dissertation, several experimental methods are applied for the preparation and characterization of thermoelectric materials and converters. The methods can be grouped in four categories: (i) the synthesis of powders and preparation of sintered polycrystalline materials, (ii) the characterization of the sample morphology, structure, and phase composition, (iii) the characterization of the thermoelectric properties, and (iv) the fabrication and characterization of thermoelectric converters. Those methods, and their application in this work, are introduced in this chapter.

4.1 Synthesis methods and sintering

Conventional solid state reaction and soft chemistry methods were used for the synthesis of polycrystalline $[Ca_2CoO_{3-\delta}][CoO_2]_{1.62}$ base compounds investigated in this work. While the project started by using solid state reaction chemistry (see the results in Chapter 5 and 6), soft chemistry methods combined with spark plasma sintering turned out to be superior in yielding larger ZT values (cf. Chapter 6 7 and 8).

4.1.1 Solid state reaction (SSR)

For conventional solid state reaction synthesis, stoichiometric amounts of oxide or carbonate powders are mixed with each other. The level of intermixing of the different cations is limited by the particle size of the precursor powders, which is usually in the range of several micrometers. The thermally activated phase formation begins at the contact points between the different grains and the thickness of the product phase increases with the square root of the diffusion time (cf. Fick's law of diffusion). Due to the grain sizes and the slow kinetics, long diffusion times and high temperatures are necessary for the phase formation. In order to increase the homogeneity and the reaction rate, the starting powders should be finely ground and pelletized during temperature treatment to increase the contact area between the particles. Additionally, intermittent grinding steps are beneficial.

In this work, polycrystalline $Ca_3Co_{4-x}Ru_xO_9$ ($x = 0$; 0.1; 0.2) and $Co_3Co_{4-x}In_xO_9$ ($x = 0$; 0.1; 0.21) powders were synthesized via conventional solid-state-reaction route starting from $CaCO_3$, Co_3O_4, In_2O_3 or RuO_2 powders. Details about the temperature treatment and intermittent grinding are given in Section 5.2.

4.1.2 Soft chemistry

Compared to conventional solid state reaction synthesis, soft chemistry allows for the synthesis of materials at relatively low temperatures and short diffusion times [155]. The main idea is to dissolve metal alkoxides or metal salts to obtain a stoichiometric solution of metal cations, stabilized by complexation with chelating agents like citric acid to avoid re-crystallization on solvent evaporation [155, 156]. In the dissolved state the metal cations are homogenously distributed. This homogeneity is preserved in the dried phase and because of polymerization a xerogel is formed. Due to the homogeneous distribution, the diffusion times are small and the final phase forms quickly during calcination at relatively low temperatures.

For the synthesis of the misfit-layered cobalt oxide, a citric-gel-complexation method is used. Citric acid is a triprotic acid, which can potentially donate three protons. It acts as a polydentate chelate and substitutes the water ligands available in the solution. Here, the increase of entropy is the driving force for the substitution because substitution increases the number of molecules in the solution. To ensure a complete substitution, the molar ratio between citric acid and the metal ions $R_{ca/m}$ should exceed one, and larger ratios were found to result in larger average grain sizes [157]. Polymerization between the different citric acid molecules leads to the formation of a sol-gel and a xerogel after drying.

Two different routes based on different precursors were tested for the synthesis of $[Ca_2CoO_{3-\delta}][CoO_2]_{1.62}$. First, the hydrated metal salts $Ca(NO_3)_2{\cdot}4H_2O$ and $Co(NO_3)_2{\cdot}6H_2O$ were chosen as precursors. Both are relatively cheap and can easily be dissolved in water, but the crystal water can result in small uncertainties of the stoichiometry. A higher accuracy was achieved for dissolving elemental Co and $CaCO_3$ using nitric acid (HNO_3>69% aq.) as suggested by Ref. [158]. Therefore, this route was used within this work as described in the following. In order to synthesize $[Ca_2CoO_{3-\delta}][CoO_2]_{1.62}$, stoichiometric amounts of Co metal and $CaCO_3$ were suspended in ultrapure water. Nitric acid (>69% aq.) was added continuously using a dropping-funnel, while the suspension was stirred and cooled using an ice/water bath. The resulting solution was transferred into an aqueous solution of citric acid, where a ratio $R_{ca/m}$=2/1 was used. In order to dry the resulting clear pink solution (Figure 4.1 (a)), it is heated (at 25 K/h) in a furnace to a temperature of 373 K and dwelled there for four hours, followed by further heating (at 25 K/h) up to 573 K, where it was kept for ten hours. The solution undergoes a volume expansion and forms a porous xerogel during the drying process, which becomes black when organic solvents are partly released (Figure 4.1 (b) and

(c)). After drying, the xerogel was crushed in a mortar and the resulting powder was filled into an aluminum oxide crucible. For calcination, the citrate precursor powder was heated (at 320K/h) up to 1073 K and dwelled for ten hours, followed by free cooling. During this process, the organic material burned completely and phase formation started. After a final grinding step, the powder was ready for pelletizing and sintering.

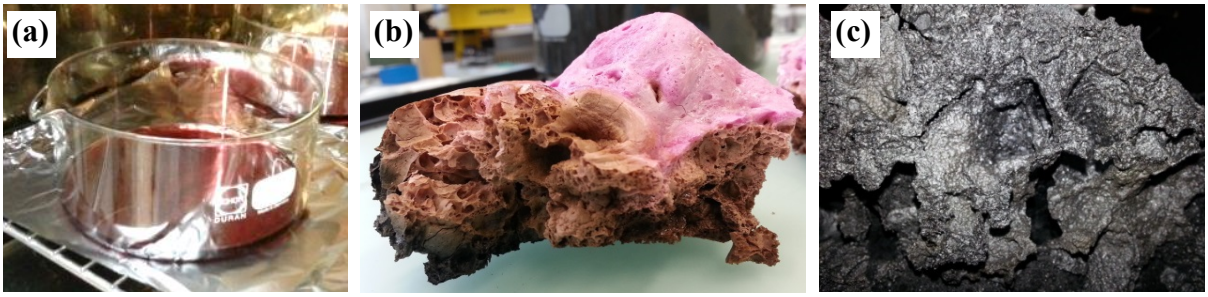

Figure 4.1: Steps during soft chemistry synthesis: (a) Clear pink solution containing the complexated metal cations. (b) Partly dried xerogel recorded during the drying process. (b) Xerogel after drying.

4.1.3 Spark plasma sintering (SPS)

Sintering denotes the formation of solid bulk materials from powdery compounds by means of heating without exceeding the melting point. During the process, the powder particles grow together due to diffusion driven by the diminishment of the surfaces area and hence the free energy. The sintering starts with the formation of necks between the particles, while in a later state pores can be eliminated. Improved sintering behavior can be achieved by the application of pressure.

In this work, Spark Plasma Sintering (SPS) is used for sintering the powders synthesized by soft chemistry methods. The pressing tool and the compacted powder sample are directly heated by DC electrical current pulses (Figure 4.2 (a)). Heat is generated within the sample due to joule heating, which results in faster and more homogeneous heating compared to conventional techniques like hot pressing. While on the macroscopic scale the heat distributes homogeneously across the entire sample, on the microscopic scale the heat dissipation is inhomogeneous (Figure 4.2 (b)): it is mainly dissipated at the contact points between different grains, where the electrical current density and hence the Joule heating is large. This leads to a beneficial sintering behavior, as heat is dissipated exactly where it is needed for sintering while the overall temperature is kept low to prevent grain growth [159].

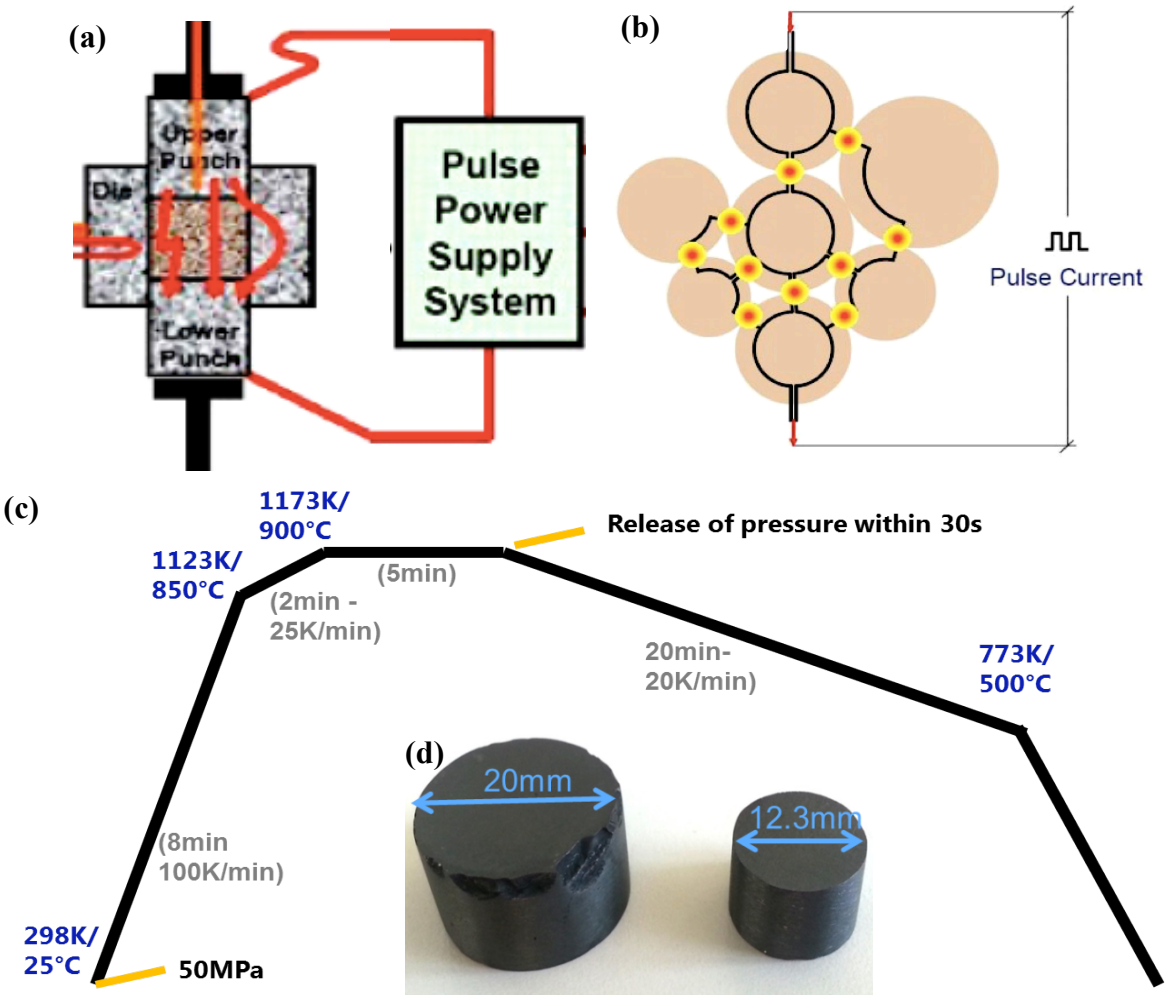

Figure 4.2: (a) Schematic picture of SPS sintering: The sample and the die are heated by DC electrical current pulses, modified from Ref. [159]. (b) Joule heating heats the sample mainly at the contact points between different particles, reproduced from Ref. [159]. Applied SPS sintering program (c) and $[Ca_2CoO_{3-\delta}][CoO_2]_{1.62}$ pellets sintered via SPS (d).

For spark plasma sintering, the powder is filled in a graphite die, which is covered with a graphite sheet. Sintering is done in vacuum and the sintering temperature is controlled using on a thermocouple plunged into the sidewall of the die. The used sintering program (Figure 4.2 (c)) was developed based on studies focusing on the influence of different sintering parameter on the properties of $[Ca_2CoO_{3-\delta}][CoO_2]_{1.62}$ [135, 144]. Modifications like a slower cooling rate were introduced to avoid cracking of the pellets. In Figure 4.2 (d) sintered $[Ca_2CoO_{3-\delta}][CoO_2]_{1.62}$ pellet after removal of the graphite foil are presented. The pellets were cut into pieces of desirable size for sample characterization, before the equilibrium oxygen composition was restored by post-annealed of the pieces at 1173 K in air for 20 h.

4.2 Sample morphology, structure and phase composition

4.2.1 X-ray diffraction (XRD)

X-ray diffraction method is based on the interaction of X-rays with the electron clouds surrounding atoms. In a crystalline material, the atoms occupy sites in a periodic lattice and lattice planes perpendicular to the lattice vector (h,k,l) can be indexed according to the Miller indices h, k, and l. Each family of lattice planes has a characteristic interplanar distance d_{hkl}.

A diffraction pattern is recorded by varying the angle θ of the incident beam while detecting the intensity of the reflected beam at an angle 2θ. If the Bragg condition $n\lambda = 2d_{hkl}\sin(\theta)$ is satisfied (cf. Figure 4.3 (a)) the scattered waves interfere constructively, where $n \in \mathbb{N}$ is the order of the reflex and λ the wavelength of the X-rays. Every reflex corresponds to a particular interplanar spacing d_{hkl}. In general, the intensity of the deflected X-rays can be calculated from the square of the absolute value of the structure factor. Depending on the symmetry of the crystal structure systematic extinction of reflexes is observed due to destructive interference. Thus, the crystal structure and the lattice parameters can be determined from XRD patterns.

Diffraction patterns are additionally determined by the occupancy of the lattice sites, the residual stress, the crystallite size, a preferred orientation and the instrumental conditions, which can alter the shape, the exact position or the intensity of the reflexes. To extract all of these information the patterns can be fitted via Rietveld refinement using the FullProf suite [160, 161]. However, in the present work only the lattice parameters could be extracted by simplified Le Bail fitting due to the complexity of the crystal structure and the pronounced preferred orientation [162].

X-ray diffraction patterns of polycrystalline powder samples and sintered pellets were recorded by a PANalytical X'pert PRO MRD diffractometer using Cu-Kα_1 radiation with a wavelength of $\lambda = 0.15406$ nm. The Bragg-Brentano configuration was used, where the intensity of the deflected X-ray beam is recorded in the θ-2θ-geometry (cf. Figure 4.3). Collimators (Soller slits) were placed behind the X-ray source and in front of the detector, to increases the signal-to-noise ratio by blocking of non-parallel rays.

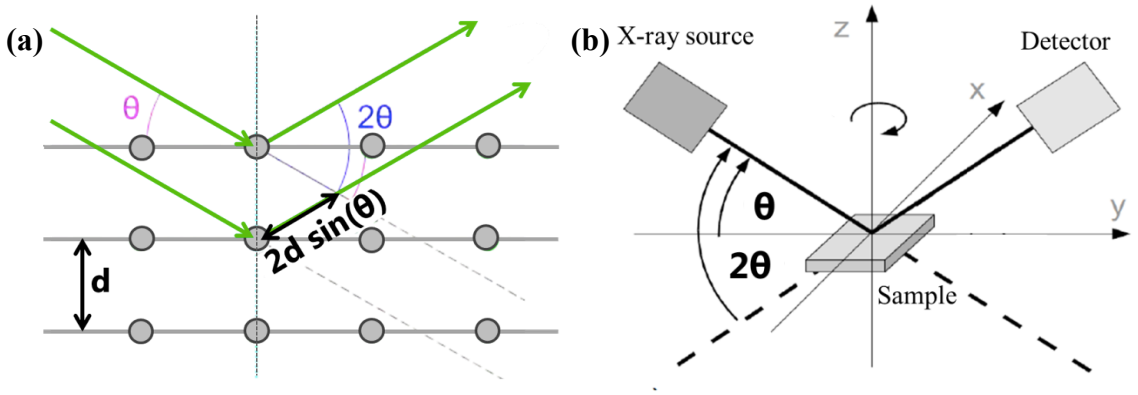

Figure 4.3: (a) Illustration of the Bragg condition. The X-rays (green) are reflected at the lattice planes with inter-planar distance d with an angle 2θ. (b) Schematic picture of the Bragg-Brentano configuration, used for collecting powder XRD-diffraction pattern in Θ-2Θ-geometry. In order to reduce effects caused by an alignment of the powder particles the sample is rotated around the z-direction continuously.

4.2.2 Electron microscopy

The microstructural morphology, the compositional distribution, and the chemical composition are investigated by Scanning electron microscopy (SEM). In this technique, a fine electron beam is scanned over the surface of the sample interacting with a pear-shaped sample volume. Kinetic energy is transferred to the valence electrons of the atom within that volume, allowing near-surface electrons to exit the sample. The number of these ejected secondary electrons depends strongly on the topology of the sample because the fraction of the pear-shaped volume that is close to the surface increases for a sloped sample surface compared to a flat one. The number of the ejected electrons depends only weakly on the type of the atoms and therefore the contrast of the SEM image in secondary electron mode reflects the topology.

In addition to the previously described inelastic scattering the incident electrons can also be reflected by the sample due to elastic interaction with the nuclei. The number of these backscattered electrons (BSE) strongly depends on the atomic number Z of the nucleus, and hence the BSE-image contrast reveals information about the chemical composition and in particular spatial distribution of different chemical phases. For local elemental analysis, energy-dispersive X-ray spectroscopy (EDX) is used. Here, the incident electron beam excites electrons from the inner shells of the atoms. The generated holes are refilled with electrons from higher energy levels and the excess energy is emitted as characteristic X-radiation. A unique set of peaks with different wave length and fixed relative intensities can be identified for each element due to its unique atomic structure. The relative elemental composition can be derived from the relative intensities

of the characteristic spectra because the peak intensity increases with the number of excited atoms.

In the present work, the preparation of the sample surface was adapted to the applied detection method. The morphology and the preferred orientation of the $[Ca_2CoO_{3-\delta}][CoO_2]_{1.62}$ particles were investigated with secondary electrons at a breaking edge of a sintered pellet (Chapter 5), while for the analytical quantification via EDX and the collection of BSE images (Chapter 7), the sample surfaces were polished carefully, to reduce influences resulting from the topology.

4.2.3 Thermogravimetric Analysis (TGA)[d]

The oxygen content of a compound can be determined via Thermogravimetric Analysis (TGA). During the measurement, the sample is heated with a constant heating rate in a defined gas flow and the change of weight due to physical transitions, chemical reactions like decomposition, release of crystal water, combustion or reduction of metal oxides is recorded. To reach a high accuracy, the influence of the chosen gas flow (buoyancy effects) is compensated by subtraction of a blind measurement recorded with an empty crucible under the same conditions. Volatile decomposition products can be tracked in the exhaust gas using a mass spectrometer.

In Chapter 7, TG analysis is used to investigate the oxygen content of $[Ca_{2-w}CoO_{3-\delta}][CoO_2]_{1.62}$ - Co_3O_4 composite samples with 0 %, 1 % and 3 % of Co_3O_4 impurities. The amount-of-substance fraction $\Psi = n_{Co3O4}/n_{Ca3Co4O9}$ of the Co_3O_4 secondary phase compared to the $[Ca_{2-w}CoO_{3-\delta}][CoO_2]_{1.62}$ phase was determined via SEM. In order to identify the oxygen content of the $[Ca_{2-w}CoO_{3-\delta}][CoO_2]_{1.62}$ phase in the composite material, advantage can be taken from the known phase transitions occurring in air (cf. phase diagram in Figure 3.2): When the samples are heated, a stepwise decomposition occurs that results in a change of mass (cf. Figure 4.4 (a)): Above 1196 K, the mixture of $[Ca_{2-w}CoO_{3-\delta}][CoO_2]_{1.62}$ and Co_3O_4 decomposes into a composite of $[Ca_{2-w}CoO_{3-\delta}][CoO_2]_{1.62}$ and $Co_{1-x}Ca_xO$(s), followed by decomposition to $Ca_3Co_2O_6$(s) and $Co_{1-x}Ca_xO$(s) above 1222 K. Finally, a

[d] Partly adapted from: Büttner, G., Populoh, S., Xie, W., Trottmann, M., Hertrampf, J., Döbeli, M., Karvonen, L., Songhak, Y., Thiel, P., Niewa, R., Weidenkaff, A.: Thermoelectric properties of $[Ca_2CoO_{3-\delta}][CoO_2]_{1.62}$ as a function of Co/Ca defects and Co_3O_4 inclusions. submitted. (2016).

mixture of $Ca_{1-x}Co_xO$(s) and $Co_{1-x}Ca_xO$(s) is formed above 1313 K. The total decomposition equation for heating above 1313 K can be written as

$$Ca_3Co_yO_{9+\delta'}\,(s) + \Psi\ Co_3O_4\,(s) \rightarrow A\ Ca_{1-x}Co_xO\ (s) + B\ Co_{1-x*}Ca_{x*}O\ (s) + 1/2(9+\delta'+\Psi-3-y)\ O_2\,(g), \tag{27}$$

where the elemental composition $Ca_3Co_yO_{9+\delta'}$ of $[Ca_{2-w}CoO_{3-\delta}][CoO_2]_{1.62}$ was used for simplicity. Here, Co_3O_4 is assumed to be fully oxidized, and A, and B are temperature-dependent constants, which can be determined from the nominal composition and the exact form of the phase diagram. As the oxygen content in the product phases does not depend on A and B, the oxygen content in the decomposition product is known. Therefore, the oxygen content δ' in the starting phase $Ca_3Co_yO_{9+\delta'}$, can be calculate from the relative mass loss Δm between the starting and the product material:

$$\delta' = \frac{\Delta m(3M_{Ca}+(y+3\Psi)M_{Co}+4\Psi M_O)-(\Psi-3-y)M_O}{(1-\Delta m)M_O} - 9. \tag{28}$$

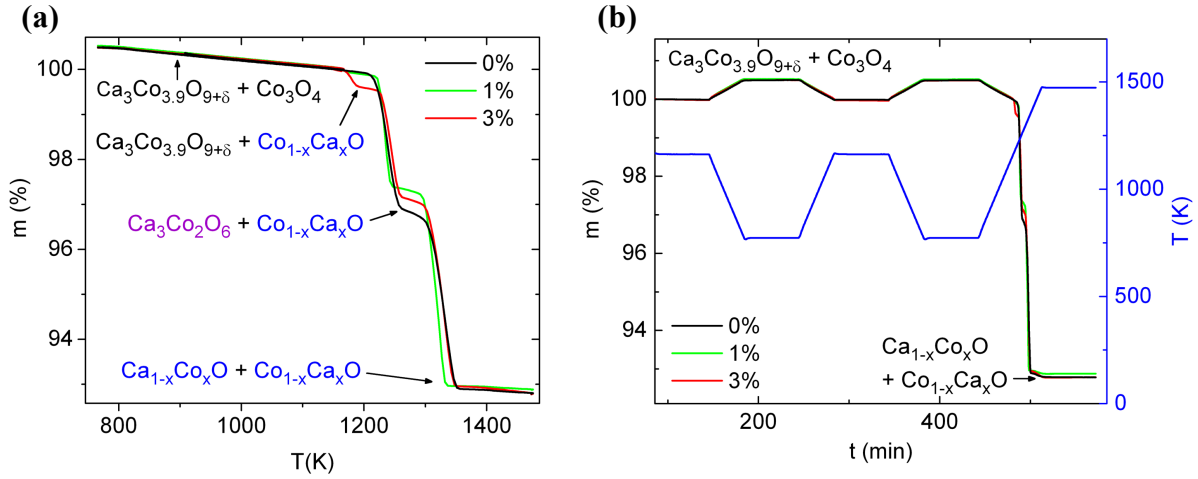

Figure 4.4: Thermogravimetric analysis (TGA) measurements in air for $[Ca_{2-w}CoO_{3-\delta}][CoO_2]_{1.62}$ samples with 0 %, 1 % and 4 % Co_3O_4 content. (a) Relative mass loss m as a function of temperature. A sudden decrease of the mass m followed by a stable plateau indicates the formation of a new phase that contains less oxygen. The phases that appear during the decomposition reaction are denoted for each plateau, where the misfit-layered oxide is abbreviated as $Ca_3Co_{3.9}O_{9+\delta}$ (b) Temperature program used during the measurement with corresponding mass loss. The decomposition was started after cycling the temperature within the stability range of the $[Ca_{2-w}CoO_{3-\delta}][CoO_2]_{1.62}$ phase.

In the present work the oxygen content of the $[Ca_{2-w}CoO_{3-\delta}][CoO_2]_{1.62}$ phase was determined by TGA using a Netzsch STA 449 C thermobalance. For the measurement, 40-110 mg of sample were heated while synthetic air was streamed through the apparatus with a rate of 50 ml/min. In order to confirm a reversible change of the oxygen content in the starting phase,

the temperature was cycled before starting the decomposition. The used temperature program and the corresponding mass loss are presented in Figure 4.4 (b).

4.3 Thermoelectric properties and charge carrier density

4.3.1 Seebeck coefficient

The Seebeck coefficient was determined via a RZ2001i unit (Ozawa Science, Japan) above room temperature, while a Physical Properties Measurement System (PPMS, Quantum Design) equipped with a Thermal Transport Option (TTO) was used for measurements below 300 K. In the RZ2001i unit, a bar-shaped sample is fixed between two platinum electrodes through which the electrical current is applied. The temperature difference ΔT is adjusted by cooling one end of the sample using cold air that flows through the glass capillary which supports the Pt electrode (Figure 4.5 (a)), while the overall sample temperature is controlled by an external furnace. For the determination of the Seebeck coefficient, ΔT was varied between 0 and 5 K across the length of the sample and the voltage ΔV was recorded after reaching a steady state. In the RZ2001i unit, ΔT and the voltage ΔV_1 as defined in Figure 4.5 (a) are measured at the edges of the sample. The Seebeck coefficient $\alpha = \Delta V_1/\Delta T$ is determined by the slope of the ΔV_1-ΔT curve.

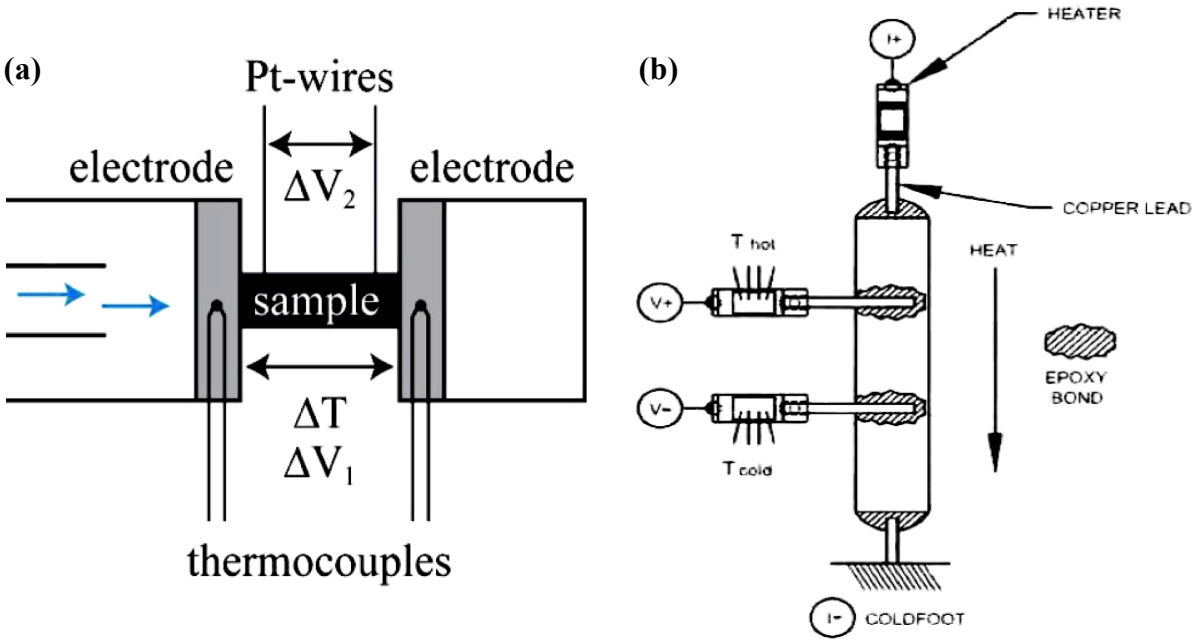

Figure 4.5: Geometry for the determination of the Seebeck coefficient. (a) For high temperature measurements in the RZ2001i unit, the generated voltage and the temperature are measured at the outer edges of the sample [163]. (b) For low temperature measurements in the PPMS both quantities are measured at the inner electrodes glued to the sample [164].

For low temperature measurements in the PPMS, the voltage drop and ΔT are measured at the inner electrodes glued on the sample with Ag-paste (Figure 4.5 (b)). The measurement of the Seebeck coefficient is done in a quasi-steady state, while the sample is cooled slowly with a constant cooling rate. A pulsed heater heats one end of the bar-shaped sample. During the pulse length, the voltage and ΔT increase asymptotically against their equilibrium values ΔV_∞ and ΔT_∞ which would be reached after an infinite pulse length (Figure 4.6). The equilibrium values can be determined by fitting the time dependence of the voltage and ΔT [164]. The Seebeck coefficient is given by $\alpha = \Delta V_\infty / \Delta T_\infty$. In the present work, the temperature rise was chosen to be about 1% of the average temperature. Typical measurement errors of the Seebeck coefficient are on the order of 5%.

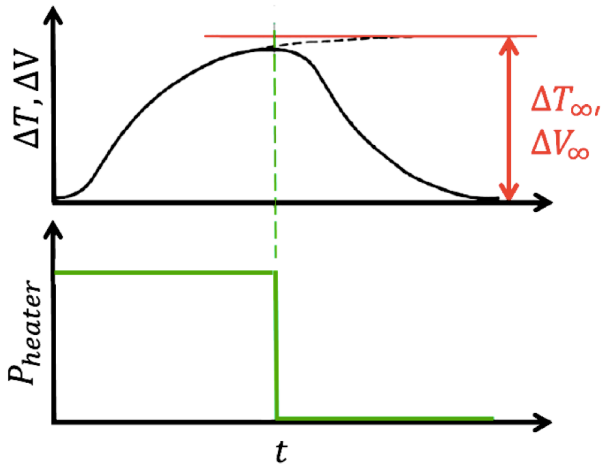

Figure 4.6: Schematic illustration of the determination of the Seebeck coefficient in the PPMS. One end of the sample is heated during a time t with heating power P_{heater}. The heat pulse leads to a time-dependent response of ΔT and the Seebeck voltage ΔV across the sample. The equilibrium values ΔT_∞ and ΔV_∞ can be determined by fitting.

4.3.2 Electrical conductivity

Just as for the determination of the Seebeck coefficient, the electrical resistivity is measured in the RZ2001i unit (Ozawa Science, Japan) at high temperatures and in the physical properties measurement system (PPMS) with thermal transport option (TTO) at low temperatures. Both machines measure the electrical conductivity via four-wire sensing to exclude the contact resistances. In this method, an electrical current is supplied to the edges of a bar shaped sample, while the voltage drop is measured at the two inner electrodes. Here, the voltage drop in the sensing wires and hence their resistance is negligible, since almost no current is flowing to the measurement instrument. While in the RZ2001i unit, thin platinum

wires are wrapped around the sample as inner contacts (cf. ΔV_2 in Figure 4.5 (a)), Cu wires are wrapped around and glued on the sample using Ag-paste in the PPMS (Figure 4.5 (b)). The electrical conductivity $\sigma = l/AR$ is calculated from the measured resistance $R = \Delta V_2/\mathrm{I}$, the cross-section area A of the bar-shaped sample, and the distance l between the inner electrodes.

4.3.3 Thermal conductivity

The low-temperature thermal conductivity κ is determined simultaneously with the Seebeck coefficient (Section 4.3.1) using the TTO option in the PPMS. According to the Fourier heat transport equation, the thermal conductivity

$$\kappa = -\frac{q}{\nabla T} = \frac{lQ}{\Delta T A}$$

is determined by the heat flux $q = Q/A$ through the sample with cross section area A and the temperature gradient $\nabla T = \Delta T/l$ across the distance l. In the PPMS, l is the distance between the inner electrodes and κ is calculated from the equilibrium temperature $\Delta T = \Delta T_\infty$ (cf. Figure 4.6) and the heat flow $Q = P_{\mathrm{heater}} - Q_{\mathrm{cond}} - P_{\mathrm{rad}}$. The heat flow is estimated from constant power supplied to the heater P_{heater}, the conductive Q_{cond}, and the radiative heat losses P_{rad}, which are estimated by the PPMS software considering the sample surface [164]. According to the Stefan-Boltzmann law, the radiative losses increase $\propto T^4$ and therefore the estimated P_{rad} and κ becomes unreliable above 300 K.

Due to the increasing radiative losses, a combination of different methods has to be used at high temperatures. The thermal conductivity $\kappa = \varrho\, c_p \lambda$ of a material depends on the density ϱ, the specific heat c_p and the thermal diffusivity λ of the material [165]. Thus, κ can be determined by independent measurements of thermal diffusivity and the specific heat using a laser flash apparatus and a differential scanning calorimeter, which are introduced in the next subsections.

4.3.3.1 Laser Flash Apparatus (LFA)

The thermal diffusivity is measured via laser flash method using a NETZSCH LFA 457 MicroFlash machine. During the measurement, the front side of a disc-shaped sample is heated for a few nanoseconds via a laser flash (cf. Figure 4.7 (a)). The resulting temperature

rise at the back side of the sample is tracked via an infrared sensor (Figure 4.7 (b)). Depending on the experimental conditions the signal can either reach a constant value for the adiabatic case (A) or decrease with time after reaching a maximum temperature (B). The difference results from differing heat losses at the back surface, which are typically larger for high temperatures ($\propto T^4$, Stefan-Boltzmann law).

To achieve good absorption and emission the samples are usually coated with graphite [166], which proved to be unnecessary for the used nearly black oxides with high absorption coefficients. In the adiabatic case the diffusivity can be calculated via

$$\lambda = 1.38\, d^2/\pi^2 t_{1/2}, \tag{29}$$

where $t_{1/2}$, is the time the back surface needs to reach half of the maximum temperature rise $\Delta T_{max}/2$ (cf. Figure 4.7 (b)) and d is the thickness of the sample [165]. To extract the thermal diffusivity for the common non-adiabatic case, the measured temperature response was fitted via the improved Cape-Lehman-method, which takes in account radial and facial heat losses and corrections due to the finite pulse-time [167, 168].

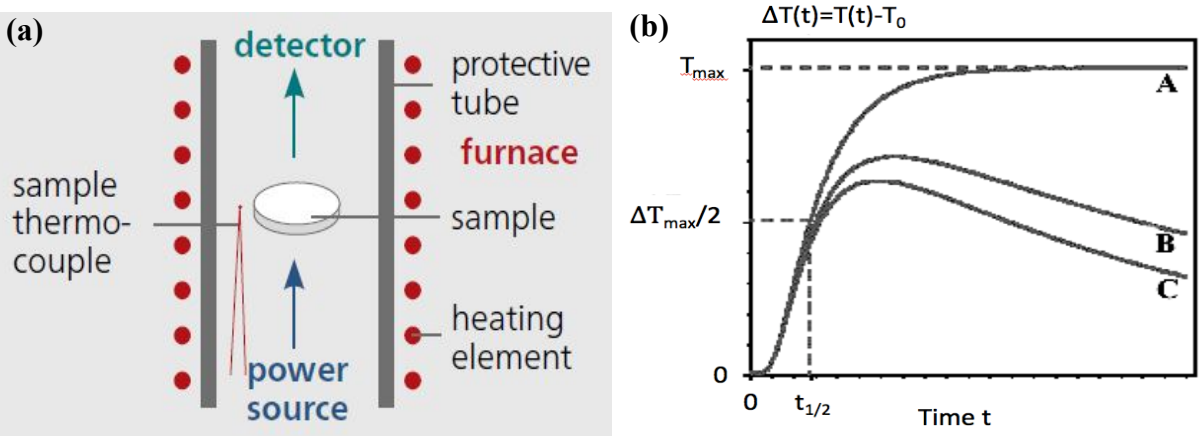

Figure 4.7: Measurement principle of the laser flash apparatus. (a) The disk shaped sample absorbs heat delivered by a laser flash (power source) and the temperature rise on the opposite side of the sample is recorded by an infrared detector, reproduced from Ref. [169]. (b) The time-dependent temperature rise at the backside of the sample depends on the experimental conditions. In the adiabatic case (A), T approaches a constant value ΔT_{max}, while radiative losses (B and C) lead to a decrease of the sample temperature with time. The time $t_{1/2}$ is defined by the half temperature rise $\Delta T_{max}/2$, which would be reached without radiative losses, reproduced from Ref. [170].

4.3.3.2 Differential scanning calorimetry (DSC)

For the determination of the specific heat capacity at constant pressure c_p, a heat-flux differential scanning calorimeter (DSC, Netzsch Pegasus 404C) is used. The measurement

principle is depicted in Figure 4.8. The temperatures of an empty reference crucible and a crucible containing the sample are compared, while the temperature of the DSC furnace is increased with linear heating rate. Due to differences in the heat capacities or the heat absorption of the crucibles, the reference usually heats faster than the sample and thermocouples below the crucibles record the temperature difference. This difference is recorded as a voltage signal, from which the difference in the heat flow can be deduced.

The heat capacity c_p can be determined from a series of measurements. First the temperature dependent signal for an empty sample crucible U_{base}, second the one of a reference sample U_{ref} and finally the one for the sample U are recorded. From these DSC-voltages, the specific heat of the sample

$$c_p = \frac{m_{ref}}{m} \frac{U - U_{base}}{U_{ref} - U_{base}} c_{p,ref} \tag{30}$$

can be calculated using the known specific heat $c_{p,ref}$ and mass m_{ref} of the reference sample and the mass m of the sample. For the evaluation, the standard procedure (DIN51007) was followed.

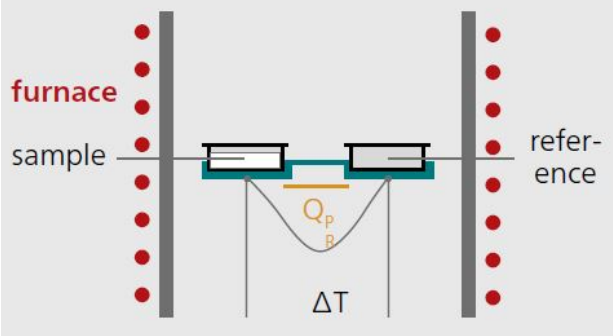

Figure 4.8: Measurement principle of the differential scanning calorimeter. Reproduced from Ref. [169].

Theoretically, the high temperature specific heat of the lattice can be estimated from the law of Dulong-Petit. Because for solids the boundary conditions of constant pressure and constant volume are comparable, the molar specific heat $C_p \approx C_v = 3R_{gas}/M_{av}$ can be estimated from the gas constant R_{gas} and the average atomic weight M_{av} of a multi compound material.

4.3.3.3 Measurement of the density

For all samples, the density was determined in two ways: geometrically by dividing the sample mass by the volume determined using a micrometer screw and additionally via the

Archimedes methods. While for the geometrical method uncertainties mainly result from irregularity of the disk shape, Archimedes methods leads to uncertainties in the case of porosities. To minimize the measurement errors, Archimedes method was chosen for the high density samples (Chapter 6, 7 and 8), while the geometrical method is more reliable for samples with lower density (Chapter 5 and 6).

4.3.4 Charge carrier density - Hall effect measurements

The charge carrier concentration, the mobility and the type of the dominating charge carriers can be determined by Hall measurement. The method is based on the Lorenz force, which deflects the charge carriers perpendicular to the magnetic field $\vec{B}$ and the direction of the carrier movement (Figure 4.9). Due to this force, the mobile charge carries accumulate at one face of the sample until the electrical field resulting from the charge separation counterbalances the force. The resulting Hall voltage

$$V_H = \frac{1}{nq}\frac{IB}{t} \tag{31}$$

depends on the magnetic field B, the electrical current I, the thickness t of the sample defined in Figure 4.9, the charge $q = \pm e$, and the charge carrier concentration n.

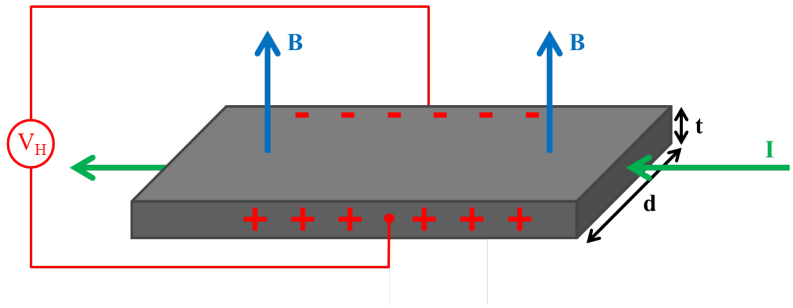

Figure 4.9: Schematic illustration of the Hall effect. A current I flows perpendicular to the magnetic field B through the sample with thickness t and width d. Moving charge carriers experience a Lorenz force and thus accumulate at the faces of the sample. A Hall voltage V_H builds up due to the charge separation.

In order to determine the charge carrier density, the Hall resistivity $\rho_H = \frac{V_H}{I} = \frac{1}{nq}\frac{B}{t}$ is measured as a function of the magnetic field. From a fit of this linear dependence, the Hall coefficient $R_H = 1/nq$ and hence the charge carrier density and the type of carriers can be extracted. In the present work, Hall effect measurements are performed using the Alternating Current Transport (ACT) option in the PPMS. After reaching the desired temperature, the Hall resistivity is measured using an AC current while the B-field is slowly swept between $\pm$ 1T.

4.4 Thermoelectric converters[e]

4.4.1 Fabrication and design of thermoelectric converters

During this work, the power output of the oxide converters was more than doubled by the improvement of the design and the electrical contacts. A conventional 4-leg oxide module with two Al_2O_3-plates and an improved half-skeleton module are presented in Figure 4.10 (a) and (b). The removal of one Al_2O_3-plate reduces the total thermal resistance of the module, allowing for a better usage of the available heat flux, while the remaining plate ensures the mechanical stability. This design is particularly advantageous for cascading with high efficiency low temperature modules (e.g. Bi_2Te_3) with conventional design with two Al_2O_3 plates because one plate is sufficient for electrical insulation between the two modules. While for the conventional converter Ag contacts are soldered in a muffle furnace without pressure, the improved half-skeleton modules are soldered via hot pressing under an uniaxial pressure of 6.3 MPa using Ag-paste containing 6 wt.% of $Ca_{2.97}Bi_{0.03}Co_4O_{9+\delta}$ power [31, 64].

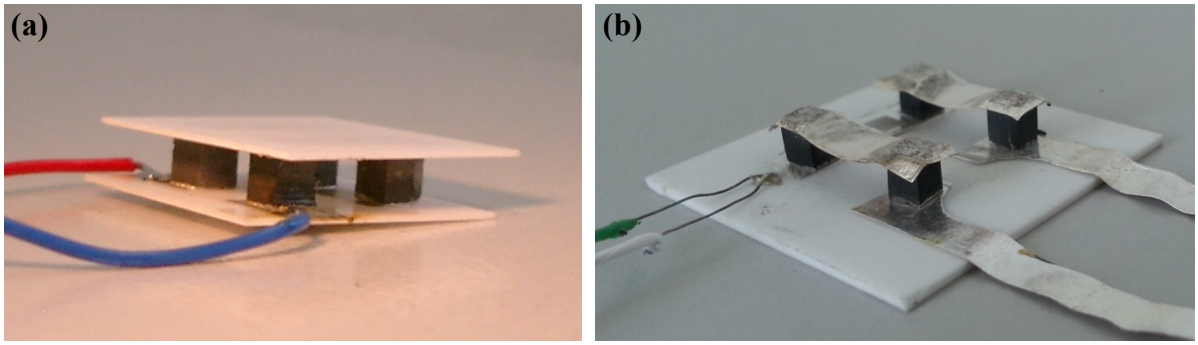

Figure 4.10: Four-leg thermoelectric oxide converters: Conventional design with two Al_2O_3-plates (a) and improved half-skeleton design (b).

The current-voltage characteristics recorded for a conventional four-leg and a half-skeleton module fabricated from p-type $[Ca_2CoO_{3-\delta}][CoO_2]_{1.62}$ and n-type $CaMn_{0.97}W_{0.03}O_{3-\delta}$ with the same leg dimensions illustrates the converter improvement (Figure 4.11). While the temperatures and accordingly the open circuit voltages are comparable, the power output of the half-skeleton-module is more than doubled due to the decreased contact resistance.

[e] Partly adapted from: Saucke, G., Weidenkaff, A., Populoh, S.: Kostengünstige und verlässliche thermoelektrische Konverter für die Nutzung industrieller Abwärme - Abschlussbericht. BFE - Bundesamt für Energie (2014).

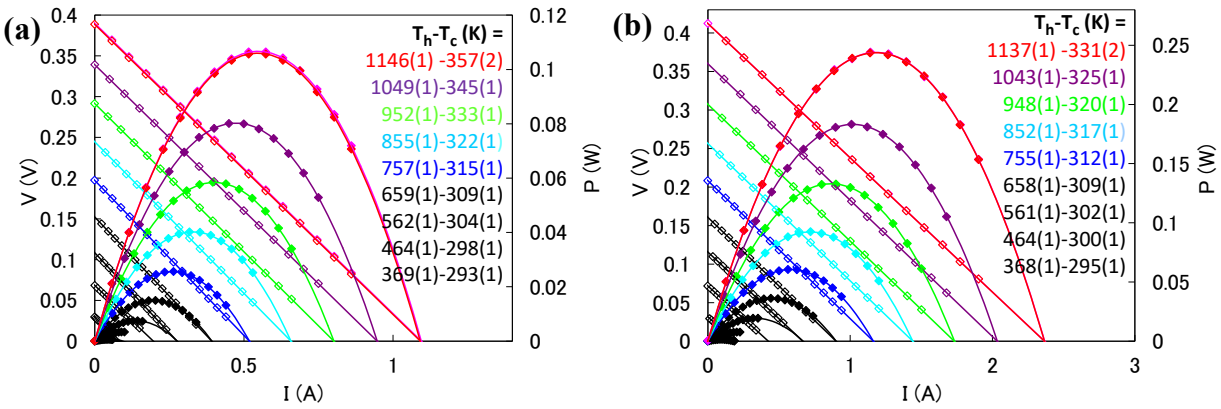

Figure 4.11: Current-voltage characteristics and power output *P* of a conventional (a) and a half-skeleton module (b) with the same leg dimensions for different temperature differences.

For fabrication of thermoelectric converters, thermoelectric legs with desired dimensions were cut from n- and p-type bulk pellets using a diamond wire saw. A similar height of all legs was assured by polishing, which it is essential for a homogeneous soldering process and the overall stability of the module. Metallic interconnects with desired dimensions were cut from an Ag-sheet. The upper and the lower faces of the legs as well as the parts of the interconnects, which are afterwards connected with the legs, were covered with a thin layer of Ag-paste.

The assembly of half-skeleton thermoelectric converters is depicted in Figure 4.12 (a). Double-faced sticky tape was used to fix the Ag-interconnects and the supply wires on the Al_2O_3-plate as well as the legs on top of the interconnects. Next, the upper interconnects were glued on top. Larger converters were produced in the same way, but extra attention was paid on avoiding shortcuts between the legs: Thus, a metallic grid is used for positioning of the legs, before the metallic interconnects are attached with sticky tape (Figure 4.12 (b) and (c)). To keep the distance, strings were placed in between the legs, which combusted during soldering in the hot press. For soldering, the converters were arranged on the piston-plate and inserted into the hot press (Figure 4.12 (d) and (e)). Here, additional dummy legs were added to distribute the supplied minimum force, such that a maximum pressure of about 6.2 MPa was applied during soldering. The pressure and the temperature were increased stepwise with intermediate holding steps to allow for burning of organic solvents, the sticky tape and the spacer strings (Figure 4.12 (f)). A final soldering temperature of 1133 K was applied for 5h. During soldering, the metal interconnects at the upper side of the module were covered with a thin Al_2O_3 sheet, which can be easily removed by polishing.

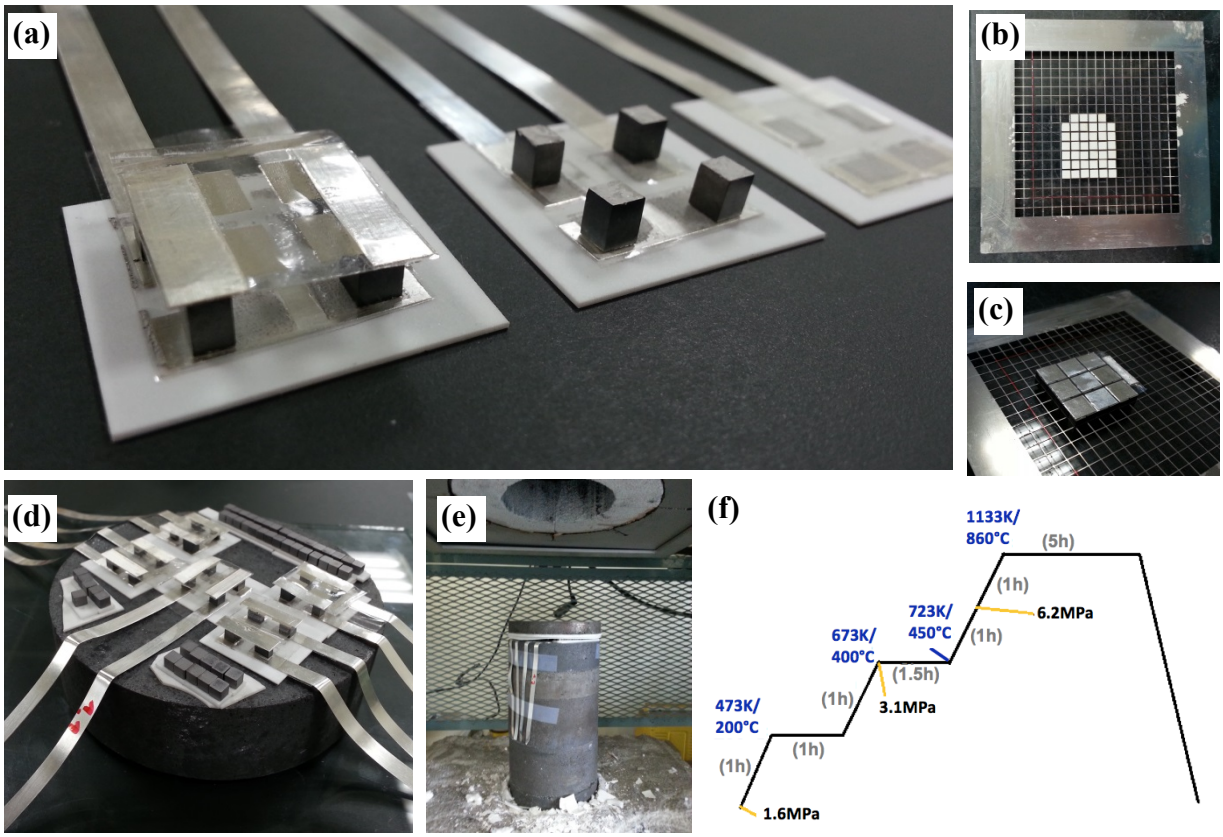

Figure 4.12: Fabrication and design of half-skeleton thermoelectric converters. (a) Preparation steps of four-leg thermoelectric converters. (b) Positioning of the legs using a metal gird. (c) Gluing of metal interconnects. (d) Preparation of modules and dummy materials for hot pressing and (e) mounting in the hot press. (f) Soldering program applied in the hot press.

In contrast to the conventional design (cf. Section 2.2.1), for the fabricated multi-leg converters two legs were connected in parallel. Thus, the metal interconnects always connect two n- and two p-type legs (cf. Figure 4.13). This special design was chosen to increase the reliability of the converter. In case of failure of one leg, the total current will flow through the second one, which results only in a small decrease of the overall efficiency, as the increase of the total resistivity is small.

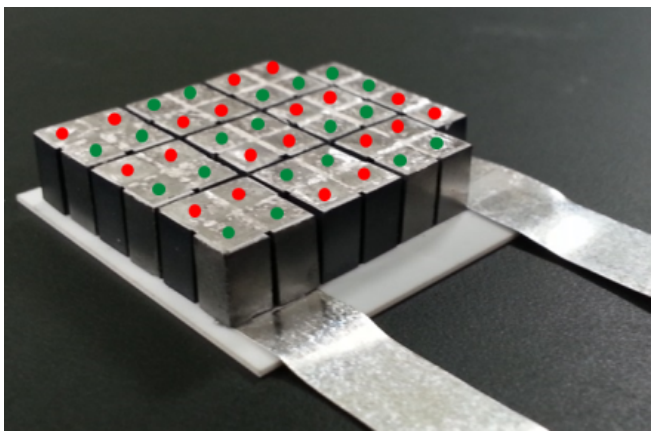

Figure 4.13: Design of the half-skeleton converter, with two legs connected in parallel. The position of the n- and p-type legs are marked with green and red circles, respectively.

4.4.2 Characterization of thermoelectric converters

For the characterization of the thermoelectric converters, the converter is placed in between the cooling and the heating plate of a test stand and a constant pressure is applied to achieve a good thermal coupling. Current-voltage characteristics are recorded, while the hot T_h and the cold side temperature T_c are controlled by the test stand. The hot side temperature of the module is adjustable by a planar heater, while the cold side is cooled with water passing through a Cu-plate. While electrical insulation to the heater is achieved by the Al_2O_3-plate of the converter, extra insulation between the exposed metal contacts of the converter and the Cu-plate is necessary. As illustrated in Figure 4.14 (a), a soft silicone gel (AlphaGel COH, grey sheet, stable up to 200°C, $\kappa \approx 6.5$W/mK, electrical insulator, good shock absorber [171]) is placed on the Cu-plate to balance the unevenness resulting from slight variations of the leg lengths. The silicone gel and the Cu-plate are covered with Kapton to avoid sticking of the heated gel to the module and for additional electrical insulation. The self-made thermocouple is glued on the hot side of the Al_2O_3-plate next to the leg at the inner side of the module using Ag-paste, which is dried in a furnace at 100°C for 30 min Figure 4.14 (b). The cold side temperature T_c is measured by a thermocouple placed between the bare contacts of the legs and the covered silicone gel, with additional Kapton insulation between leg and thermocouple (Figure 4.14 (c)). Finally, an Al_2O_3 wool sheet is placed around the converter to reduce the heat radiation from the heating to the cooling plate (d) and the heating-plate is pressed on the module using a weight attached on a lever (e).

As a first characterization, the room temperature resistivity of the entire module is determined from current-voltage characteristics recorded using a Keithley 2440 as source meter and a Keithley 2010 as voltmeter. The four-wire technique is used to exclude the resistance form the supply wires. During heating, the open circuit voltage V_{OC} and the temperature at the hot side, the cold side, and at the water supply (in and out) are measured via a Keithley 2700 voltmeter. After thermal stabilization at the desired temperature, current-voltage characteristics are recorded in the same way as for the room temperature measurement. The internal resistance $R_i = \Delta V/\Delta I$ is calculated from the slope of the IV-characteristic (cf. Figure 4.11) and the maximum power output $P_{max=}U_{OC}^2/4R_i$ is calculated from R_i and V_{OC}.

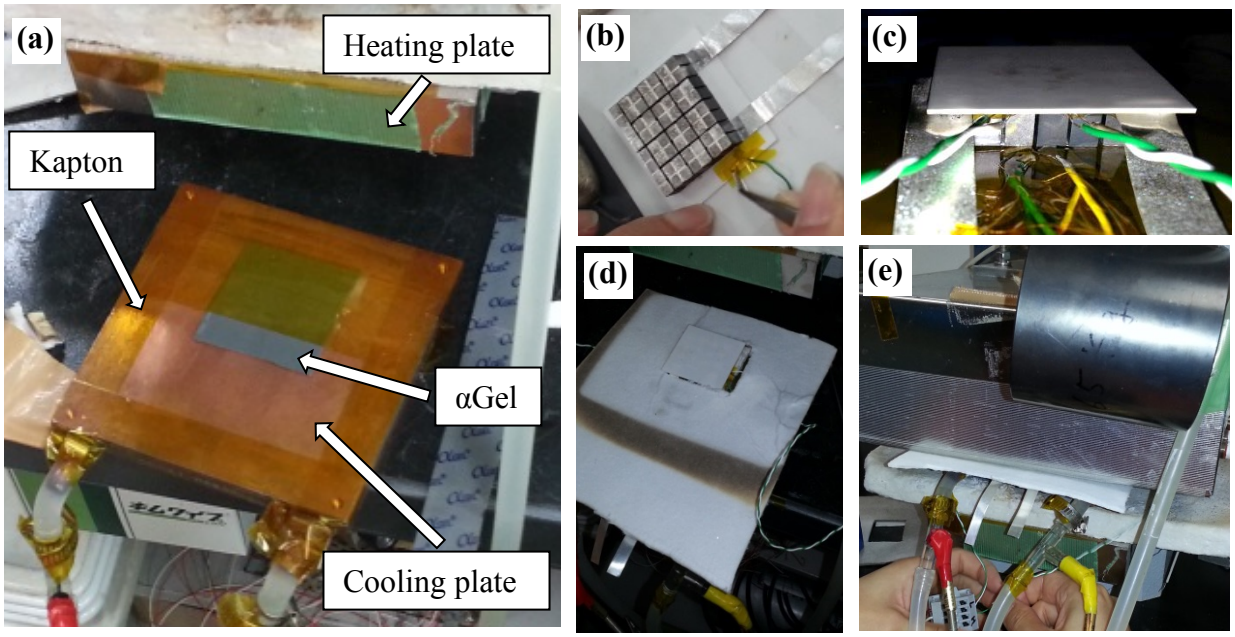

Figure 4.14: Characterization of thermoelectric modules in the test stand. (a) The water-cooled Cu-plate is covered with the grey AlphaGel and yellowish Kapton tape. (b) Ag-paste is used to glue a self-made thermocouple on the Al_2O_3 plate next to the legs. For stabilization, it is additionally fixed with Kapton tape. (c) Module on the cooling plate with the hot side thermocouples glued on the Al_2O_3 plate and the tips of the cold side thermocouples placed below the legs of the half-skeleton converter. (d) Al_2O_3 wool is placed around the converter to reduce the heat radiation from the heating to the cooling plate. (e) The heater is pressed on the module using a weight attached on a lever.

4.4.3 Contact resistivity

In order to fabricate converters with high conversion efficiencies, stable contacts with low contact resistances are necessary. For the determination of the contact resistance (in Chapter 8), legs with different length l but the same cross section area A were cut from the same pellet. All cross-sectional areas were completely covered with the electrode material and supply wires were attached to each contact before soldering. A series of legs, which were fabricated in the hot press in the same way as the contacts during module fabrication and a typical Ag-$[Ca_2CoO_{3-\delta}][CoO_2]_{1.62}$ interface recorded via SEM are presented in Figure 4.15 (a) and (b).

In order to exclude the wire resistances, current-voltage characteristics were recorded in four-wire configuration using a Keithley 2450. The measured total resistance

$$R_{tot} = R_{leg} + 2R_{cont} + 2R_{Ag} \approx \rho l/A + 2R_{cont}$$

is determined by the resistance of the oxide leg R_{leg}, the contact resistance R_{cont} and the resistance R_{Ag} of the electrode material, which is considered as negligible. Because the leg resistance $R_{leg} = \rho l/A$ depends on the resistivity ρ of the leg material and scales with lengh l, a plot of the measured total resistance against the different leg length shows a linear trend (Figure 4.15 (c)). The contact resistivity can be determined from the y-intercept of the $R_{tot}(l)$ fit and is given by $\rho_c = AR_c$.

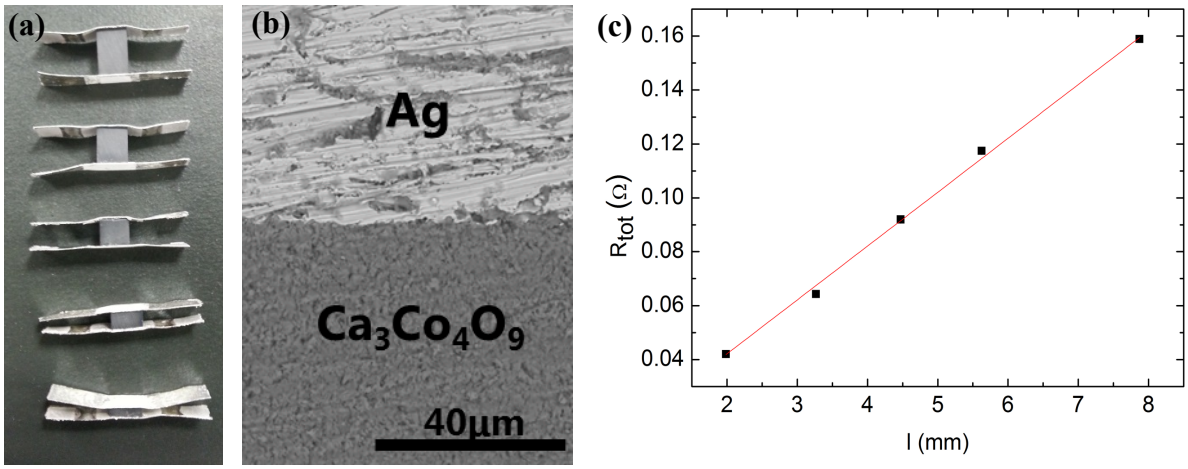

Figure 4.15: (a) Series of $[Ca_2CoO_{3-\delta}][CoO_2]_{1.62}$ legs for the determination of the contact resistance, which were prepared and soldered in the hot press in the same way as the modules. (b) Typical Ag-$[Ca_2CoO_{3-\delta}][CoO_2]_{1.62}$ interface recorded via SEM in backscattering mode. (c) The measured total resistance increases with the length l of the legs. The contact resistivity can be extracted from a linear fit.

5 Thermoelectric properties of Ru and In substituted misfit-layered $[Ca_2CoO_{3-\delta}][CoO_2]_{1.62}$[f]

The misfit-layered cobalt oxide shows outstanding thermoelectric properties, which can be further improved by cationic substitutions. The complex incommensurate structure and correlation effects make it difficult to reliably predict the thermoelectric performance for substituted compounds. To better understand the effect of ruthenium and indium substitution on the thermoelectric properties, polycrystalline samples with elemental formulas $Ca_3Co_{4-x}Ru_xO_9$ and $Ca_3Co_{4-x}In_xO_9$ ($0 < x < 0.21$) were investigated experimentally within a temperature range of 300 K < T < 1125 K. Both substitution strategies result in a significant decrease of the thermal conductivity and an enhancement of the thermoelectric figure of merit of up to 25 % for $x = 0.1$ Ru substitution. The large reduction of the thermal conductivity induced by Ru substitution (up to 30 %) is attributed to resonance scattering of phonons at local resonance vibrations of the Ru atoms. Increasing Ru substitution decreases the p-type carrier concentration, which increases the electrical resistivity and the Seebeck coefficient at low temperatures. For indium substitution, the increase of the p-type carrier density is accompanied by a decrease of the Seebeck coefficient while the resistivity is nearly constant. Both substitutions shift the metal-semiconductor transition toward higher temperatures, which may be connected to the distortions introduced into the lattice by the atom. Ru substitution is a promising strategy for a further ZT improvement. Especially the large reduction of the thermal conductivity makes Ru a promising candidate for co-substitution with a second atom that mainly increases the power factor.

5.1 Introduction

The outstanding thermoelectric properties of the misfit-layered $[Ca_2CoO_{3-\delta}][CoO_2]_{1.62}$ can be further improvement by cationic substitutions [25, 120, 133, 145]. The band structure and the origin of the good thermoelectric performance were analyzed by several theoretical studies (cf. Chapters 3.1.3 and 3.1.5), but the complex incommensurate structure and correlation

[f] Adapted and partly vertatim from: Saucke, G., Populoh, S., Vogel-Schäuble, N., Sagarna, L., Mogare, K., Karvonen, L., Weidenkaff, A.: Thermoelectric properties of Ru and In substituted misfit-layered $Ca_3Co_4O_9$. MRS Proceedings. 1543, 83–92 (2013).

effects make it difficult to reliably predict the thermoelectric performance for substituted compounds. In this context, the present chapter systematically investigates the thermoelectric properties of polycrystalline $[Ca_2CoO_{3-\delta}][CoO_2]_{1.62}$ as a function of doping with ruthenium and indium. In the following, the samples are denoted according to their elemental formula because the layer of Co-substitution is not clear. In order to understand the effect of the substitution atoms better, polycrystalline $Ca_3Co_{4-x}Ru_xO_9$ and $Ca_3Co_{4-x}In_xO_9$ ($0 < x < 0.21$) were prepared via a solid-state-reaction route and the thermoelectric properties were measured within a temperature range of $300\ K < T < 1125\ K$. This chapter presents the microstructure of the samples and discusses the effect of the substitution atoms on the resistivity, the metal-semiconductor transition temperature, the Seebeck coefficient, and the thermal conductivity.

5.2 Experimental procedures

Polycrystalline $Ca_3Co_{4-x}Ru_xO_9$ (x =0; 0.1; 0.2) and $Co_3Co_{4-x}In_xO_9$ (x = 0; 0.1; 0.21) powders were synthesized via conventional solid-state-reaction route (SSR) starting from $CaCO_3$, Co_3O_4, In_2O_3 or RuO_2 powders. Stoichiometric amounts of reactants were mixed and ball-milled (400 rpm for 1 h) using isooctane as dispersing medium, whereupon the originally intended composition of $Ca_{3-x}In_xCo_4O_9$ (x = 0; 0.1; 0.2) for substitution on the Ca-site was considered. Pelletized (Perkin Elmer hydraulic press, pellet diameter 13 mm, pressure 70 kN) samples were placed in alumina boats and calcined in air at 900 °C for 24 h. The calcined pellets were ground manually using agate mortar and pestle, re-pelletized under similar conditions and sintered in air at 920 °C for 24 h (pristine and In-substituted samples) or 48 h (Ru-substituted samples). The as-sintered pellets were annealed in oxygen flow for 36 h with one intermittent grinding. X-ray measurements were done using a powder diffractometer (XRD; PANalytical X'pert PRO MRD; Cu-Kα_1 radiation, $\lambda_{Cu} = 0.15406$ nm). The recorded diffraction patterns were fitted using LeBail method as implemented in the program FullProf. In order to investigate the preferred orientation in the pressed samples, XRD patterns were recorded from the plain top side of the disk-shaped pellets ($\parallel z$), before they were cut into lamella and measured again ($\perp z$) after turning them by 90° (inset in Figure 5.2 (a)).

To investigate the thermoelectric properties, each pellet was cut into two slices: one part was used for the determination of the thermal diffusivity λ, while the second part was cut into bars for the measurement of the Seebeck coefficient α and the electrical conductivity σ. Pieces left

over from cutting were used for the specific heat C_p measurements. After measuring the thermal diffusivity parallel to the pressing direction ($\parallel z$), the pellet was cut into lamella and the lamella were turned by 90° (similar to Ref. [172]) to measure λ perpendicular to z (cf. inset of Figure 5.2 (a) and [173] for more experimental details). The error induced by the cutting is lower than 5 % as apparent from the comparison of the diffusivity measurement of the uncut sample with the cut lamella (both along the pressing direction, cf. Figure 5.4 (d)). All temperature dependent measurements were performed in O_2 flow. The Seebeck coefficient and the electrical conductivity were measured using the Ozawa Science RZ2001i system. The error limits $\Delta\sigma = 7$ % and $\Delta\alpha = 5$ % for the system were estimated based on the errors in the measurement of the distance between the electrode-contact wires and the sample dimensions [174]. For the determination of $\kappa = \varrho\lambda C_p$, λ was measured using Laser Flash Absorption (LFA; Netzsch LFA 457 Microfash) and C_p using a Differential Scanning Calorimeter (DSC; Netzsch DSC 404 C). The densities ϱ of the samples were determined through weighing and measuring the geometric dimensions. The error $\Delta\lambda$ was calculated based on the measurement uncertainty and the inhomogeneity in the thickness of the samples (2-5 %). For C_p three independent measurements suggest a standard deviation $\Delta C_p < 5$ % over the whole temperature range. The error $\Delta\varrho$ was additionally considered as 2-8 % depending on the sample. The error of the figure of merit $\Delta ZT =$ 13-19 % follows from error propagation.

Hall measurements were performed in the Physical Property Measurement System (PPMS; Quantum Design) using the AC Transport option with a frequency of 1 Hz. The magnetic field strength was varied between -25 and +25 kOe, while the excitation currents were between 10 and 300 mA. For the Hall measurements, the statistical error of the Hall-resistivity-magnetic-flux fitting and the errors in the measurement of the dimensions (8 %) were considered.

Finally, the morphology and the mean particle size of the different samples were investigated with scanning electron microscopy (SEM; Hitachi S-4800 and XL30 ESEM (FEI)) with a secondary electron detector. The SEM images were recorded at a breaking edge with a perspective perpendicular to the pressing direction.

5.3 Results and discussion

The XRD-patterns presented in Figure 5.1 (a) confirm the phase formation of the misfit-layered cobalt oxide. For all patterns, the lattice parameters were extracted via LeBail fits

(FullProf) using the space group *C 2/m* with two independent axis parameters b_1 and b_2 of the CoO_2 and the rock salt type layers. In addition to the layered oxide, a minor impurity phase of Co_3O_4 ($Fd\bar{3}m$) is found for In substitution and two weak reflexes (marked by arrows in Figure 5.1 (a)) were unidentified. All of the LeBail fits had a good statistical quality ($1.57 < \chi < 3.05$, $1.01 < R_p < 1.28$, $1.35 < R_{wp} < 1.89$, $1.04 < R_{exp} < 1.09$). Nevertheless, the asymmetric peak shape especially of the c-axis reflexes leads to a nonzero asymmetric difference plot.

For both substitutions, characteristic changes of the lattice parameters for increasing substitution level suggest an introduction of the substitution atoms into the lattice (Table 5.1 and inset of Figure 5.1 (a)). In the case of Ru substitution, no impurity phase is observed, which confirms a substitution of Co with Ru. For Ru, the a- and the c-axis parameter expand with the substitution level, while b_2 decreases. The systematic decrease of the b_2-parameter indicates a substitution in the rock salt layer, while partly substitution in the CoO_2 layer cannot be excluded due to the minor change of the b_1 parameter.

	ϱ_{rel} (%)	a (Å)	b_2 (Å)	b_1(Å)	c (Å)	β (°)	b_1/b_2
$Ca_3Co_4O_9$	75(1)	4.832(1)	4.572(1)	2.808(1)	10.834(1)	98.11(2)	0.6142(4)
$Ru_{0.1}$	72(1)	4.834(1)	4.569(1)	2.807(1)	10.851(1)	98.10(2)	0.6144(4)
$Ru_{0.2}$	69(5)	4.837(1)	4.563(1)	2.812(1)	10.868(1)	98.10(2)	0.6162(4)
$In_{0.1}$	71(1)	4.828(1)	4.563(1)	2.812(1)	10.873(1)	98.11(2)	0.6164(4)
$In_{0.2}$	71(1)	4.821(1)	4.555(1)	2.817(1)	10.880(1)	98.13(2)	0.6184(4)

Table 5.1: Relative density compared to the theoretical density (ϱ_{rel}), as determined by geometrical measurements and weighing of the sample pellets, and the lattice parameters determined by LeBail fitting (FullProf). The parameter b_1/b_2 describes the lattice misfit between the CoO_2 and the rock salt layer.

For increasing In substitution, the amount of the Co_3O_4 phase increases, while no In-based impurities were observed. The Co excess indicates that indium drives Co out of the structure by substituting the Co site instead of the attempted Ca site. Nevertheless, systematic changes of the lattice parameters are observed for both sub layers: The lattice parameters a and b_1 of the rock salt layer decrease, while b_2 and c increase for increasing substitution level. Hence, the substitution occurs in both sub-layers. Considering Co substitution, the initial precursor mixture should lead to the composition $Ca_3Co_{4-x}In_xO_9$ (x = 0; 0.1; 0.21). The effect of Co_3O_4 impurities on the transport properties will be discussed in detail in Chapter 7.

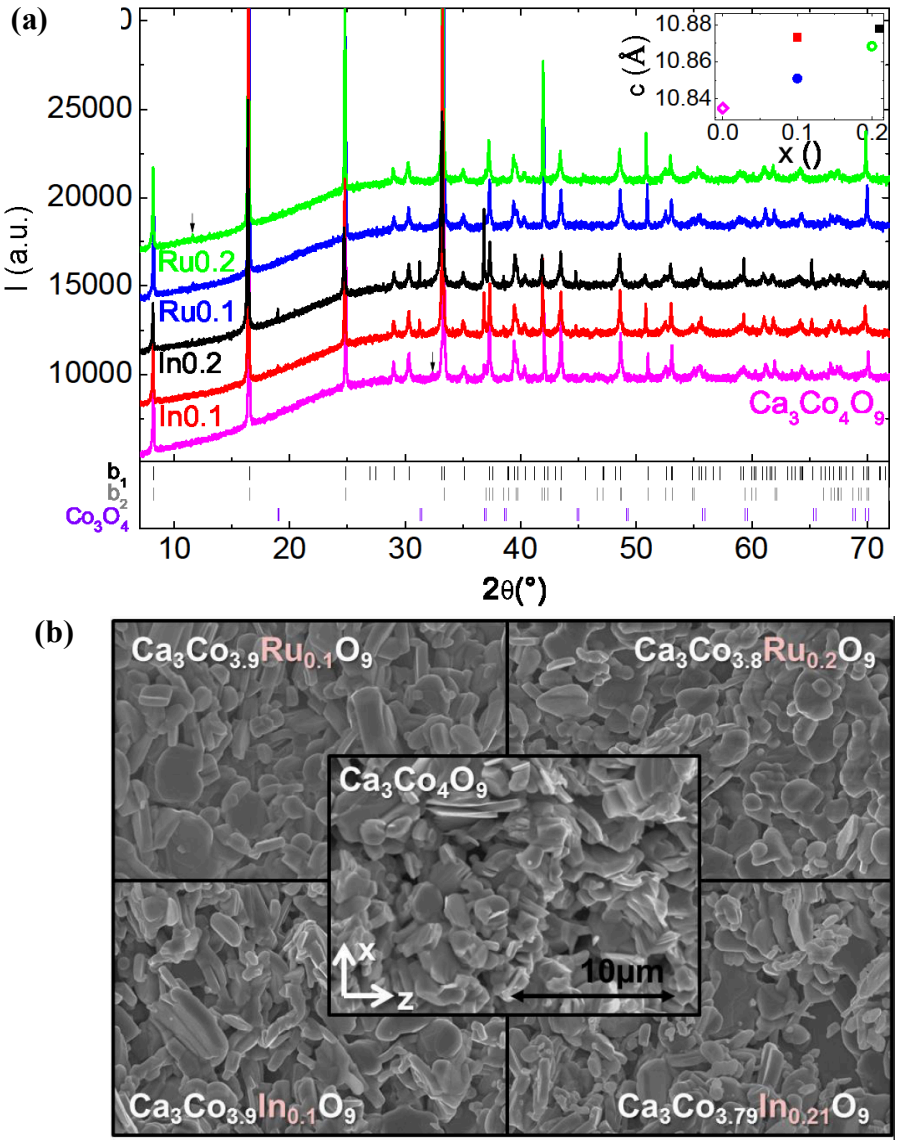

Figure 5.1: (a) X-ray diffraction pattern for different In and Ru substitution levels. Peak positions presented at the bottom were calculated via LeBail fitting (FullProf) of the $Ca_3Co_4O_9$ sample in the space group *C 2/m* with two independent b-axis parameters and Co_3O_4 with the symmetry $Fd\bar{3}m$. Two weak reflexes are unidentified and marked by arrows. The inset shows the determined expansion of the c-axis parameter due to Ru (circles) and In substitution (squares). Samples are named according to the substitution atom and the substitution level in the whole Chapter. (b) The SEM micrographs of $Ca_3Co_4O_9$-based sintered pellets with different substitution levels show the microstructure of the samples with a perspective perpendicular to the pressing direction z.

The SEM images recorded in secondary electron mode show very similar features for all samples (Figure 5.1 (b)): plate-like crystallites with thicknesses between 0.2-0.9 µm and diameters in the range of 0.4-4 µm. The XRD patterns recorded for $x = 0.1$ Ru-substitution parallel and perpendicular to the pressing direction z reveal a preferred orientation of the c-axis parallel to z, which is obvious from the alteration in the intensity of the [00l] reflection intensities in comparison to the intensities of the reflections related to the other crystal planes. SEM secondary electron micrographs taken in the two directions show different

characteristics due to the alignment of the grains (Figure 5.2 (b)). A plain view perspective parallel to the pressing direction (polished surface) reveals regular shaped particles with diameters between 0.5-4 µm, while the plate like character of the particles with thicknesses in the range of 0.3-0.9 µm is recognizable from the cross-sectional view.

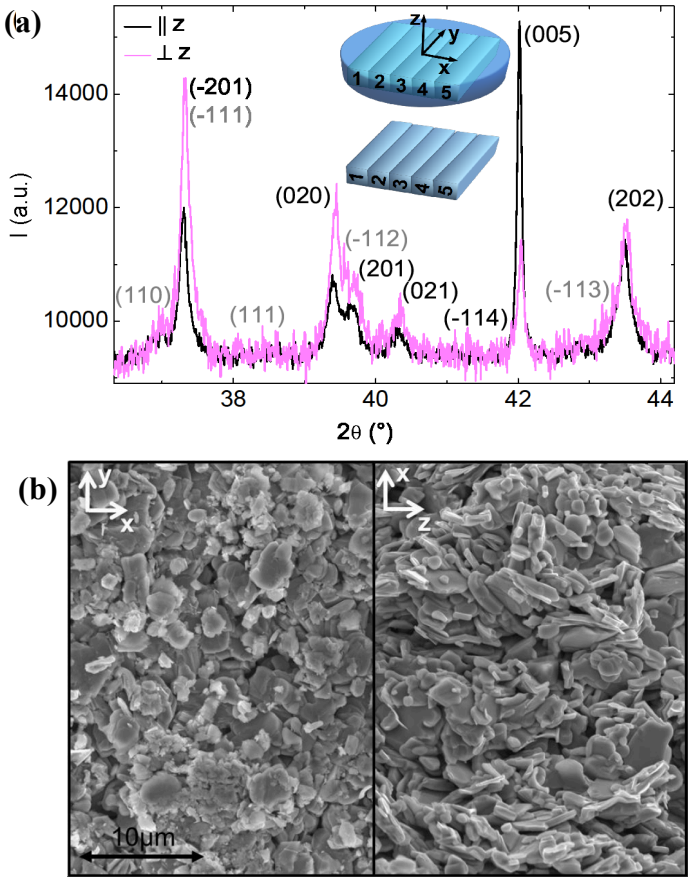

Figure 5.2: Preferred orientation in the pellets due to the uniaxial pressing direction z ($x = 0.1$ Ru-substituted sample): (a) Intensity change of XRD intensities for a measurement parallel and perpendicular to z. For measurements perpendicular to z the pellet was cut into bars, which were turned by 90° (inset, defined coordinate system valid for the whole Chapter). (b) Alignment of particles perpendicular to the pressing direction z obvious from a comparison of SEM images recorded in perpendicular directions.

Weighing and geometrical measurements indicated similar densities between 3.25 g/cm^3 and 3.45 g/cm^3 for all samples. Using the measured lattice parameters and a substitution dependent unit cell mass, the relative densities (ϱ_{rel}, relative to theoretical densities) are between 69 % and 75 % (Table 5.1).

Ruthenium for cobalt substitution increases the electrical resistivity ρ over the whole temperature range, while the Seebeck coefficient α is increased for $T < 650$ K (Figure 5.3 (a) and (b)). The electrical resistivity ($\rho \propto p^{-1}$) and the Seebeck coefficient $\left(\alpha \propto p^{-2/3}\right)$ depend on the charge carrier density p [35], therefore both of these trends indicate a reduction of

holes for $T < 650$ K. The decrease of the hole carrier density is confirmed by room temperature Hall measurements (cf. inset of Figure 5.3 (b)) and indicates that the valence state of the introduced ruthenium, which can have different states, is greater or equal to 4+. This is the case because only a larger valence than the mixed Co valence state of 3.5+ in the CoO_2 layer or 3.0+ in the rock salt layer [105] can induce this change.

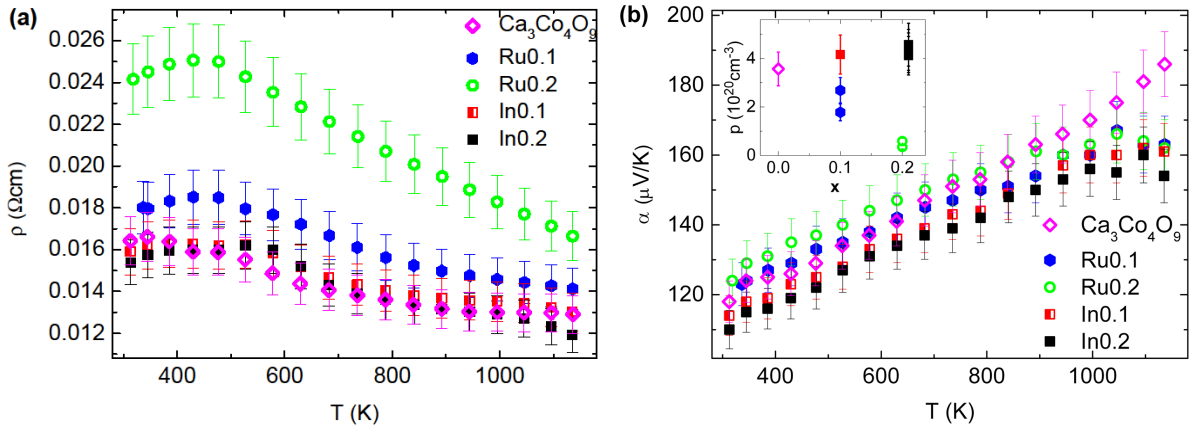

Figure 5.3: (a) Temperature-dependent electrical resistivity ρ, (b) Seebeck coefficient α, and p-type charge carrier density p versus substitution level x (inset).

In contrast, the valence state of indium can only be 3+. Isovalent Co substitution in the rock salt layer should not have any effect. Therefore, the measured increase of the hole carrier density (cf. inset of Figure 5.3 (b)) indicates at least a partly substitution of Co with indium in the CoO_2 layer. The room temperature resistivity and the Seebeck coefficient both decrease with the In substitution level as expected from the increase of the Hall carrier density (Figure 5.3 (a) and (b)). But despite of the increase of the charge carrier density, the substitution of Co with In does not decrease the electrical resistivity over the whole temperature range (Figure 5.3 (a)). The detected Co_3O_4 impurities might be responsible for the non-existent decrease because it has a larger resistivity compared to cobalt oxide (cf. Chapter 7).

The electrical resistivity ρ of all samples changes from metal like behavior $(d\rho/dT > 0)$ at low temperatures to semiconducting behavior $(d\rho/dT < 0)$ at elevated temperatures (Figure 5.3 (a)), which is typical for the misfit-layered cobalt oxides (cf. Section 3.1.5.1). The substitutions shift the transition temperature T_{MS} from $T_{MS}^{0} \approx 344(25)$ K for the pure compound to $T_{MS}^{In0.1} \approx 385(25)$ K and $T_{MS}^{In0.21} \approx 527(25)$ K for $x = 0.1$ and $x = 0.21$ In-substitution and $T_{MS}^{Ru} \approx 430(25)$ K for both Ru substitutions. This means that indium and ruthenium substitution both stabilize the metallic regime. In literature, a destabilization of this regime was found, e.g., for a substitution of Co with Ti^{4+} [132], and of Ca^{2+} with Y^{3+} [175], which both reduce the hole carrier density. While the latter reference assumed that the shift of

the transition temperature T_{MS} to lower values correlates with the decreasing hole carrier density, the opposite trend was observed for Co substitution with Rh^{3+} [111]. The Hall measurements in the present study confirm that an increase of T_{MS} is observed for both decreasing and increasing carrier densities induced by Ru and In substitution, respectively (cf. inset in Figure 5.3 (b)). That is why another effect than the change of the charge carrier density should influence the metal semiconductor transition.

A connection of the metal semiconductor transition (MST) with the known spin state transition can be excluded because the latter happens at lower temperatures [100]. Some authors discuss the transition in the framework of the virial theorem and assume that the transition originates from the localization of the itinerant charge carriers in the narrow e_g' band due to the decreasing overlap of the orbitals induced by the thermal expansion [113, 175]. However, a structural change classified as a first-order transition [113] seem to be responsible for the MST: Muguera and Grebille observed a disorder-order transition in the central Co-O layer of the rock salt block. This rearrangement of the Co-O layer (average structure not affected) can change the modulation and hence partially increase the in-plane atomic distances. This, in turn, decreases the orbital overlap in the CoO_2 layer, which can induce a partial localization of the carriers at the Fermi energy [93]. Additionally, the rearrangement of the atoms in the rock salt layer can influence the electrical conductivity in the CoO_2 layer via electronic and coulomb interactions [115]. These interactions are crucial for the existence of the metallic regime [37] and hence the MST because the pure layered CoO_2 compound without inter-layers is a Mott insulator [114]. In the present study, the increasing substitution levels increases the lattice misfit b_2/b_1 (cf. Table 5.1). The lattice distortion induced by the dissimilar radius of the substitution atom accompanied by a change of the coulomb interactions is likely to influence the temperature of the structural transition and thus the MST.

In the high temperature regime, the transport is often interpreted as small-polaron hopping [116–120] or a mixture of thermally activated behavior and three dimensional variable range hopping [175]. However, the transport behavior above the metal semiconductor transition in the intermediate temperature regime is not fully understood yet and will be discussed in detail in Chapter 6.

In Figure 5.4 (a), the temperature dependence of the specific heat capacity $C_p = c_p/\bar{M}$ is shown, where $\bar{M}$ is the average atomic mass of the compound. Theoretically, the isobaric molar specific heat for solids

$$c_p \approx c_v = \underbrace{\frac{12\,\pi^4 R}{5}\left(\frac{T}{T_D}\right)^3}_{c_{V,ph}} + \underbrace{\frac{\pi^2 R}{2}\frac{T}{T_F}}_{c_{V,el}} + c_{v,an} \tag{32}$$

is approximately equal to the isochoric heat c_V, which is determined by the sum of phononic $c_{V,ph}$, electronic $c_{V,el}$, and anharmonic $c_{V,an}$ contributions. In Equation (34), R is the gas constant of the ideal gas, T_D the Debye temperature, and T_F the Fermi temperature. According to the law of Dulong-Petit, the phononic contribution can be approximated by $c_{V,ph} = 3R$ above the Debye temperature. This contribution to $C_p = c_p/\bar{M}$ is marked as horizontal lines in Figure 5.4 (a). In accordance with the Debye theory, the heat capacity C_p increases with T and reaches or exceeds the Dulong-Petit limit around 600-700 K for all samples, which is in good agreement with an observed Debye temperature of $T_D = 660$ K found for $Ca_3Co_4O_9$ [123]. At higher temperature, a further increase of C_p is observed. This could be explained by electronic or anharmonic contributions, but more likely it result from the onset of a phase transition: The stability range of the $Ca_3Co_4O_9$ phase decreases above 1196K (cf. Figure 3.2 or [84–86]) so that minor amounts of the cobalt rich $Co_{1-x}Ca_xO$ phase are formed for compositions close to the upper phase boundary. Additionally, the $Ca_3Co_4O_9$ phase decomposes above 1222 K. Hence, the measured high temperature heat capacity is probably larger than the actual one. Due to this difference, the thermal conductivity is overestimated while the actual ZT should be even larger than the values presented in this work. A comparison of the different degrees of substitution reveals that the substitution does not have a significant influence on C_p for In and $x = 0.1$ Ru substitution. However, for the sample with $x = 0.2$ Ru substitution the increase of C_p at high temperatures seems to be less pronounced which might be connected to a shift of the phase transition toward higher temperatures.

The thermal diffusivity $\lambda = \frac{1}{3} v_g^2\, \tau$, which depends on the phonon group velocity v_g and the relaxation time τ, decreases with increasing temperature for all samples (Figure 5.4 (b)). This general temperature trend is in agreement with Umklapp-phonon scattering for which the relaxation time

$$\tau_U(\omega) \propto \frac{\bar{M} v_g \ v_p^2}{\gamma^2 T} \tag{33}$$

is determined by the phase velocity v_p of the phonons, the Grüneisen parameter γ and the average atomic mass $\bar{M}$ of the compound and decreases with T [36]. Compared to the unsubstituted $Ca_3Co_4O_9$, the diffusivity is reduced by 5-17 % and 18-27 % for the In and the Ru substituted samples, respectively (see Figure 5.4 (b)). This decrease is partly connected to point defect scattering, for which the relaxation time τ_{PD} depends on the mass difference between a point defect and the average mass $\bar{M}$ of the structure

$$\tau_{PD}^{-1} = \frac{1}{x_{Ca}}\left(\frac{M_{Ca}-\bar{M}}{\bar{M}}\right)^2 + \frac{1}{x_{Co}}\left(\frac{M_{Co}-\bar{M}}{\bar{M}}\right)^2 + \frac{1}{x_O}\left(\frac{M_O-\bar{M}}{\bar{M}}\right)^2 + \frac{1}{x_{subst}}\left(\frac{M_{subst}-\bar{M}}{\bar{M}}\right)^2, \tag{34}$$

where x_{Ca}, x_{Co}, x_O, and x_{subst} describe the concentration of the Ca, Co, Oxygen, and substitution atoms, and M_{Ca}, M_{Co}, M_O, and M_{Subst} their masses [34, 176]. The atomic masses of the substitution atoms $M_{\mathrm{In}} = 114.8$ and $M_{\mathrm{Ru}} = 101.1$ are much heavier than the masses of the substituted lattice atoms of $M_{\mathrm{Ca}} = 40.1$ and $M_{\mathrm{Co}} = 58.9$. Using these parameters in Equation (36) predicts a decrease of the diffusivity ($\tau \propto \lambda$) of 8 % for $x = 0.1$ In, 15 % for $x = 0.2$ In, 6 % for $x = 0.1$ Ru, and 10 % for $x = 0.1$ Ru substitution, respectively, compared to non-substituted samples. In contrast, experiments show a slight increase with increasing Ru or In substitution level over an extended part of the measured temperature range (Figure 5.4 (b)). This trend can be explained by Umklapp-scattering according to Equation (33) if we take into account a higher value of $\bar{M}$. However, $\bar{M}$ is very similar when comparing Ru and In substituted samples and hence the large difference of the diffusivity between Ru and In substitution cannot be explained by a simple change in the average mass. Opposite to the prediction of the point defect scattering model, Ru substitution decreases the diffusivity much more than indium substitution (Figure 5.4 (b)) and the decrease due to ruthenium substitution is much larger than expected. This large decrease might be partly induced by resonance scattering [37], which means that phonons are absorbed if they tune into resonance with the locale resonance vibrations of the substituted Ru atoms.

Finally, in Figure 5.4 (c) the resulting thermal conductivity $\kappa = \varrho C_p \lambda$ along the pressing direction z is presented. For the unsubstituted sample the peaks in the heat capacity curve were excluded using a linear baseline. The diffusivity mainly determines the magnitude of the thermal conductivity, but for $x = 0.2$ Ru substitution a slightly smaller density and the

deviation in the heat capacity C_p have to be considered. The thermal conductivity is mainly determined by the lattice contribution because the electronic contribution, which can be estimated from the Wiedemann-Franz law, is below 0.22 W/Km for all samples in the whole temperature range.

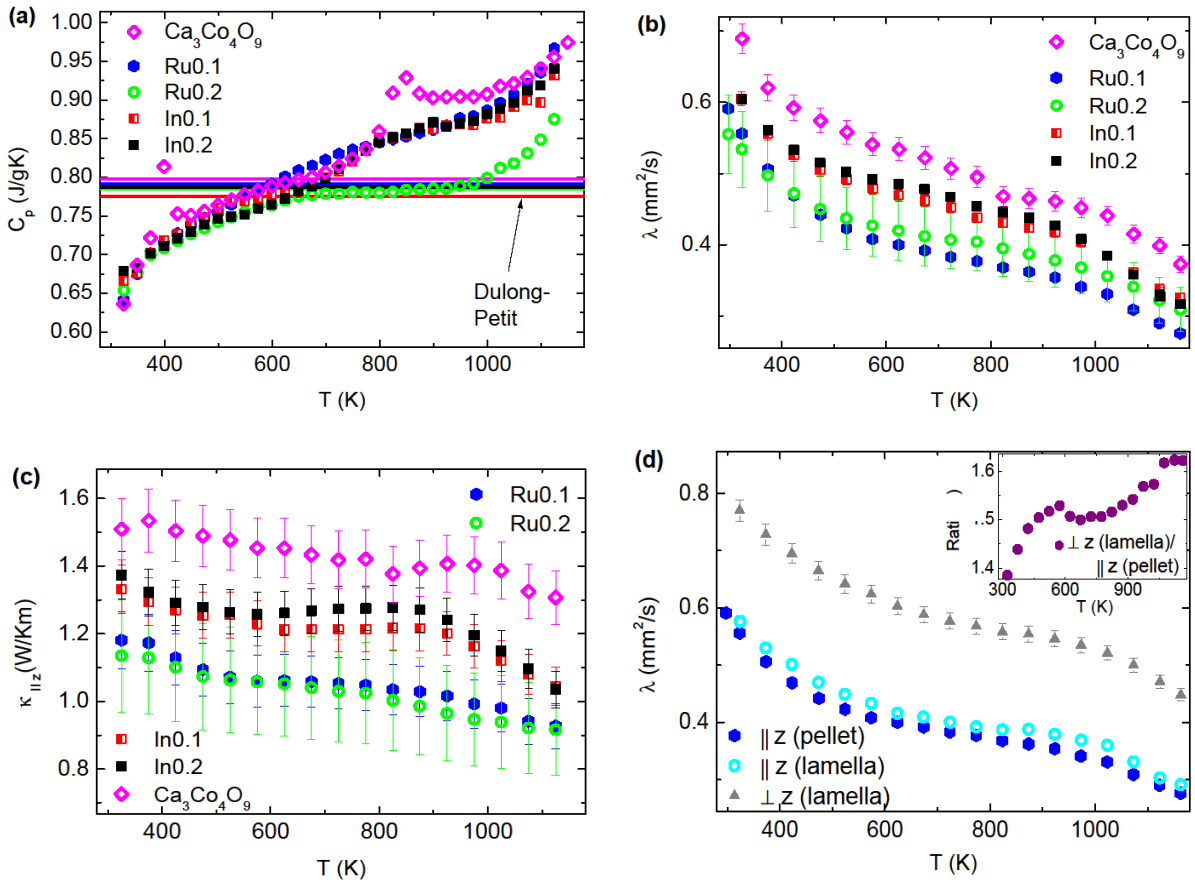

Figure 5.4: (a) Temperature-dependent specific heat capacity C_p measured with DSC (symbols) and high temperature limit calculated by Dulong-Petit (lines). (b) Thermal diffusivities λ, and (c) thermal conductivities parallel to z $\kappa_{||z}$ as a function of temperature. (d) Thermal diffusivity of the $x = 0.1$ Ru substituted sample parallel and perpendicular to the pressing direction z. The inset shows the ratio $\lambda_{||z}/\lambda_{\perp z}$ of the perpendicular diffusivities.

The preferred orientation of the crystallites reflects in anisotropic thermoelectric properties, and hence the thermal diffusivity needs to be determined in the x-y-plane similar to the electrical conductivity. Figure 5.4 (d) shows the thermal diffusivities $\lambda_{||z}$ and $\lambda_{\perp z}$ measured for the whole pellet parallel to the pressing direction z and perpendicular to it, revealing a higher diffusivity in the perpendicular direction. This observation is in agreement with the alignment of the plate-like crystallites because the relaxation time increases (i) due to less grain-boundary scattering of the phonons in the x-y plane compared to z, and (ii) a better thermal conductivity along the a- and b-axis of the cobalt oxide than along the c-axis (perpendicular to layers) [122]. A similar behavior was found in Ref. [177]. The temperature dependent ratio

$(\lambda_{||z})/(\lambda_{\perp z})$ (inset of Figure 5.4 (d),) was used to calculate κ along the x-y direction for all samples.

The figure of merit ZT was calculated from measurement data parallel to the x-y direction for the different substitutions (Figure 5.5). No enhancement of ZT was observed for In substitution, while $x = 0.1$ Ru substitution leads to an increase of ZT of up to 25 %, due to the strong reduction of the thermal diffusivity. At 1125 K a maximum $ZT = 0.14$ was reached for the $x = 0.1$ Ru substituted sample. Consequently, testing lower Ru substitution levels seem to be a promising strategy for a further improvement of ZT.

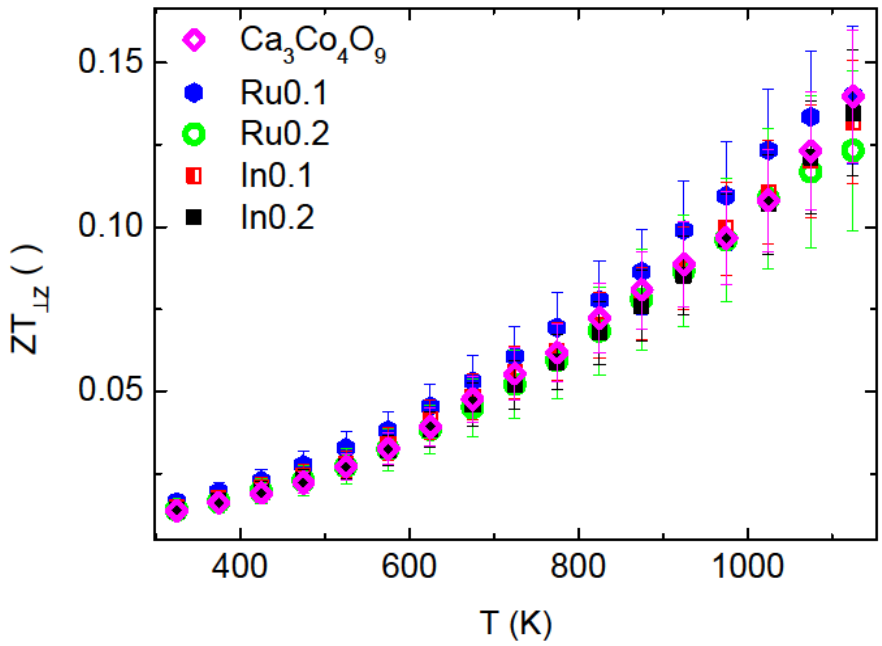

Figure 5.5: Figure of merit ZT perpendicular to the pressing direction. The thermal diffusivity λ was measured perpendicular to the pressing direction for the $x = 0.1$ Ru substituted sample and calculated for the other samples based on the $(\lambda_{||z})/(\lambda_{\perp z})$ factor determined in Figure 5.4 (b).

5.4 Conclusions

Ruthenium for cobalt substitution leads to an enhancement of the thermoelectric figure of merit of up to 25 % over a wide temperature range, while indium substitution has a negligible effect. An increasing Ru^{4+} level decreases the charge carrier density and increases the resistivity and the Seebeck coefficient below 650 K. However, the increase of the figure of merit mainly originates from the significant decrease of the thermal conductivity. The huge decrease of the thermal conductivity induced by Ru substitution cannot be explained by point defect scattering, and therefore phonons are assumed to be scattered by local resonance

vibrations of the Ru atoms. Indium and ruthenium substitution shift the metal-semiconductor transition toward larger temperatures, which might be connected to the disorder introduced into the lattice. A detailed discussion about the transport data above 400 K and the influence of Ru on the transport behavior is given in the following chapter. The increase in the figure of merit indicates that Ru substitution is a promising strategy for a further ZT improvement. Moreover, the large reduction of the thermal conductivity makes Ru substitution a promising candidate for co-substitution with a second substitution atom that mainly increases the power factor.

6 High temperature transport properties of $[Ca_2CoO_{3-\delta}][CoO_2]_{1.62}$ and the effect of Ru substitution[g]

The misfit-layered $[Ca_2CoO_{3-\delta}][CoO_2]_{1.62}$ shows promising thermoelectric properties, which can be further improved by Ru substitution, as shown in the previous chapter. The high temperature transport is usually interpreted as small-polaron hopping, but the temperature dependence of the resistivity and the Seebeck coefficient between 600 K and 900 K is not completely understood yet. Surprisingly, the Anderson localization model is found to describe the data in this temperature range successfully. This model is usually used to describe the transport in the impurity band of a semiconductor, where localization originates from a random potential induced by charged impurity centers. For $[Ca_2CoO_{3-\delta}][CoO_2]_{1.62}$, the good agreement of the model with the experimental data indicates a localization of the charge carriers on the Co-sites in the CoO_2 layer. Here, the random potential is suspected to originate from Coulomb interactions with the incommensurate rock salt layer and its randomly distributed oxygen vacancies. The ionized Ru substitution atoms further increase the disorder and thus the localization, which is reflected in a change of the temperature dependence (activation energy) of the transport behavior. The intelligence that disorder and interactions between the layers play a major role in the transport might help to improve theoretical models used to predict the thermoelectric properties of substituted $[Ca_2CoO_{3-\delta}][CoO_2]_{1.62}$ compounds.

6.1 Introduction

The misfit-layered $[Ca_2CoO_{3-\delta}][CoO_2]_q$ consists of incommensurate CoO_2 and triple rock salt-type Ca_2CoO_3 layers, where $q \approx 1.62$ is the misfit parameter between the two layers. For the thermoelectric performance, the interactions between the two layers are of major importance: The lattice misfit induces static displacements in the Ca_2CoO_3 layer, which reduce the thermal conductivity due to displacement scattering [37]. The interactions also influence the electric transport behavior, which is determined by the electronic states of the

[g] Partly adapted and partly vertatim from: Saucke, G., Populoh, S., Vogel-Schäuble, N., Sagarna, L., Mogare, K., Karvonen, L., Weidenkaff, A.: Thermoelectric properties of Ru and In substituted misfit-layered $Ca_3Co_4O_9$. MRS Proceedings. 1543, 83–92 (2013).

CoO_2 layer [88, 89]: DFT+U calculations indicate that pure CoO_2 is a Mott insulator [37], while metallic behavior is predicted for $[Ca_2CoO_{3-\delta}][CoO_2]_{1.62}$ and confirmed experimentally between 63 K and 510 K [100]. For larger temperatures, $[Ca_2CoO_{3-\delta}][CoO_2]_{1.62}$ shows activated transport behavior, which is interpreted as small-polaron hopping by several authors [116–120]. However, Schrade *et al.* excluded small-polaron transport in favor of an itinerant transport model above 400 K because (ii) a mobility of 0.145 cm^2/Vs is rather high for small-polaron hopping and (ii) the Heikes formula could not describe the change of the Seebeck coefficient with the charge carrier concentration [107]. They concluded that the activated behavior of $\sigma(T)$ results from a combination of the temperature dependent mobility and the thermal excitation of charge carriers due to the reduction of Co^{3+} ions to Co^{2+} in the rock salt layer.

In contrast to this itinerant picture, X-ray Photoemission Spectroscopy (XPS) studies between 300 K and 450 K show that the Co 3d t_{2g} electrons at the upper valence band are mainly localized [178]. As a reason for the localization, the authors discuss the structural modulation of the Co-O bond length induced by the misfit structure [179]. Accordingly, the Co states in the CoO_2 layer are not equal anymore. The Coulomb potential experienced by a charge carrier depends on the surrounding atoms, which leads to a spread of the energy levels.

Inspired by this idea, the present work interprets the electrical transport properties of $[Ca_2CoO_{3-\delta}][CoO_2]_{1.62}$ in the framework of Anderson localization, which is usually used to describe impurity band conduction in semiconductors [49]. The model assumes that charge carriers are localized due to the presence of a random potential created by Coulomb interactions with the ionized impurity atoms [50]. To gain deeper insight, the electrical transport data of different $[Ca_2CoO_{3-\delta}][CoO_2]_{1.62}$ samples which differ in the synthesis route and by different amounts of Ru for Co substitution are analyzed using the Anderson and the small-polaron model. The fits of the electrical conductivity data and the Seebeck coefficient show that the Anderson model can describe the experimental results between 630 K and 890 K. At higher temperatures, small-polaron hopping dominates the temperature dependence of the resistivity.

6.2 Theoretical models

According to Anderson, a lattice with random potential can induce a localization of charge carriers within an electronic band or at the band edges [49, 50]. Within such a potential, charge carriers hop between adjacent localized energy states with different energies. The electrical conductivity in this model is given by

$$\sigma = \frac{e^2 L^2}{\tau_0} N(E_F) \exp\left(-\frac{W(E_F)}{k_B T}\right), \tag{35}$$

where $N(E_F)$ is the density of states (DOS) at the Fermi level, L^2 is the mean-squared distance between states with the same energy, and $\tau^{-1} = \frac{1}{\tau_0}\tau_0^{-1} \exp(-W(E_F)/k_B T)$ the mean frequency of hopping with phonon frequency τ_0^{-1} [50]. The hopping frequency is determined by the overlap integral and the energy levels of the participating energy states. More precisely, the activation energy $W(E)$ correlates with the highest intermittent energy level a charge carrier has to pass between two states with the same energy E. Introducing Cutler's conductivity (Equation (15)) into the Mott formula for states distributed over an energy range leads to a Seebeck coefficient of

$$\alpha = -\frac{\pi^2 k_B^2 T}{3e}\left(\frac{\partial \ln(\sigma)}{\partial E}\right)_{E=E_F} = -\frac{\pi^2 k_B}{3e}\left(k_B T \frac{\partial \ln(\mu_0 N)}{\partial E} - \frac{\partial \mathrm{W}}{\partial E}\right)_{E=E_F}, \tag{36}$$

where $\mu_0 = \frac{eL^2}{\tau_0 k_B T}$ [50]. The Seebeck coefficient is dominated by a linear temperature dependence and the values $\frac{\partial \ln(\mu_0 N)}{\partial E}$ and $\frac{\partial \mathrm{W}}{\partial E}$ can be extracted from the slope and the y-intercept.

The adiabatic small-polaron hopping model is often used to explain the activated high temperature transport [116–120]. In this model, the temperature dependence of the electrical conductivity

$$\sigma = \frac{enA}{T} \exp\left(-\frac{E_A^\sigma}{k_B T}\right), \tag{37}$$

is determined by the activated mobility, where E_A^σ is the activation energy, n the charge carrier density and A a constant [180]. The model can be falsified by a plot of $\ln(\sigma T)$ vs. T^{-1},

which should reveal a linear correlation. The Seebeck coefficient determined by polaron hopping can be described in the narrow band limit of a p-type semiconductor

$$\alpha = \frac{k_B}{e}\left(\frac{E_A^\alpha}{k_B T} + A'\right). \tag{38}$$

Here, $E_A^\alpha = E_F - E_B$ is the activation energy of the Seebeck coefficient determined by the distance between energy level of the p-type polaron band and the Fermi level E_F, and A' is a constant [47, 48, 181]. Both, σ and α show characteristic features that can be used to determine which of the two introduced models best describe the given material system as will be shown subsequently.

6.3 Results and discussion

The electrical conductivity and the Seebeck coefficient of polycrystalline $Ca_3Co_4O_{9+\delta}$, $Ca_3Co_{3.9}Ru_{0.1}O_{9+\delta}$ and $Ca_3Co_{3.9}Ru_{0.2}O_{9+\delta}$ are presented in Figure 6.1 (a) and (b). As in the previous Chapter, the samples are abbreviated according to their elemental formulas. All samples show a similar temperature dependence of the electrical conductivity (Figure 6.1 (a)), which is typical for cobalt oxides [100]: above 380 K - 420 K, the temperature dependence of the conductivity changes from metallic ($d\sigma/dT < 0$) to thermal activated behavior ($d\sigma/dT > 0$). Below the transition temperature, the metallic temperature dependence of the resistivity and the increasing Seebeck coefficient of the layered cobalt oxides can be described by Boltzmann equations within a quasi-particle model [91, 94]. In contrast, close to the transition temperature, the quasi particle picture breaks down and a bad metal behavior is found.

In order to analyze the activated high temperature electrical conductivity, $\ln(\sigma T)$ and $\ln(\sigma)$ are plotted against T^{-1} (Figure 6.1 (c) and (d)). In agreement with the small-polaron hopping model (Equation (37)), the plot of $\ln(\sigma T)$ reveals a linear dependence at high temperatures: For pure $Ca_3Co_4O_{9+\delta}$ a linear behavior is observable above 780 K, while a significant upwards curvature is visible at lower temperatures. For $Ca_3Co_{3.9}Ru_{0.1}O_{9+\delta}$ and $Ca_3Co_{3.8}Ru_{0.2}O_{9+\delta}$, the Ru substitution shifts the small-polaron hopping regime toward higher temperatures, so that a linear dependence is only observable above 890K and 940K, respectively (cf. solid lines in Figure 6.1 (c)).

The activation energies for polaron hopping E_A^{σ} increases with the Ru substitution level from 92(2) meV for the pure sample to 103(2) meV and 143(4) meV (Table 6.1). This increase of activation energy might result from the decreasing carrier density induced by Ru substitution (cf. inset of Figure 5.3 or [151]). This trend is in line with literature results, which found the same trend for a decrease of the charge carrier density induced by a Gd-for-Ca substitution [117], Nd-for-Ca substitution [119], or a reduction of the oxygen content [116]. The authors claim that the increase of the activation energy results from the larger intersite hopping distance a. However, the transport in the cobalt oxide is determined by the conductive CoO_2 layer, while the substitution of Ca and the change of the oxygen content happen in the rock salt layer and leave the CoO_2 layer unaffected [109]. This means that the distances between the Co atoms in the conducting CoO_2 layer and thus the intersite hopping distance should not be effected and not be responsible for the change of the activation energy.

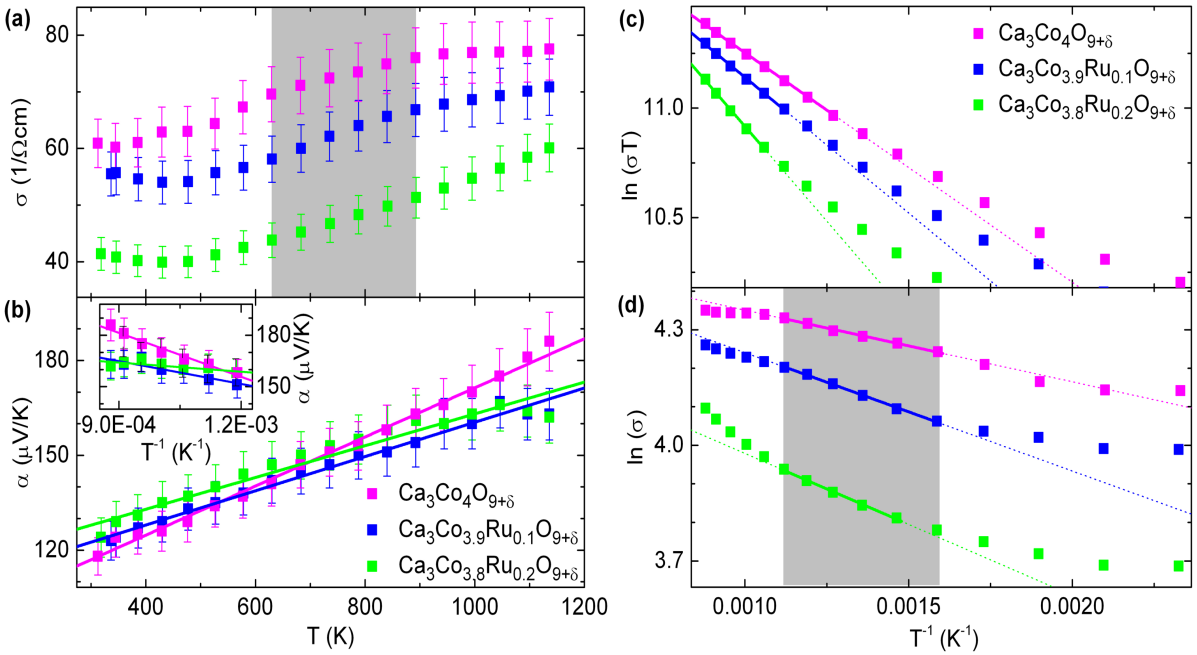

Figure 6.1: Temperature dependence of the electrical conductivity (a), and the Seebeck coefficient with linear fits (b) for pure $Ca_3Co_4O_{9+\delta}$, $Ca_3Co_{3.9}Ru_{0.1}O_{9+\delta}$ and $Ca_3Co_{3.8}Ru_{0.2}O_{9+\delta}$. The inset shows the high temperature behavior $\alpha \propto T^{-1}$ typical for polarons. (c) Fits of the electrical conductivity in the small-polaron model at high temperatures and (d) the Anderson model between 630 K and 890 K (range marked in grey). Solid lines mark the fitting range.

A different way to interpret the change of the activation energy can be deduced from the findings of Yao *et al.* [120]: In line with prior findings, the authors report that Ni, Mn, and Fe for Co substitutions decrease the carrier density and thus increase the activation energy. But surprisingly, Co substitution with Cu does not have an effect on the activation energy, even though the relative change of the resistivity and the Seebeck coefficient indicate an increase

of the carrier concentration for increasing Cu content. Yao *et al.* concluded that the increase of the activation energy results from scattering on the impurity atoms substituted into the conductive CoO_2 layer, while a constant activation energy is signature for substitution in the $CaCo_2O_3$ layer.

A closer look at the adiabatic small-polaron model reveals that a change of the intersite distance or the scattering mechanism should rather affect the intercept than the activation energy (c.f. Equation (37)). In contrast to the questionable former interpretations, we assume that a spread of the energy levels participating in the transport alter the activation energy. This interpretation is based on the findings of Austin and Mott who state that the total activation energy $W_{tot} = W_H + W_D/2$ is given by the sum of the hopping energy W_H resulting from the self localization of the polaronic charge carrier and the static disorder term $W_D/2$ which is connected to the energy spread of the hopping sites [180]. For $Ca_3Co_4O_{9+\delta}$, we assume that the misfit structure induces an energy spread of the Co 3d states in the CoO_2 layers. This is because the interactions with the incommensurate Ca_2CoO_3 layer can create a different atomic surrounding and Coulomb potential at each Co site. In addition to this intrinsic disorder, ionized Ru atoms further increase the disorder which leads to the observed increase of the activation energy. This interpretation is in line with literature trends, which usually show an increase of activation energy with the amount of the substituent. For similar substitution level, the activation energy depends on the type of substitution atom, which suggest that the properties of the substitution atom and its interaction with the charge carries in the CoO_2 layer determine the energy spread.

	$Ca_3Co_4O_{9+\delta}$ (ss)	$Ca_3Co_{3.9}Ru_{0.1}O_{9+\delta}$	$Ca_3Co_{3.8}Ru_{0.2}O_{9+\delta}$	$Ca_3Co_4O_{9+\delta}$ (sc)
E_A^{σ} (meV)	92(2)	103(2)	143(4)	111(2)
E_A^{α} (meV)	85(7)	44(1)	18(7)	59(11)
W_D^A (meV)	16(1)	26(1)	32(1)	37(1)
$\partial \ln(\mu_0 N)/\partial E$ ($(eV)^{-1}$)	-3.2(1)	-2.2(1)	-2.1(1)	-2.4(1)

Table 6.1: Activation energies E_A^{σ} and E_A^{α} of the electrical transport and the Seebeck coefficient in the small-polaron regime. For the fit with the Anderson model, the activation energy W_D^A and the slope of the Seebeck coefficient $\partial \ln(\mu_0 N)/\partial E$ are presented.

Deviations from the polaron model at lower temperatures (Figure 6.1 (c)) suggest the presence of a different transport mechanism in the intermediate temperature range. In agreement with Anderson localization (Equation (15)), a plot of $ln(\sigma)$ vs. T^{-1} yields a

straight line between 630 K and 890 K, whereas the corresponding temperature range becomes smaller upon $Ru_{0.02}$ substitution (Figure 6.1 (d)). The activation energies extracted via Equation (15) increase with the substitution level from $W_D^A = 16(1)$ meV for $Ca_3Co_4O_{9+\delta}$ to 26(1) meV and 32(1) meV for the $Ca_3Co_{3.9}Ru_{0.1}O_{9+\delta}$ and the $Ca_3Co_{3.8}Ru_{0.2}O_{9+\delta}$ samples. In the Anderson picture, the increase of the activation energy with the substitution level means an increasing energy spread so that charge carriers moving between two energy levels with the same energy (separated by spatially intermittent states with random energy) have to pass higher energy level on their way in average.

At higher temperatures, the experimental conductivities are lower than the extrapolated values of the Anderson model fitted in the linear range marked in grey (Figure 6.1(d)). This flattening of the slope corresponds to a decrease of the activation energy at higher temperatures and can partly result from the formation of oxygen vacancies [107, 182, 183] as indicated by the results of Liu *et al.,* who stated activation energies of 100 meV in oxygen atmosphere and 104 meV in air (more vacancies) [116]. The effect of the vacancies on the activation energy can result from (i) a decrease of the hole carrier concentration and (ii) an increase of the disorder in the rock salt layer which increases the energy spread in the CoO_2 layer. However, the deviation should mainly originate from a change of the transport mechanism to small-polaron hopping.

Both, the activation energy of the polaron transport model E_A^σ and that of the Anderson model W_D^A confirm the increase of disorder and hence an increasing energy spread with the amount of substitution atoms. Although it is not clear whether Ru for Co substitution takes place in the rock salt or in the CoO_2 layer [151], a substitution in either layer can alter the energy spread due to the differing coulomb potentials of the Ru and the Co ions combined with strain and a variation in the misfit due to different ion radii. Compared to the observed small-polaron hopping activation energies, which consists of a hopping term induced by the electron-phonon interaction and a disorder term, the activation energies of the Anderson model are smaller because they are only determined by the disorder (Table 6.1). This is in line with the smaller thermal energies available at lower temperatures.

The electrical transport properties depend on the synthesis routes (Figure 6.2 (a)-(b)). Similar to the Ru substituted samples, the $Ca_3Co_4O_{9+\delta}$ (ss) sample was prepared via solid state reaction followed by cold pressing and conventional sintering and post annealing in oxygen atmosphere [151]. In comparison, the $Ca_3Co_4O_{9+\delta}$ (sc) sample was prepared by citric

complexation method followed by SPS sintering and post annealing in air (cf. [183] or Chapter 7 for details). The analysis of the electrical transport data (Figure 6.2 (c)-(d)) reveals that the activation energy of the Anderson model increases from $W_D^A = 16(1)$ meV for the cold pressed $Ca_3Co_4O_{9+\delta}$ (sc) sample to $W_D^A = 37(1)$ meV for $Ca_3Co_4O_{9+\delta}$ (sc). Similarly, the polaron hopping energy increases from $E_A^\sigma = 92(2)$ meV for $Ca_3Co_4O_{9+\delta}$ (ss) to 111(2) meV for $Ca_3Co_4O_{9+\delta}$ (sc). Accordingly, both models indicate a larger disorder in the $Ca_3Co_4O_{9+\delta}$ (sc) samples. The disorder might result from a larger amount of oxygen vacancies in the air annealed $Ca_3Co_4O_{9+\delta}$ (sc) sample, a larger density which might induce stress and hence increases the disorder, or a difference in the Co/Ca ratio of the samples fabricated from independent batches. A change of the carrier density might also contribute.

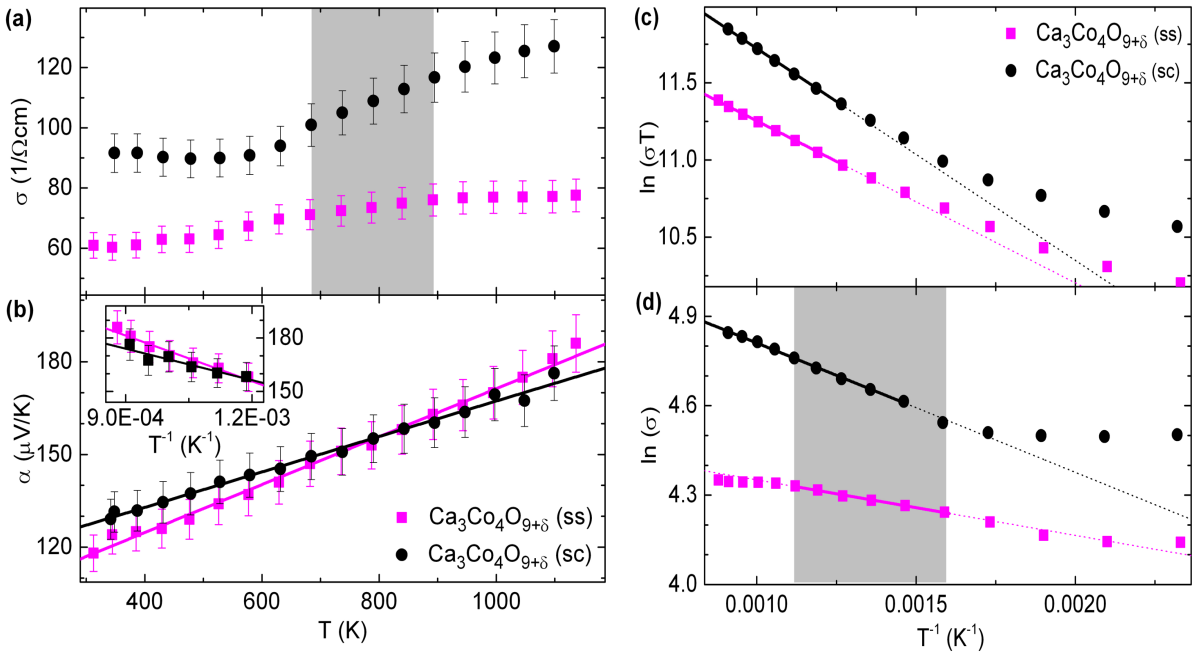

Figure 6.2: Temperature dependence of the electrical conductivity (a) and Seebeck coefficient with linear fit (b) for $Ca_3Co_4O_{9+\delta}$ (ss) and $Ca_3Co_4O_{9+\delta}$ (sc) which differ in the synthesis route. The inset shows the high temperature behavior $\alpha \propto T^{-1}$ typical for polarons. (c) Fits of the electrical conductivity in the small-polaron model at high temperatures and (b) the Anderson model between 630 K and 890 K (temperature range marked in grey). Solid lines mark the fitting range.

For all samples, the Seebeck coefficient increases linearly with temperature (Figure 6.1 (b) and Figure 6.2 (b)). In the Anderson picture (Equation (16)), the increase of the Seebeck coefficient with temperature is determined by the term $\frac{\partial \ln(\mu_0 N)}{\partial E}$. The negative value of the term is in line with the decreasing DOS at the upper edge of a valance band. For increasing Ru substitution, the absolute value $\left|\frac{\partial \ln(\mu_0 N)}{\partial E}\right|$ decreases from about 3.2(1)/eV to 2.4(1)/eV and 2.2(1)/eV, respectively. This decrease probably results from the increase of disorder with Ru substitution because the disorder increases the energy spread by smearing out the density of

states N, which also influences its energy dependence. Additionally, the larger spread can also influence the mean-squared distance L^2 between states with the same energy and its energy dependence, which effects the slope of Equation (16) via μ_0.

The temperature dependence of the Seebeck coefficient is determined by $\alpha \propto T^{-1}$ (inset of Figure 6.1 (b) and Figure 6.2 (b)), which is typical for small-polaron hoping (Equation (38)). The increasing Ru substitution decreases the activation energy of the Seebeck coefficient from $E_A^\alpha = 85(7)$ meV to 44(1) meV and 18(7) meV. For all samples, the activation energies of the Seebeck coefficient are smaller than those of the electrical transport. This is an indicator for small-polaron conduction [47]. The activation energies differ by the activation energy of the semi-classical mobility of the polaron $E_A^\mu := E_A^\sigma - E_A^\alpha$ [47]. Hence, the increase of E_A^μ with increasing Ru level means that a lower charge carrier densities has a positive effect on the polaron mobility. For the two pure samples, the activation energy $E_A^\alpha = 85(7)$ meV of $Ca_3Co_4O_{9+\delta}$ (ss) is larger than the one of the $Ca_3Co_4O_{9+\delta}$ (sc) with $E_A^\alpha = 59(11)$ meV. The differences in E_A^α might result from a shift of the Fermi level due to a variation in the charge carrier density induced by stoichiometric differences.

Based on our analysis a full picture of the high temperature transport properties can be drawn: The transport properties are strongly determined by the electron phonon interaction and the energy spread of the Co energy states in the CoO_2 layer. Between 630 K and 890 K, the small-polaron states form a Bloch-like polaron band in which the polarons can move without thermal activation due to their zero point energy [184]. However, Anderson localization disturbs the free movement and leads to an activated electrical conductivity. The activation energies are between 16(1) and 34(1) meV and describe the energy spread due to the random potential. The Seebeck coefficient is characterized by a linear temperature dependence. With increasing temperature the polaron band width decreases continuously until the states get localized and the charge carriers move by small-polaron hopping [184]. The localization induced by the electron-phonon interaction is stronger than the Anderson localization and leads to larger activation energies. The transition to polaron hopping typically occurs above half of the Debye temperature [184], which is on the order of $\frac{\theta_D}{2} \approx 330K$ for $Ca_3Co_4O_9$ compounds [123]. The high temperature conductivity is clearly determined by small-polaron hopping with activation energies between 92(1) meV and 143(4) meV. Here, the total activation energy is determined by the activation energy for hopping in addition to a term connected to the disorder. The Seebeck coefficient increases proportional to T^{-1}.

6.4 Conclusion

A full picture of the high temperature transport properties of $Ca_3Co_4O_{9+\delta}$ was developed: Between 630 K and 890 K the transport behavior of $Ca_3Co_4O_{9+\delta}$ can be understood within the frame of Anderson localization while small-polaron hopping is observable at higher temperatures. Anderson localization is assumed to result from the random Coulomb potential a charge carrier experiences due to the variable atomic surrounding created by the misfit structure. Ionized substitution atoms can additionally increase the disorder, which results in elevated activation energies for larger substitution levels in both transport regimes. This advanced understanding might help to improve the prediction power of theoretical models that predict the thermoelectric properties of substituted compounds.

7 Thermoelectric properties of $[Ca_2CoO_{3-\delta}][CoO_2]_{1,62}$ as a function of Co/Ca defects and Co_3O_4 inclusions [h]

The misfit-layered cobalt oxide $[Ca_{2-w}CoO_{3-\delta}][CoO_2]_{1.62}$ has been fabricated and characterized by many different authors. Here we show that discrepancies in the numerously reported thermoelectric performances can result from Co_3O_4 impurities or a change of the defects, i.e. the relative Co content in the $[Ca_{2-w}CoO_{3-\delta}][CoO_2]_{1.62}$ phase. We observe that increasing the relative Co content in the $[Ca_{2-w}CoO_{3-\delta}][CoO_2]_{1.62}$ phase leads to a larger figure of merit ZT. We attribute this increase of ZT to additional p-type charge carriers introduced by Ca vacancies and the resulting reduction of the electrical resistivity. For Co/Ca ratios above the miscibility limit, the increase in thermal conductivity due to the formation of Co_3O_4 impurities leads to a reduction of ZT when the volume fraction of the Co_3O_4 phase is increased from 1% to 3%. Hence, the best figure of merit is expected close to the upper phase boundary of the $[Ca_{2-w}CoO_{3-\delta}][CoO_2]_{1.62}$ phase.

7.1 Introduction

Among the oxides, $[Ca_{2-w}CoO_{3-\delta}][CoO_2]_q$ stands out due to its exceptional thermoelectric properties [25, 28]. The layered structure with misfit parameter $q \approx 1.62$ is characterized by a flexible Co/Ca ratio [85] and a flexible oxygen content [107] denoted by the parameters w and δ in the formula $[Ca_{2-w}CoO_{3-\delta}][CoO_2]_{1.62}$. The cobalt oxide phase is stable within a limited compositional range $w \in [-0.7, 0.06]$ or $y \in [3.8, 4.05]$ considering the elemental composition $Ca_3Co_yO_{9+\delta}$, [84, 85, 182]. Beyond the miscibility limits of the $[Ca_{2-w}CoO_{3-\delta}][CoO_2]_{1.62}$ phase, $Ca_3Co_2O_6$ and Co_3O_4 secondary phases coexist with the misfit-layered phase in the Co deficient and the Co rich area, respectively [84–86] (cf. phase diagram in Chapter 3.1.2).

In the last 15 years, the thermoelectric properties of the misfit-layered oxide have been intensively studied but the reported thermoelectric figures of merit *ZT* differ significantly [25]. The reason for the large differences in the performance of $[Ca_{2-w}CoO_{3-\delta}][CoO_2]_{1.62}$ might result from (i) the different oxygen content [90, 107], (ii) variations in density and

[h] Largely vertatim from: Büttner, G., Populoh, S., Xie, W., Trottmann, M., Hertrampf, J., Döbeli, M., Karvonen, L., Songhak, Y., Thiel, P., Niewa, R., Weidenkaff, A.: Thermoelectric properties of $[Ca_2CoO_{3-\delta}][CoO_2]_{1.62}$ as a function of Co/Ca defects and Co_3O_4 inclusions. Journal of Applied Physics. 121, 215101 (2017)

microstructure resulting from the sample preparation process [134, 135, 144, 185], (iii) the influence of impurity phases, or (iv) variations of the Co content. While the first two aspects were investigated in detail, only large amounts of the Co_3O_4 phase with unknown grain size were explored in the past [182, 186] and the observed changes of the thermoelectric properties were not understood in detail. How the figure of merit depends on the Co content is even less clear. Accordingly, the question to what extent the cationic Co/Ca stoichiometry influences the thermoelectric properties and if it could be adjusted to improve the figure of merit has yet to be answered. Both of these open issues, (iii) and (iv), are addressed in the present study, where we investigate the influence of Co_3O_4 impurities and the influence of the flexible Ca/Co ratio in the $[Ca_{2-w}CoO_{3-\delta}][CoO_2]_{1.62}$ phase. This Chapter summarizes the properties of the composite samples, explores the origin of the stoichiometric flexibility, and clarifies the influence of the impurities and the flexible cation stoichiometry on the thermoelectric properties.

7.2 Calculations

The thermoelectric properties of a composite material can be predicted from the known phase fractions of the individual components according to the effective medium approach [187, 188]. Here, we briefly review how this model has so far been applied to our Co_3O_4 impurities in a $[Ca_{2-w}CoO_{3-\delta}][CoO_2]_{1.62}$ matrix. First note that our Co_3O_4 impurities are of limited extension and randomly distributed. As such, they are best described as an assemblage of coated spheres, also known as a Hashin–Shtrikman microstructure [187]. The effective medium model for this structure predicts the resistivity ρ_E, the Seebeck coefficient α_E, and the thermal conductivity κ_E of the composite to be:

$$\sigma_E = \sigma_m + \frac{V_i}{D}\left(\frac{\delta_\sigma}{d_{im}} + \frac{1-V_i}{3}\frac{\sigma_m}{d_m}\right), \tag{39}$$

$$\kappa_E = \kappa_m + \frac{V_i}{D}\left(\frac{\delta_\kappa}{d_{im}} + \frac{1-V_i}{3}\frac{\kappa_m}{d_m}\right), \tag{40}$$

$$\alpha_E = \left[\alpha_m\sigma_m + \frac{V_i}{D}\left(\frac{\delta_{\alpha\sigma}}{d_{im}} + \frac{1-V_i}{3}\frac{\alpha_m\sigma_m}{d_m}\right)\right]\frac{1}{\sigma_E}. \tag{41}$$

Here, α, ρ, and κ with index m are the properties of the pure $[Ca_{2-w}CoO_{3-\delta}][CoO_2]_{1.62}$ matrix phase. Similarly, the index i indicates bulk quantities of a pure Co_3O_4 phase. Furthermore, we used the abbreviations $\delta_\sigma = \sigma_i - \sigma_m$, $\delta_\kappa = \kappa_i - \kappa_m$, $\delta_{\alpha\sigma} = \alpha_i\sigma_i - \alpha_m\sigma_m$, $d_m = \frac{\sigma_m\kappa_m}{T} -$

$(\sigma_m\alpha_m)^2$, $d_{im} = \frac{\delta_\sigma\delta_\kappa}{T} - \delta_{\alpha\sigma}^2$ and $D = \left(\frac{\delta_\sigma}{d_{im}} + \frac{1-V_i}{3}\frac{\sigma_m}{d_m}\right)\left(\frac{\delta_\kappa}{Td_{im}} + \frac{1-V_i}{3}\frac{\kappa_m}{Td_m}\right) - \left(\frac{\delta_{\alpha\sigma}}{d_{im}} + \frac{1-V_i}{3}\frac{\alpha_m\sigma_m}{d_m}\right)^2$.

The model of Eqs. (1)-(3) describes the thermoelectric properties of the composite based on effective medium approximation. It is based on averaging the bulk properties of the constituents and does not consider additional effects such as interface effects. In this model, the ZT of the composite is always smaller than the largest ZT of its constituents [188]. However, interactions between the two composites and interface effects can enhance ZT beyond that limit [189]. In particular, κ has been found to be decreased due to phonon scattering at large interfaces. At the same time, α can increase due to hot carrier filtering at interfaces [190] and ρ can be reduced by charge carrier injection [191, 192].

7.3 Materials and experimental methods

The $[Ca_{2-w}CoO_{3-\delta}][CoO_2]_{1.62}$ - Co_3O_4 composite samples were synthesized from Co and $CaCO_3$ precursor materials via the citrate complexation method and sintered in vacuum by Spark Plasma Sintering (SPS, FCT-HP D 10), as described in Section 4.1.3 or Ref. [193]. The volume fraction of Co_3O_4 inclusions depends on the nominal composition $x = \frac{N_{Co}}{N_{Ca}+N_{Co}}$, where N_{Co} and N_{Ca} describe the number of Co and Ca atoms, respectively. Here, we analyze materials with $x = 0.561$, 0.566, 0.571, and 0.586. The compositions can also be described by $w =$ -0.04, 0, 0.04, and 0.15 in $[Ca_{2-w}CoO_{3-\delta}][CoO_2]_{1.62}$, or by $y = 3.84$, 3.92, 4.00, and 4.24 in $Ca_3Co_yO_{9+\delta'}$.

The uniaxial pressing direction during the sintering process creates an anisotropy in the polycrystalline samples. To perform thermal and electrical conductivity measurements perpendicular to and along the pressing direction, a thin square-shaped sample (surface normal perpendicular to the pressing direction) and a bar-shaped sample (long axis perpendicular to the pressing direction) were cut from the sintered pellets (Ø = 12 mm × h = 11 mm), respectively. The cut samples were post annealed in air at 1123 K for 20 h to enhance homogeneity and to ensure a similar oxygen stoichiometry. The cation stoichiometry x was verified by Rutherford Backscattering Spectrometry (RBS) using a 2 MeV He beam and a silicon PIN diode detector at an angle of 168° with respect to the incident beam. The RUMP software [194] was used to determine the cation ratio from the RBS data.

The polished surface of the square-shaped samples was used to determine the crystal structure of the composites via X-Ray Diffraction (XRD) and Scanning Electron Microscopy (SEM). Specifically, XRD spectra were collected using a powder X-ray diffractometer (PANalytical X'pert PRO MRD; Cu-Kα1 radiation, λ = 0.15406 nm) and the lattice parameters were calculated using the Le Bail method as implemented in the program FullProf [160, 162]. The morphology, the size, and the volume fraction of the impurity phases were determined by SEM (FEI NovaNanoSEM 230) in backscattering mode and the type of impurity was confirmed with an Energy Dispersive X-ray (EDX) detector.

All samples were characterized in air between room temperature and 1163 K. The Seebeck coefficient α and the electrical conductivity σ were determined using an Ozawa Science RZ2001i system. Laser Flash Analysis (LFA; Netzsch LFA 457 Microflash) and Differential Scanning Calorimetry (DSC; Netzsch DSC 404 C) were used to measure the thermal diffusivity λ and the specific heat C_p, respectively. In addition, the density ϱ of the samples was determined at room temperature by the Archimedes method, yielding the temperature-dependent thermal conductivity $\kappa = \varrho\lambda C_p$. Below room temperature, κ, σ, and α were measured in vacuum atmosphere using the thermal-transport-option in a Physical Property Measurement System (PPMS; Quantum Design). The charge carrier concentration was determined via Hall measurements in the PPMS using the AC transport option with a frequency of 31 Hz. The magnetic field strength was varied between -50 kOe and +50 kOe, and the excitation current was 100 mA. The Hall coefficient R_H yields the hole carrier density via $p = 1/R_H e$.

The oxygen content of the $[Ca_{2-w}CoO_{3-\delta}][CoO_2]_{1.62}$ phase was determined by Thermogravimetric Analysis (TGA) using a Netzsch STA 449C thermal analyzer. All measurements were corrected for buoyancy effects. For the measurement, 40 – 110 mg of pulverized sample were heated while synthetic air (20.5 ± 0.5 % O_2 in N_2) was flowing through the apparatus with a rate of 50 ml/min. Under heating in air, the mixture of $[Ca_{2-w}CoO_{3-\delta}][CoO_2]_{1.62}$ and Co_3O_4 undergoes different phase transitions until it finally decomposes into a mixture of Ca-rich $Ca_{1-n}Co_nO$ (s) and Co-rich $Co_{1-n*}Ca_{n*}O$ (s) above 1313 K, where all cations are divalent [84–86]. The total decomposition equation for heating above 1313 K can be written as

$$Ca_3Co_yO_{9+\delta'}\,(s) + \Psi\ Co_3O_4\,(s) \rightarrow A\ Ca_{1-n}Co_nO\,(s) + B\ Co_{1-n*}Ca_{n*}O\,(s) + 1/2(9+\delta'+\Psi-3-y)\ O_2\,(g). \quad (42)$$

Here, the elemental composition $Ca_3Co_yO_{9+\delta'}$ of $[Ca_{2-w}CoO_{3-\delta}][CoO_2]_{1.62}$ was used for simplicity. The oxygen content in the Co_3O_4 phase does not depend on temperature [195, 196] and in air it is assumed to be saturated. Furthermore, the stoichiometry of the pure phase $w = 0$ ($y = 3.92$) is assumed for the cation stoichiometry of the misfit-layered phase for all samples and $\Psi = n_i/n_m$ is the amount-of-substance fraction of the Co_3O_4 impurity phase compared to the matrix phase, which was determined via SEM. The constants A and B are temperature-dependent and can be determined from the nominal composition x and the exact positions of the phase boundaries. The oxygen content in the product phases (solid phases on the right-hand side of Equation (42)) does not depend on A and B. Hence, the oxygen content δ' (or δ) in the misfit-layered oxide starting phase (left-hand side of Equation (42)) can be calculate from the relative weight loss Δm induced by a partial oxygen loss during the decomposition

$$\delta' = \frac{\Delta m(3M_{Ca}+(y+3\Psi)M_{Co}+4\Psi M_O)-(\Psi-3-y)M_O}{(1-\Delta m)M_O} - 9. \quad (43)$$

More details about the measurement program and the decomposition are given in Section 4.2.3.

7.4 Results

The X-ray diffraction patterns confirm that the misfit-layered cobalt oxide phase was formed for all nominal compositions $x = \frac{N_{Co}}{N_{Ca}+N_{Co}}$. While the sample with $x = 0.566$ (corresponds to $[Ca_{2-w}CoO_{3-\delta}][CoO_2]_{1.62}$ with $w = 0$) is phase pure, additional reflection peaks indicate the formation of the secondary phases $Ca_3Co_2O_6$ and Co_3O_4 for smaller and larger compositions, respectively (Figure 7.1 (a)). Note, that SEM images confirm the existence of the Co_3O_4 phase for $x = 0.571$, despite the fact that the weak main reflex of Co_3O_4 at $2\theta \approx 31.1°$ is barely visible, (Figure 7.1 (c)).

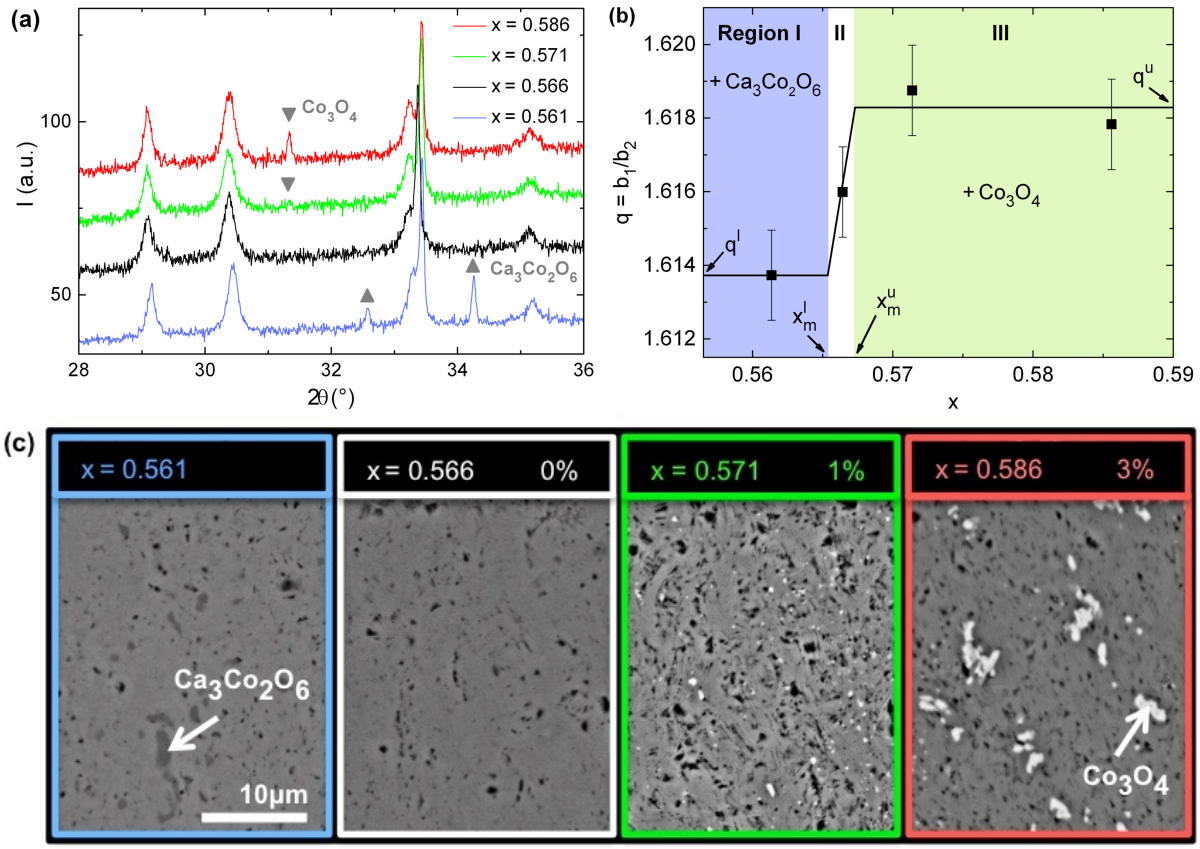

Figure 7.1: (a) XRD patterns of the composite materials for different compositions x confirming the phase formation of $[Ca_{2-w}CoO_{3-\delta}][CoO_2]_q$. Additional reflexes belonging to the $Ca_3Co_2O_6$ and Co_3O_4 secondary phases are marked by triangles. (b) Dependence of the misfit parameter $q = b_1/b_2$ on the nominal composition x. Between the upper and the lower phase boundary x_m^l and x_m^u (region II), $[Ca_{2-w}CoO_{3-\delta}][CoO_2]_q$ is phase pure and the misfit parameter increases with x from q^l to q^u. In contrast, q is constant in the two-phase regions I and III, were the misfit phase coexists with $Ca_3Co_2O_6$ and Co_3O_4, respectively. For clarity, the two-phase regions and the behavior of q (solid line) are schematically illustrated. (c) Microstructure of the polished samples recorded via SEM in backscattering mode (pressing direction points along the horizontal image plane). The $[Ca_{2-w}CoO_{3-\delta}][CoO_2]_{1.62}$ phase (medium grey) consists of platelet-shaped particles with small amounts of pores (black). The secondary phase $Ca_3Co_2O_6$ (dark gray) was detected for $x = 0.561$, while the Co_3O_4 phase (light grey) appears within the $[Ca_{2-w}CoO_{3-\delta}][CoO_2]_{1.62}$ matrix for $x = 0.571$ and 0.586. The values 0%, 1% and 3% state the rounded volume fractions V_i^{SEM} of the Co_3O_4 phase.

The microstructure of the samples recorded via SEM in backscattering mode is presented in Figure 7.1 (c), where a brighter contrast indicates phases with higher average atomic number. In line with the XRD results, the SEM images and EDX measurements confirm the formation of the $Ca_3Co_2O_6$ impurity-phase (dark grey) within the $[Ca_{2-w}CoO_{3-\delta}][CoO_2]_{1.62}$ matrix (grey) for $x = 0.561$ and increasing amounts of the heavier Co_3O_4 phase (light grey) for $x > 0.566$ (Figure 7.1 (c)). A nearly phase-pure $[Ca_{2-w}CoO_{3-\delta}][CoO_2]_{1.62}$ phase with only minor traces of the Co_3O_4 impurity (volume fraction $V_i^{SEM} < 0.002\%$) is formed for the composition $x = 0.566$. This composition is considered to lie within the stability range of the misfit-layered phase while traces of Co_3O_4 are assumed to result from local inhomogeneities. This

interpretation is supported by the fact that the misfit parameter increases still at $x = 0.566$, which demonstrates that $x_m^l < 0.566 < x_m^u$, i.e., that $x = 0.566$ is located within the single-phase region (region II in Figure 7.1 (b)). The fact that q has reached its maximum value already at $x = 0.571$ shows that the upper $[Ca_{2-w}CoO_{3-\delta}][CoO_2]_{1.62}$ phase boundary is located between $x_m^u = 0.566$ and 0.571. Similarly, $0.561 < x_m^l < 0.566$. These limits for the phase boundaries confirm and refine existing literature values, where the phase pure misfit-layered phase was identified for $0.568 < x < 0.574$ [182] and $0.559 < x < 0.571$ [84, 85]. The deviation in the literature values probably results from the fact that small amounts of Co_3O_4 phase are barely detectable via XRD (cf. Figure 7.1 (a)). This means that the pure $[Ca_{2-w}CoO_{3-\delta}][CoO_2]_{1.62}$ phase exists only within a very limited compositional range smaller than $0.561 < x < 0.571$ (or $-0.04 < w < 0.04$) nominal composition. For completeness, the compositions x of our samples were confirmed via RBS (Table 7.2).

x	w	a (Å)	b_1 (Å)	b_2 (Å)	c (Å)	β (°)
0.561	-0.04	4.836(1)	4.552(2)	2.821(1)	10.848(2)	98.15(2)
0.566	0	4.836(1)	4.555(2)	2.818(1)	10.849(2)	98.17(2)
0.571	0.04	4.835(1)	4.563(2)	2.819(1)	10.843(2)	98.16(2)
0.586	0.15	4.835(1)	4.561(1)	2.819(1)	10.843(2)	98.18(2)

Table 7.1: Lattice parameters of the $[Ca_{2-w}CoO_{3-\delta}][CoO_2]_{1.62}$ phase determined by Le Bail fitting for different nominal atomic number fraction x.

The small volume fraction of the Co_3O_4 phase cannot be quantified reliably via XRD. Instead, the volume fractions of the Co_3O_4 impurity V_i^{SEM} and the $[Ca_{2-w}CoO_{3-\delta}][CoO_2]_{1.62}$ matrix V_m^{SEM} were evaluated from the color contrast of representative SEM backscattering images. For the samples with compositions $x = 0.566$, 0.571, and 0.586, Co_3O_4-volume fractions V_i^{SEM} of 0%, 0.8(1)% and 2.6(3)% were determined, respectively. These values are close to the theoretical values V_i^{th} of 0%, 0.56%, and 2.21%. These theoretical volume fractions were calculated from the lever rule assuming the compositions $x_m^u = 0.566$ and $x_i = 1$ for the $[Ca_{2-w}CoO_{3-\delta}][CoO_2]_{1.62}$ matrix phase and the Co_3O_4 impurity phase, respectively. The lever rule states that for x in the two-phase region, the number of Co atoms in the impurity N_i and the matrix phase N_m relative to each other is given by $\frac{N_i}{N_m} = \frac{x - x_m^u}{x_i - x}$. The volume fraction V_i^{th} is related to the number fraction N_i/N_m via the theoretical densities (value for a perfect crystal) and the molar masses of the two phases. The theoretical density of the $[Ca_2CoO_{3-\delta}][CoO_2]_{1.62}$ matrix is $\varrho_m^{th} = 4.69$ g/cm^3, as derived from the measured lattice parameters and tabulated

atomic weights. For the density of Co_3O_4 we used the literature value [195] $\varrho_i^{th} = 6.06$ g/cm^3. In the following, the samples are referred to by using the rounded volume fractions V_i^{SEM} of 0%, 1%, and 3%. An overview of the sample properties is given in Table 7.2.

Not only the volume fractions, but also the density of the sample or the distribution of the secondary phase and the area of the interfaces can influence the thermoelectric properties. We therefore now discuss the structure of the composites in more detail. The $[Ca_{2-w}CoO_{3-\delta}][CoO_2]_{1.62}$ matrix consists of platelet-shaped particles, whose short axes tend to align parallel to the pressing direction, i.e., along the horizontal direction of the image plane in Figure 7.1 (c). This alignment is in agreement with the preferred orientation of the c-axis revealed by the XRD patterns. The smallest observed Co_3O_4-impurities found in the 1% and the 3% sample have a similar diameter of about 90 nm. However, the largest impurities in the 3% sample have irregular shapes and reach a length of up to 3.8 µm, which is about two till four times larger than what we typically observe in the 1% sample. The increased average size of particles in the 3% sample (cf. Figure 7.1 (c)) leads to a decrease of the particle density C_i (from $C_i = 0.12(5)$ µm^{-2} in the 1% to 0.063(8) µm^{-2} in the 3% sample) despite the larger volume of the impurity phase. At the same time, the $[Ca_{2-w}CoO_{3-\delta}][CoO_2]_{1.62}$ - Co_3O_4 interface-area-per-sample-volume a_{int} increases from 0.14(6) µm^2/µm^3 to 0.21(3) µm^2/µm^3. (Table 7.2).

After discussing the structural differences, which might be relevant for the thermoelectric properties of the samples, we want to consider one more aspect. This is the oxygen content δ in the matrix phase, which is known to alter the thermoelectric properties of $[Ca_{2-w}CoO_{3-\delta}][CoO_2]_{1.62}$ [90, 107]. The oxygen content was calculated via Equation (43) from the measured volume fractions V_i^{SEM} and the mass losses Δm determined via TGA measurements. As expected [107, 182], the oxygen content in the matrix changes with temperature (cf. Table 7.2). But most important, the oxygen content in the matrix of the three samples was found to be identical, considering the experimental errors of the TGA evaluation. Accordingly, changes in the thermoelectric properties cannot be attributed to different oxygen contents.

The thermoelectric properties α, ρ, κ, and ZT of the composite samples with different amounts of Co_3O_4 impurities are presented in Figure 7.2 (a)-(d). The changes with respect to the phase-pure 0% sample are illustrated in the insets of Figure 7.2 (a)-(d). As a comparison, the effective medium values of the thermoelectric parameters α_E, ρ_E, and κ_E were calculated

via Equations (18)-(41) using the properties of the two phases and the measured volume fractions V_i^{SEM}. The result is shown for T = 425 K and T = 760 K in Figure 7.2 (e)-(h). The effective medium values were obtained from the thermoelectric properties of our phase-pure matrix phase and literature values for Co_3O_4 with particles sizes of 200 – 400 nm [197] (Figure E.1 in the Appendix). The ratios of these quantities are depicted in Figure 7.2 (i).

	Sample	0% Co_3O_4	1% Co_3O_4	3% Co_3O_4
Composition:	x	0.566	0.571	0.586
	x^{RBS}	0.57(6)	0.57(6)	0.58(6)
Phase fractions:	V_i^{th}	0	0.56	2.21
	V_i^{SEM}	0	0.8(1)	2.6(3)
	Ψ_i^{th}	0	0.015	0.060
	Ψ_i^{SEM}	0	0.022	0.074
Microstructure:	C_{part} (μm^{-2})	<0.0005	0.12(4)	0.063(8)
	a_{int} ($\mu m^2/\mu m^3$)	<0.0016(6)	0.14(5)	0.21(3)
Densities:	ϱ (gcm^{-3})	4.62(3)	4.64(1)	4.68(2)
	ϱ/ϱ^{th} (%)	98.5(6)	98.6(2)	99.1(3)
Oxygen content:	Δm_{1163K} (%)	7.21(4)	7.13(1)	7.23(1)
	Δm_{773K} (%)	7.67(4)	7.60(1)	7.68(1)
	δ_{1163K}	0.12(2)	0.13(1)	0.11(1)
	δ_{773K}	0.01(2)	0.03(2)	0.01(2)

Table 7.2: Summary of the sample properties: Nominal and experimental composition x and x^{RBS} of the composite, theoretical and experimental volume fraction V_i^{th} and V_i^{SEM} of the Co_3O_4 phase, theoretical and experimental molar fraction Ψ_i^{th} and Ψ_i^{SEM} of the Co_3O_4 phase, number of Co_3O_4 particle per unit area C_{part}, $[Ca_{2-w}CoO_{3-\delta}][CoO_2]_{1.62}$ - Co_3O_4 interface-area-per-volume a_{int}, absolute density ϱ and density relative to the theoretical density ϱ/ϱ^{th} of the samples. Mass loss Δm determined via thermogravimetric analysis used for the calculation of the oxygen content δ in $[Ca_{2-w}CoO_{3-\delta}][CoO_2]_{1.62}$ assuming a composition $w = 0$ for all samples..

We observe a small decrease of the Seebeck coefficient of up to 3% in the samples with Co_3O_4 phase (Figure 7.2 (a) and inset). There is hardly any difference between the 1% and the 3% samples. The smaller Seebeck coefficient compared to the pure sample contradicts the predictions of the effective medium model (Figure 7.2 (e)), considering the 1.8 – 3.5 (425 K – 760 K) times larger Seebeck coefficient of Co_3O_4 compared to $[Ca_{2-w}CoO_{3-\delta}][CoO_2]_{1.62}$ (Figure 7.2 (i)). While the trend of a decreasing Seebeck coefficient is still within the

measurement error range, it is in line with earlier publications [182, 186]. For instance, Delorme *et al.* report a decrease of the Seebeck coefficient for volume fractions of 10% and 20% Co_3O_4. Only at 50% Co_3O_4 an increasing Seebeck coefficient was observed [186].

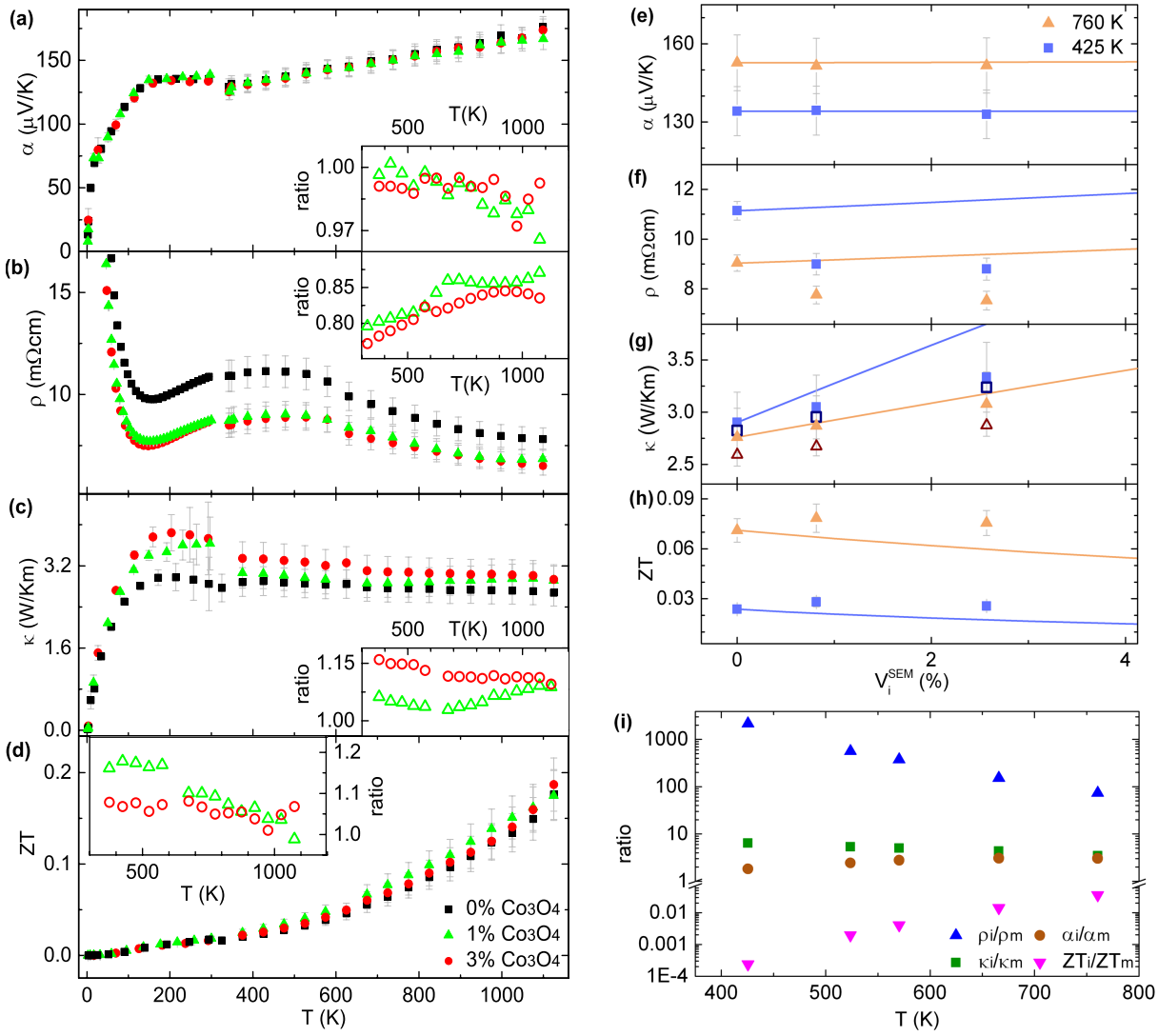

Figure 7.2: (a) Seebeck coefficient α, (b) electrical resistivity ρ, (c) thermal conductivity κ, and (d) figure of merit ZT for 0%, 1% and 3% of Co_3O_4 phase. The insets show α, ρ, κ, and ZT of the samples with 1% (open triangles) and the 3% Co_3O_4 phase (open circles) normalized to the values of the 0 % sample. (e-h) Comparison of the determined α, ρ, κ, and ZT (symbols) with theoretical values calculated according to the effective medium approximation as a function of the Co_3O_4 volume fraction V_i^{SEM} (lines) at 425 K and at 760 K. Open symbols show the lattice thermal conductivity. (i) Properties of the pure Co_3O_4 impurity phase normalized to the properties of the misfit-layered cobalt oxide matrix with 0 % Co_3O_4. Values for Co_3O_4 were extrapolated from literature values measured for particle sizes of 200 – 400 nm [197] (cf. Figure E.1 in the Appendix).

Most surprisingly, the resistivity decreases significantly in the samples with 1 % and 3 % Co_3O_4 (Figure 7.2 (b) and inset). The decrease again contradicts the effective medium model (Figure 7.2 (f)) since the resistivity of Co_3O_4 is magnitudes larger than the one of the $[Ca_{2-w}CoO_{3-\delta}][CoO_2]_{1.62}$. The resistivity decreases a lot compared to the pure sample (up to

23%). Other authors also reported a decrease of the resistivity for increasing nominal Co content [110] from $x = 0.565$ to $x = 0.571$ and for the presence of up to 10% Co_3O_4 impurity [186] below 800 K. Literature indicates [186] that a reversal of this anomalous trend happens at a volume fraction of Co_3O_4 impurities that is much larger than the 1% and 3% studied here (note that the exact value of the critical volume fraction beyond which the reversal is observe seems to vary as a decrease of resistivity was reported for 10% Co_3O_4 impurity [186] while an increase was found for 7% Co_3O_4 [182]). The thermal conductivity increases with the amount of Co_3O_4 in the whole temperature range (Figure 7.2 (g) and inset). This is in line with the predictions (Figure 7.2 (c)) and expected due to the 6.5 – 3.5 times larger thermal conductivity of Co_3O_4 compared to $[Ca_{2-w}CoO_{3-\delta}][CoO_2]_{1.62}$ (Figure 7.2 (i)). Altogether, the variation of x and the corresponding introduction of the impurity phase increase the figure of merit ZT up to 18 % (Figure 7.2 (h)), although the figure of merit of Co_3O_4 is magnitudes smaller than the one of $[Ca_{2-w}CoO_{3-\delta}][CoO_2]_{1.62}$ (Figure 7.2 (i)). An increase of ZT was also reported for more than 10% Co_3O_4 [186]. The effective medium model cannot describe these observations.

7.5 Discussion

The surprising increase of the figure of merit in the presence of Co_3O_4 impurities (Figure 2 (d) and (h)) is induced by the unexpected decrease of the resistivity (Figure 2 (b) and (f)). First note that the drop in resistivity of up to 23 % cannot be related to a compression of the matrix phase since the measured porosity precludes a similarly dramatic change of density. A hint to the solution is given by the slight reduction of α and the decrease of ρ that both indicate an increase of the charge carrier concentration p with the composition x ($\alpha \propto p^{-2/3}$ for degenerate systems [35, 53]). This increase of p is indeed seen in Hall measurements performed between 100 K and 300 K. Note that Hall effect measurements in Co-based systems are potentially unreliable due to the anomalous Hall effect of the magnetic Co [56]. Indeed, the unusual temperature dependence of the hole carrier density p (Figure 7.3) indicates contributions from the anomalous Hall effect [198]. However, for our particular system, previous studies have shown that relative changes of p, such as the increase found by us, are qualitatively accurate, as long as data is compared at constant temperature [145, 149, 151, 199]. We find that the hole carrier density increases by about 20 % in the presence of Co_3O_4. The larger charge density explains the drop in resistivity both qualitatively and

quantitatively. Remarkably, the carrier density is independent of the exact volume fraction of the Co_3O_4 phase, which again is reflected in the same way in the resistivity.

The increase of the carrier density is rather unexpected because, in comparison to $[Ca_{2-w}CoO_{3-\delta}][CoO_2]_{1.62}$ with carrier densities beyond 10^{20} cm^{-3}, for Co_3O_4 films much lower p-type charge carrier concentrations on the order of 10^{10} to 10^{19} cm^{-3} were reported [200–202]. Note also that an increase of the charge carrier density should lead to a decrease of the Seebeck coefficient via $\alpha \propto p^{-2/3}$. The Seebeck coefficient decreases upon the formation of Co_3O_4 impurities, but quantitatively the change is much smaller than expected from the large increase of p. This means that additional effects must be present that soften the decrease of α with p. A possible explanation is energy filtering [203] at the p-P type heterojunction at the $[Ca_{2-w}CoO_{3-\delta}][CoO_2]_{1.62}$ - Co_3O_4 interfaces.

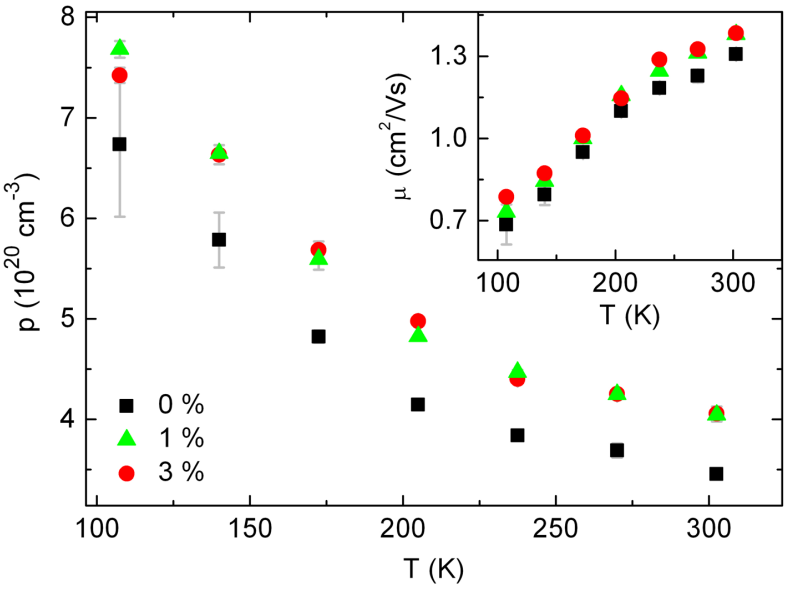

Figure 7.3: Effective hole carrier concentration for different amounts of Co_3O_4 impurity phase. The mobility of the charge carriers is presented in the inset.

The change of the charge carrier concentration with the nominal composition x can have different origins. Most probably, the stoichiometry of the $[Ca_{2-w}CoO_{3-\delta}][CoO_2]_{1.62}$ phase is decisive for the carrier density and the resistivity. The pure sample has composition $x = 0.566$ (or $w = 0$), while the matrix has the composition x_m^u (or $w = w_m^u$) for both the 1% and 3% samples. This picture readily explains why the exact amount of the Co_3O_4 impurity phase seems to be irrelevant (within the small range investigated here). In principle, the formation of an accumulation zone near the $[Ca_{2-w}CoO_{3-\delta}][CoO_2]_{1.62}$ - Co_3O_4 interfaces due to band bending could also explain the larger p. However, this scenario seems much less likely given

that the carrier density is constant for the 1% and the 3% Co_3O_4 sample while the density of interfaces a_{int} increases by about 50% (cf. Table 7.2). Also, a difference of the oxygen content in the matrix has been excluded by our TGA measurement results.

It is expected that the compositional flexibility and defect structure of the $[Ca_{2-w}CoO_{3-\delta}][CoO_2]_{1.62}$ system is limited to the $Ca_{2-w}CoO_{3-\delta}$ rock salt layer [109], where Co is assumed to have a valence state of 3+ [105]. In the perfect lattice of $[Ca_2CoO_{3-\delta}][CoO_2]_{1.62}$ all cation sites are occupied; this correspond to an elemental composition $Ca_3Co_{3.92}O_{9+\delta'}$. Compared to this ideal configuration with $x = 0.566$, the relative or local Co content can change within the limits $x_m^l \leq x \leq x_m^u$. Microscopically, the matrix phase can flexibly increase its relative Co content by (I) the introduction of interstitial Co atoms, (II) the formation of Ca vacancies, or (III) Co^{3+} atoms occupying Ca^{2+} sites. Similarly, the relative Co content can be reduced below the perfect lattice formula by (IV) introducing interstitial Ca^{2+} atoms, (V) the formation of Co vacancies, (VI) or Ca^{2+} for Co^{3+} substitution. Depending on the exact microscopic mechanism, the hole carrier density is expected to decrease (scenarios (I), (III), (V), and (VI)) or to increase (scenarios (II) and (IV)) with increasing Co content. Specifically, each new Co^{3+} interstitial or eliminated Co vacancy leads to three more free electrons in the system while Ca^{2+} for Co^{3+} and Co^{3+} for Ca^{2+} substitution removes or adds an electron, respectively. The rock salt layer acts as a charge reservoir and hence the additional negative charges reduce Co^{4+} to Co^{3+} in the CoO_2 layer, which corresponds to a decrease of the hole carrier density. However, our measurements show an increase of the hole carrier density for increasing Co/Ca ratios. This can only be explained by scenarios (II) and (IV), because the removal of Ca^{2+} interstitials or the formation of Ca vacancies both remove two electrons from the system.

The observed increase of the lattice parameter of the rock salt layer with increasing relative Co content excludes interstitial Ca^{2+} atoms (IV), leaving Ca vacancies as the only consistent explanation for the larger charge carrier density at larger composition x. This is because within the triple rock salt type CaO-CoO-CaO layer, the oxygen ions form an fcc lattice with octahedral and tetrahedral gaps with radii $r_{Octaeder}$=0.0574 nm and $r_{tetraeder}$=0.0308 nm. Here, the solid sphere model with an oxygen radius of r_O=0.14 nm has been applied [204]. In the ideal $x = 0.566$ structure, all octahedral gaps are occupied. Specifically, Co^{3+} ions with a smaller radius of r_{Co}=0.055-0.061 nm occupy the gaps in the middle layer while the larger Ca^{2+} ions with a radius of r_{Co}=0.1 nm [204] occupy the octahedral positions in the outer layers, where they can use more space due to the loose binding caused by the lattice misfit

with the CoO_2 layer. The radius of the tetrahedral gaps is about half the size of the octahedral gap and thus much smaller than the Ca and the Co ions. This means that any interstitials would expand the lattice. As a consequence, Ca interstitials are expected to expand the lattice parameter b_1 of the rock salt layer towards lower x^{nom}. Our measurements, however, show the opposite trend within the whole miscibility region, which clearly excludes the formation of interstitial Ca (IV). In contrast, the formation of Ca^{2+} vacancies (II) agrees with the observed lattice expansion of b_1 toward larger x because the repulsion between the negative oxygen ions increases when the positive charge of the cation is missing. Therefore, it can be concluded that the formation of Ca^{2+} vacancies is responsible for the compositional flexibility for $x > 0.566$ and causes the change of the charge carrier concentration and the lattice parameter.

A further reason for the change of the resistivity is the change of the mobility $\mu = \sigma/(ep)$ presented in the inset of Figure 7.3. Although the charge carrier mobility in Co_3O_4 (about 10^{-7} to 10^{-5} cm^2/Vs [200, 201]) is smaller than the one in $[Ca_{2-w}CoO_{3-\delta}][CoO_2]_{1.62}$, the carrier mobility in the composite samples increases in the presence of Co_3O_4. This means that the difference in the mobility can either result from (a) interface effects, (b) a dependence of the mobility on the charge carrier density, or (c) the interaction of the Ca vacancies with the conductive CoO_2 layer. Interface effects include enhanced grain boundary conductivity [205] or an acceleration of the carriers due to the interaction with inclusions [206]. But the similar mobilities of the 1% and the 3% sample above 150K show that the increasing interface density a_{int} does not affect the mobility. Hence $[Ca_{2-w}CoO_{3-\delta}][CoO_2]_{1.62}$ - Co_3O_4 interfaces (a) can only have a minor effect. Literature results further show that the alteration of the carrier density, as introduced by oxygen vacancies, has no significant influence on the mobility [56]. Hence a dependence of the mobility on the amount of charge carriers (b) seems unlikely in our case. Compared to oxygen vacancies formed in the middle layer of the CaO-CoO-CaO rock salt block [109], the Ca vacancies are located next to the conducting CoO_2 layers, which makes an interaction with plausible. Hence, the formation of Ca vacancies could change the interaction between the layers, which might alter the band structure and thus influence the charge localization [93]. In total, the resistivity is mainly governed by the change of the carrier density (about 20%) while the change of the mobility (up to 8%) is rather small.

While the change of the resistivity could be clearly attributed to stoichiometric changes in the $[Ca_{2-w}CoO_{3-\delta}][CoO_2]_{1.62}$ matrix phase, the thermal conductivity κ was found to increases with

the volume fraction of the Co_3O_4 phase (Figure 7.2 (g)). This trend is in line with the predictions of the model and literature results [186]. The thermal conductivity is composed of a lattice κ_{lat} and an electronic contribution $\kappa_{el} = L\rho^{-1}T$, where $L = 2.4453 \cdot 10^{-8}\ \mathrm{W\Omega/K^2}$ is the Lorenz number. The analysis of both contributions reveals that the Co_3O_4 impurities increase the electronic and the lattice contribution $\kappa_{lat} = \kappa - \kappa_{el}$ (open symbols in Figure 7.2 (g)). However, the change of the thermal conductivity is dominated by the influence of the impurities on the much larger lattice contribution. Compared to the predictions of the effective medium model, the measured thermal conductivities κ are lower. The observed differences might result from interface scattering on the impurity particles. This assumption is supported by the fact that the difference between κ_E and κ decreases for higher temperatures. This is because boundary effects are dominant at low temperatures while their effect is less visible at higher temperatures when Umklapp scattering dominates the thermal conductivity (cf. Figure 7.2 (g)). An alternative explanation for the deviation of κ and κ_E, is the possibility that the stoichiometric change of the matrix phase also affect the thermal conductivity κ. Calculations [207] indicate that the substitution of Ca with a smaller atom should lead to a reduction of the thermal conductivity. Ca vacancies could have a similar effect on the thermal conductivity, which makes further theoretical and experimental investigations thrilling.

Altogether, the increase of the nominal composition x leads to an improvement of the figure of merit despite the fact that the effective medium model predicts the opposite behavior (Figure 7.3 (h)). The improvement of the ZT values in the presence of Co_3O_4 results from the strong decrease of the electrical resistivity induced by the formation of Ca vacancies in the $[Ca_{2-w}CoO_{3-\delta}][CoO_2]_{1.62}$ matrix phase. The larger thermal conductivity of Co_3O_4 increases the effective thermal conductivity κ and thus reduces ZT for an increase from 1% to 3% Co_3O_4. Therefore, ZT increases for the 1% sample, while larger amounts of Co_3O_4 result in a reduction. In consequence, the largest ZT is expected for the pure $[Ca_{2-w}CoO_{3-\delta}][CoO_2]_{1.62}$ phase close to the upper miscibility limit x_m^u. The dependence of the carrier density on the relative Co content and the very limited miscibility range of the misfit-layered cobalt oxide might be responsible for the large variation of the ZT values found in literature.

7.6 Conclusion

The formation of Ca vacancies allows for the compositional flexibility of the misfit- layered cobalt oxide $[Ca_{2-w}CoO_{3-\delta}][CoO_2]_{1.62}$ for $0 \leq w < w_m^u$. The upper phase boundary is located

around $0 < w_m^u < 0.04$ which corresponds to $0.566 < x_m^u < 0.571$. For increasing relative Co content, the Ca vacancies induce an expansion of the lattice parameter of the rock salt layer and increase the p-type charge carrier density. The associated drop of the resistivity induces an increase of the figure of merit ZT. Beyond the phase boundary, the Co_3O_4 secondary phase increases the thermal conductivity of the composite sample, which leads to a decrease of ZT when the volume fraction is increased from 1% to 3% Co_3O_4. We conclude that the thermoelectric properties of the $[Ca_{2-w}CoO_{3-\delta}][CoO_2]_{1.62}$ phase can be tuned by adjusting the Co/Ca defect structure, where the best values are expected close to the upper phase boundary. For enhancing the thermoelectric properties the stoichiometry of the $[Ca_{2-w}CoO_{3-\delta}][CoO_2]_{1.62}$ phase seems to be more critical than the Co_3O_4 impurities.

8 Compatibility approach for the improvement of oxide thermoelectric converters for industrial heat recovery applications[i]

The improvement of thermoelectric materials is only the first step toward the application of thermoelectric devices for heat recovery applications. Additionally, the fabrication of thermoelectric converters with a proper design is of major importance. In order to investigate the influence of the converter design on the power output, new $[Ca_2CoO_{3-\delta}][CoO_2]_{1.62}/CaMn_{0.97}W_{0.03}O_{3-\delta}$ *thermoelectric generators with different cross-sectional areas* A_p *and* A_n *of the p- and the n-type leg are fabricated, characterized and tested at high temperatures in long-term tests. The variation of the measured power output and the efficiency with changing* A_p/A_n *ratio is discussed and compared with calculations based on the measured material properties. The highest conversion efficiencies are reached for ratios close to the one predicted by the compatibility approach, whereas an improper choice of* A_p/A_n *leads to a strong reduction of the efficiency. A volume power density of 1.4 W/cm³ and an efficiency of 1.08 % are found for the most promising generator (temperature difference* $\Delta T = 734\ K$ *and* $A_p/A_n = 1.12$*). The results reveal the major importance of the* A_p/A_n *ratio for the conversion efficiency and subsequently cost and weight reduction issues, both crucial for a large-scale application of thermoelectric converters. Additionally, the oxide generators proved to be very reliable, as after more than 110 h of high temperature energy conversion, no degradation is observable.*

8.1 Introduction

Even modern industrial casting processes consume several GWh of electricity and release waste heat from large induction furnaces to melt tons of metals. For the implementation of thermoelectricity in such a potential high temperature energy harvesting application, the fabrication of reliable, economical and efficient thermoelectric generators is necessary.

[i] Largely verbatim from: Saucke, G., Populoh, S., Thiel, P., Xie, W., Funahashi, R., Weidenkaff, A.: Compatibility approach for the improvement of oxide thermoelectric converters for industrial heat recovery applications. Journal of Applied Physics. 118, 035106 (2015).

Oxides are promising candidates for cheap high-temperature applications, and hence various oxide converters were manufactured and characterized [7, 63–66, 68, 71], with many of them based on the promising p-type misfit-layered $[Ca_2CoO_{3-\delta}][CoO_2]_{1.62}$ and its Gd or Bi substituted compounds. A detailed summary about the performance of state of the art converters is given in Section 2.2.3. Typically, only the power output of the converters is reported and no attention is put on adjusting the different cross-sectional areas A_p and A_n of the p- and the n-type leg or on determining the efficiency. Hence, the present Chapter illustrates the importance of optimizing oxide converters according to the A_p/A_n ratio and address the determination of the efficiency using the compatibility approach introduced in detail in Section 2.2.2.

According to the compatibility approach, the efficiency of a thermoelectric material depends on the reduced current density u that is defined as the ratio of electrical current density (J) to conductive heat flux [57]. For a specific reduced current density u the efficiency reaches a maximum. This ratio is called the compatibility factor s. It can be calculated from the materials properties and depends on temperature (T). The reduced current density u^*, leading to the highest efficiency of the entire leg, has to be chosen considering $s(T)$. For the combination of p- and n-type material it is important that both legs can work with their most efficient u^*. In this case, the legs are called compatible with each other. This compatibility can be reached by adjusting the ratio A_p/A_n of the cross-sectional areas A_p and A_n of the p- and the n-type leg. However, the most efficient A_p/A_n ratio depends on the hot side temperature T_h and the cold side temperature T_c of the legs, which can strongly fluctuate in time for e.g. mobile applications [208]. Therefore, knowledge about the dependency of the efficiency on the cross-sectional ratio A_p/A_n and its temperature dependency can help to tailor thermoelectric converters accordingly. On top of that, an adjustment allows for cost, volume or weight reduction, making the converters more economical. The model and its basic equations used for the theoretical calculations are presented in Section 2.2.2.

In the present Chapter, the effect of a varied cross section area ratio A_p/A_n on the efficiency of thermoelectric generators is investigated theoretically and experimentally. Therefore, a series of 4-leg thermoelectric generators with $A_p/A_n = 0.74$, 1.01, 1.12, 1.24, and 2.74 was fabricated from the p-type $[Ca_2CoO_{3-\delta}][CoO_2]_{1.62}$ and the n-type $CaMn_{0.97}W_{0.03}O_{3-\delta}$. These oxides stand out due to their relatively high thermoelectric figures of merit ZT, non-toxicity, and high chemical and temperature stability ($T_{max} \approx 1200$ K)[209] in air. Moreover, their low

material and synthesis costs [25, 30] allow the fabrication of competitive thermoelectric converters. Mechanically stable generators with low contact resistances can be fabricated using Ag-paste mixed with cobalt oxide powder soldered via hot pressing [70]. Therefore, this material combination provides a good basis for studying the influence of the leg geometry. For both materials, the Seebeck coefficient α, the electrical σ and the thermal conductivities κ are measured and used to calculate the most efficient cross-sectional ratio, the maximum power output, and the efficiency for different temperature gradients. Furthermore, a comparison of the theoretical key figures and the experimental data is made.

8.2 Materials and experimental methods

To synthesize 0.14 mol $[Ca_2CoO_{3-\delta}][CoO_2]_{1.62}$, 0.549 mol Co metal and 0.42 mol $CaCO_3$ were suspended in about 300 ml water. Under cooling, 400 ml of nitric acid (>69 % aq.) were added continuously. The resulting clear pink solution was transferred into about 200 ml of an aqueous solution of 1.94 mol citric acid. After drying at 573K, the residuum of the gel was crushed and calcined in air at 1073K for 10 h. Next a pellet (Ø = 20 mm × h = 11 mm) was sintered in vacuum by Spark Plasma Sintering (FCT-HP D 10, 50 MPa, heating 100 K/min to 1123 K, then 25 K/min to 1153 K and 5 min holding time. Cooling at 25 MPa and 25 K/min to 773 K followed by free cooling). Finally, the legs for the generators and samples for the material characterizations were cut from the same pellet. The samples were post annealed in air at 1123 K for 20 h to ensure similar and homogeneous oxygen content. The highest ZT was found perpendicular to the pressing direction. Therefore, the modules were manufactured accordingly ($Q \perp$ pressing direction). The material for the n-type legs ($CaMn_{0.97}W_{0.03}O_{3-\delta}$) of the generators was synthesized via a citrate process [30]. A hydrostatically pressed (2000 bar) green body (Ø = 40 mm × h = 9 mm) was produced and pre-sintered at 1373 K in a muffle furnace. Afterwards, the samples for the characterization and the legs for the modules were cut from the pellet and sintered in air with a maximum temperature of 1573 K and a dwelling time of 5 h.

Both materials were characterized in air from room temperature to 1163 K. The Seebeck coefficient and the electrical conductivity were measured using the Ozawa Science RZ2001i system. The thermal conductivity $\kappa = \rho\, \lambda\, C_p$ was determined using Laser Flash Absorption (LFA; Netzsch LFA 457 Microfash) and a differential scanning calorimeter (DSC; Netzsch DSC 404 C) for the measurement of the thermal diffusivity λ and the specific heat C_p,

respectively. For the calculation of κ, the endothermic C_p-peak of the p-type material was excluded. The densities of the samples were determined by the Archimedes method.

A series of four-leg half-skeleton modules (inset in Figure 8.3) was fabricated from $[Ca_2CoO_{3-\delta}][CoO_2]_{1.62}$ and $CaMn_{0.97}W_{0.03}O_{3-\delta}$. For each module, the total leg cross-sectional area of the four legs was chosen to be 40.77(6) mm^2 with varying cross-sectional ratio (A_p/A_n= 0.74, 1.01, 1.12, 1.24 and 2.74). The legs were electrically connected by Ag-sheets and joined with a Ag-paste containing 6 wt.% of $Ca_{2.97}Bi_{0.03}Co_4O_{9+\delta}$ powder [31, 64]. The whole module was soldered in air at 1123 K and 6.3 MPa uniaxial pressure.

All generators were characterized in a thermoelectric test stand under identical conditions. The hot-side temperature T_h was measured with two thermocouples fixed on the inner side of the Al_2O_3 plate close to the p- and the n-type legs, while the cold side thermocouples were placed between the silver contact of the p-/n-type leg and the cooling plate. Current-voltage characteristics were recorded at different temperature differences using a Keithley2440 SourceMeter (4-wire mode). Independent of the A_p/A_n ratio all modules should supply the same open circuit voltage $V_{OC} = \int_{T_c}^{T_h} \alpha(T)\, dT$ for the same T_h and T_c. To compensate for small temperature drifts, the power output was extracted from an extrapolation of the measured P-V_{OC} dependency to the same V_{OC} for all converters (cf. Section D.1 in the Appendix). In Table 8.1, V_{OC} and the corresponding T_h and T_c measured for the module with $A_p/A_n = 1.12$ are presented for different heater temperatures. Finally, the module efficiencies were calculated using the theoretical total heat flow entering the legs at the hot side. Here, the flow was calculated from the materials' properties, the leg dimensions and the measured T_c and T_h via Equation (25), using u or Φ optimized for maximum power output.

T_h (K)	369	464	563	658	759	856	949	1051
T_c (K)	297	300	303	308	310	315	321	324
V_{OC} (V)	0.030	0.071	0.115	0.161	0.210	0.259	0.310	0.364

Table 8.1: Temperature of hot T_h and cold side T_c with corresponding V_{OC} measured for the module with $A_p/A_n = 1.12$.

The contact resistivity ρ_c of the oxide-Ag composite (6 wt.% $Ca_{2.97}Bi_{0.03}Co_4O_{9+\delta}$) interface was determined on series of 7 legs with equal cross section but variable length. Ag contacts were joined to the legs with the same soldering procedure used for the modules. Additionally, a series of $Ca_{2.97}Bi_{0.03}Co_4O_{9+\delta}$ legs was soldered without pressure (5h at 1123 K). The length l

of the legs was determined prior to soldering. The leg resistances R_{tot} were measured in 4-probe geometry with both clamps connected to the supply-leads. As $R_{tot}(l) = R_{leg}(l) + 2R_{contact}$ changes linear with l the contact resistance R_c and thus the resistivity $\rho_c = R_c A$ can be extracted from a fit.

8.3 Results and Discussion

The materials' properties of both oxides were investigated to as a basis for the theoretical calculations of, e.g. the theoretical generator efficiency, the heat flow through the generator, and a proper A_p/A_n. The misfit-layered $[Ca_2CoO_{3-\delta}][CoO_2]_{1.62}$ and the perovskite-type manganite $CaMn_{0.97}W_{0.03}O_{3-\delta}$ exhibit 99% (4.63(10) g/cm^3) and 97 % (4.52(18) g/cm^3) of the theoretical densities [79], respectively. The electrical conductivity, the absolute Seebeck coefficient and the thermal conductivity of the two oxides are of comparable magnitude (Figure 8.1 (a)-(c)). For both materials, the experimental data are in agreement with literature [25, 30], although the thermal conductivity of the cobaltite is in the upper region of the literature values, which may be due to the measurement parallel to the aligned particles [151]. Because of the higher electrical conductivity at elevated temperatures, the figure of merit $ZT = \frac{\alpha^2 \sigma}{\kappa} T$ of the p-type material is superior to that of the n-type material (Figure 8.1 (d)). The $CaMn_{0.97}W_{0.03}O_{3-\delta}$ samples reached a peak value of $ZT = 0.11$ at 1123 K, which is comparable with other substituted manganites [25]. At the same temperature, the $[Ca_2CoO_{3-\delta}][CoO_2]_{1.62}$ sample reached a $ZT = 0.17$, which is in agreement with the smaller values reported in literature [25].

The compatibility factors $s_p(T)$ and $s_p(T)$ of the p- and the n-type of the oxide show an increase with temperature, where the latter one is more pronounced (Figure 8.1 (e)). In comparison, the most efficient reduced current densities $u_p^*(T)$ and $u_n^*(T)$ calculated for $\Delta T = 1051$ K- 324 K show a relatively flat temperature rise. Because the electrical current density J is constant within the legs and the conductive heat flows change moderately, the slope of both u is rather small.

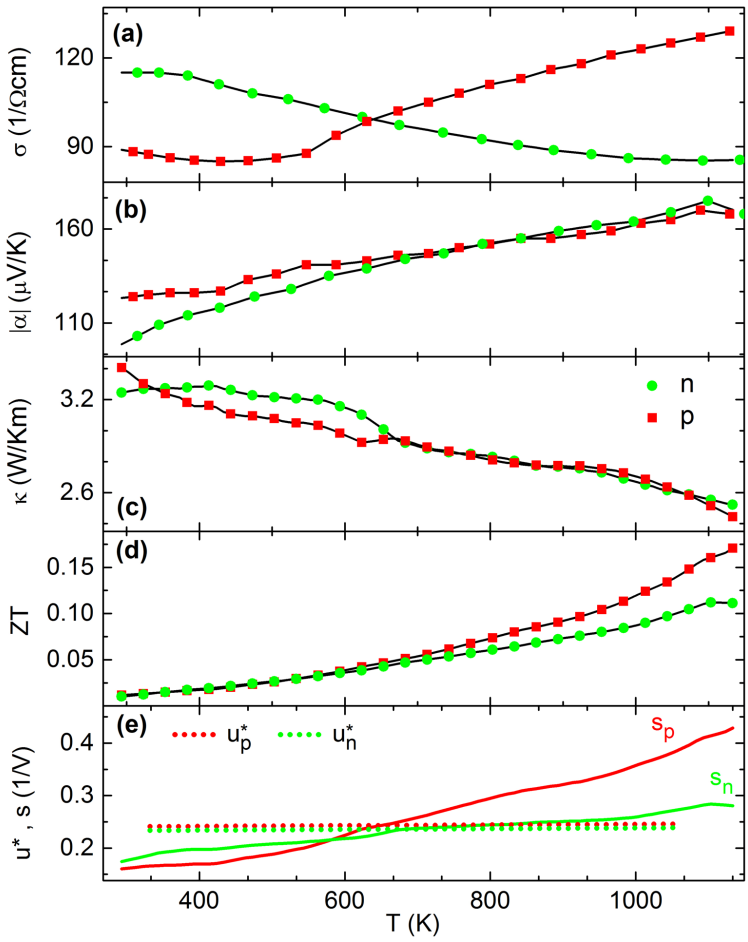

Figure 8.1: Temperature-dependent thermoelectric properties of $[Ca_2CoO_{3-\delta}][CoO_2]_{1.62}$ (p-type) and $CaMn_{0.97}W_{0.03}O_{3-\delta}$ (n-type): (a) Electrical conductivity σ (b) absolute Seebeck coefficient $|\alpha|$ (c) thermal conductivity κ (d) figure of merit ZT and (e) compatibility factor s with most efficient reduced current densities for ΔT = 1051 K- 324 K. Based on the uncertainties in the distance measurement between the electrode-contact wires and the sample dimensions as well as non-optimal thermal contacts, uncertainties of $\Delta\sigma$ = 7 % and $\Delta\alpha$ = 5 % are expected [174]. Error propagation of the uncertainties of the density, the thermal diffusivity $\Delta\lambda$ = 2 %, and the heat capacity ΔC_p < 5 % results in uncertainties of $\Delta\kappa$ = 5.5 % and ΔZT = 13.4 % (error bars are omitted for the sake of clarity).

To allow both legs to work with the most efficient reduced current densities u_p^* and u_n^*, the ratio of the cross-sectional areas should be equal to the most efficient ratio $\left(\mathrm{A_p/A_n}\right)^*$ (see Equation (23)). This temperature dependent cross-sectional ratio and the corresponding p-n-couple efficiency η_{p+n}^* are presented in Figure 8.2 (a) and (b) for different T_h and T_c. Here η_{p+n}^* illustrates the potential of this material combination for different ΔT, giving a maximum value of 1.48 % at ΔT = 1148 - 298 K. The ratio $\left(\mathrm{A_p/A_n}\right)^*$ tends to decrease with increasing T_h and T_c (Figure 8.2 (a)). For a thermoelectric generator, the A_p/A_n ratio is fixed and can only be adjusted to a single ΔT. A series of generators was fabricated to investigate the influence of a non-adjusted A_p/A_n ratio on the module performance. Their ratios are presented in Figure 8.2 (c) in comparison with the most efficient $\left(\mathrm{A_p/A_n}\right)^*$-ratios calculated

for the experimentally applied ΔT. The ratios 1.12 and 1.24 are equal or close to $\left(\mathrm{A_p/A_n}\right)^*$ between 370 K and 660 K whereas the ratio 1.01 is adjusted to T_h around 920 K. In contrast, the ratios 0.74 and 2.74 are smaller or much larger than $\left(\mathrm{A_p/A_n}\right)^*$, respectively.

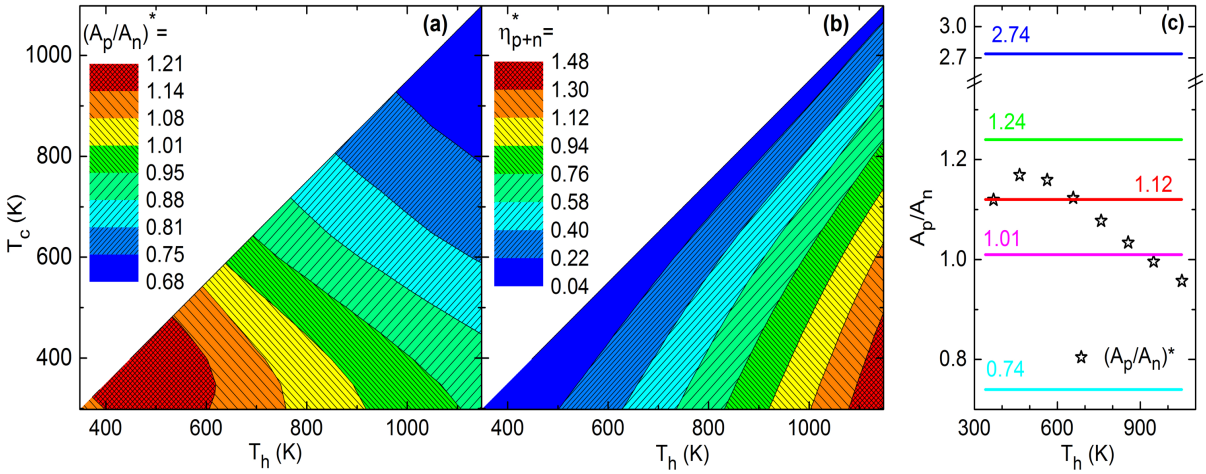

Figure 8.2: Cross section area $\left(A_p/A_n\right)^*$ ensuring the highest efficiencies of both legs (a) and maximum efficiency η^*_{p+n} of a generator with ratio $\left(A_p/A_n\right)^*$ for different cold T_c and hot side temperatures T_h (b). The most efficient $\left(A_p/A_n\right)^*$ ratios for the used experimental T_h and T_c (symbols) in comparison with the ratios of the fabricated generators (lines) (c).

A picture of the fabricated modules and the measured room temperature resistances R^{exp} are presented in Figure 8.3. A minimal value of 152.12 mΩ was found for $\mathrm{A_p/A_n} = 1.24$. This is about 7 % smaller than the room temperature resistance R^{calc} calculated from the geometry of the four generator legs connected in series. As a guide for the eye the continuous function

$$R_{av}^{calc}\left(\frac{A_p}{A_n}\right) = 2\left(R_n + R_p\right) = 2\,\frac{d}{A_p + A_n}\left(\frac{1}{\sigma_n}\left(1+\frac{A_p}{A_n}\right)+\frac{1}{\sigma_p}\left(\frac{1}{\frac{A_p}{A_n}}+1\right)\right) \tag{44}$$

is plotted, which describes the summarized room temperature resistances for the p- and the n-type legs R_p and R_n with varying A_p/A_n using the constant average leg height $d = 0.411(4)$ cm and the constant average $A_p + A_n$ of all modules (Figure 8.3). The very small discrepancy between the average function R_{av}^{calc} and R^{calc} emphasizes the precise cutting of the leg geometry and the homogeneity of the material. The fact that $R^{calc} > R^{exp}$ cannot result from additional contact resistances. Instead a change of the resistance of the p-type material during the hot pressing of the module is observed (cf. Appendix D.2).

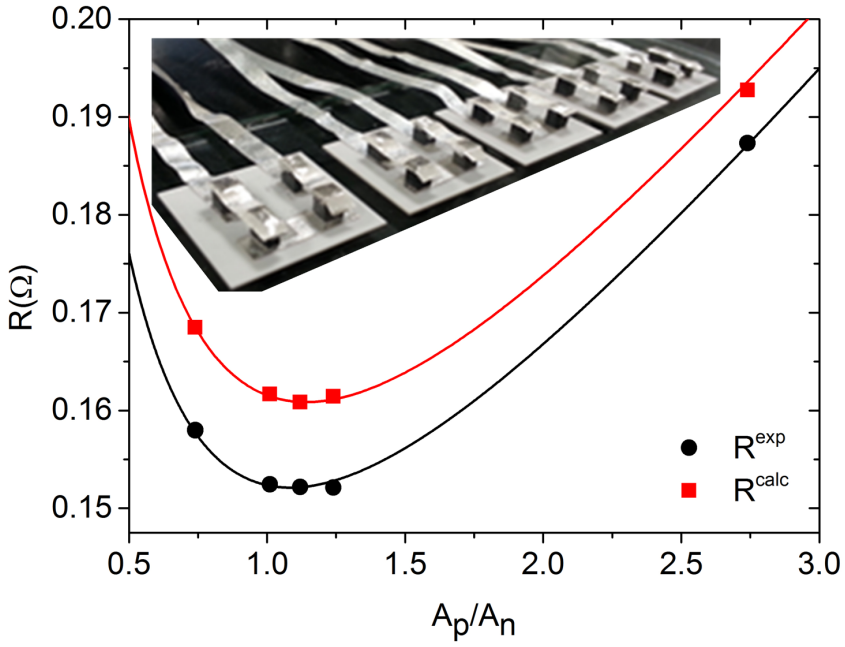

Figure 8.3: Room temperature module resistances R^{exp} (black circles) as a function of the A_p/A_n ratios with corresponding fit of $R_{av}^{calc}(A_p/A_n)$ (Equation (44)). Additionally, the module resistances R^{calc} calculated from the leg dimensions and resistivities are presented (squares). The red line shows the resistance $R_{av}^{calc}(A_p/A_n)$ calculated for the average module area and leg height. For R^{calc} an additional contribution from the contact resistance smaller than 4 mΩ has to be considered. In the inset a picture of the fabricated 4-leg generators is presented.

The contact resistances of the oxide-Ag interfaces, which contribute to R^{calc}, are estimated here based on measurements on a series of legs soldered in the same way as the modules. For $CaMn_{0.97}W_{0.03}O_{3-\delta}$ a contact resistivity of ρ_n^c =0.04(2) mΩcm^2 was found. As the contact resistivity of the Ag-$Ca_3Co_{3.9}O_{9.3+\delta}$ contacts soldered this way is too small for a reliable determination, it was determined for a Ag-$Ca_{2.97}Bi_{0.03}Co_4O_{9+\delta}$-interface soldered without pressure. Here a contact resistivity of ρ_p^c =0.025(16) mΩcm^2 was found. Adding the contacts resistances leads to contact resistance of about $R_c = 4\ m\Omega$ per generator. Because this value amounts to only about 2 % of the total module resistance, its omission in the performed theoretical calculations is reasonable.

A comparison of the measured power outputs of the fabricated generators is presented in Figure 8.4 (a) and (b). The absolute power outputs $P_{1.01}$ and $P_{2.74}$ of the generators with A_p/A_n = 1.01 and 2.74 are depicted in Figure 8.4 (a), while small differences between all the generators are displayed in (b) via a normalization to $P_{1.01}$. Depending on the A_p/A_n ratio different temperature dependencies are observed, although the power outputs of all generators increase with T_h (or ΔT). For T_h around 400 K, the highest power outputs (1.45 mW) are produced by generators with the ratios 1.12 and 1.24, whereas the ratios 1.12 and 1.01 are

most suitable for T_h around 1051 K (P_{max} = 200.4 mW). In contrast, a strong reduction of the power output is observed in the full temperature range for the ratios 0.74 and 2.74, which differ strongly from $\left(\mathrm{A_p/A_n}\right)^*$. At the largest ΔT a reduction of up to 23 % is found for $P_{2.74}$ compared to $P_{1.01}$.

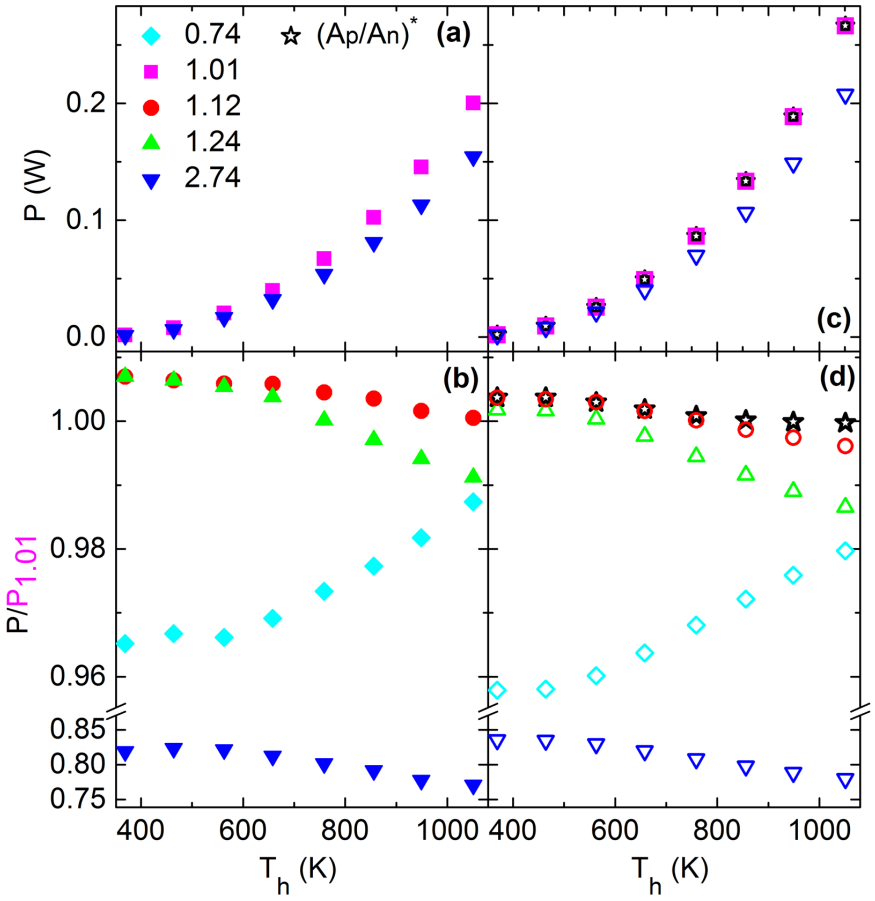

Figure 8.4: Temperature-dependent experimental power outputs for A_p/A_n = 1.01 and 2.74 (a). A normalization of the experimental power outputs to the power output measured for the generator with A_p/A_n = 1.01 reveals also small differences between the different ratios (b). In comparison to the experimental values (open symbols) the corresponding theoretical values (filled symbols) are presented in (c) and (d). Additionally, the values of a generator with $\left(A_p/A_n\right)^*$ adapted to each temperature difference are shown.

To better understand the observed trends, the theoretical power outputs are calculated based on the measured T_h, T_c, and the materials properties (Figure 8.4 (c) and (d)). Additionally, for every T_h the theoretical power output of a module with the ratio $\left(\mathrm{A_p/A_n}\right)^*$ is depicted. The theoretical power output exceeds the experimental ones by up to 35 %. However, the model describes the relative changes very well (cf. Figure 8.4 (b) and (d)). In agreement with the experimental values it predicts the strongly reduced power outputs for the ratios 0.74 and 2.74. Furthermore, it also confirms that the highest power outputs are produced for the ratios

1.12 and 1.01 in the low- and the high-temperature regions, respectively. Comparing the power outputs with the one of $\left(\mathrm{A_p/A_n}\right)^*$ it can be concluded that the closer $\mathrm{A_p/A_n}$ is to $\left(\mathrm{A_p/A_n}\right)^*$ the higher is the power output (cf. Figure 8.2 (c)).

This dependency of the power output on the A_p/A_n ratio can be understood by having a closer look at the reduced current densities within the legs. In line with the introduced theoretical model (Section 2.2.2), we will use the symbols u_p^* and u_n^* for the reduced current densities leading to the highest leg efficiencies and the symbols u_p^{**} and u_n^{**} for the reduced current densities that lead to the highest efficiency of the entire generator. The total efficiency of one leg is calculated from the reduced efficiency $\eta_r(u)$ which reaches to a maximum value $\eta_{r,max}$ for $u = s$. While the slope of the compatibility factor $s(T)$ is fixed by the material properties of the two oxides, the slope of $u(T)$ is determined by the heat equation, cf. Figure 8.5 (a). The highest leg efficiency is reached for the u^* that is closest to s within the whole temperature range. For a generator with $\left(\mathrm{A_p/A_n}\right)^*$this is the case for both legs, but for different ratios, u_p^{**} and u_n^{**} differ from u_p^* and u_n^*. This is illustrated in Figure 8.5 (a) and (b). For a generator with ratio $\mathrm{A_p/A_n} = 1.01$ the η_r and u^{**} nearly coincide with the values of a generator with $\left(\mathrm{A_p/A_n}\right)^* = 0.96$. In contrast, for $\mathrm{A_p/A_n} = 2.74$ the u_p^{**} and u_n^{**} deviate strongly from u_p^* and u_n^* and $\eta_r/\eta_{r,max}$ is reduced by up to 43 % and 73 % for the p- and the n-leg, respectively. A closer look reveals that for the p-type leg the highest efficiency losses are observed at high T, where the ratio u_p^{**} between electrical current density and heat flux is smaller than s_p. Accordingly, the thermoelectric segment produces a Seebeck voltage, but the electrical current is much smaller than for $u = s$. Thus, the efficiency and the power output which increase linearly with the current are small. For the n-type leg the efficiency is also reduced, but in this case u_n^{**} is larger than s_n. Here, the decrease results from Joule heating that is proportional to the square of the current and thus more dominant for higher values. Consequently, the two legs cannot work efficiently at the same time because for a given u_n^{**} the reduced current u_p^{**} is fixed by the A_p/A_n ratio and thus in at least one leg the reduced current is unfavorable.

For the largest temperature difference $\Delta T = 727$ K, the highest experimental power output is reached for the module with the ratio $\mathrm{A_p/A_n} = 1.12$ (cf. Figure 8.4). The measured maximum power output, the maximum power density normalized to the total cross-sectional area of the legs, the leg volume and the mass of the thermoelectric legs are found to be

P_{max} = 200.4 mW, 0.49 W/cm^2, 1.2 W/cm^3 and 0.26 W/g for ΔT = 727 K and A_p/A_n = 1.12, respectively. These values are comparable with values found for other oxide converters [63, 65, 66]. The measured volume and area power densities are even 24 % and 9 % larger than the most promising literature values of 0.96 W/cm^3 and 0.45 W/cm^2 found for a $Ca_{2.7}Bi_{0.3}Co_4O_9$ /$LaNiO_3$ generator with similar T_h of 1073 K [70].

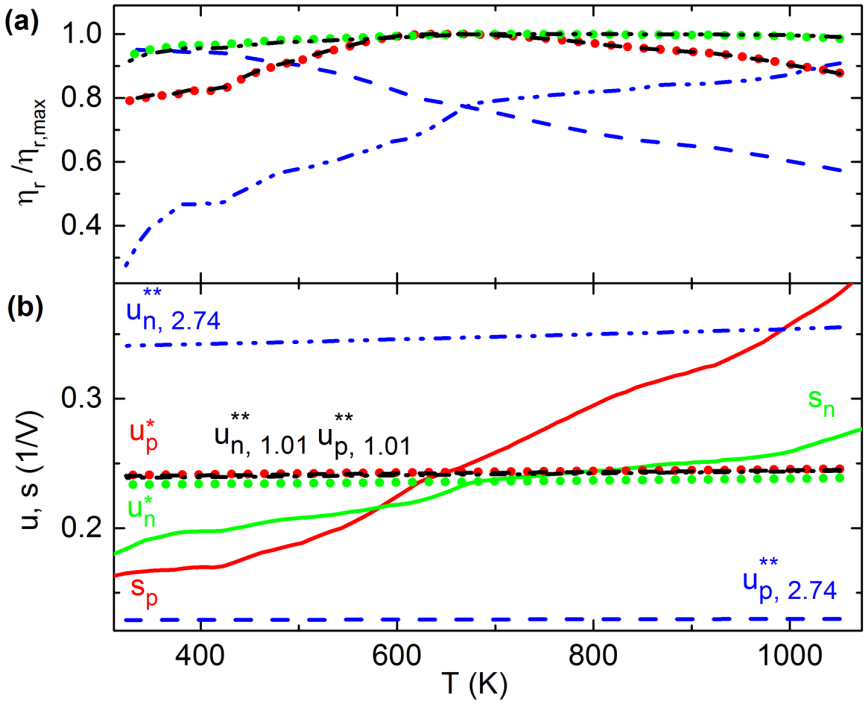

Figure 8.5: (a) Local reduced efficiency η_r normalized to the maximum reduced efficiency $\eta_{r,max}$ of the material with (b) corresponding reduced current densities u^* and compatibility factors s calculated for ΔT = 1133 K - 293 K.

The power densities are not the most adequate parameters for a comparison of generator performance since they depend on the height of the legs (l_{tot}). Informative is the calculation of the figure of merit $Z_M = 4P_{max}/(K\Delta T^2)$ of the module [210], where K is the thermal conductance $K = \frac{N}{l_{tot}}(\overline{\kappa_n}A_n + \overline{\kappa_p}A_p)$, N the number of p-n couples and $\overline{\kappa_n}$ and $\overline{\kappa_p}$ the average values of the conductivities at the hot and the cold side of the legs. For the A_p/A_n = 1.12 module at the highest applied temperature a value of Z_M = 52/μK was calculated.

The calculation of the efficiency allows the direct estimation of the power output for a given heat flow, which is an important value for the application. The heat flow is calculated from the measured T_h = 1051 K and T_c = 324 K, the leg dimensions and the materials properties via Equation (25). However, T_h seems to overestimate the actual temperature because it was measured on the Al_2O_3-plate next to the legs. The measured open circuit voltage

($V_{OC} = \int_{T_c}^{T_h} \alpha(T)\, dT$) leads to a value of $T_h^{Voc} = 970$ K, which is about 8 % smaller than T_h. This difference might originate from the active cooling of the legs, which has only a small effect on T_h. For the generator with $A_p/A_n = 1.12$ for T_h a total heat flow of $Q_{tot} = 22.0$ W and an experimental converter efficiency of $\eta_{p+n}^{T_h} = 0.91$ % is found. In contrast, for T_h^{Voc} a heat flow of Q_{tot} =19.7 W is calculated and the measured efficiency reaches an even higher value of $\eta_{p+n}^{T_h^{Voc}} = 1.02$ %.

For the same T_h and T_h^{Voc} a detailed overview on the change of the experimental and the theoretical couple efficiency with the A_p/A_n ratio is given in Figure 8.6. As discussed for the power output, also the generator efficiency decreases dramatically (up to 23 %) for A_p/A_n deviating strongly from the most efficient $(A_p/A_n)^*$. Experimental and theoretical values show a similar A_p/A_n dependency. For T_h the experimental efficiencies stay up to 25 % below the theoretical values. In contrast, if the heat flow and the theoretical power output are calculated for T_h^{Voc} the difference between the theoretical and the experimental efficiency is smaller than 3 %. Thus, T_h^{Voc} seems to be the more reliable temperature.

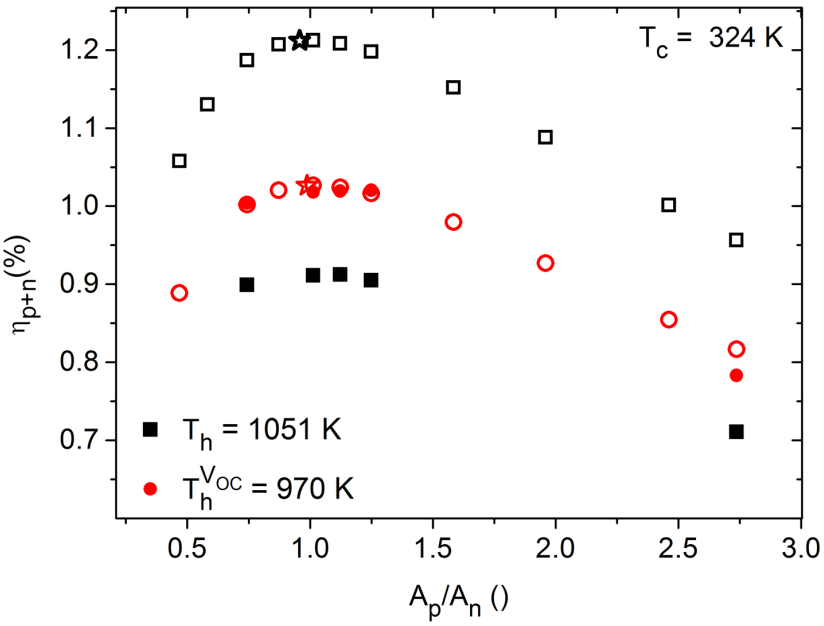

Figure 8.6: Experimental (filled) and theoretical converter efficiency (open symbols) for the fabricated and additional A_p/A_n ratios for T_c = 324 K. For the calculation of the heat flow and the efficiency either the measured T_h or the estimated temperature T_h^{Voc} was used. For both temperatures $(A_p/A_n)^*$ is shown (stars). As radiative losses are neglected, η_{p+n} is overestimated by about 8 % (cf. Appendix D.3).

From the theoretical calculations, it can be seen that $\left(\mathrm{A_p/A_n}\right)^*$ does not lead to the maximum efficiency of the whole module, but it is obviously very close to it (Figure 8.6): compared to the optimal ratio for T_h a 0.04 % higher efficiency is found for an increase of the cross section area by 6 %. This can be explained by the definition of the generator efficiency (Equation (24)). A change of the A_p/A_n ratio changes the total heat flow and more important the weighting of the p- and the n-leg efficiency that determines the power output $P = \eta_p Q_p^h + \eta_n Q_n^h$. For $\mathrm{A_p/A_n} > \left(\mathrm{A_p/A_n}\right)^*$ the larger A_p increases the heat flow $Q_p = J_p \Phi_p A_p$ through the p-leg with the higher efficiency η_p, whereas Q_n decreases with A_n. Additionally, the leg efficiencies of one or both legs decrease because $u_n \neq u_n^*$ or $u_p \neq u_p^*$. In case that the change of the heat flows dominates the change of leg efficiency, this can lead to a higher power output. Accordingly, higher values can be reached through A_p/A_n ratio different from $\left(\mathrm{A_p/A_n}\right)^*$, although the efficiencies of the single legs are smaller. Regarding the efficiency, it has to be considered that an increase of A_p/A_n leads to a higher heat flow $Q = Q_p + Q_n$ for the same ΔT, due to different Φ of the legs. Thus, it is possible that maximum efficiency and maximum power can be found at slightly different ratios. However, this difference is considered to be rather small [211].

For the presented material combination, the most efficient ratio is close to $A_p/A_n = 1$, but for material combinations with very different properties this commonly used ratio may result in a tremendous decrease of the efficiency. Thus, a fast calculation of the most efficient ratio according to Equation (23) is highly recommended prior to generator fabrication. Furthermore, around the maximum efficiency the curve is relatively flat (Figure 8.6). This offers the opportunity for cost weight or volume reduction without remarkable efficiency losses, which is of particular importance for mobile applications, e.g., in the automotive industry.

Finally, the long-term stability of the generator with $\mathrm{A_p/A_n} = 1.12$ is investigated for 114 h (Figure 8.7) for the final application on a casting furnace at vonRoll casting. The test is performed at $T_h \approx 1160$ K and $T_c \approx 355$ K. Although T_h is close to the decomposition temperature (1200 K) of the cobalt oxide [209] and the melting point of silver (1235 K), no degradation effects are observed. The internal resistance R_i of the generator is constant (Figure 8.7 (d)), which points out the long-time stability of the Ag-contacts achieved by intermixing with the oxide powder. The maximum power output reaches a peak value of 237 mW and varies by about 2 %. This variation is probably induced by the 3 % variation of

ΔT, which also reflects in a change of V_{OC}. Normalization of the maximum power output to the total cross-sectional area of the legs, the leg volume and the mass of the thermoelectric legs lead to values of 0.58 W/cm^2, 1.4 W/cm^3 and 0.31 W/g, respectively. This power corresponds to a maximum efficiency of 0.99 % for the measured T_h and 1.08 % if the more reliable estimated $T_h^{V_{OC}} = 1085$ K is used for the calculation of the heat flow.

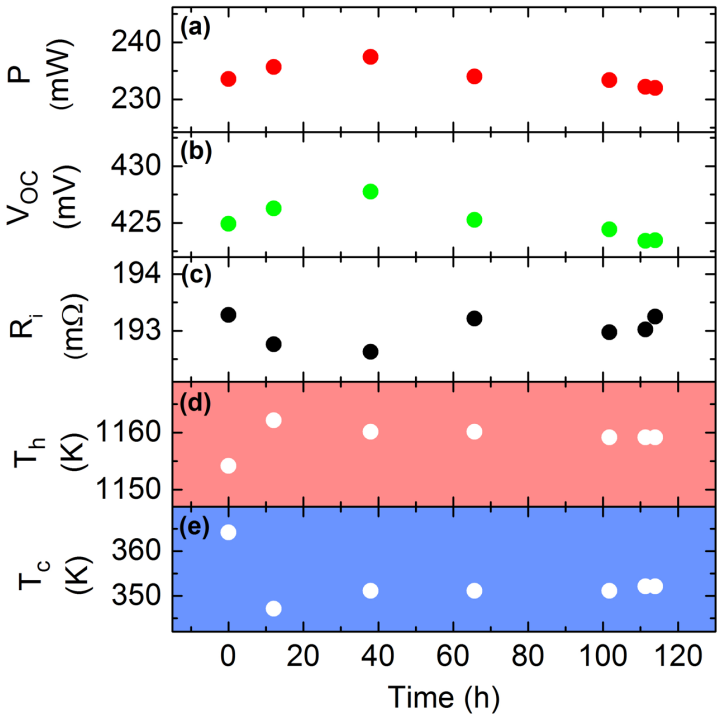

Figure 8.7: Stability of the generator with $A_p/A_n = 1.12$ during 114 h of energy conversion. The maximum power output (a), the open circuit voltage (b) and the internal resistance (c) are constant. Small variations might result from small drifts of the hot (d) and the cold side temperature (e).

8.4 Conclusion

A series of four-leg thermoelectric modules with varying A_p/A_n ratio was fabricated, characterized and successfully tested in long-term tests at very high temperatures. It was shown that the power output and the efficiency of the thermoelectric generators increase strongly for an adjustment of the cross-sectional ratio A_p/A_n according to the compatibility approach. For A_p/A_n differing considerably from the most efficient $(A_p/A_n)^*$ a relative decrease of the experimental efficiency of up to 23 % was observed. For the best performing module with $A_p/A_n = 1.12$ the long-term thermal stability was demonstrated, which emphasizes the reliability and the potential of the oxide thermoelectric converters for high

temperature applications. The measured maximum power output, the maximum power density normalized to the total cross-sectional area of the legs, the leg volume and the mass of the thermoelectric legs were found to be 237 mW, 0.58 W/cm^2, 1.4 W/cm^3 and 0.31 W/g, respectively. Based on the measured temperature $T_h = 1160$ K and the smaller estimated $T_h^{VOC} = 1085$ K, the calculated heat flow leads to efficiencies of 0.99 % and 1.08 %, respectively. Theoretically, even higher efficiencies are possible since for $[Ca_2CoO_{3-\delta}][CoO_2]_{1.62}$ higher ZT were reported in literature.

Despite its simplifications, the theoretical compatibility model describes the experimental trends very well and offers an easy way for the improvement of thermoelectric converters. Especially, the calculated dependency of the efficiency on the A_p/A_n ratio can be used for cost, weight and volume reduction, which is crucial for large-scale applications of thermoelectric converters for waste heat recovery.

9 Summary and Outlook

In this work a deeper understanding of the thermoelectric properties of the promising misfit-layered $[Ca_{2-w}CoO_{3-\delta}][CoO_2]_{1.62}$ was achieved by analyzing the high temperature transport properties, the effect of the modulation of the Co/Ca ratio, and the influence of Ru substitution on the thermoelectric properties.

Ru substitution on the Co site leads to a remarkable decrease of the thermal conductivity of up to 30 %, which is assumed to result from the scattering of phonons on local resonance vibrations of the ruthenium atoms. The substitution decreases the p-type carrier density, which is accompanied by an increase of the electrical resistivity and the Seebeck coefficient below 650 K. Despite the reduction of the power factor, Ru substitution improves the figure of merit up to 25 % over a wide temperature range. This improvement makes Ru-substitution an interesting strategy for a further ZT improvement. The substitution further affects the electrical conductivity because it shifts the metal semiconductor transition toward higher temperatures, which might result from distortions of the lattice that hinder the connected structural transition.

The disorder induced through the misfit structure or through substitution plays a major role in the electrical transport. The high temperature transport is dominated by small-polaron hopping, while the transport in the intermediate temperature range can be understood in the framework of Anderson localization. This type of localization is characterized by an energy spread of the Co 3d states in the conducting CoO_2 layer. The energy spread results from the random potential that a charge carrier experiences. Such a random potential occurs due to different atomic surroundings and hence different Coulomb interaction at each site created by the misfit-layered structure. A substitution of Co with Ru alters the Coulomb potential and thus increases the disorder, which leads to an increase of the activation energy in both transport regimes. The developed picture of the high temperature transport properties of $[Ca_{2-w}CoO_{3-\delta}][CoO_2]_{1.62}$ indicates that the disorder introduced through substitution is an important factor that influences the transport properties beyond the change of the charge carrier density. Including this effect in theoretical models should improve the prediction power regarding the thermoelectric properties of substituted $[Ca_{2-w}CoO_{3-\delta}][CoO_2]_{1.62}$ compounds.

The thermoelectric properties of $[Ca_{2-w}CoO_{3-\delta}][CoO_2]_{1.62}$ also depend on the cation stoichiometry in the misfit layered phase. Compared to the ideal composition, an increase of the Co/Ca ratio leads to the formation of Ca vacancies. The Ca vacancies remove electrons from the system, which results in an increasing amount of Co^{4+} ions in the CoO_2 layer and hence a larger p-type charge carrier density. The increase of the carrier density induces an increase of the power factor because the minor decrease of the Seebeck coefficient is accompanied by a significant decrease of the electrical resistivity. The best thermoelectric performance is found for large Co contents at the upper phase boundary of $[Ca_{2-w}CoO_{3-\delta}][CoO_2]_{1.62}$. Beyond the phase boundary, the Co_3O_4 impurity phase increases the thermal conductivity of the $[Ca_{2-w}CoO_{3-\delta}][CoO_2]_{1.62}$ - Co_3O_4 composites, which leads to a reduction of ZT for an increasing Co_3O_4 volume fraction.

In addition to understanding and improving the material properties, devices were fabricated and engineered to reach their maximum efficiency. Thermoelectric modules consisting of p-type $[Ca_2CoO_{3-\delta}][CoO_2]_{1.62}$ and n-tpye $CaMn_{0.97}W_{0.03}O_{3-\delta}$ legs with varying cross-sectional areas A_p and A_n were fabricated, characterized and the long-term thermal stability was demonstrated at 1085 K. An adjustment of the A_p/A_n ratio according to the compatibility approach increases the power output and the efficiency strongly, and the maximum values were found close to the ratios recommended by the model. Around $T_h^{Voc} = 1085$ K, the measured maximum power densities normalized to the total cross-sectional area of the legs (0.58 W/cm^2) and the leg volume (1.4 W/cm^3) exceeds published values found for other oxide converters [63, 65, 66]. A thermoelectric efficiency of 1.08 % was achieved, which is close to the theoretical expectation. The strong decrease of the efficiency for non-adjusted cross-sectional areas demonstrates that an adjustment according to the prediction of the compatibility approach allows to tap the full potential of the p- and the n-type material. The good agreement between the theoretical and the experimental results confirms that the compatibility model can indeed be used to predict efficient A_p/A_n ratios. This predictive power can be used for the enhancement of thermoelectric converters considering cost, weight and volume reduction, i.e., factors that are important for large-scale applications for waste heat recovery.

Based on the deeper understanding of the thermoelectric properties of $[Ca_{2-w}CoO_{3-\delta}][CoO_2]_{1.62}$ developed here, the strategies for a future enhancement of the figure of merit are clear: The thermoelectric properties of the misfit layered phase can be enhanced by adjusting the Co/Ca ratio, which partly explains the variation of the published figures of

merit. Therefore, a stoichiometry close to the upper miscibility limit is recommended to reach the best performance for the pure non-substituted material. To complete the picture, further studies on the material should investigate the Co deficient phase with Co/Ca ratios below the ideal composition $[Ca_2CoO_{3-\delta}][CoO_2]_{1.62}$, which was beyond the scope of this work. In the Co deficient phase, the formation of Co vacancies can be expected. Studies of the phase region with Co-deficient stoichiometry would complete the knowledge about the effect of the stoichiometry on the thermoelectric properties of $[Ca_{2-w}CoO_{3-\delta}][CoO_2]_{1.62}$ and provide full prediction power regarding the ideal composition for applications.

A very exciting finding of the present work is the observed large decrease of the thermal conductivity for Ru substitution because Ru can be used as a co-substituent. For future experiments a co-substitution with Ag seems promising because a very high figure of merit $ZT = 0.5$ was reported at 1000 K for polycrystalline $Ca_{2.7}Ag_{0.3}Co_4O_9$/Ag-10% samples with substituted and added Ag [154]. Ag increases the power factor significantly, but decreases the thermal conductivity. Here, resonance scattering of phonons on Ru atoms could counterbalance the increase or even induce a decrease of the thermal conductivity. Similar to Ru, Lu substitution is also known to decrease the thermal conductivity significantly [126]. Thus, the so far best figure of merit ($ZT = 0.61$ at 1118 K) was reported for a co-substitution of Ca with Ag/Lu, where the oxide with nominal composition $Ca_{2.87}Ag_{0.05}Lu_{0.15}Co_4O_9$ forms a complex multi-scale microstructure [29]. Different from Ag and Lu, Ru does not substitute the Ca but the Co atoms. Both a co-substitution with Ag/Ru and a substitution with Ag/Lu/Ru, seem worth investigating in the future.

For a long time the figure of merit was believed to be limited to values below 1. But nano-structuring approaches or new materials with phonon glass-electron crystal properties were able to overcome this limitation. Theoretical calculations predict that, for an ideal case band structure with a delta function in the DOS, a figure of merit of up to $ZT = 14$ is possible [51]. Together with the slow but steady increase of the achieved thermoelectric figures of merit during the last years (Figure 9.1), this prediction indicates that further investigations are very promising. The results found in this work, such as the identification of promising substitution strategies, achieving a deeper understanding of the transport properties and the influence of stoichiometric changes, are all small steps toward a better understanding of the complicated thermoelectric materials and thus contribute indirectly to better ZT values.

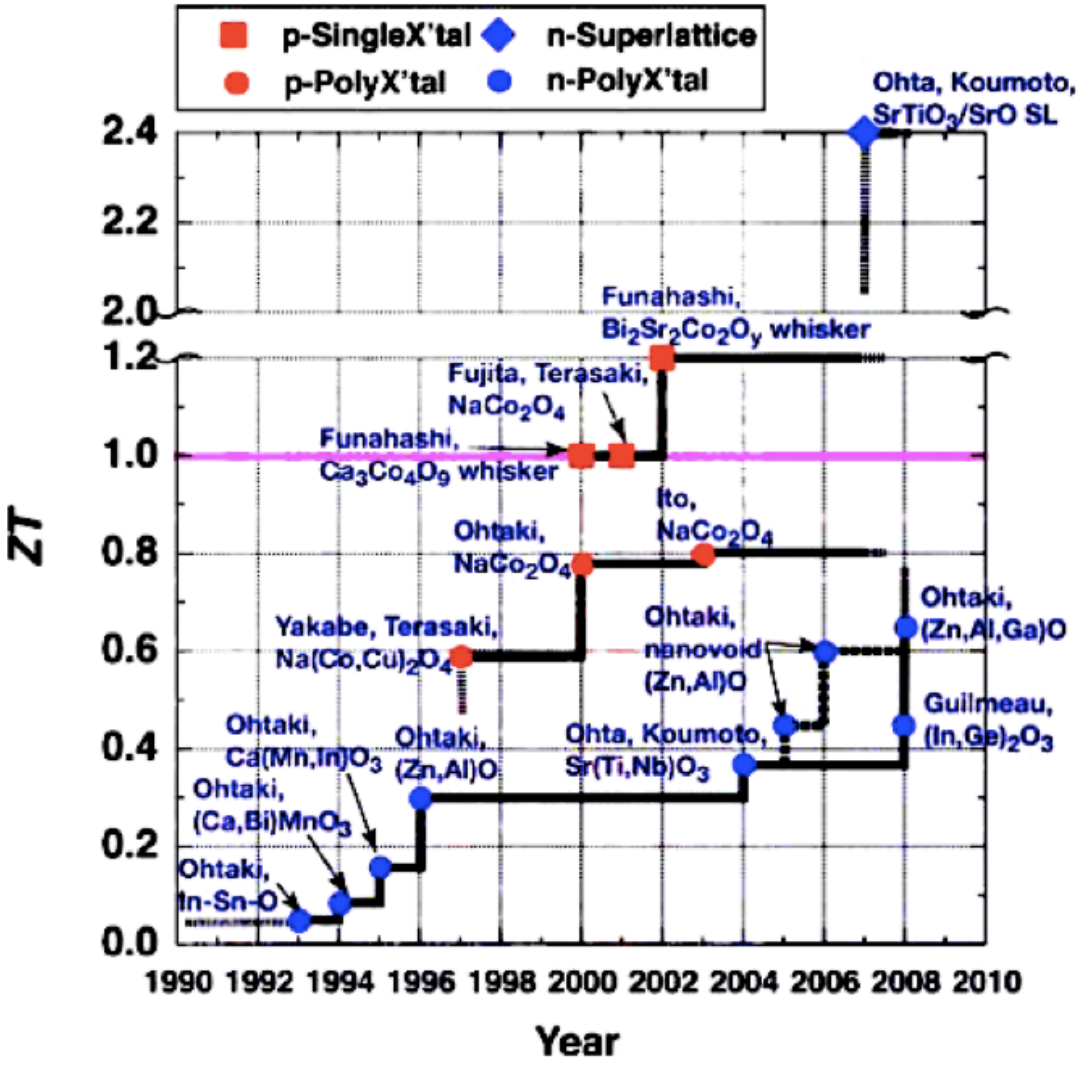

Figure 9.1: Timeline of the highest *ZT* values of oxide thermoelectric materials. Research lead to a continuous improvement. Reproduced from Ref. [212].

Appendix

A Demonstration of energy conversion[j]

Thermoelectric heat recovery was demonstrated in the lab and under the rough conditions in the foundry vonRoll casting. For the demonstration in the lab, multi-leg thermoelectric converters were fabricated, characterized, and used as current source for different consumers. For the demonstration of heat recovery in the foundry, an air-cooled demonstrator was developed for the recovery of conductive or mixed radiative and convective heat emitted by an induction furnace. The temperatures, heat fluxes, and power outputs were investigated and the total amount of energy available during a production day was estimated for conductive coupling.

A.1 Multi-leg converter for the demonstration of heat recovery

The fabrication of simple four-leg converters is sufficient for experiments in the lab. For real heat recovery applications, multi-leg converters are necessary to achieve power outputs that are sufficient for the operation of external consumers. To demonstrate the scalability, devices with 4, 36, and 40 legs were investigated and compared to one another (Figure A.1). The multi-leg converters were fabricated according to the new half-skeleton design with two parallel legs (cf. Section 4.4.1) and characterized in the thermoelectric test stand.

The power output P, the power density per leg area P/A, and the internal resistance R_i of the 4-, the 36-, the 40-leg converters are presented in Figure A.2 (a)-(d). The internal resistance is nearly temperature independent, which results from the contrary temperature dependencies of the p- and the n-type material (cf. Figure 8.1). The power output is proportional to the Carnot efficiency and thus increases with ΔT. As expected, the power output and internal resistance increase with the number of legs. A maximum power density of 0.35 W/cm^2 was reached for the four-leg converter at $\Delta T = 725$ K, while the same heating power resulted in smaller ΔT and P_{max} for the multi-leg converters. Remarkably, the power output normalized to the total leg area does not depend on the number of legs, despite the increase of the packing density.

[j] Partly adapted from: Saucke, G., Weidenkaff, A., Populoh, S.: Kostengünstige und verlässliche thermoelektrische Konverter für die Nutzung industrieller Abwärme - Abschlussbericht. BFE - Bundesamt für Energie (2014).

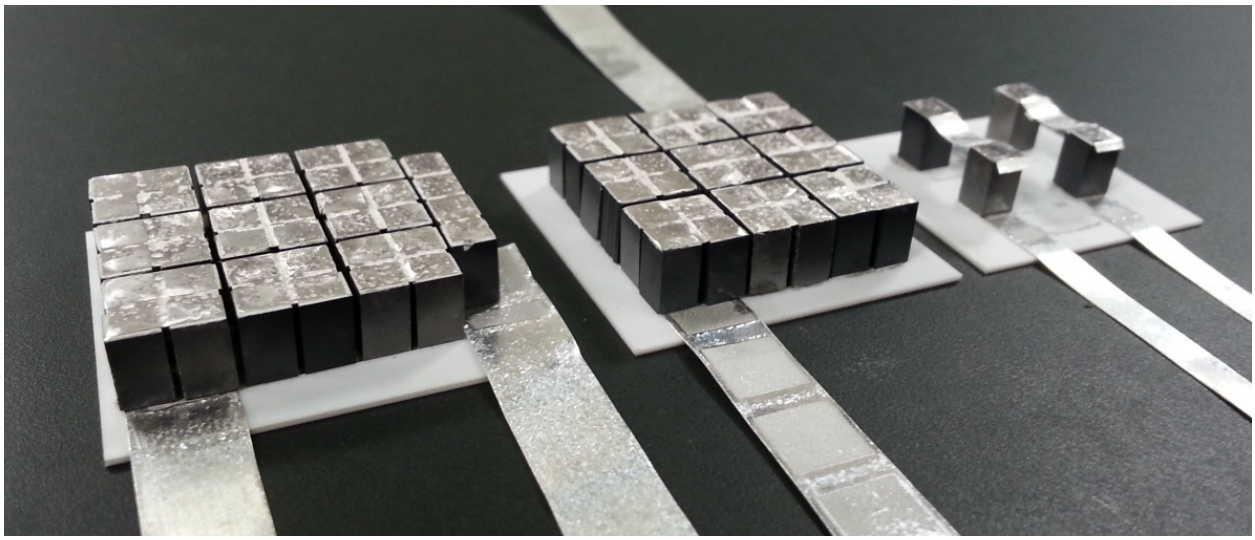

Figure A.1: Photograph of a 40-leg, a 36-leg, and a four-leg half-skeleton converter (left to right).

For high packing density, the radiative heat emitted from the lateral surfaces of the legs can be reabsorbed by the neighboring legs. In contrast, for the four-leg configuration, the distance between the legs is large and a major part of the radiative heat is lost to the surrounding. Therefore, the heat losses per leg are expected to be larger for the four-leg converter and accordingly only a smaller heat flow should be available for the generation of electrical power. However, no clear trends were observable for the power density and thus differences due to radiative losses are negligible. The good agreement between the power densities shows that the four-leg converters are good prototypes.

In order to increase the generated power output for the demonstration of heat recovery in the lab, the 36- and the 40-leg converter were connected in series. The resulting current-voltage characteristics and the associated power output of the series connection of the 36- and the 40-leg converters are presented in Figure A.2 (d). A total power output of 2.2 W was reached for $\Delta T = 645$ K. The generated direct current was used for the conversion into mechanical energy (powering of a ventilator) or into light produced by LEDs (Figure A.3 (a) and (b)).

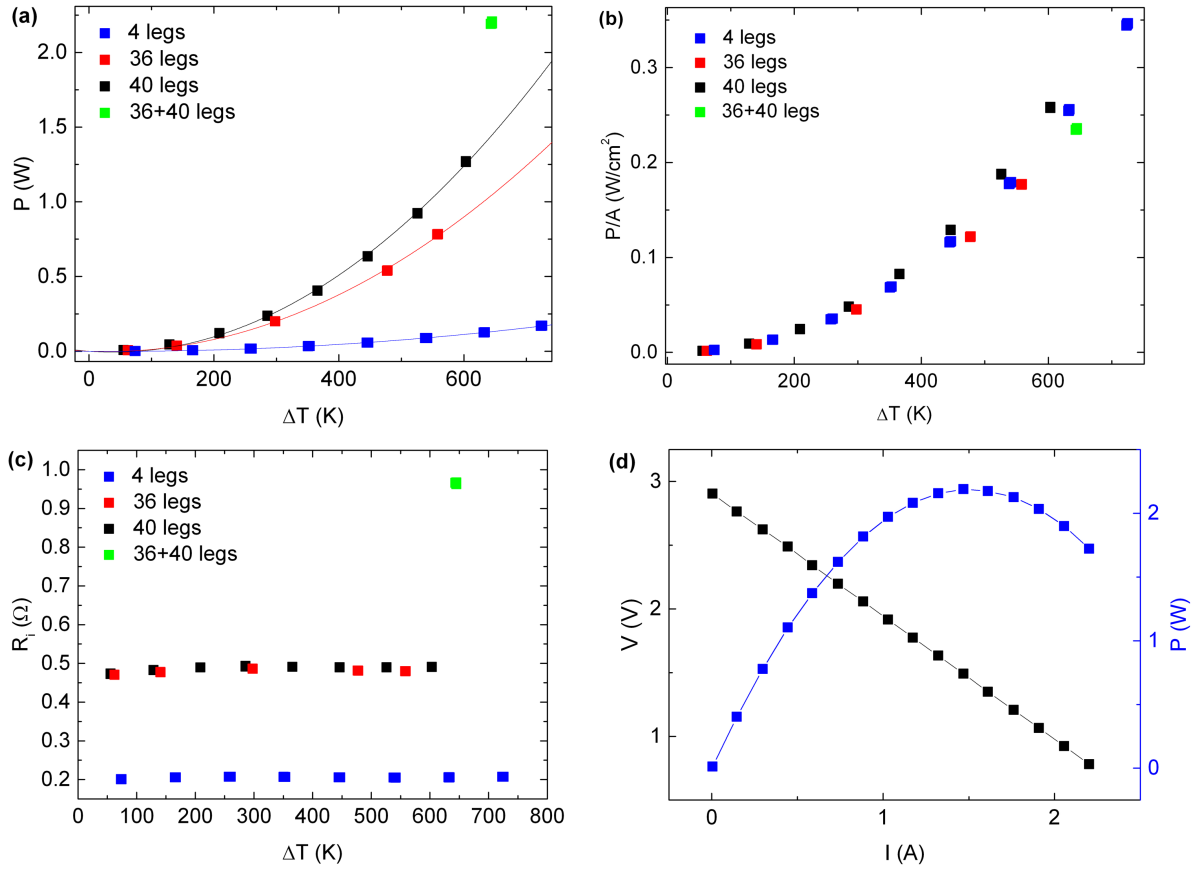

Figure A.2: Power output P (a), power density per area P/A (b), and internal resistance R_i (c) of the 4-, the 36-, the 40-leg converters, and a series connection of the 36- and the 40-leg converters as a function of temperature gradient ΔT. (d) Output voltage V (black symbols) and power output P (blue symbols) as a function of the output current I for the series connection of the 36- and the 40-leg converters recorded at $\Delta T = 645$°C (d). The power reaches a maximum value of $P_{max} = 2.2$ W and the y-intercept and the slope of the I-V characteristics reveal an open circuit voltage of $V_{OC} = 2.9$ V and an internal resistance of $R_i = 0.97\ \Omega$.

Additionally, an iPhone was charged with the electrical energy supplied by the thermoelectric generators (c). The series connection of the converters can only deliver voltages smaller than the open circuit voltage $V_{OC} = 2.9$ V, but a stable input voltage of about 5 V is needed for charging. Therefore, a DC-DC converter was used to increase the voltage followed by down conversion of the voltage to a stable value of about 5 V. While a stable input voltage is necessary for charging, the magnitude of the current determines the charging time $t = \frac{Q_{max}}{\eta_k I}$ of the lithium ion battery of the iPhone 4 (nominal voltage 3.7 V, maximum charge $Q_{max} = 1420$ mAh). The time can be estimated assuming a charging efficiency of $\eta_k = \frac{Q_s}{Q_{in}} = 0.97$ [213, 214], which describes the amount of charge carriers Q_s stored by the battery relative to the supplied charge carriers Q_{in}. The measured constant charging current $I = 0.22$ A results in a charging time of 6:39 h.

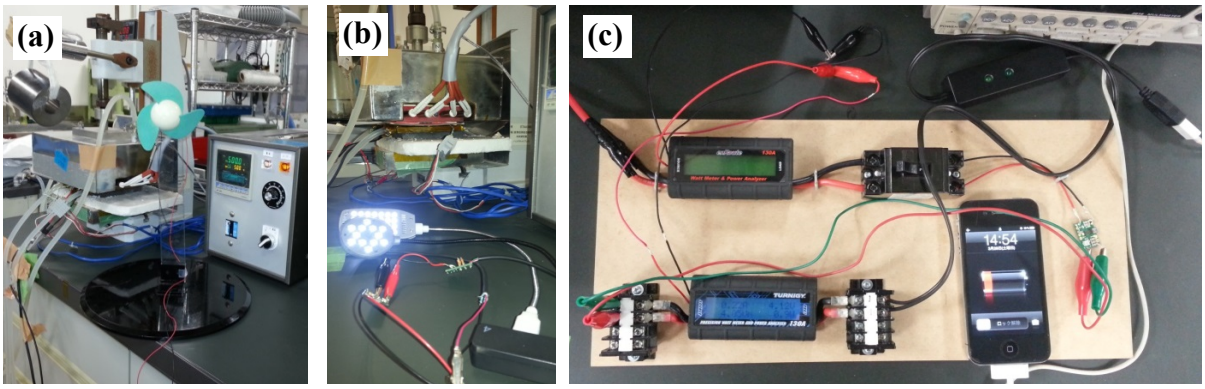

Figure A.3: Demonstration of thermoelectric heat recovery in the lab. Conversion into mechanical energy by powering a ventilator (a) into light produced by LEDs (b) and into chemical energy by charging the battery of an iPhone (c). For charging, a voltage of about 5V is required hence it is increased by a DC-DC converter followed by DC-DC down-conversion to a stable value.

The fabricated oxide converters were successfully used for energy conversion under controlled lab conditions in the test stand. Additionally, the reliability was proven in a long-term test for the four-leg converters (cf. Figure 8.7 in Section 8.3). However, the heat recovery in an actual application is more challenging. Therefore, energy conversion under rough production conditions in a foundry was demonstrated and is presented in the following.

A.2 Demonstration of heat recovery in the foundry vonRoll casting

A.2.1 Introduction

In the casting industry tremendous amounts of energy are used for heating and melting of metals. Temperatures up to 1858 K are regularly reached inside of casting furnaces and heat energy is dissipated during melting and the subsequent processing. Thermoelectric converters can recover this heat. While reliable, long-term heat recovery was successfully demonstrated by radioisotope thermoelectric generators used in space operations, a reliable high temperature operation in air under harsh conditions, including strong temperature variations, mechanical vibrations and dusty atmosphere remains challenging. Here, thermoelectric heat recovery using oxide based converters is demonstrated on a casting furnace in the foundry vonRoll casting. An air-cooled demonstrator is developed to recover either conductive or a mixture of radiative and convective heat emitted from the furnace.

A.2.2 Experimental details

For the demonstration of energy conversion, a $Ca_{2.7}Bi_{0.3}Co_4O_9$ - $CaMnO_3$ half-skeleton-converter with 256 legs was equipped with an air-cooled heat sink (Figure A.4). The converter was fabricated by TES-NEW-energy in the same way as the half-skeleton modules in the present work (cf. Section 4.4.1). In order to connect the demonstrator with the furnace, the setup was fixed on an aluminum ground plate, which offers a high thermal conductivity of $\kappa_{Al} = 235$ W/mK. The heat sink was used to press the oxide converter on the plate. To ensure low thermal contact resistances, heat-conductive paste (FEROTHERM 4, $\kappa = 3.3$ W/mK) was applied between the ground plate and the electrically insulating Al_2O_3 plate of the converter. The exposed metal interconnects of the module were insulated from the heat sink via an electrically insulating silicone gel pad (Alpha-Gel). In addition to a good thermal conductivity, the soft consistency of the gel compensates small unevenness and hence increases the mechanical stability.

The heat sink consists of a copper block and an anodized black aluminum heat sink, which both possess high thermal conductivities. In order to achieve a low thermal contact resistance between the two materials, heat-conductive paste was applied on the polished metal surfaces before they were pressed on top of each other. The black color of the heat sink and the enlarged rippled surface ensure high radiative emission. Additionally, the large surface and the open structure also have a positive effect on the emission of heat via convection. In order to determine the heat which is released by the furnace, a heat flux sensor (Hukseflux HF01) was placed next to the module. The hot and the cold side temperatures T_h and T_c at the top and the bottom of the module were measure by thermocouples. For measurement above the fluid metal, the produced electrical power is extracted via Ag cables insulated with high temperature stable glass fibers.

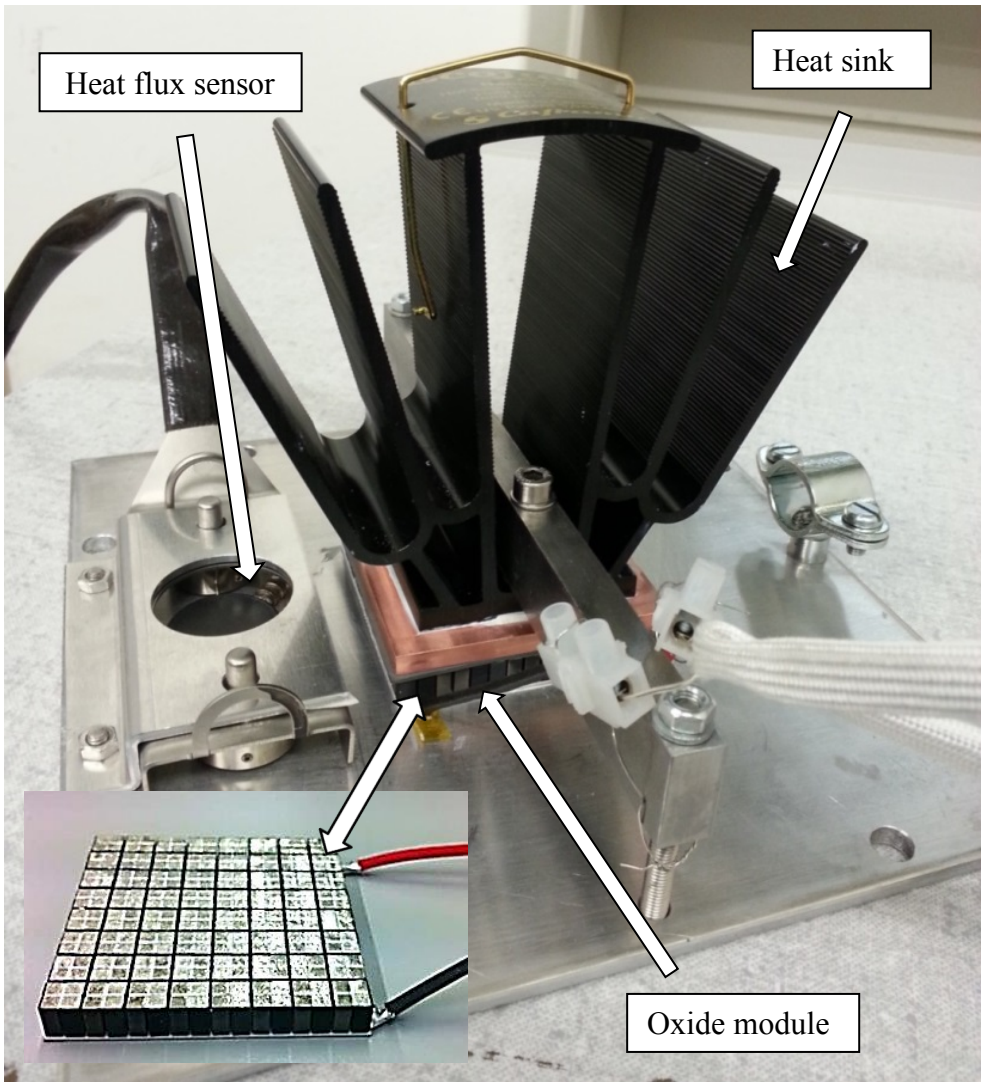

Figure A.4: Air-cooled thermoelectric demonstrator for the direct thermal coupling to the top-cover of the furnace or the mixed collection of radiative or conductive heat. In the inset the 256-leg oxide module (TES New-Energy) with a ground area of 6.5x6.5 cm^2 is presented. Apart from differing doping and larger number of legs, the module is similar to the self-made modules investigated throughout this thesis.

Heat emitted from the furnace was recovered in two different ways: by conductive coupling and by the mixed collection of radiative and convective heat. In the first case, the demonstrator was mechanically pressed on the flat polished surface of the top cover after applying heat conductive paste (Figure A.5 (a)). In the second case, the demonstrator was positioned about 1 m above the fluid metal, which was visible through an opening in the top cover (Figure A.5 (b)). Here, the demonstrator collected not only the radiative heat, which irradiated from the fluid metal, but also heat that was transported by hot air streaming through the hole. A good radiative coupling was achieved by covering the bottom side of the aluminum ground plate with graphite, which was substituted with dark soot-deposits accumulating during the measurement.

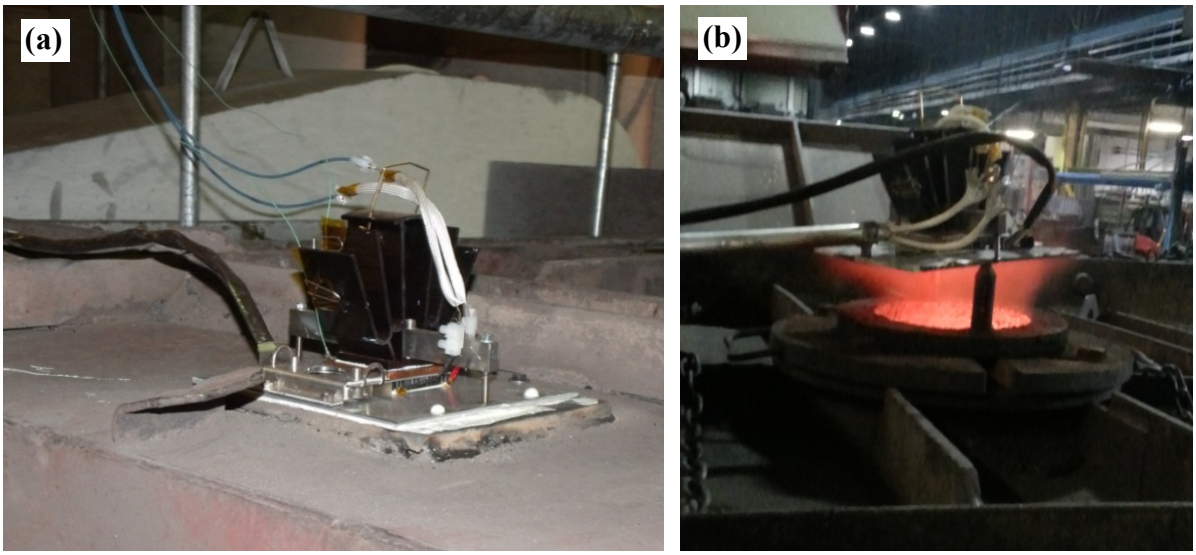

Figure A.5: Heat recovery on a casting furnace at the foundry vonRoll casting. Conductive coupling of the demonstrator by mechanical pressing on the surface of the top cover (a) and mixed heat transfer via radiation and convection through an opening in the top cover (b).

A.2.3 Results

Heat was recovered on the top cover of an induction furnace during a complete melting cycle, while the demonstrator was mechanically connected with the top cover to collect conductive heat. In Figure A.6 (a) the temperature $T_{h,HF}$ measured by the heatflux sensor, as well as the recorded hot and cold side temperature T_h and T_c of the module, are presented as a function of time. The temperature depends on the progress of the melting cycle and the position of the top cover (partly opened or closed). At the beginning of the cycle, the temperature T_h was relatively small because the cover was open and cold solid metal was filled into the preheated furnace. Recording of the temperatures began at t = -113 min when the cast started melting and was hold at a relatively low energy-saving temperature to adapt to the time flow of the subsequent processing (Figure A.6 (a)). During the final melting process the temperature increased because the cover was mainly closed and the temperature of the cast increased. After reaching the correct composition, the cast was kept at constant temperature (between t = -30 min and t = 48 min) to be ready for subsequent processing. Finally, the furnace was emptying stepwise (t = 48 min) and accordingly the temperature of the closed top cover decreased with the stepwise decrease of the liquid-metal level. After removal of the fluid cast and filling with new cold metal, the temperature at the cover had a minimum value at t =208 min and finally increases again when the metal started melting. During emptying of the furnace, the temperature at the module decreased from T_h = 628 K = 355°C and T_c = 491 K = 118°C to T_h = 493 K = 220°C and T_c = 355 K = 82°C. A more detailed

analysis about the distribution of the temperature on the top cover, as well as typical temperature cycles can be found in Appendix B .

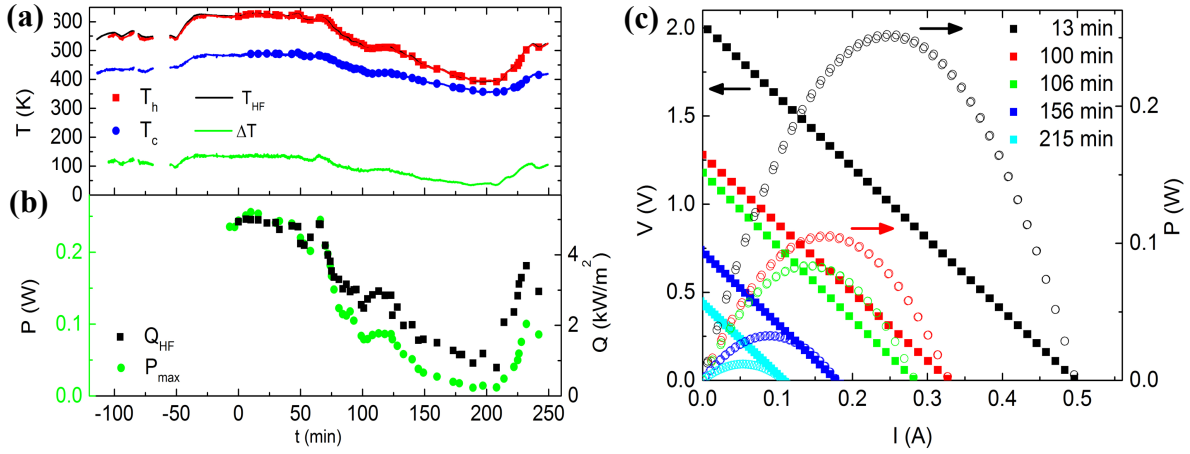

Figure A.6: Heat recovery via conductive coupling. Time dependent temperatures measured at the hot T_h and the cold side T_c of the module, the temperature difference $\Delta T = T_h - T_c$, and the temperature T_{HF} recorded by the heat flux sensor (a) and measured heat flux Q_{HF} and maximum power output P_{max} of the module (b). Output voltage (filled squares) and power output (open circles) as a function of output current I recorded at different times (c).

The temperatures, the heat flux Q_{HF} measured by the heat flux sensor, and the measured maximum power output P of the module are presented in Figure A.6 (b). A correlation between $\Delta T = T_h - T_c$, Q_{HF} and P is observable, as the heat flux in the module $Q = -\kappa' \frac{\Delta T}{\Delta x}$ and thus the power output $P = \eta Q$ are expected to be proportional to ΔT. Here, κ' is the thermal conductivity, and η the efficency of the entire module. The maximum power output $P_{max} = V_{OC}^2/4R_i$ was determined from the recorded current-voltage characteristics, where the slope describes the internal resistance $R_i = \Delta V/\Delta I$ and V_{OC} is the open circuit voltage. Current-voltage characteristics recorded at selected times t are presented in Figure A.6 (c). With progressing time, the furnace was emptied and the temperature and the heat flux decreased, which resulted in a significant reduction of V_{OC} and P_{max}. During conductive coupling, the module experienced a maximum temperature difference of $\Delta T \approx 140$ K, produced a maximum power of 256 mW, and showed a maximum efficiency of 1.3 % during the demonstration.

For the collection of radiative and convective heat, the demonstrator was positioned about 1 m above the liquid metal surface. In addition to the radiative heat transfer convection has to be considered because a stream of hot air containing glowing metallic dust was visible (cf. Figure A.5 (b)). The measured temperatures, the heat flux and the maximum power output are

presented in Figure A.7. In total a maximum temperature difference of $\Delta T \approx 207$ K and a maximum power output of 357 mW were achieved. The time-dependent change of the temperature is mainly determined by the distance between the demonstrator and the surface of the liquid metal. Additionally, an overall heating of the generator is observed. The temperatures T_h and T_c increase with time, while ΔT, Q and P stay constant. The increasing hot side temperature shows, that theoretically higher Q and P would be possible, if the heat sink would work more efficiently. More effective cooling could be reached by increasing the convective heat dissipation of the heat sink by active cooling with a ventilator, a further increase of the surface area or by the introduction of a cooling water system.

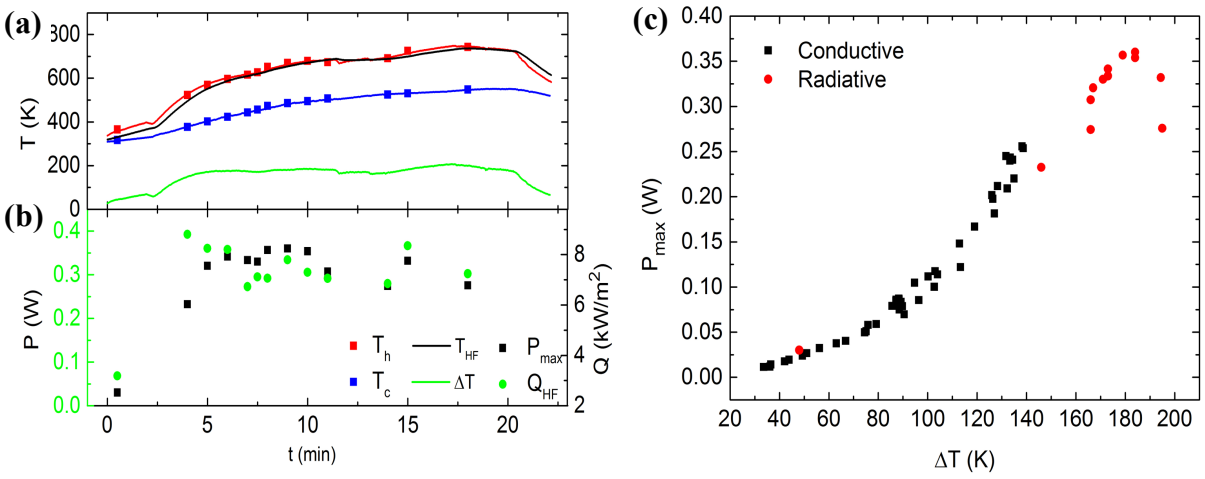

Figure A.7: Heat recovery via radiation and convection. Temperatures measured at the hot T_h and the cold side T_c of the module, the temperature difference $\Delta T = T_h - T_c$, and the temperature T_{HF} recorded by the heat flux sensor (a) and measured heat flux Q_{HF} and maximum power output P_{max} of the module (b). Larger power outputs and ΔT are reached for mixed radiative and convective heating (c).

A comparison of the obtained power outputs (Figure A.7 (c)) shows, that for mixed radiative and convective coupling larger ΔT and P are achieved. Although the conductive coupling is more direct, this difference is expected because larger amounts of heat are dissipated through the opening than through the insulated top cover.

A.2.4 Discussion

During normal operation, the opening in the top cover is closed to keep the heat within the furnace. Therefore, only the heat fluxes collected by conductive coupling are available for heat recovery during the regular production process. The amount of energy which can be recovered during a production day is estimated in the following. An expected power output can be assigned to every temperature $T_{HF} \approx T_h$, where $P(T_{HF})$ can be roughly approximated

by a parabola (cf. Figure A.8 (a)). Using this approximation, the performance of the demonstrator can be estimated for every measured temperature T_{HF} (cf. Figure A.8 (b)). Hence, the overall performance during the whole melting cycle can be estimated by integration of P over the time: $E_{tot} = \int P(T_{HF})\, dt$ = 2775 J = 0.77 Wh. Assuming that this six-hour melting cycle is repeated four times per day, the demonstrator recovers about 3 Wh per day. Referring to the area of the module, this corresponds to value of 0.7 kWh/m^2. If an area of 2 m^2 with similar temperatures is covered with air-cooled demonstrators, 1.5 kWh could be produced per day.

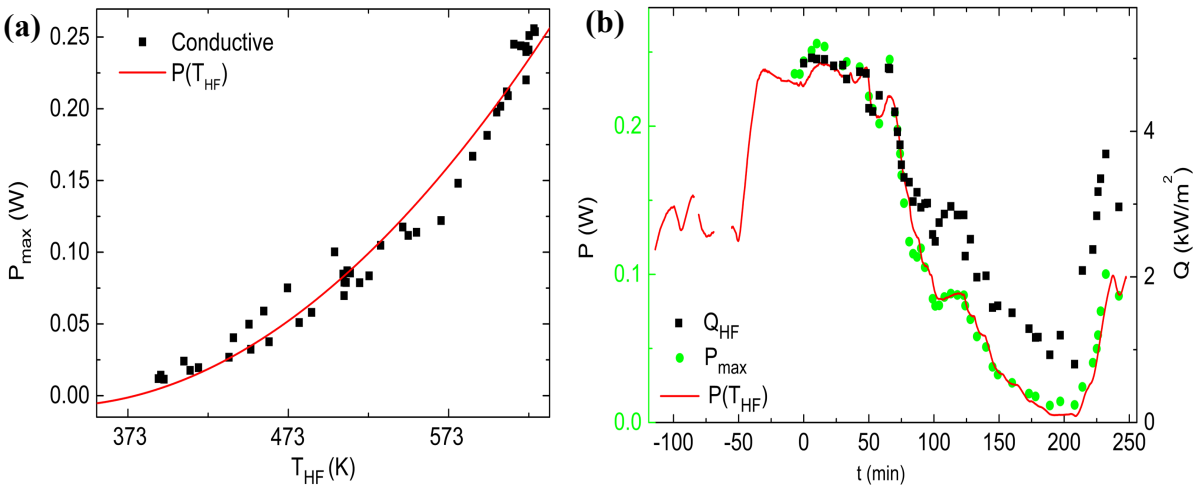

Figure A.8: (a) The dependency between the maximum power output and the temperature T_{HF} is approximated by a parabola $P(T_{HF})$. (b) Power output estimated via $P(T_{HF})$ during the complete metling cycle.

For the demonstration, oxide materials were used because the molten metal inside of the furnace is heated up to 1858 K and the operation temperatures achievable for radiative coupling were not known a priori. During the recovery, maximum temperatures of about T_{HF} = 627 K and 743 K were observed for conductive and mixed radiative and convective coupling. Due to these moderate operation temperatures and the small ΔT, the oxide modules lag far behind their potential. For an increase of the heat flux or the temperature difference to about $\Delta T \approx$ 670 K the oxide module would produce a power of 8.56 W (Figure A.9). This corresponds to 205 Wh per generator and day or 49 kWh/m^2 per day. However, such large heat fluxes are unrealistic for this kind of application because the heat should be kept within the furnace. In general, the application of renewable energies becomes economical when the costs fall below 1$/Watt, hence a brief discussion about the actual and the expected cost per watt for thermoelectric converters is given in Appendix C .

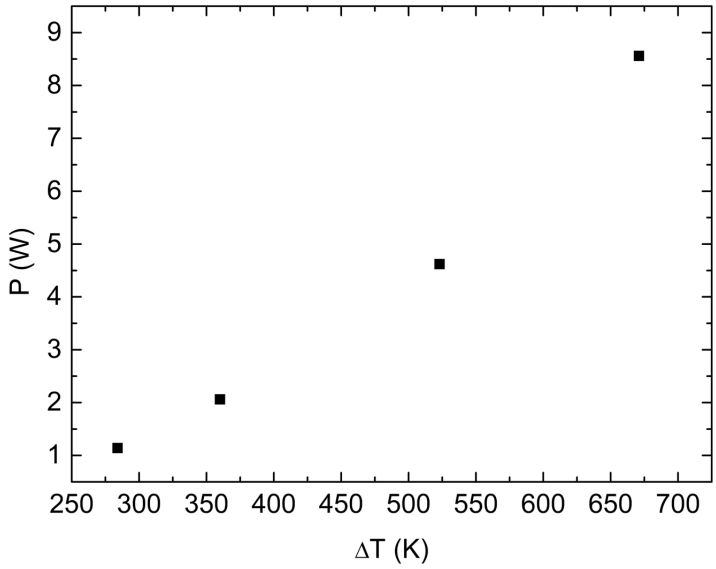

Figure A.9: Power output of the $Ca_{2.7}Bi_{0.3}Co_4O_{9+\delta}$-$CaMnO_{3-\delta}$-half-skeleton-modul with 256 legs and a ground area of 6.5x6.5cm² (TES-new energy).

A.2.5 Conclusion

The demonstrator produced maximum power outputs of about 256 mW and 357 mW for conductive and mixed radiative and convective coupling, respectively. During the tests a maximum conversion efficiency of 1.3% was reached. For conductive coupling, the maximum temperature difference and the highest hot side temperature were $\Delta T \approx 140$ K and $T_h \approx 630$ K, respectively. Considering the investigated melting cycle of the furnace, about 0.7 kWh/m² can be recovered per day. Due to the small ΔT, the oxide module stayed far behind their capabilities. For an increase of the heat flux or the temperature difference to about $\Delta T \approx 670$ K the oxide module would produce a power of 8.56 W, which corresponds to 49 kWh/m² per day. However, the demonstration shows that oxide thermoelectric converters can be successfully applied for industrial heat recovery. A reliable operation under harsh conditions, including strong temperature variations, mechanical vibrations due to the movement of the top-cover and a dusty atmosphere is demonstrated. While for a casting furnace, the energy efficiency is easier and more efficiently improved by a better insulation, the demonstrated properties are a good basis for a successful application in, e.g., the automotive industry or in a solid oxide fuel cell, where the generation of unused heat cannot be avoided.

B Quantification of heat fluxes in the foundry vonRoll casting[k]

Here, the temperatures and heat fluxes on the induction furnaces in the foundry vonRoll casting are discussed because these quantities strongly influence the efficiency of thermoelectric modules. The melting furnaces at vonRoll casting (Figure B.1 (a)) are continuously operated during the week, while a gas burner keeps them at relatively high temperature during weekends to prevent corrosion. During the industrial production process, metals are molten in the oven, the cast is removed (Figure B.1 (b)), and the oven is refilled (Figure B.1 (c)) periodically, which leads to varying temperatures and fluxes at the top cover of the furnace.

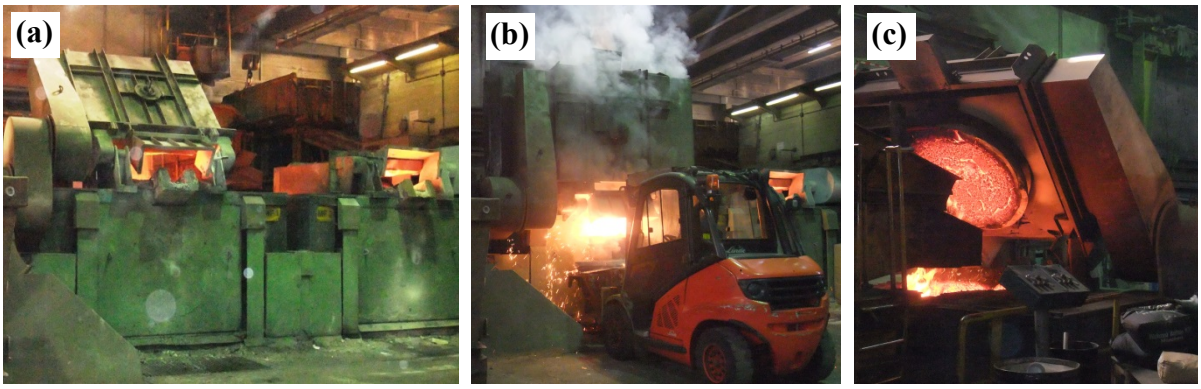

Figure B.1: (a) Induction furnaces in the foundry vonRoll casting. The top cover of the left one is open, while the one of the right furnace is closed. (b) Tilting of the complete furnace during removal of the molten metal. (c) Furnace with open top cover during filling with cold metal.

The recorded infrared image reveals the strongly inhomogeneous temperature (Figure B.2 (a)). The inhomogeneity results from the construction of the furnace and top cover. While the metal is heated in a round-shaped furnace chamber with two opening for deslagging and emptying at the upper edge, the top cover is square-shaped and its top and bottom view are presented in Figure B.2 (b) and (c). In order to track the temperature variations during a full production day, the top cover was equipped with eight thermocouples (positions marked in Figure B.2 (b)). Temperatures were recorded every 10 seconds and averaged over intervals of 2 minutes.

[k] Partly adapted from: Saucke, G., Moser, D., Weidenkaff, A.: Cost-efficient and reliable thermoelectric converters for industrial waste heat recovery - Jahresbericht 2011. BFE - Bundesamt für Energie (2011); and Saucke, G., Weidenkaff, A.: Cost-efficient and reliable thermoelectric converters for industrial waste heat recovery - Jahresbericht 2012. BFE - Bundesamt für Energie (2012).

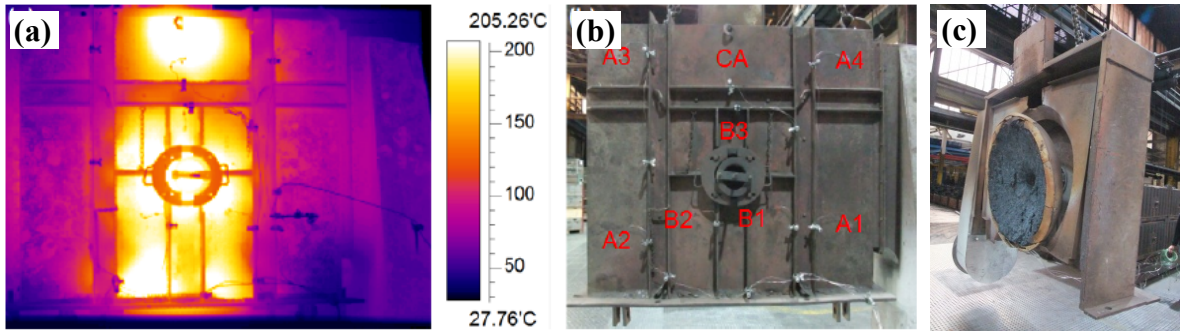

Figure B.2: (a) Inhomogeneous temperature distribution on the top-cover on the induction furnace in the foundry vonRoll casting recorded using an infrared camera. (b) Top cover equipped with thermocouples for time dependent temperature measurements. (c) Bottom view of the top cover.

The temperatures vary strongly with time (Figure B.3 (a)). During the production day, the furnace ran through four melting cycles. During a melting cycle, cold metals are filled in the preheated furnace, resulting in minimum T at the top cover. During the melting process T increases and finally decreases again while the liquid metal is removed successively. The histogram in Figure B.3 (b) illustrates the total time that a given temperature was available at the top cover at position CA. Based on the measured temperature, the heat flux

$$\dot{Q} = h_{conv}(T_s - T_0) + \epsilon\sigma_B T_s^4 \tag{45}$$

released from the top cover by radiation and convection can be estimated. Here, $h_{conv} = 5$ W/m^{2}K is the heat transfer coefficient, $\epsilon = 1$ the emissivity assumed for the dark dusty surface, σ_B the Stephan-Boltzmann constant, T_s the surface temperature and $T_0 = 20$°C the temperature of the surroundings. Integration over time reveals that during a day a heat amount of $Q = 346$ MJ/m^2 is lost. The measured maximum temperature exceeds 350°C. Hence, the application of conventional Bi_2Te_3-modules is problematic [13].

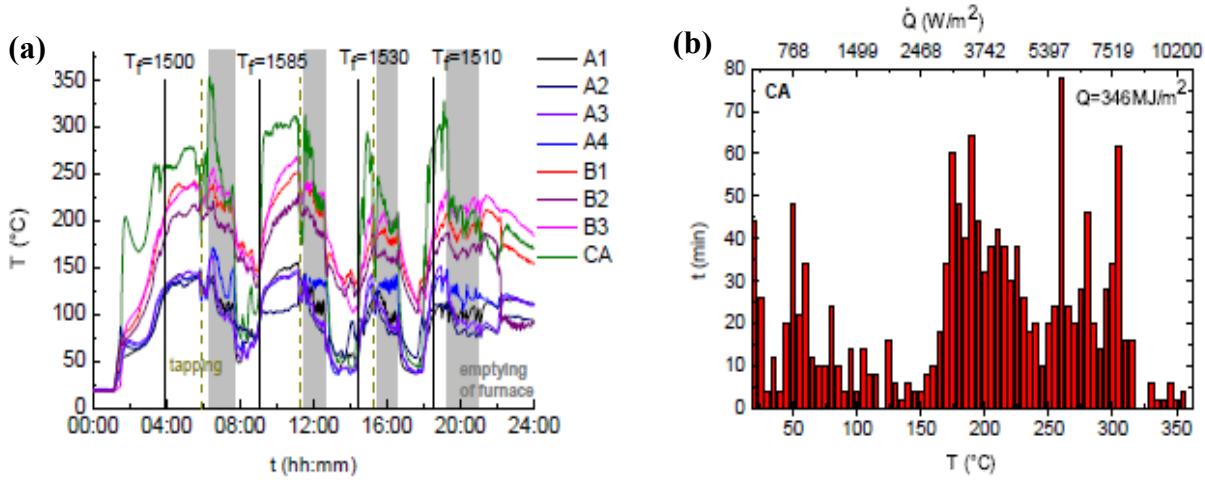

Figure B.3: (a) Variation of the temperature at different positions (cf. Figure B.2 (b)) of the top cover. Temperatures inside of the furnace T_f are indicated and the interval in which the furnace was emptied successively are marked in grey. (b) Time t each temperature was measured at position CA. The corresponding heat flux was determined by Equation (45). Integration reveals daily heat losses of Q =346 MJ/m².

C Potential of oxide converters for a widespread application[1]

The sales price of the oxide-base converters with a ground area of 6.5x6.5 cm^2 and a maximum power output of 8.55 W at $\Delta T \approx 670$ K [215] lies around 302 $ which corresponds to about 35 $/W. In contrast, Bi_2Te_3-based thermoelectric converters with ground areas of 5.6x5.6 cm^2 work with efficiencies of about 6.3 % and produce a maximum power of 19.3 W at $\Delta T \approx 270$ K (converter TEHP1-12656-0.3 from [216]). For large quantities above 10000 pieces the selling prices reduces to 18 $ per piece. This corresponds to about 0.93US$/W. Tin telluride based thermoelectric module can work at larger temperature up to 873 K. For $\Delta T \approx 507$ K an efficiency of 7 % and a power output of 14.8 W are reached by a converter with an area of 0.4x0.4 cm^2 (converter TELP1-0704-0.5 from [216]). This results in costs of 20 $ per piece for large quantities, which corresponds to 1.35$/W.

Compared to the oxide modules, the costs of the latter converters are much lower, although Te is one of the rarest elements. This large difference results from the learning-curve and the law of mass production because Bi_2Te_3-based converters were commercially distributed in large quantities for many years, while oxide-based converters became available just recently.

According to Karl Bücher's law of mass production the production costs can be decreased significantly if the amount of the product exceeds the break-even point ([217], S.240). The introduction of advanced production technologies increases the costs per piece for small quantities, but with increasing number a continuous decrease is observed that finally saturates at a lower cost level. The development of the solar industry shows how the costs of thermoelectric energy conversion might develop in the future. While in 1974 cost of around 27.5 CHF/W had to be paid, a significant decrease to about 0.9 CHF/W has been reached until 2007, with further possibilities for cost reduction available [218]. Cost can in general be decreased by a further technology development, the law of mass production and conventional advances in productivity. In recent years the effect of mass production led to a decrease of the costs by 15 - 20 % for a doubling of the installed power [218].

[1] Adapted from: Saucke, G., Weidenkaff, A., Populoh, S.: Kostengünstige und verlässliche thermoelektrische Konverter für die Nutzung industrieller Abwärme - Abschlussbericht. BFE - Bundesamt für Energie (2014).

A similar development is possible for thermoelectric converters. Especially, for oxide converters very small production cost seem possible because of (i) low costs of the abundant elements, (ii) low synthesis costs because purity and oxidation issues are of minor importance and the energy consumption during the synthesis can be kept low via soft chemistry methods. Additionally, nowadays only few oxide converters are produced and most of the manufacturing steps do heavily rely on manpower. Thus, a significant cost reduction should be achieved by automation techniques, which become economic for large quantities.

D Enhanced characterization of thermoelectric converters[m]

D.1 Determination of the power output at the same open circuit voltage

In Chapter 8 the power output of thermoelectric converters was determined. In order to detect small differences between the converters, all generators have to be measured precisely for the same temperature difference ΔT. The required accuracy is tricky to achieve with the experimental setup due to temperature fluctuations. Accordingly, the power outputs $P(V_{OV})$ recorded for independent measurements were correlated to the open circuit voltage V_{OC} measured at the same time. These $P(V_{OV})$ values were extrapolated to the same open circuit voltage for each converter (cf. arrow Figure D.1), where the slope of the $P(V_{OV})$ curves was determined from the three independent measurements of the module with $A_p/A_n = 1.01$.

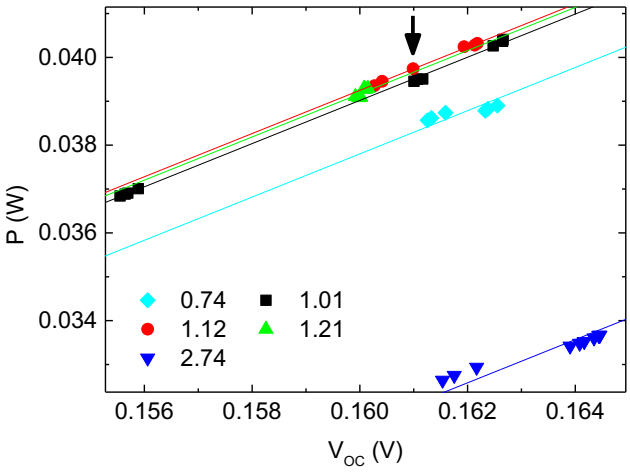

Figure D.1: Example for the determination of the power output via an extrapolation of the power to the same open circuit voltage V_{OC} (arrow), which should correspond to the same ΔT. The slope for the extrapolation was determined by the three independent measurements of the module with $A_p/A_n = 1.01$.

D.2 Analysis of the converter resistance

As presented in Figure 8.3 of Chapter 8, the measured room temperature resistances R^{exp} of the thermoelectric converters is smaller than the resistance R^{calc} calculated from the

[m] Adapted from: Saucke, G., Populoh, S., Thiel, P., Xie, W., Funahashi, R., Weidenkaff, A.: Compatibility approach for the improvement of oxide thermoelectric converters for industrial heat recovery applications. Journal of Applied Physics. 118, 035106 (2015) – Supplementary material.

resistivities and dimensions of the p- and n-type legs. This difference reveals a non-realistic negative contact resistance, which means that the resistivity of the legs themselves decreased during converter fabrication. A deeper understanding can be achieved by a fit of R^{exp} via Equation (44), which determines the actual electrical conductivities of both materials in the converter. The electrical conductivity extracted from the fit reveals that the conductivity of the p-type leg σ_p decreased by 11 % during the module fabrication process, while the one of the n-type material is constant. This modification may result from a change of the oxygen stoichiometry [107], the orientation of the plate-like $[Ca_2CoO_{3-\delta}][CoO_2]_{1.62}$ particles [151, 219] or the density due to the hot-pressing (1133K for 5h with a pressure of 6.2 MPa) of the module.

D.3 Estimation of radiative losses

In addition to uncertainties resulting from the temperature measurements, radiative and convective losses on the surfaces of the thermoelectric legs can lead to further uncertainties in the determination of the heat flow. While the convective contribution within the module is small, for T_h radiation from the outer surfaces of the legs leads to an additional heat flow of $Q^{Rad} = 3.4$ mW. For the calculation, the Stefan-Boltzmann law was applied using the measured room temperature emissivities $\epsilon_n = 0.82$ and $\epsilon_p = 0.89$, which were measured between 473 - 573 K. As this additional heat is also entering the legs at the hot side, this leads to an overestimation of η_{p+n} by about 8 %. However, in a device with more legs and a higher packing density it gets negligible.

E Electrical conductivity of the Co_3O_4 impurity phase[n]

Chapter 7 discusses the thermoelectric properties of $[Ca_2CoO_{3-\delta}][CoO_2]_{1,62}$ as a function of the Co/Ca ratio and Co_3O_4 inclusions. The application of the effective medium model allows separating of these two effects when the properties of the bulk material are known. The

[n] Adapted from: Büttner, G., Populoh, S., Xie, W., Trottmann, M., Hertrampf, J., Döbeli, M., Karvonen, L., Songhak, Y., Thiel, P., Niewa, R., Weidenkaff, A.: Thermoelectric properties of $[Ca_2CoO_{3-\delta}][CoO_2]_{1.62}$ as a function of Co/Ca ratio and Co_3O_4 inclusions. submitted. (2016).

effective medium calculations are based on the bulk properties of the pure $[Ca_2CoO_{3-\delta}][CoO_2]_{1,62}$ sample and literature values for the small Co_3O_4 impurities. A comparison of the electrical conductivity of the misfit-layered cobalt oxide with elemental formula $Ca_3Co_{3.92}O_{9+\delta}$, and the electrical conductivities reported for different Co_3O_4 samples [197, 201, 220] reveals that the conductivity of Co_3O_4 is about 2-3 magnitudes smaller than the one of the misfit-layered oxide (Figure E.1). The Co_3O_4 literature values are in good agreement with each other, and the data "Co_3O_4 Sahoo 2013*" with particle sizes of 200 - 400 nm [197] were used for the calculation of the effective electrical resistivity in Chapter 7.

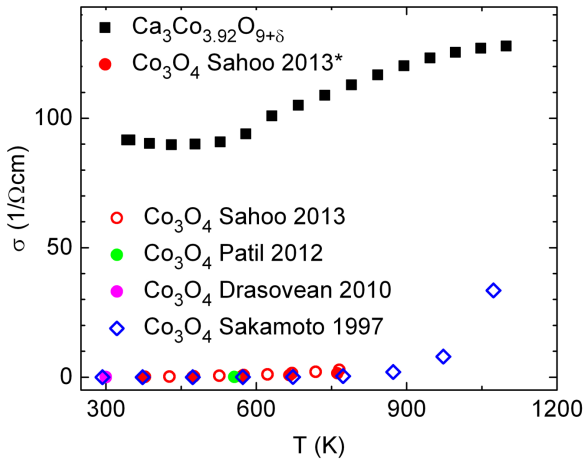

Figure E.1: Electrical conductivity of $Ca_3Co_{3.92}O_{9+\delta}$, and Co_3O_4. The Co_3O_4 data were recorded using thin film (circles) [197, 201, 220] and dense bulk samples (diamonds) [221]. The data "Co_3O_4 Sahoo 2013*" with particle sizes of 200 - 400 nm [197] were used for the calculation of the effective electrical resistivity.

Literature

1. International Energy Agency: World energy outlook 2014 Factsheet. International Energy Agency (2014)

2. Bell, L.E.: Cooling, heating, generating power, and recovering waste heat with thermoelectric systems. Science. 321, 1457–1461 (2008). doi:10.1126/science.1158899

3. Fleurial, J.-P.: Thermoelectric power generation materials: Technology and application opportunities. JOM. 61, 79–85 (2009). doi:10.1007/s11837-009-0057-z

4. Karni, J.: Solar energy: The thermoelectric alternative. Nat. Mater. 10, 481–482 (2011). doi:10.1038/nmat3057

5. Kraemer, D., Poudel, B., Feng, H.-P., Caylor, J.C., Yu, B., Yan, X., Ma, Y., Wang, X., Wang, D., Muto, A., McEnaney, K., Chiesa, M., Ren, Z., Chen, G.: High-performance flat-panel solar thermoelectric generators with high thermal concentration. Nat. Mater. 10, 532–538 (2011). doi:10.1038/nmat3013

6. Tomeš, P., Suter, C., Trottmann, M., Steinfeld, A., Weidenkaff, A.: Thermoelectric oxide modules tested in a solar cavity-receiver. J. Mater. Res. 26, 1975–1982 (2011). doi:10.1557/jmr.2011.125

7. Tomeš, P., Trottmann, M., Suter, C., Aguirre, M.H., Steinfeld, A., Haueter, P., Weidenkaff, A.: Thermoelectric Oxide Modules (TOMs) for the Direct Conversion of Simulated Solar Radiation into Electrical Energy. Materials. 3, 2801–2814 (2010). doi:10.3390/ma3042801

8. Zebarjadi, M., Esfarjani, K., Dresselhaus, M.S., Ren, Z.F., Chen, G.: Perspectives on thermoelectrics: from fundamentals to device applications. Energy Environ. Sci. 5, 5147–5162 (2012). doi:10.1039/C1EE02497C

9. Dresselhaus, M.S., Chen, G., Tang, M.Y., Yang, R.G., Lee, H., Wang, D.Z., Ren, Z.F., Fleurial, J.-P., Gogna, P.: New Directions for Low-Dimensional Thermoelectric Materials. Adv. Mater. 19, 1043–1053 (2007). doi:10.1002/adma.200600527

10. Abdellahi, M., Bahmanpour, M., Bahmanpour, M.: Modeling Seebeck coefficient of $Ca_{3-x}M_xCo_4O_9$ (M=Sr, Pr, Ga, Ca, Ba, La, Ag) thermoelectric ceramics. Ceram. Int. 41, 345–352 (2015). doi:10.1016/j.ceramint.2014.08.077

11. Kim, S.I., Lee, K.H., Mun, H.A., Kim, H.S., Hwang, S.W., Roh, J.W., Yang, D.J., Shin, W.H., Li, X.S., Lee, Y.H., Snyder, G.J., Kim, S.W.: Dense dislocation arrays embedded in grain boundaries for high-performance bulk thermoelectrics. Science. 348, 109–114 (2015). doi:10.1126/science.aaa4166

12. Venkatasubramanian, R., Siivola, E., Colpitts, T., O'Quinn, B.: Thin-film thermoelectric devices with high room-temperature figures of merit. Nature. 413, 597–602 (2001). doi:10.1038/35098012

13. Brostow, W., Datashvili, T., Hagg Lobland, H.E., Hilbig, T., Su, L., Vinado, C., White, J.: Bismuth telluride-based thermoelectric materials: Coatings as protection against thermal cycling effects. J. Mater. Res. 27, 2930–2936 (2012). doi:10.1557/jmr.2012.335

14. Gałązka, K., Populoh, S., Sagarna, L., Karvonen, L., Xie, W., Beni, A., Schmutz, P., Hulliger, J., Weidenkaff, A.: Phase formation, stability, and oxidation in (Ti,Zr,Hf)NiSn half-Heusler compounds. Phys. Status Solidi A. 211, 1259–1266 (2014). doi:10.1002/pssa.201300209

15. Populoh, S., Brunko, O.C., Gałązka, K., Xie, W., Weidenkaff, A.: Half-Heusler (TiZrHf)NiSn Unileg Module with High Powder Density. Materials. 6, 1326–1332 (2013). doi:10.3390/ma6041326

16. Weidenkaff, A., Aguirre, M.H., Bocher, L., Trottmann, M., Tomes, P., Robert, R.: Development of Perovskite-type Cobaltates and Manganates for Thermoelectric Oxide Modules. J. Korean Ceram. Soc. 47, 47–53 (2010). doi:10.4191/KCERS.2010.47.1.047

17. Yan, X., Liu, W., Wang, H., Chen, S., Shiomi, J., Esfarjani, K., Wang, H., Wang, D., Chen, G., Ren, Z.: Stronger phonon scattering by larger differences in atomic mass and size in p-type half-Heuslers $Hf_{1-x}Ti_xCoSb_{0.8}Sn_{0.2}$. Energy Environ. Sci. 5, 7543–7548 (2012). doi:10.1039/C2EE21554C

18. Ohta, M., Biswas, K., Lo, S.-H., He, J., Chung, D.Y., Dravid, V.P., Kanatzidis, M.G.: Enhancement of Thermoelectric Figure of Merit by the Insertion of MgTe Nanostructures in p-type PbTe Doped with Na_2Te. Adv. Energy Mater. 2, 1117–1123 (2012). doi:10.1002/aenm.201100756

19. Wang, S., Tan, X., Tan, G., She, X., Liu, W., Li, H., Liu, H., Tang, X.: The realization of a high thermoelectric figure of merit in Ge-substituted β-Zn_4Sb_3 through band structure modification. J. Mater. Chem. 22, 13977–13985 (2012). doi:10.1039/C2JM30906H

20. Leszczynski, J., Wojciechowski, K.T., Malecki, A.L.: Studies on thermal decomposition and oxidation of $CoSb_3$. J. Therm. Anal. Calorim. 105, 211–222 (2011). doi:10.1007/s10973-011-1461-5

21. Zhao, D., Tian, C., Tang, S., Liu, Y., Chen, L.: High temperature oxidation behavior of cobalt triantimonide thermoelectric material. J. Alloys Compd. 504, 552–558 (2010). doi:10.1016/j.jallcom.2010.05.160

22. Sadia, Y., Gelbstein, Y.: Silicon-Rich Higher Manganese Silicides for Thermoelectric Applications. J. Electron. Mater. 41, 1504–1508 (2012). doi:10.1007/s11664-012-1936-6

23. Brown, S.R., Kauzlarich, S.M., Gascoin, F., Snyder, G.J.: $Yb_{14}MnSb_{11}$: New High Efficiency Thermoelectric Material for Power Generation. ChemInform. 37, (2006). doi:10.1002/chin.200625011

24. Joshi, G., Lee, H., Lan, Y., Wang, X., Zhu, G., Wang, D., Gould, R.W., Cuff, D.C., Tang, M.Y., Dresselhaus, M.S., Chen, G., Ren, Z.: Enhanced Thermoelectric Figure-of-

Merit in Nanostructured p-type Silicon Germanium Bulk Alloys. Nano Lett. 8, 4670–4674 (2008). doi:10.1021/nl8026795

25. Fergus, J.W.: Oxide materials for high temperature thermoelectric energy conversion. J. Eur. Ceram. Soc. 32, 525–540 (2012). doi:10.1016/j.jeurceramsoc.2011.10.007

26. Haxel, G.B., Hedrick, J.B., Orris, G.J.: Rare Earth Elements - Critical Resources for High Technology | USGS Fact Sheet 087-02. (2002)

27. Lu, N., Ferguson, I.: III-nitrides for energy production: photovoltaic and thermoelectric applications. Semicond. Sci. Technol. 28, 074023 (2013). doi:10.1088/0268-1242/28/7/074023

28. Shikano, M., Funahashi, R.: Electrical and thermal properties of single-crystalline $(Ca_2CoO_3)_{0.7}CoO_2$ with a $Ca_3Co_4O_9$ structure. Appl. Phys. Lett. 82, 1851 (2003). doi:10.1063/1.1562337

29. Van Nong, N., Pryds, N., Linderoth, S., Ohtaki, M.: Enhancement of the thermoelectric performance of p-Type layered oxide $Ca_3Co_4O_{9+\delta}$ through heavy doping and metallic nanoinclusions. Adv. Mater. 23, 2484–2490 (2011). doi:10.1002/adma.201004782

30. Thiel, P., Eilertsen, J., Populoh, S., Saucke, G., Döbeli, M., Shkabko, A., Sagarna, L., Karvonen, L., Weidenkaff, A.: Influence of tungsten substitution and oxygen deficiency on the thermoelectric properties of $CaMnO_{3-\delta}$. J. Appl. Phys. 114, 243707 (2013). doi:10.1063/1.4854475

31. Urata, S., Funahashi, R., Mihara, T., Kosuga, A., Sodeoka, S., Tanaka, T.: Power Generation of a p-Type $Ca_3Co_4O_9$/n-Type $CaMnO_3$ Module. Int. J. Appl. Ceram. Technol. 4, 535–540 (2007). doi:10.1111/j.1744-7402.2007.02173.x

32. Nemir, D., Beck, J.: On the Significance of the Thermoelectric Figure of Merit Z. J. Electron. Mater. 39, 1897–1901 (2010). doi:10.1007/s11664-009-1060-4

33. Nolas, G.S., Sharp, J., Goldsmid, H.J.: Thermoelectrics: basic principles and new materials developments. Springer, Berlin ; London (2001)

34. Tritt, T.M.: Thermal Conductivity: Theory, Properties, and Applications. Springer Science & Business Media (2004)

35. Snyder, G.J., Toberer, E.S.: Complex thermoelectric materials. Nat. Mater. 7, 105–114 (2008). doi:10.1038/nmat2090

36. Toberer, E.S., Zevalkink, A., Snyder, G.J.: Phonon engineering through crystal chemistry. J. Mater. Chem. 21, 15843 (2011). doi:10.1039/c1jm11754h

37. Wu, L., Meng, Q., Jooss, C., Zheng, J.-C., Inada, H., Su, D., Li, Q., Zhu, Y.: Origin of Phonon Glass–Electron Crystal Behavior in Thermoelectric Layered Cobaltate. Adv. Funct. Mater. 23, 5728–5736 (2013). doi:10.1002/adfm.201301098

38. Nolas, G.S., Poon, J., Kanatzidis, M.: Recent Developments in Bulk Thermoelectric Materials. MRS Bull. 31, 199–205 (2006). doi:10.1557/mrs2006.45

39. Yu, J.-K., Mitrovic, S., Tham, D., Varghese, J., Heath, J.R.: Reduction of thermal conductivity in phononic nanomesh structures. Nat. Nanotechnol. 5, 718–721 (2010). doi:10.1038/nnano.2010.149

40. Biswas, K., He, J., Blum, I.D., Wu, C.-I., Hogan, T.P., Seidman, D.N., Dravid, V.P., Kanatzidis, M.G.: High-performance bulk thermoelectrics with all-scale hierarchical architectures. Nature. 489, 414–418 (2012). doi:10.1038/nature11439

41. Pichanusakorn, P., Bandaru, P.: Nanostructured thermoelectrics. Mater. Sci. Eng. R Rep. 67, 19–63 (2010). doi:10.1016/j.mser.2009.10.001

42. Rowe, D.M.: Thermoelectrics handbook: Macro to Nano. Taylor & Francis, CRC Press., Boca Raton (2006)

43. Heikes, R.R., Ure, R.W.: Thermoelectricity: science and engineering. Interscience Publishers (1961)

44. Chaikin, P.M., Beni, G.: Thermopower in the correlated hopping regime. Phys. Rev. B. 13, 647–651 (1976). doi:10.1103/PhysRevB.13.647

45. Koshibae, W., Tsutsui, K., Maekawa, S.: Thermopower in cobalt oxides. Phys. Rev. B. 62, 6869–6872 (2000). doi:10.1103/PhysRevB.62.6869

46. Mott, N.F.: Electrons in disordered structures. Adv. Phys. 16, 49–144 (1967). doi:10.1080/00018736700101265

47. Emin, D.: Polarons. Cambridge University Press (2013)

48. Wang, Y., Sui, Y., Su, W.: High temperature thermoelectric characteristics of $Ca_{0.9}R_{0.1}MnO_3$ (R=La,Pr,...,Yb). J. Appl. Phys. 104, 093703 (2008). doi:10.1063/1.3003065

49. Anderson, P.W.: Absence of Diffusion in Certain Random Lattices. Phys. Rev. 109, 1492–1505 (1958). doi:10.1103/PhysRev.109.1492

50. Cutler, M., Mott, N.F.: Observation of Anderson Localization in an Electron Gas. Phys. Rev. 181, 1336–1340 (1969). doi:10.1103/PhysRev.181.1336

51. Mahan, G.D., Sofo, J.O.: The best thermoelectric. Proc. Natl. Acad. Sci. 93, 7436–7439 (1996)

52. Heremans, J.P., Wiendlocha, B., Chamoire, A.M.: Resonant levels in bulk thermoelectric semiconductors. Energy Environ. Sci. 5, 5510–5530 (2012). doi:10.1039/C1EE02612G

53. Wilson, A.H.: The Theory of Metals. I. Proc. R. Soc. Lond. Ser. Contain. Pap. Math. Phys. Character. 138, 594–606 (1932)

54. Jonker, G.H.: Application of combined conductivity and Seebeck-effect plots for analysis of semiconductor properties. Philips Res Rep. 23, 131–138 (1986)

55. Zhu, Q., Hopper, E.M., Ingram, B.J., Mason, T.O.: Combined Jonker and Ioffe Analysis of Oxide Conductors and Semiconductors. J. Am. Ceram. Soc. 94, 187–193 (2011). doi:10.1111/j.1551-2916.2010.04047.x

56. Schrade, M., Norby, T., Finstad, T.G.: Hall effect measurements on thermoelectric $Ca_3Co_4O_9$: On how to determine the charge carrier concentration in strongly correlated misfit cobaltites. J. Appl. Phys. 117, 205103 (2015). doi:10.1063/1.4921861

57. Snyder, G., Ursell, T.: Thermoelectric Efficiency and Compatibility. Phys. Rev. Lett. 91, 148301 (2003). doi:10.1103/PhysRevLett.91.148301

58. Rowe, D.M., CRC Press.: Thermoelectrics handbook macro to nano-structured materials - Chapter 9. Taylor & Francis, Boca Raton, FL (2005)

59. Snyder, G.J.: Thermoelectrics handbook: Macro to Nano - Chapter 9. Taylor & Francis, CRC Press., Boca Raton (2006)

60. Baranowski, L.L., Snyder, G.J., Toberer, E.S.: Effective thermal conductivity in thermoelectric materials. J. Appl. Phys. 113, 204904 (2013). doi:10.1063/1.4807314

61. Wijesekara, W., Rosendahl, L.: Expanding the reduced-current approach for thermoelectric generators to achieve higher volumetric power density. Phys. Status Solidi A. 591–599 (2015). doi:10.1002/pssa.201431335

62. Clingman, W.H.: Entropy production and optimum device design. Adv. Energy Convers. 1, 61–79 (1961). doi:10.1016/0365-1789(61)90008-X

63. Choi, S.-M., Lee, K.-H., Lim, C.-H., Seo, W.-S.: Oxide-based thermoelectric power generation module using p-type $Ca_3Co_4O_9$ and n-type $(ZnO)_7In_2O_3$ legs. Energy Convers. Manag. 52, 335–339 (2011). doi:10.1016/j.enconman.2010.07.005

64. Funahashi, R., Urata, S., Mizuno, K., Kouuchi, T., Mikami, M.: $Ca_{2.7}Bi_{0.3}Co_4O_9$/$La_{0.9}Bi_{0.1}NiO_3$ thermoelectric devices with high output power density. Appl. Phys. Lett. 85, 1036–1038 (2004). doi:doi:10.1063/1.1780593

65. Inagoya, A., Sawaki, D., Horiuchi, Y., Urata, S., Funahashi, R., Terasaki, I.: Thermoelectric module made of perovskite cobalt oxides with large thermopower. J. Appl. Phys. 110, 123712 (2011). doi:10.1063/1.3671070

66. Lim, C.-H., Choi, S.-M., Seo, W.-S., Park, H.-H.: A Power-Generation Test for Oxide-Based Thermoelectric Modules Using p-Type $Ca_3Co_4O_9$ and n-Type $Ca_{0.9}Nd_{0.1}MnO_3$ Legs. J. Electron. Mater. 41, 1247–1255 (2012). doi:10.1007/s11664-011-1868-6

67. Mele, P., Kamei, H., Yasumune, H., Matsumoto, K., Miyazaki, K.: Development of thermoelectric module based on dense $Ca_3Co_4O_9$ and $Zn_{0.98}Al_{0.02}O$ legs. Met. Mater. Int. 20, 389–397 (2014). doi:10.1007/s12540-014-2024-7

68. Reddy, E.S., Noudem, J.G., Hebert, S., Goupil, C.: Fabrication and properties of four-leg oxide thermoelectric modules. J. Phys. Appl. Phys. 38, 3751–3755 (2005). doi:10.1088/0022-3727/38/19/026

69. Funahashi, R., Mikami, M., Mihara, T., Urata, S., Ando, N.: A portable thermoelectric-power-generating module composed of oxide devices. J. Appl. Phys. 99, 066117 (2006). doi:10.1063/1.2180449

70. Funahashi, R., Urata, S.: Fabrication and Application of an Oxide Thermoelectric System. Int. J. Appl. Ceram. Technol. 4, 297–307 (2007). doi:10.1111/j.1744-7402.2007.02144.x

71. Mele, P., Matsumoto, K., Azuma, T., Kamesawa, K., Tanaka, S., Kurosaki, J.-I., Miyazaki, K.: Development of Al_2O_3-ZnO/$Ca_3Co_4O_9$ module for thermoelectric power generation. Mater. Res. Soc. Symp. Proc. 1166 N03-23, 223–228 (2009)

72. Matsubara, I., Funahashi, R., Takeuchi, T., Sodeoka, S., Shimizu, T., Ueno, K.: Fabrication of an all-oxide thermoelectric power generator. Appl. Phys. Lett. 78, 3627–3629 (2001). doi:10.1063/1.1376155

73. Noudem, J.G., Lemonnier, S., Prevel, M., Reddy, E.S., Guilmeau, E., Goupil, C.: Thermoelectric ceramics for generators. J. Eur. Ceram. Soc. 28, 41–48 (2008). doi:10.1016/j.jeurceramsoc.2007.05.012

74. Wang, H., McCarty, R., Salvador, J.R., Yamamoto, A., König, J.: Determination of Thermoelectric Module Efficiency: A Survey. J. Electron. Mater. 43, 2274–2286 (2014). doi:10.1007/s11664-014-3044-2

75. Funahashi, R.: Waste heat recovery using thermoelectric oxide materials. Sci. Adv. Mater. 3, 682–686 (2011). doi:10.1166/sam.2011.1200

76. Populoh, S., Trottmann, M., Brunko, O.C., Thiel, P., Weidenkaff, A.: Construction of a high temperature TEG measurement system for the evaluation of thermoelectric oxide modules. Funct. Mater. Lett. 06, 1340012 (2013). doi:10.1142/S1793604713400122

77. Hung, T.: Segmented thermoelectric oxide-based module, Technical University of Denmark, (2014)

78. Hung, L.T., Van Nong, N., Snyder, G.J., Viet, M.H., Balke, B., Han, L., Stamate, E., Linderoth, S., Pryds, N.: High performance p-type segmented leg of misfit-layered cobaltite and half-Heusler alloy. Energy Convers. Manag. 99, 20–27 (2015). doi:10.1016/j.enconman.2015.03.112

79. Masset, A.C., Michel, C., Maignan, A., Hervieu, M., Toulemonde, O., Studer, F., Raveau, B., Hejtmanek, J.: Misfit-layered cobaltite with an anisotropic giant magnetoresistance: $Ca_3Co_4O_9$. Phys. Rev. B. 62, 166–175 (2000). doi:10.1103/PhysRevB.62.166

80. Lambert, S., Leligny, H., Grebille, D.: Three forms of the misfit layered cobaltite $[Ca_2CoO_3]$ $[CoO_2]_{1.62}$: A 4D structural investigation. J. Solid State Chem. 160, 322–331 (2001). doi:10.1006/jssc.2001.9235

81. Klie, R.F., Qiao, Q., Paulauskas, T., Ramasse, Q., Oxley, M.P., Idrobo, J.C.: Examining the structure and bonding in complex oxides using aberration-corrected imaging and spectroscopy. Phys. Rev. B. 85, 054106 (2012). doi:10.1103/PhysRevB.85.054106

82. Koumoto, Kunihito, Terasaki, Ichiro, Funahashi, Rioji: Complex oxide material for potential thermoelectric applications. MRS Bull. 31, 206–210 (2006). doi:http://dx.doi.org/10.1557/mrs2006.46

83. Miyazaki, Y.: Crystal structure and thermoelectric properties of the misfit-layered cobalt oxides. Solid State Ion. 172, 463–467 (2004). doi:10.1016/j.ssi.2004.01.046

84. Jankovsky, O., Sedmidubsky, D., Sofer, Z., Simek, P., Hejtmanek, J.: Thermodynamic behavior of $Ca_3Co_{3.93+x}O_{9+\delta}$ ceramics. Ceram. - Silik. 56, 139–144 (2012)

85. Sedmidubský, D., Jakeš, V., Jankovský, O., Leitner, J., Sofer, Z., Hejtmánek, J.: Phase equilibria in Ca–Co–O system. J. Solid State Chem. 194, 199–205 (2012). doi:10.1016/j.jssc.2012.05.014

86. Woermann, E., Muan, A.: Phase equilibria in the system CaO-cobalt oxide in air. J. Inorg. Nucl. Chem. 32, 1455–1459 (1970). doi:10.1016/0022-1902(70)80631-5

87. Takeuchi, T., Kondo, T., Soda, K., Mizutani, U., Funahashi, R., Shikano, M., Tsuda, S., Yokoya, T., Shin, S., Muro, T.: Electronic structure and large thermoelectric power in $Ca_3Co_4O_9$. J. Electron Spectrosc. Relat. Phenom. 137–140, 595–599 (2004). doi:10.1016/j.elspec.2004.02.013

88. Takeuchi, T., Kondo, T., Kitao, T., Soda, K., Shikano, M., Funahashi, R., Mikami, M., Mizutani, U.: Electronic structure near the Fermi level in the Ca Co layered cobalt oxide. J. Electron Spectrosc. Relat. Phenom. 144–147, 849–852 (2005). doi:10.1016/j.elspec.2005.01.235

89. Takeuchi, T., Kondo, T., Takami, T., Takahashi, H., Ikuta, H., Mizutani, U., Soda, K., Funahashi, R., Shikano, M., Mikami, M., Tsuda, S., Yokoya, T., Shin, S., Muro, T.: Contribution of electronic structure to the large thermoelectric power in layered cobalt oxides. Phys. Rev. B. 69, 125410 (2004). doi:10.1103/PhysRevB.69.125410

90. Moser, D., Karvonen, L., Populoh, S., Trottmann, M., Weidenkaff, A.: Influence of the oxygen content on thermoelectric properties of $Ca_{3-x}Bi_xCo_4O_{9+\delta}$ system. Solid State Sci. 13, 2160–2164 (2011). doi:10.1016/j.solidstatesciences.2011.10.001

91. Lemal, S.: First-principles study of the electronic and thermoelectric properties of $Ca_3Co_4O_9$, (2013)

92. Landron, S., Lepetit, M.-B.: Importance of t_{2g}-e_g hybridization in transition metal oxides. Phys. Rev. B. 77, 125106 (2008). doi:10.1103/PhysRevB.77.125106

93. Soret, J., Lepetit, M.-B.: Electronic structure of the $Ca_3Co_4O_9$ compound from ab initio local interactions. Phys. Rev. B. 85, (2012). doi:10.1103/PhysRevB.85.165145

94. Singh, D.J., Kasinathan, D.: Thermoelectric Properties of Na x CoO2 and Prospects for Other Oxide Thermoelectrics. J. Electron. Mater. 36, 736–739 (2007). doi:10.1007/s11664-007-0154-0

95. Asahi, R., Sugiyama, J., Tani, T.: Electronic structure of misfit-layered calcium cobaltite. Phys. Rev. B. 66, 155103 (2002). doi:10.1103/PhysRevB.66.155103

96. Rébola, A., Klie, R., Zapol, P., Öğüt, S.: First-principles study of the atomic and electronic structures of misfit-layered calcium cobaltite $(Ca_2CoO_3)(CoO_2)_{1.62}$ using rational approximants. Phys. Rev. B. 85, 155132 (2012). doi:10.1103/PhysRevB.85.155132

97. Kawabata, A.: A self-consistent treatment of Anderson localization. Solid State Commun. 38, 823–825 (1981). doi:10.1016/0038-1098(81)90304-5

98. Krishnamurthy, H.R., Jayaprakash, C., Sarker, S., Wenzel, W.: Mott-Hubbard metal-insulator transition in nonbipartite lattices. Phys. Rev. Lett. 64, 950–953 (1990). doi:10.1103/PhysRevLett.64.950

99. Hsieh, Y.-C., Okazaki, R., Taniguchi, H., Terasaki, I.: Pseudogap Observed in the Charge Transport in the Thermoelectric Oxide $Ca_{3-x}Bi_xCo_4O_9$ Single Crystals. J. Phys. Soc. Jpn. 83, 054710 (2014). doi:10.7566/JPSJ.83.054710

100. Limelette, P., Hardy, V., Auban-Senzier, P., Jérome, D., Flahaut, D., Hébert, S., Frésard, R., Simon, C., Noudem, J., Maignan, A.: Strongly correlated properties of the thermoelectric cobalt oxide $Ca_3Co_4O_9$. Phys. Rev. B. 71, (2005). doi:10.1103/PhysRevB.71.233108

101. Sugiyama, J., Brewer, J.H., Ansaldo, E.J., Itahara, H., Dohmae, K., Xia, C., Seno, Y., Hitti, B., Tani, T.: A common behaviour of thermoelectric layered cobaltites: incommensurate spin density wave states in $[Ca_2Co_{4/3}Cu_{2/3}O_4]_{0.62}[CoO_2]$ and $[Ca_2CoO_3]_{0.62}[CoO_2]$. J. Phys. Condens. Matter. 15, 8619 (2003). doi:10.1088/0953-8984/15/49/031

102. Altin, S., Aksan, M.A., Bayri, A.: High temperature spin state transitions in misfit-layered $Ca_3Co_4O_9$. J. Alloys Compd. 587, 40–44 (2014). doi:10.1016/j.jallcom.2013.10.170

103. Sugiyama, J., Brewer, J.H., Ansaldo, E.J., Itahara, H., Dohmae, K., Seno, Y., Xia, C., Tani, T.: Hidden magnetic transitions in the thermoelectric layered cobaltite $[Ca_2CoO_3]_{0.62}[CoO_2]$. Phys. Rev. B. 68, 134423 (2003). doi:10.1103/PhysRevB.68.134423

104. Mizokawa, T., Tjeng, L.H., Lin, H.-J., Chen, C.T., Kitawaki, R., Terasaki, I., Lambert, S., Michel, C.: X-ray absorption study of layered Co oxides with a Co-O triangular lattice. Phys. Rev. B. 71, 193107 (2005). doi:10.1103/PhysRevB.71.193107

105. Yang, G., Ramasse, Q., Klie, R.F.: Direct measurement of charge transfer in thermoelectric $Ca_3Co_4O_9$. Phys. Rev. B. 78, 153109 (2008). doi:10.1103/PhysRevB.78.153109

106. Morita, Y., Poulsen, J., Sakai, K., Motohashi, T., Fujii, T., Terasaki, I., Yamauchi, H., Karppinen, M.: Oxygen nonstoichiometry and cobalt valence in misfit-layered cobalt oxides. J. Solid State Chem. 177, 3149–3155 (2004). doi:10.1016/j.jssc.2004.05.023

107. Schrade, M., Fjeld, H., Finstad, T.G., Norby, T.: Electronic Transport Properties of $[Ca_2CoO_{3-\delta}]_q[CoO_2]$. J. Phys. Chem. C. (2014). doi:10.1021/jp409581n

108. Shimoyama, J., Horii, S., Otzschi, K., Sano, M., Kishio, K.: Oxygen Nonstoichiometry in Layered Cobaltite $Ca_3Co_4O_y$. Jpn. J. Appl. Phys. 42, L194 (2003). doi:10.1143/JJAP.42.L194

109. Ling, C.D., Aivazian, K., Schmid, S., Jensen, P.: Structural investigation of oxygen non-stoichiometry and cation doping in misfit-layered thermoelectric $(Ca_2CoO_{3-x})(CoO_2)_\delta$, $\delta \approx 1.61$ $Ca_3Co_4O_9$. J. Solid State Chem. 180, 1446–1455 (2007). doi:10.1016/j.jssc.2007.02.016

110. Huang, Y., Zhao, B., Lin, S., Sun, Y.: Enhanced Thermoelectric Performance Induced by Misplaced Substitution in Layered $Ca_3Co_4O_9$. J. Phys. Chem. C. (2015). doi:10.1021/jp512012d

111. Huang, Y., Zhao, B., Ang, R., Lin, S., Huang, Z., Tan, S., Liu, Y., Song, W., Sun, Y.: Enhanced Thermoelectric Performance and Room-Temperature Spin-State Transition of Co^{4+} Ions in the $Ca_3Co_{4-x}Rh_xO_9$ System. J. Phys. Chem. C. 117, 11459–11470 (2013). doi:10.1021/jp400146y

112. Merino, J., McKenzie, R.H.: Transport properties of strongly correlated metals: A dynamical mean-field approach. Phys. Rev. B. 61, 7996–8008 (2000). doi:10.1103/PhysRevB.61.7996

113. Cheng, J., Sui, Y., Wang, Y., Wang, X., Su, W.: First-order phase transition characteristic of the high temperature metal–semiconductor transition in $[Ca_2CoO_3]_{0.62}[CoO_2]$. Appl. Phys. A. 94, 911–916 (2008). doi:10.1007/s00339-008-4849-8

114. Zhang, P., Luo, W., Crespi, V.H., Cohen, M.L., Louie, S.G.: Doping effects on the electronic and structural properties of CoO_2: An LSDA+U study. Phys. Rev. B. 70, 085108 (2004). doi:10.1103/PhysRevB.70.085108

115. Muguerra, H., Grebille, D.: Original disorder–order transition related to electronic and magnetic properties in the thermoelectric misfit phase $[Ca_2CoO_3][CoO_2]_{1.62}$. Acta Crystallogr. Sect. B. 64, 676–683 (2008). doi:10.1107/S0108768108030152

116. Liu, H., Yu, Z., Gu, Y., Chen, Y.: Effect of micro-structure on electrical transport properties in $Ca_3Co_4O_9$ ceramics. Rare Met. 30, 77–80 (2011). doi:10.1007/s12598-011-0242-4

117. Liu, H.Q., Zhao, X.B., Liu, F., Song, Y., Sun, Q., Zhu, T.J., Wang, F.P.: Effect of Gd-doping on thermoelectric properties of $Ca_3Co_4O_{9+\delta}$ ceramics. J. Mater. Sci. 43, 6933–6937 (2008). doi:10.1007/s10853-008-2990-6

118. Nag, A., Shubha, V.: Oxide thermoelectric materials: A structure-property relationship. J. Electron. Mater. 43, 962–977 (2014). doi:10.1007/s11664-014-3024-6

119. Pei, J., Chen, G., Lu, D.Q., Liu, P.S., Zhou, N.: Synthesis and high temperature thermoelectric properties of $Ca_{3.0-x-y}Nd_xNa_yCo_4O_{9+\delta}$. Solid State Commun. 146, 283–286 (2008). doi:10.1016/j.ssc.2008.03.012

120. Yao, Q., Wang, D.L., Chen, L.D., Shi, X., Zhou, M.: Effects of partial substitution of transition metals for cobalt on the high-temperature thermoelectric properties of $Ca_3Co_4O_{9+\delta}$. J. Appl. Phys. 97, 103905 (2005). doi:10.1063/1.1898443

121. Satake, A., Tanaka, H., Ohkawa, T., Fujii, T., Terasaki, I.: Thermal conductivity of the thermoelectric layered cobalt oxides measured by the Harman method. J. Appl. Phys. 96, 931–933 (2004). doi:10.1063/1.1753070

122. Rébola, A., Klie, R.F., Zapol, P., Öğüt, S.: Phonon and thermal transport properties of the misfit-layered oxide thermoelectric $Ca_3Co_4O_9$ from first principles. Appl. Phys. Lett. 104, 251910 (2014). doi:10.1063/1.4885389

123. Wang, Y., Sui, Y., Cheng, J., Wang, X., Su, W.: The thermal-transport properties of the $Ca_{3-x}Ag_xCo_4O_9$ system ($0 \leq x \leq 0.3$). J. Phys. Condens. Matter. 19, 356216 (2007). doi:10.1088/0953-8984/19/35/356216

124. Zhang, F.P., Zhang, X., Lu, Q.M., Zhang, J.X., Liu, Y.Q., Zhang, G.Z.: Preparation and high temperature thermoelectric properties of $Ca_{3-x}Ag_xCo_4O_{9+\delta}$ oxides. Solid State Ion. 201, 1–5 (2011). doi:10.1016/j.ssi.2011.07.023

125. Wang, D., Chen, L., Yao, Q., Li, J.: High-temperature thermoelectric properties of $Ca_3Co_4O_{9+\delta}$ with Eu substitution. Solid State Commun. 129, 615–618 (2004). doi:10.1016/j.ssc.2003.11.045

126. Nong, N.V., Liu, C.-J., Ohtaki, M.: High-temperature thermoelectric properties of late rare earth-doped $Ca_3Co_4O_{9+\delta}$. J. Alloys Compd. 509, 977–981 (2011). doi:10.1016/j.jallcom.2010.09.150

127. Liu, H.Q., Song, Y., Zhang, S.N., Zhao, X.B., Wang, F.P.: Thermoelectric properties of $Ca_{3-x}Y_xCo_4O_{9+\delta}$ ceramics. J. Phys. Chem. Solids. 70, 600–603 (2009). doi:10.1016/j.jpcs.2009.01.003

128. Delorme, F., Martin, C.F., Marudhachalam, P., Ovono Ovono, D., Guzman, G.: Effect of Ca substitution by Sr on the thermoelectric properties of $Ca_3Co_4O_9$ ceramics. J. Alloys Compd. 509, 2311–2315 (2011). doi:10.1016/j.jallcom.2010.10.209

129. Huang, Y., Zhao, B., Lin, S., Ang, R., Sun, Y.: Enhanced Thermoelectric Performance Induced by Cr Doping at Ca-Sites in $Ca_3Co_4O_9$ System. J. Am. Ceram. Soc. 97, 3589–3596 (2014). doi:10.1111/jace.13144

130. Altin, S., Bayri, A., Demirel, S., Aksan, M.A.: Thermal conductivity and magnetic properties of the b substituted $Ca_3Co_4O_9$. Curr. Appl. Phys. 14, 590–595 (2014). doi:10.1016/j.cap.2014.02.004

131. Wang, Y., Sui, Y., Wang, X., Su, W., Liu, X.: Enhanced high temperature thermoelectric characteristics of transition metals doped $Ca_3Co_4O_{9+\delta}$ by cold high-pressure fabrication. J. Appl. Phys. 107, 033708 (2010). doi:10.1063/1.3291125

132. Xu, L., Li, F., Wang, Y.: High-temperature transport and thermoelectric properties of $Ca_3Co_{4-x}Ti_xO_9$. J. Alloys Compd. 501, 115–119 (2010). doi:10.1016/j.jallcom.2010.04.055

133. Nong, N.V., Liu, C.-J., Ohtaki, M.: Improvement on the high temperature thermoelectric performance of Ga-doped misfit-layered $Ca_3Co_{4-x}Ga_xO_{9+\delta}$ (x=0, 0.05, 0.1, and 0.2). J. Alloys Compd. 491, 53–56 (2010). doi:10.1016/j.jallcom.2009.11.009

134. Kenfaui, D., Chateigner, D., Gomina, M., Noudem, J.G.: Texture, mechanical and thermoelectric properties of $Ca_3Co_4O_9$ ceramics. J. Alloys Compd. 490, 472–479 (2010). doi:10.1016/j.jallcom.2009.10.048

135. Kenfaui, D., Bonnefont, G., Chateigner, D., Fantozzi, G., Gomina, M., Noudem, J.G.: $Ca_3Co_4O_9$ ceramics consolidated by SPS process: Optimisation of mechanical and thermoelectric properties. Mater. Res. Bull. 45, 1240–1249 (2010). doi:10.1016/j.materresbull.2010.05.006

136. Feng, J., Wei, C., Xu, J.: Effects of doping metal ions on thermoelectric properties of $Ca_3Co_4O_9$. Kuei Suan Jen Hsueh Pao J. Chin. Ceram. Soc. 36, 1501–1504 (2008)

137. Han, L., Jiang, Y., Li, S., Su, H., Lan, X., Qin, K., Han, T., Zhong, H., Chen, L., Yu, D.: High temperature thermoelectric properties and energy transfer devices of $Ca_3Co_{4-x}Ag_xO_9$ and $Ca_{1-y}Sm_yMnO_3$. J. Alloys Compd. 509, 8970–8977 (2011). doi:10.1016/j.jallcom.2011.06.113

138. Lin, Y.-H., Lan, J., Shen, Z., Liu, Y., Nan, C.-W., Li, J.-F.: High-temperature electrical transport behaviors in textured $Ca_3Co_4O_9$-based polycrystalline ceramics. Appl. Phys. Lett. 94, 072107 (2009). doi:10.1063/1.3086875

139. Prevel, M., Reddy, E.S., Perez, O., Kobayashi, W., Terasaki, I., Goupil, C., Noudem, J.G.: Thermoelectric Properties of Sintered and Textured Nd-Substituted $Ca_3Co_4O_9$ Ceramics. Jpn. J. Appl. Phys. 46, 6533 (2007). doi:10.1143/JJAP.46.6533

140. Song, X., Chen, Y., Chen, S., Barbero, E., Thomas, E.L., Barnes, P.: Significant enhancement of electrical transport properties of thermoelectric $Ca_3Co_4O_{9+\delta}$ through Yb doping. Solid State Commun. 152, 1509–1512 (2012). doi:10.1016/j.ssc.2012.06.014

141. Xu, J., Wei, C., Jia, K.: Thermoelectric performance of textured $Ca_{3-x}Yb_xCo_4O_{9-\delta}$ ceramics. J. Alloys Compd. 500, 227–230 (2010). doi:10.1016/j.jallcom.2010.04.014

142. Lim, C.-H., Choi, S., Seo, W.-S.: High-temperature Thermoelectric Properties of the $Ca_{3-x}K_xCo_4O_9$ ($0 \leq x \leq 0.3$) System. J. Korean Phys. Soc. 57, 1054 (2010). doi:10.3938/jkps.57.1054

143. Lin, Y.-H., Nan, C.-W., Liu, Y., Li, J., Mizokawa, T., Shen, Z.: High-Temperature Electrical Transport and Thermoelectric Power of Partially Substituted $Ca_3Co_4O_9$-Based Ceramics. J. Am. Ceram. Soc. 90, 132–136 (2007). doi:10.1111/j.1551-2916.2006.01370.x

144. Lu, Q.M., Zhang, J.X., Zhang, Q.Y., Liu, Y.Q., Liu, D.M.: Improved Thermoelectric Properties of $Ca_{3-x}Ba_xCo_4O_9$ (x=0 0.4) Bulks by Sol-Gel and SPS Method. In: 25th International Conference on Thermoelectrics, 2006. ICT ’06. pp. 66–69 (2006)

145. Wang, Y., Xu, L., Sui, Y., Wang, X., Cheng, J., Su, W.: Enhanced electron correlation in rare-earth doped $Ca_3Co_4O_9$. Appl. Phys. Lett. 97, 062114 (2010). doi:10.1063/1.3479923

146. Rasekh, S., Torres, M.A., Constantinescu, G., Madre, M.A., Diez, J.C., Sotelo, A.: Effect of Cu by Co substitution on $Ca_3Co_4O_9$ thermoelectric ceramics. J. Mater. Sci. Mater. Electron. 24, 2309–2314 (2013). doi:10.1007/s10854-013-1094-5

147. Oide, Y., Miyazaki, Y., Ono, Y., Huang, X.Y., Kajitani, T.: Thermogravimetric Study and High-Temperature Thermoelectric Properties of $[Ca_2(Co_{1-x}A_x)O_3]_{0.62}CoO_2$. In: 25th International Conference on Thermoelectrics, 2006. ICT '06. pp. 402–405 (2006)

148. Fu, Y., Tang, X., Yang, J., Jian, H., Zhu, X., Sun, Y.: Preparation and Characterization of $Ca_3Co_4O_9$ Thin Films on Polycrystalline Al_2O_3 Substrates by Chemical Solution Deposition. J. Mater. Sci. Technol. 29, 13–16 (2013). doi:10.1016/j.jmst.2012.12.007

149. Huang, Y., Zhao, B., Lin, S., Song, W., Sun, Y.: Renormalized bands and low-temperature colossal thermopower induced by Ir doping in $Ca_3Co_4O_9$ system. J. Appl. Phys. 114, 093709 (2013). doi:10.1063/1.4820464

150. Pinitsoontorn, S., Lerssongkram, N., Harnwunggmoung, A., Kurosaki, K., Yamanaka, S.: Synthesis, mechanical and magnetic properties of transition metals-doped $Ca_3Co_{3.8}M_{0.2}O_9$. J. Alloys Compd. 503, 431–435 (2010). doi:10.1016/j.jallcom.2010.05.027

151. Saucke, G., Populoh, S., Vogel-Schäuble, N., Sagarna, L., Mogare, K., Karvonen, L., Weidenkaff, A.: Thermoelectric properties of Ru and In substituted misfit-layered $Ca_3Co_4O_9$. MRS Proc. 1543, 83–92 (2013). doi:10.1557/opl.2013.972

152. Huang, Y., Zhao, B., Ang, R., Lin, S., Huang, Z., Yin, L., Tan, S., Liu, Y., Song, W., Sun, Y.: Enhanced Electron Correlation in the In-doped Misfit-Layered Cobaltite $Ca_3Co_4O_9$ Ceramics. J. Am. Ceram. Soc. 96, 791–797 (2013). doi:10.1111/jace.12083

153. Science Notes - Periodic Table, http://sciencenotes.org/wp-content/uploads/2014/05/PeriodicTableOxidation-BW.pdf

154. Wang, Y., Sui, Y., Cheng, J., Wang, X., Su, W.: Comparison of the high temperature thermoelectric properties for Ag-doped and Ag-added $Ca_3Co_4O_9$. J. Alloys Compd. 477, 817–821 (2009). doi:10.1016/j.jallcom.2008.10.162

155. Sakka, S.: Handbook of sol-gel science and technology. 1. Sol-gel processing. Springer Science & Business Media (2005)

156. Livage, J., Sanchez, C.: Sol-gel chemistry. J. Non-Cryst. Solids. 145, 11–19 (1992). doi:10.1016/S0022-3093(05)80422-3

157. Chai, Y.L., Ray, D.T., Chen, G.J., Chang, Y.H.: Synthesis of $La_{0.8}Sr_{0.2}Co_{0.5}Ni_{0.5}O_{3-\delta}$ thin films for high sensitivity CO sensing material using the Pechini process. J. Alloys Compd. 333, 147–153 (2002). doi:10.1016/S0925-8388(01)01688-7

158. Karvonen, L., Yoon, S., Hug, P., Yamauchi, H., Weidenkaff, A., Karppinen, M.: The n = 3 member of the $SrCoO_{(3n-1)/n}$ series of layered oxygen-defect perovskites. Mater. Res. Bull. 46, 1340–1345 (2011). doi:10.1016/j.materresbull.2011.05.028

159. Kessel, H.U., Hennicke, J., Kirchner, R., Kessel, T.: Rapid sintering of novel materials by FAST/SPS -further development to the point of an industrial production process with high cost efficiency. FCT Systeme GmbH, Rauenstein, Germany (2015)

160. Rietveld, H.M.: A profile refinement method for nuclear and magnetic structures. J. Appl. Crystallogr. 2, 65–71 (1969). doi:10.1107/S0021889869006558

161. Rodríguez-Carvajal, J.: Recent advances in magnetic structure determination by neutron powder diffraction. Phys. B Condens. Matter. 192, 55–69 (1993). doi:10.1016/0921-4526(93)90108-I

162. Le Bail, A., Duroy, H., Fourquet, J.L.: Ab-initio structure determination of $LiSbWO_6$ by X-ray powder diffraction. Mater. Res. Bull. 23, 447–452 (1988). doi:10.1016/0025-5408(88)90019-0

163. Sagarna, L.: Thermoelectric properties of $EuTiO_3$ and related materials, University of Bern, (2014)

164. Quantum Design, Inc.: PPMS Thermal Transport Option User's Manual. Quantum Design, San Diego, USA (2002)

165. Parker, W.J., Jenkins, R.J., Butler, C.P., Abbott, G.L.: Flash Method of Determining Thermal Diffusivity, Heat Capacity, and Thermal Conductivity. J. Appl. Phys. 32, 1679–1684 (2004). doi:10.1063/1.1728417

166. Mehling, H., Hautzinger, G., Nilsson, O., Fricke, J., Hofmann, R., Hahn, O.: Thermal Diffusivity of Semitransparent Materials Determined by the Laser-Flash Method Applying a New Analytical Model. Int. J. Thermophys. 19, 941–949 (1998). doi:10.1023/A:1022611527321

167. Blumm, J., Opfermann, J.: Improvement of the mathematical modeling of flash measurements. High Temp. High Press. 34, 515–521 (2002)

168. Cape, J.A., Lehman, G.W.: Temperature and Finite Pulse-Time Effects in the Flash Method for Measuring Thermal Diffusivity. J. Appl. Phys. 34, 1909–1913 (1963). doi:10.1063/1.1729711

169. NETZSCH-Gerätebau GmbH: Thermoelectric Materials Material Characterization - Phase Changes, Thermal Conductivity, www.netzsch.com/n47875

170. Anter Corporation: Measurement of Thermal Diffusivity Using the Flash Method, http://www.azom.com/article.aspx?ArticleID=5613

171. Taica Corporation: αGEL® COH Series (Sheet-type thermal gel), http://www.taica.co.jp/gel-english/products/product/gel.html

172. Xie, W., He, J., Zhu, S., Holgate, T., Wang, S., Tang, X., Zhang, Q., Tritt, T.M.: Investigation of the sintering pressure and thermal conductivity anisotropy of melt-spun spark-plasma-sintered $(Bi,Sb)_2Te_3$ thermoelectric materials. J. Mater. Res. 26, 1791–1799 (2011). doi:10.1557/jmr.2011.170

173. Note: For the laser flash measurement the lamella were put into a square-shaped sample holder and the upper side was coated with an Ethanol - $Ca_3Co_4O_9$ slurry, sprayed on the lamella with an airbrush (A709 by AZTEK), to fill the small gaps between the lamella. The cobalt oxide powder for the slurry was produced through a soft chemistry method.

174. Populoh, S., Aguirre, M.H., Brunko, O.C., Galazka, K., Lu, Y., Weidenkaff, A.: High figure of merit in (Ti,Zr,Hf)NiSn half-Heusler alloys. Scr. Mater. 66, 1073–1076 (2012). doi:10.1016/j.scriptamat.2012.03.002

175. Wang, Y., Sui, Y., Cheng, J., Wang, X., Su, W., Fan, H.: Influence of Y^{3+} doping on the high-temperature transport mechanism and thermoelectric response of misfit-layered $Ca_3Co_4O_9$. Appl. Phys. A. 99, 451–458 (2010). doi:10.1007/s00339-010-5543-1

176. Schrade, M.: On the Oxygen Nonstoichiometry in Thermoelectric Oxides, University of Oslo, (2014)

177. Zhang, L., Okinaka, N., Tosho, T., Akiyama, T.: Preparation and thermoelectric properties of highly oriented calcium cobalt oxides by solution combustion synthesis with post-spark plasma sintering. J. Optoelectron. Adv. Mater. 14, 67 (2012)

178. Wakisaka, Y., Hirata, S., Mizokawa, T., Suzuki, Y., Miyazaki, Y., Kajitani, T.: Electronic structure of $Ca_3Co_4O_9$ studied by photoemission spectroscopy: Phase separation and charge localization. Phys. Rev. B. 78, 235107 (2008). doi:10.1103/PhysRevB.78.235107

179. Miyazaki, Y., Onoda, M., Oku, T., Kikuchi, M, Ishii, Y., Ono, Y., Morii, Y., Kajitani, T.: Modulated Structure of the Thermoelectric Compound $[Ca_2CoO_3]_{0.62}CoO_2$. J. Phys. Soc. Jpn. 71, 491–497 (2002). doi:10.1143/JPSJ.71.491

180. Austin, I.G., Mott, N.F.: Polarons in crystalline and non-crystalline materials. Adv. Phys. 18, 41–102 (1969). doi:10.1080/00018736900101267

181. Mott, N.F., Davis, E.A.: Electronic Processes in Non-Crystalline Materials. OUP Oxford (2012)

182. Zhou, X.-D., Pederson, L.R., Thomsen, E., Nie, Z., Coffey, G.: Nonstoichiometry and Transport Properties of $Ca_3Co_{4\pm x}O_{9+\delta}$ (x =0–0.4). Electrochem. Solid-State Lett. 12, F1–F3 (2009). doi:10.1149/1.3039948

183. Saucke, G., Populoh, S., Xie, W., Trottmann, M., Hertrampf, J., Döbeli, M., Karvonen, L., Songhak, Y., Thiel, P., Niewa, R., Weidenkaff, A.: Thermoelectric properties of $[Ca_2CoO_{3-\delta}][CoO_2]_{1.62}$ as a function of Co/Ca ratio and Co_3O_4 inclusions. submitted. (2016)

184. Baltz, R. v., Birkholz, U.: Polaronen. In: Advances in Solid State Physics. pp. 233–341. Elsevier (1972)

185. Yin, T., Liu, D., Ou, Y., Ma, F., Xie, S., Li, J.-F., Li, J.: Nanocrystalline Thermoelectric $Ca_3Co_4O_9$ Ceramics by Sol−Gel Based Electrospinning and Spark Plasma Sintering. J. Phys. Chem. C. 114, 10061–10065 (2010). doi:10.1021/jp1024872

186. Delorme, F., Diaz-Chao, P., Guilmeau, E., Giovannelli, F.: Thermoelectric properties of $Ca_3Co_4O_9$–Co_3O_4 composites. Ceram. Int. 41, 10038–10043 (2015). doi:10.1016/j.ceramint.2015.04.091

187. Bergman, D.J., Fel, L.G.: Enhancement of thermoelectric power factor in composite thermoelectrics. J. Appl. Phys. 85, 8205–8216 (1999). doi:10.1063/1.370660

188. Bergman, D.J., Levy, O.: Thermoelectric properties of a composite medium. J. Appl. Phys. 70, 6821–6833 (1991). doi:10.1063/1.349830

189. Li, J., Tan, Q., Li, J.-F., Liu, D.-W., Li, F., Li, Z.-Y., Zou, M., Wang, K.: BiSbTe-Based Nanocomposites with High ZT: The Effect of SiC Nanodispersion on Thermoelectric Properties. Adv. Funct. Mater. 23, 4317–4323 (2013). doi:10.1002/adfm.201300146

190. Zhang, Y., Bahk, J.-H., Lee, J., Birkel, C.S., Snedaker, M.L., Liu, D., Zeng, H., Moskovits, M., Shakouri, A., Stucky, G.D.: Hot Carrier Filtering in Solution Processed Heterostructures: A Paradigm for Improving Thermoelectric Efficiency. Adv. Mater. 26, 2755–2761 (2014). doi:10.1002/adma.201304419

191. Faleev, S.V., Léonard, F.: Theory of enhancement of thermoelectric properties of materials with nanoinclusions. Phys. Rev. B. 77, 214304 (2008). doi:10.1103/PhysRevB.77.214304

192. Xie, W.J., He, J., Zhu, S., Su, X.L., Wang, S.Y., Holgate, T., Graff, J.W., Ponnambalam, V., Poon, S.J., Tang, X.F., Zhang, Q.J., Tritt, T.M.: Simultaneously optimizing the independent thermoelectric properties in (Ti,Zr,Hf)(Co,Ni)Sb alloy by in situ forming InSb nanoinclusions. Acta Mater. 58, 4705–4713 (2010). doi:10.1016/j.actamat.2010.05.005

193. Saucke, G., Populoh, S., Thiel, P., Xie, W., Funahashi, R., Weidenkaff, A.: Compatibility approach for the improvement of oxide thermoelectric converters for industrial heat recovery applications. J. Appl. Phys. 118, 035106 (2015). doi:10.1063/1.4926476

194. Doolittle, L.R.: A semiautomatic algorithm for rutherford backscattering analysis. Nucl. Instrum. Methods Phys. Res. Sect. B Beam Interact. Mater. At. 15, 227–231 (1986). doi:10.1016/0168-583X(86)90291-0

195. Knop, O., Reid, K.I.G., Sutarno, Nakagawa, Y.: Chalkogenides of the transition elements. VI. X-Ray, neutron, and magnetic investigation of the spinels Co_3O_4, $NiCo_2O_4$, Co_3S_4, and $NiCo_2S_4$. Can. J. Chem. 46, 3463–3476 (1968). doi:10.1139/v68-576

196. Wang, Z., Wang, W., Zhang, L., Jiang, D.: Surface oxygen vacancies on Co_3O_4 mediated catalytic formaldehyde oxidation at room temperature. Catal. Sci. Technol. 6, 3845–3853 (2016). doi:10.1039/C5CY01709B

197. Sahoo, P., Djieutedjeu, H., Poudeu, P.F.P.: Co_3O_4 nanostructures: the effect of synthesis conditions on particles size, magnetism and transport properties. J. Mater. Chem. A. 1, 15022–15030 (2013). doi:10.1039/C3TA13442C

198. Eng, H.W., Limelette, P., Prellier, W., Simon, C., Frésard, R.: Unconventional Hall effect in oriented $Ca_3Co_4O_9$ thin films. Phys. Rev. B. 73, 033403 (2006). doi:10.1103/PhysRevB.73.033403

199. Wu, T., Tyson, T.A., Bai, J., Pandya, K., Jaye, C., Fischer, D.: On the origin of enhanced thermoelectricity in Fe doped $Ca_3Co_4O_9$. J. Mater. Chem. C. 1, 4114–4121 (2013). doi:10.1039/C3TC30481G

200. Cheng, C.-S., Serizawa, M., Sakata, H., Hirayama, T.: Electrical conductivity of Co_3O_4 films prepared by chemical vapour deposition. Mater. Chem. Phys. 53, 225–230 (1998). doi:10.1016/S0254-0584(98)00044-3

201. Patil, V., Joshi, P., Chougule, M., Sen, S.: Synthesis and Characterization of Co_3O_4 Thin Film. Soft Nanosci. Lett. 02, 1 (2011). doi:10.4236/snl.2012.21001

202. Thota, S., Kumar, A., Kumar, J.: Optical, electrical and magnetic properties of Co_3O_4 nanocrystallites obtained by thermal decomposition of sol–gel derived oxalates. Mater. Sci. Eng. B. 164, 30–37 (2009). doi:10.1016/j.mseb.2009.06.002

203. Yang, X.H., Qin, X.Y., Zhang, J., Li, D., Xin, H.X., Liu, M.: Enhanced thermopower and energy filtering effect from synergetic scattering at heterojunction potentials in the thermoelectric composites with semiconducting nanoinclusions. J. Alloys Compd. 558, 203–211 (2013). doi:10.1016/j.jallcom.2012.12.048

204. Shannon, R.D.: Revised effective ionic radii and systematic studies of interatomic distances in halides and chalcogenides. Acta Crystallogr. Sect. A. 32, 751–767 (1976). doi:10.1107/S0567739476001551

205. Peng, J., Fu, L., Liu, Q., Liu, M., Yang, J., Hitchcock, D., Zhou, M., He, J.: A study of $Yb_{0.2}Co_4Sb_{12}$–$AgSbTe_2$ nanocomposites: simultaneous enhancement of all three thermoelectric properties. J. Mater. Chem. A. 2, 73–79 (2013). doi:10.1039/C3TA13729E

206. Choudhury, K.R., Winiarz, J.G., Samoc, M., Prasad, P.N.: Charge carrier mobility in an organic-inorganic hybrid nanocomposite. Appl. Phys. Lett. 82, 406–408 (2003). doi:10.1063/1.1537054

207. Fujii, S., Yoshiya, M.: Manipulating Thermal Conductivity by Interfacial Modification of Misfit-Layered Cobaltites $Ca_3Co_4O_9$. J. Electron. Mater. 45, 1217 (2016). doi:10.1007/s11664-015-3938-7

208. Crane, D., LaGrandeur, J., Jovovic, V., Ranalli, M., Adldinger, M., Poliquin, E., Dean, J., Kossakovski, D., Mazar, B., Maranville, C.: TEG On-Vehicle Performance and Model Validation and What It Means for Further TEG Development. J. Electron. Mater. 42, 1582–1591 (2013). doi:10.1007/s11664-012-2327-8

209. Woermann, E., Muan, A.: Phase equilibria in the system CaO-cobalt oxide in air. J. Inorg. Nucl. Chem. 32, 1455–1459 (1970). doi:10.1016/0022-1902(70)80631-5

210. Bartholomé, K., Balke, B., Zuckermann, D., Köhne, M., Müller, M., Tarantik, K., König, J.: Thermoelectric Modules Based on Half-Heusler Materials Produced in Large Quantities. J. Electron. Mater. 43, 1775–1781 (2014). doi:10.1007/s11664-013-2863-x

211. Seifert, W., Zabrocki, K., Snyder, G.J., Müller, E.: The compatibility approach in the classical theory of thermoelectricity seen from the perspective of variational calculus. Phys. Status Solidi A. 207, 760–765 (2010). doi:10.1002/pssa.200925460

212. Ohtaki, M.: Recent aspects of oxide thermoelectric materials for power generation from mid-to-high temperature heat source. J. Ceram. Soc. Jpn. 119, 770–775 (2011). doi:10.2109/jcersj2.119.770

213. Buchmann, I.: Charging Lithium-Ion Batteries, http://batteryuniversity.com/learn/article/charging_lithium_ion_batteries

214. Idota, Y., Kubota, T., Matsufuji, A., Maekawa, Y., Miyasaka, T.: Tin-Based Amorphous Oxide: A High-Capacity Lithium-Ion-Storage Material. Science. 276, 1395–1397 (1997). doi:10.1126/science.276.5317.1395

215. TES NewEnergy: Thermo Electric Generator unit, http://tes-ne.com/English/03-1_product_e.html

216. Thermonamic Electronics (Jiangxi) Corp., Ltd.: Modules for Power Generation, http://www.thermonamic.com/products.asp?cid=384

217. Koubek, N.: Jenseits und Diesseits Der Betriebswirtschaftslehre: Institutionen ? Unternehmenstheorien ? Globale Strukturen. Springer DE (2010)

218. Heindl Server GmbH: Photovoltaik: Industrie auf dem Weg zu deutlich sinkenden Herstellungskosten, http://www.solarserver.de/news/news-8904.html

219. Noudem, J.G., Kenfaui, D., Chateigner, D., Gomina, M.: Toward the enhancement of thermoelectric properties of lamellar $Ca_3Co_4O_9$ by edge-free spark plasma texturing. Scr. Mater. 66, 258–260 (2012). doi:10.1016/j.scriptamat.2011.11.004

220. Drasovean, R., Condurache-Bota, S., Tigau, N.: Structual and electrical characterization of cobalt oxide semiconductors. J. Sci. Arts. 2, 379 (2010)

221. Sakamoto, S., Yoshinaka, M., Hirota, K., Yamaguchi, O.: Fabrication, Mechanical Properties, and Electrical Conductivity of Co_3O_4 Ceramics. J. Am. Ceram. Soc. 80, 267–268 (1997). doi:10.1111/j.1151-2916.1997.tb02824.x

Acknowledgments

I would like to express my gratitude to all of those who helped and supported me during my PhD thesis.

First of all, I would particularly like to thank Prof. Anke Weidenkaff, head of the Chemical material synthesis group at the Institute of Materials Science, University of Stuttgart, and former head of the department for Solid State Chemistry and Catalysis at Empa. She gave me the opportunity to carry out my PhD thesis in her team and provided me with valuable support, advices, and ideas. I highly appreciate her scientific feedback and her approachable and congenial attitude. I also thank Prof. Jochen Mannhart for being part of the evaluation committee, and Prof. Thomas Schleid for taking the presidency of the examination committee.

Furthermore, I would like to express my gratitude to Sascha Populoh and Wenjie Xie for supervising me and giving helpful suggestions during the writing process. I deeply acknowledge their scientific support, their constructive comments, and warm encouragements.

At this point, I would also like express my appreciation for the professional support and the pleasant working atmosphere to the whole Solid State Chemistry and Catalysis group at Empa and the material synthesis group in Stuttgart. Among my colleges, I have greatly benefited from the cooperation and mutual assistance with Philipp Thiel in our BFE- and HITTEC-projects. I highly appreciated the numerous valuable discussions, his hands-on mentality and his advices concerning material synthesis in the lab. A big thanks also goes to Lassi Karvonen for discussions about the misfit-layered oxides in general and his insightful comments. I would also like to thank Songhak Yoon for his advice about crystallography, Krzysztof Galazka for introducing me to experimental methods, Leyre Sagarna for her help with SEM-measurements and Matthias Trottman for experimental support and his great assistance during the measurements in the casting company vonRoll casting. Additionally, I want to thank James Eilertsen for being a valuable counsel in scientific and language questions, Andrey Shkabko, Oliver Brunko, Nina Vogel-Schäuble, Xingxing Xiao and Corsin Battaglia who were always open for questions and discussions.

I would also like to offer my special thanks to my external collaborators, in particular Mathias Schmid for fruitful discussions about the theory of compatibility, Max Döbeli for investigating my samples via Rutherford backscattering spectrometry, Sara Romer for helping with PPMS measurements, Roman Furrer for the determination of the emissivity of my materials, and Jan Hertrampf for jumping in with DSC-measurements after a breakdown of the machine at Empa. Greatly acknowledged is also the support provided by Anton Rechsteiner for coordinating the measurements in vonRoll casting. Furthermore, I would like to express my deepest appreciation to Ryoji Funahashi and the Synthetic Nano-Function Materials for accepting me as a guest at AIST in Japan for 7 weeks. During the fruitful stay, I have received generous support and advice from him and his team, where Yoko Matsumura and Tomoyuki Urata introduced me to their technique of the module fabrication.

Finally, I would like to thank my parents, my sister and my friends who constantly supported me. In particular, I deeply appreciate the unconditional support of my husband Felix Büttner, without his encouragement and advices, this dissertation would not have materialized. Special thanks goes to him for reading through parts of this thesis.

Financial support from the Bundesamt für Energie (BFE) under Grant No. Si/500601, the Competence Centre Energy and Mobility (HITTEC Project) and Empa (Swiss Federal Laboratories for Materials Science and Technology) in Switzerland are greatly acknowledged.

Declaration of Authorship

I hereby certify that the dissertation entitled

“Misfit-layered cobalt oxides for thermoelectric energy conversion”

is entirely my own work except where otherwise indicated. Passages and ideas from other sources have been clearly indicated.

Erklärung über die Eigenständigkeit der Dissertation

Ich versichere, dass ich die vorliegende Arbeit mit dem Titel

“Misfit-layered cobalt oxides for thermoelectric energy conversion”

selbständig verfasst und keine anderen als die angegebenen Quellen und Hilfsmittel benutzt habe; aus fremden Quellen entnommene Passagen und Gedanken sind als solche kenntlich gemacht.

Name/Name: _____

Signature/Unterschrift: _____

Date/Datum: _____

Publications

- **Büttner, G**., Populoh, S., Xie, W., Trottmann, M., Hertrampf, J., Döbeli, M., Karvonen, L., Songhak, Y., Thiel, P., Niewa, R., Weidenkaff, A.: Thermoelectric properties of $[Ca_2CoO_{3-\delta}][CoO_2]_{1.62}$ as a function of Co/Ca defects and Co_3O_4 inclusions. Journal of Applied Physics. 121, 215101 (2017).

- Huber, L., Ruch, P., Hauert, R., **Saucke, G**., Matam, S.K., Michel, B., Koebel, M.M.: Monolithic nitrogen-doped carbon as a water sorbent for high-performance adsorption cooling. RSC Adv. 6, 25267–25278 (2016).

- Huber, L., Ruch, P., Hauert, R., Matam, S.K., **Saucke, G**., Yoon, S., Zhang, Y., Koebel, M.M.: Water sorption behavior of physically and chemically activated monolithic nitrogen doped carbon for adsorption cooling. RSC Adv. 6, 80729–80738 (2016).

- **Saucke, G**., Populoh, S., Thiel, P., Xie, W., Funahashi, R., Weidenkaff, A.: Compatibility approach for the improvement of oxide thermoelectric converters for industrial heat recovery applications. Journal of Applied Physics. 118, 035106 (2015).

- Thiel, P., Populoh, S., Yoon, S., **Saucke, G**., Rubenis, K., Weidenkaff, A.: Charge-Carrier Hopping in Highly Conductive $CaMn_{1-x}M_xO_{3-\delta}$ Thermoelectrics. The Journal of Physical Chemistry C. 119, 21860–21867 (2015).

- Populoh, S., Brunko, O., Karvonen, L., Sagarna, L., **Saucke, G**., Thiel, P., Trottmann, M., Vogel-Schäuble, N., Weidenkaff, A.: Perovskite and Related Oxides for Energy Harvesting by Thermoelectricity. In: Granger, P., Parvulescu, V.I., Parvulescu, V.I., and Prellier, W. (eds.) Perovskites and Related Mixed Oxides. pp. 189–210. Wiley-VCH Verlag GmbH & Co. KGaA, Weinheim, Germany (2015).

- Gałązka, K., Populoh, S., Xie, W., Yoon, S., **Saucke, G**., Hulliger, J., Weidenkaff, A.: Improved thermoelectric performance of $(Zr_{0.3}Hf_{0.7})NiSn$ half-Heusler compounds by Ta substitution. Journal of Applied Physics. 115, 183704 (2014).

- **Saucke, G**., Populoh, S., Vogel-Schäuble, N., Sagarna, L., Mogare, K., Karvonen, L., Weidenkaff, A.: Thermoelectric properties of Ru and In substituted misfit-layered $Ca_3Co_4O_9$. MRS Proceedings. 1543, 83–92 (2013).

- Thiel, P., Eilertsen, J., Populoh, S., **Saucke, G**., Döbeli, M., Shkabko, A., Sagarna, L., Karvonen, L., Weidenkaff, A.: Influence of tungsten substitution and oxygen deficiency on the thermoelectric properties of $CaMnO_{3-\delta}$. Journal of Applied Physics. 114, 243707 (2013).

- **Saucke, G**., Norpoth, J., Jooss, C., Su, D., Zhu, Y.: Polaron absorption for photovoltaic energy conversion in a manganite-titanate *pn* heterojunction. Phys. Rev. B. 85, 165315 (2012).

Project reports:

- **Saucke, G**., Weidenkaff, A., Populoh, S.: Kostengünstige und verlässliche thermoelektrische Konverter für die Nutzung industrieller Abwärme - Abschlussbericht. BFE - Bundesamt für Energie (2014).

- **Saucke, G**., Weidenkaff, A.: Kostengünstige und verlässliche thermoelektrische Konverter für die Nutzung industrieller Abwärme - Jahresbericht 2013. BFE - Bundesamt für Energie (2013).

- **Saucke, G**., Weidenkaff, A.: Kostengünstige und verlässliche thermoelektrische Konverter für die Nutzung industrieller Abwärme - Jahresbericht 2012. BFE - Bundesamt für Energie (2012).

- **Saucke, G**., Moser, D., Weidenkaff, A.: Cost-efficient and reliable thermoelectric converters for industrial waste heat recovery - Jahresbericht 2011. BFE - Bundesamt für Energie (2011).